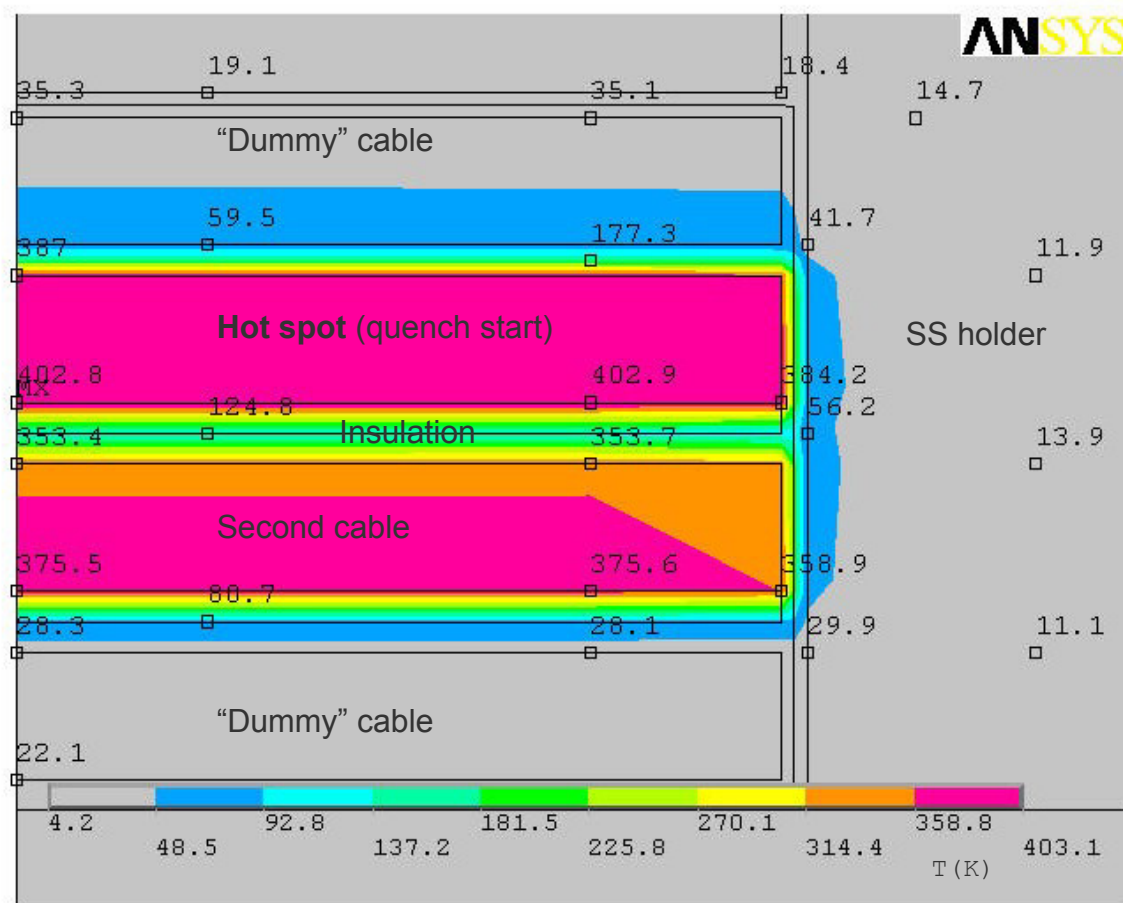


# Studies of Quench Protection in $\text{Nb}_3\text{Sn}$ Superconducting Magnets for Future Particle Accelerators



Linda Imbasciati

**TU-Wien**  
Vienna Technical University

# **Studies of Quench Protection in Nb<sub>3</sub>Sn Superconducting Magnets for Future Particle Accelerators**

A dissertation submitted to the Vienna Technical University  
Faculty of Technical and Natural Sciences  
in candidacy for the degree of Doctor of Technical Sciences  
under the supervision of

Prof. HANS R. KIRCHMAYR  
INSTITUTE of CONDENSED MATTER PHYSICS

Research performed at

FERMI NATIONAL ACCELERATOR LABORATORY  
Technical Division, Development and Test Dept., under the supervision of

Dr. PIERRE BAUER

By

**LINDA IMBASCIATI**  
V. Vittadini 9, 20136, Milan, Italy

Vienna,

June 25, 2003

# Contents

Abstract	IV
Kurzfassung	VI
<b>Chapter 1</b>	<b>Page</b>
1. Nb <sub>3</sub> Sn Superconducting Magnets for Particle Accelerators	1
1.1 Superconducting magnets for particle accelerators	2
1.2 Basic properties of Nb <sub>3</sub> Sn superconductor	3
1.3 Nb <sub>3</sub> Sn magnets for particle accelerators	6
1.3.a The Large Hadron Collider Upgrade	6
1.3.b The Very Large Hadron Collider (VLHC)	7
1.3.c VLHC-2 FNAL magnets	8
1.3.d Nb <sub>3</sub> Sn high field magnet models at Fermilab	10
1.3.e Nb <sub>3</sub> Sn high field magnets around the world	11
1.4 Conclusions	17
References	17
<b>Chapter 2</b>	<b>Page</b>
2. Quench protection calculations for Nb <sub>3</sub> Sn accelerator magnets	1
2.1 Basics of the quench process	2
2.1.a Quench causes and stabilization	2
2.1.b Consequences of the quench	3
2.1.c Common quench protection strategies	5
2.1.d Calculation of the main quench parameters	10
2.2 Quench simulations	14
2.2.a Common quench simulation programs	15
2.2.b QLASA	16
2.2.c Quenchpro	20
2.2.d Contribution of the insulation to the adiabatic quench process	22
2.2.e Parametric quench studies for VLHC dipole magnets	23
2.2.f Summary of VLHC parametric studies	27
2.3 General quench study	28
2.3.a Analytical model	28
2.3.b Peak temperature analytic calculations results	34
2.3.c Summary of the general quench study	36
2.4 Conclusions of quench protection studies	37
References	39

Chapter 3	Page
3. Material Properties and Quench Parameters	1
3.1 Scaling laws of Nb <sub>3</sub> Sn superconductor	2
3.1.a Relation between critical current density and field	2
3.1.b Temperature dependence	2
3.1.c Strain dependence	4
3.2 Thermal conductivity measurements of Nb <sub>3</sub> Sn cable stacks	7
3.2.a Description of the samples	8
3.2.b Apparatus description	8
3.2.c Experimental results	10
3.3 Thermal conductivity modeling	11
3.3.a Thermal conductivity of the insulating layer of sample # 2	12
3.3.b Thermal conductivity of the bare sample (# 3)	12
3.3.c Overall thermal conductivity of sample 1 (with e-glass insulation)	18
3.3.d Summary of thermal conductivity study	20
3.4 Material properties for quench integrals	20
3.4.a Specific heat and density	21
3.4.b Resistivity	22
3.4.c Conductivity	22
3.5 Thermo-mechanical properties	23
3.5.a Elasticity modulus	23
3.5.b Thermal contraction	25
3.6 Measurements of quench parameters	26
3.6.a Quench velocities	27
3.6.b Experimental quench heater study	28
References	31
Chapter 4	Page
4. Quench experiment on cables	1
4.1 Cable quench experiment	2
4.1.a Measurement Set-Up	2
4.1.b Measurement results	6
4.2 Adiabatic quench process simulation	10
4.3 Finite element quench process simulation	11
4.1.c Finite element models	12
4.1.d Results and Comparison with the experiment	20
4.4 Mechanical analysis	27
4.1.a Analytical estimate	28
References	33
Chapter 5	Page
5. Quench Experiment on Subscale Nb <sub>3</sub> Sn Magnet	1
5.1 Concept of the experiment	2
5.2 Experiment setup	3
5.2.a General features of LBNL Subscale Magnet Program	3
5.2.b Set up for the quench test	5
5.2.c Description of the magnet for the quench test (SM05)	7
5.3 Description of the Test	13
5.3.a Training and ramp rate study	13



### III

5.3.b Spot heater study	14
5.3.c Thermal shock study	15
5.4 Adiabatic quench process simulation	20
5.4.a Quench Integral	20
5.4.b Quench simulations	22
5.5 Mechanical analysis	23
References	27

Conclusions	Page
6. Summary and Conclusions	1
6.1 Nb <sub>3</sub> Sn accelerator magnet development	1
6.2 Quench studies	1
6.3 Material properties for quench studies	2
6.4 “Thermal-shock” quench experiments	3
6.4.a Cable quench experiment	4
6.4.b Quench simulation with ANSYS	4
6.4.c Small magnet quench experiment	5
6.4.d Contribution of insulation to thermal balance during quench	6
6.5 Conclusions	7
Acknowledgments	VIII

## Abstract

In the R&D effort towards a next generation particle accelerator, Fermilab and several other laboratories in the world are developing 10-15 T Nb<sub>3</sub>Sn magnets using several design approaches. A brief summary of these programs is given in [chapter 1](#). Protection of superconducting magnets during quench is important for the magnet safety, in particular for long accelerator models, which cannot be protected simply by energy extraction. Long accelerator magnets with Nb<sub>3</sub>Sn superconductor have not yet been built, but quench simulations indicate that peak temperatures above 300 K can arise during the quench, at the quench origin. Nb<sub>3</sub>Sn is a brittle material and it has yet to be determined to what extent it is affected by thermo-mechanical stress during a magnet quench. Rapid thermal expansion of conductor and large temperature gradients during a magnet quench can affect the performance, for example in causing detuning, or even result in permanent damage of the magnet. It is necessary to define the maximum temperatures that are allowed in the coils during a quench. Although critical current versus strain data are well established for Nb<sub>3</sub>Sn, little is known how these limitations apply in the case of the thermal shock experienced by the conductor during a magnet quench. This thesis is the first experimental and computational study addressing this issue in Nb<sub>3</sub>Sn accelerator magnets.

Quench protection studies of Nb<sub>3</sub>Sn accelerator magnets have been performed in the frame of Fermilab's development of two-layer cos $\theta$  design, and single-layer Common Coil dipole magnets ([Chapter 2](#)). Numerical codes were developed to find the requirements for the protection of these magnets. These codes were also used in studies, where magnet and conductor parameters were varied, in order to determine the optimal protection scenario. It was found that, in order to maintain the peak temperature below 400 K and the peak voltage below 1 kV, heaters covering more than 50% of the turns, or more, are necessary, conflicting with the necessity of heater redundancy. Furthermore, peak temperatures of 400 K are above the standard criterion of 300 K for NbTi magnets. Using an analytical approach to calculate the peak temperature, we were able to identify general trends of the peak temperature as a function of magnet parameters. These studies showed that in order to reduce the peak temperature during a quench in high field Nb<sub>3</sub>Sn accelerator magnet, it is necessary to find a compromise between conductor efficiency and cost while increasing the copper fraction and magnet size.

Material properties are key parameters affecting the quench process and their proper knowledge is essential for a safe design of a superconducting magnet. A collection of the main material properties affecting the quench process in Nb<sub>3</sub>Sn magnets is given in [chapter 3](#). Thermo-mechanical properties of coils are difficult to predict, because of the composite nature and complex structure, and the scarcity of experimental data. Therefore, the thermal conductivity of impregnated Nb<sub>3</sub>Sn cable stacks was measured, at cryogenic temperatures, for several samples. A model was developed to predict the thermal conductivity of a generic cable, taking into account its complex composite structure (contact thermal resistance, transposition pitch, etc.). Thermal contraction coefficients and elasticity moduli of superconducting coils are also difficult to predict, and are essential parameters for performing thermo-mechanical analysis, and therefore to understand the stress/strain conditions during quenches in superconducting magnets. Measurements of thermal contraction coefficients and elasticity moduli were performed on similar cable stack samples. The final section of chapter 3 is dedicated to measurements of critical quench parameters, performed on Nb<sub>3</sub>Sn magnets at Fermilab, such as quench propagation velocities and quench heater time delays. The measurements were also compared and used to tune quench simulation models.

To measure the critical current degradation as a function of peak temperature during a quench, quench experiments were first performed on cables, in collaboration with the National

High Magnetic Field Laboratory ([Chapter 4](#)). Two samples were tested in an 8 T background field provided by a split solenoid. Each sample-holder contained two test-cables impregnated together with two ‘dummy’ cables to better simulate the magnet environment. The experiment consisted in inducing the quench in a cable, using a spot heater, and in allowing Joule heating of the cable after the quench, for a programmed time delay, by delaying the current disconnection. The temperature rise during the quench was measured via the resistivity of the cable segment underneath the spot heater. Since the process was very fast, high thermal gradients between the “hot spot” and the surroundings induced thermo-mechanical stresses. The critical current was measured after every excursion to high temperature, and the performance degradation as a function of the peak temperature reached during the quench was assessed. The samples tested were made of ITER type Nb<sub>3</sub>Sn strands. The quench tests were performed at 8 kA, in order to operate near the critical surface of the samples. The mechanical support for the samples was provided by a pressure piston acting through the bore of the magnet (a transverse pressure on the sample of ~20 MPa was set for this test). Peak temperatures up to 420 K were reached, without seeing critical current degradation in one sample. A disruptive quench occurred in the cable after a thermal excursion to ~500 K. The peak temperature in the other sample (which had some strain due to bending after reaction) reached 330 K without critical current degradation. The quench process was simulated using numerical codes as well as using Finite Element (FE) models. Coupled electrical and thermal analyses were performed with ANSYS. Bare cable and insulation were modeled, using a fine mesh, as well as the sample holder and the other main components. The FE analysis allowed a completely integrated solution including the heat conduction from the cable to the environment. The results show high temperature gradients between the coil and the surroundings, mainly through the insulation, with temperature differences up to 320 K over 0.2 mm. These temperature gradients can produce high shear stresses, and epoxy cracking. A three-dimensional analytical model estimated the stress level to be below the irreversible limits of the conductor in all dimensions, except for shear stresses in the epoxy.

The experimental program continued, in collaboration with the Lawrence Berkeley National Laboratory, by performing the quench experiment on a small Nb<sub>3</sub>Sn magnet ([Chapter 5](#)). The use of the LBNL Small Magnet program allowed performing the quench test with a state-of-the-art conductor, in a mechanical environment similar to that of an accelerator magnet. The magnet consisted of two double-layer racetrack pancakes, assembled in a common coil configuration with a small gap in between. One of the two coils (named SC10) was prepared for this experiment. During the test, the magnet reached the maximum field of ~11 T at the short sample current of 9.1 kA. The quench experiment followed a procedure similar to that of the cable tests. Temperature excursions up to 350 K were performed during the first thermal cycle. No degradation was detected. During the second thermal cycle, to reduce the quench propagation velocity and to avoid quench back, we continued the spot heater events series at a low magnet current (3 kA), using long dump delay times (1-3 s). Temperature excursions up to 430 K did not diminish the magnet quench performance. Only after temperature excursions over 450 K, detraining effects appeared, which occasionally reduced the quench current by about 8%. Signs of irreversible degradation (reduction of the quench current by about 3%) appeared after temperature excursions over 580 K. An analytical model showed that the stresses and strains, up to ~400 K, were below the known limits of Nb<sub>3</sub>Sn. Above 430 K, the mechanical state of the coil changed, due to the glass transition of the epoxy resin.

Therefore, this study indicates that, if the stresses and strains in the conductor remain below its limits, the performance of a Nb<sub>3</sub>Sn high field magnet is not diminished by peak temperatures during a quench up to 400 K, above which the magnet safety might be compromised, with present materials, by insulation failures.

## Kurzfassung

Fermilab und andere Hochenergiephysiklabors verfolgen derzeit die Entwicklung von Hochfeldbeschleunigermagneten auf der Basis von  $\text{Nb}_3\text{Sn}$  Supraleiter im Hinblick auf die dem sich derzeit in der Schweiz im Bau befindlichen LHC folgende Generation von Hadronbeschleunigern. Nebst einem kurzen historischen Rueckblick, resumiert Kapitel 1 den derzeitigen Stand in dieser weltweiten Entwicklung, die im Falle von Dipol- (oder Steuer-) magneten Felder im Bereich von 10-12 T oder hoeher bei Betriebstemperaturen von 4-5 K anpeilen. Die sogenannte “quench protection”, d.h. die Massnahmen zur Reduktion von Spitzenspannungen und Temperaturen im Falle eines Zusammenbruchs der Supraleitung (Quench) in Elektromagneten, ist ein wesentlicher Aspekt des Designs von Beschleunigermagneten und bis heute unerforscht im Falle von  $\text{Nb}_3\text{Sn}$  Hochfeldmagneten. Obwohl die bisherige Magnetentwicklung auf kurze Prototypen beschraenkt blieb (welche leicht mit parallelen Widerstaenden beschuetzt werden koennen), haben Quenchsimulationen, die im Rahmen dieser Dissertation durchgefuehrt wurden, gezeigt, dass Spitzentemperaturen in zukuenftigen Hochfeldmagneten jenseits der 300 K zu erwarten sind.  $\text{Nb}_3\text{Sn}$  ist ein sproedes Material fuer das die Beziehung zwischen Deformation und supraleitenden Eigenschaften bereits erforscht ist. Es ist jedoch nicht bekannt ob die thermomechanischen Spannungen und hohen Temperaturgradienten die waehrend der rapiden Ausbreitung des Quenches innerhalb des Magneten auftreten, zur Beschaedigung des Supraleiters fuehren. Das hier beschriebene Forschungsprojekt hatte zum Ziel, mit Experimenten und Simulationen die maximalen Temperaturen zu definieren, die  $\text{Nb}_3\text{Sn}$  Hochfeldbeschleunigermagnete unbeschadet ueberstehen koennen.

Fuer die zuvor erwaehten Quenchsimulationen wurden Computerprogramme entwickelt, die auch zur Simulation des Quenches in den Fermilab Prototypen verwendet wurden. Desweiteren wurden mit diesen Programmen die Effekte der verschiedenen Magnetdesignparameter auf die Spitzenspannung und Spitzentemperatur ermittelt. Die Resultate dieser Simulationen wurden, unter anderem, in der in 2001 veroeffentlichten Studie fuer eine Nachfolger des LHC, des sogenannten VLHC (Very Large Hadron Collider), verwendet. Kapitel 2 beschreibt diese Programme und die Resultate der Berechnungen und zeigt, dass zur Beschraenkung der Temperaturen und Spannungen waehrend eines quenches auf unter 400 K und 1 kV, grossflaechige Heizer, die mehr als 50 % der Spulenoberflaeche bedecken, notwendig sind. Diese Heizer, die ueblicherweise 10-20 % der Spulenoberflaeche in supraleitenden Beschleunigermagneten bedecken, dienen zur grossflaechigen Ausbreitung des quenches und damit zur gleichmaessigen Verteilung der im Magneten gespeicherten Energie (die waehrend eines quenches in Waerme umgewandelt wird) ueber das groesstmoeegliche Volumen zur Verringerung der Spitzentemperatur. Solch grossflaechige Heizer sind schwer mit der aus Sicherheitsgruenden benoetigten Heizerredundanz vereinbar. Weiters muessen auch andere Parameter, wie die Stromdichte im Stabilisator (praktische Supraleiter sind multifilamentaer, d.h sie bestehen aus vielen Filamenten in einer stabilisierenden Matrix aus z.B. Kupfer um die Joule'sche Waermeentwicklung im Falle des quenches zu reduzieren) erhoeht werden was zu einer Vergroesserung des Spulenvolumens (und der Magnetkosten) fuehrt.

Materialeigenschaften sind ein wesentlichen Bestandteil der Quenchsimulationen. Im Rahmen dieser Dissertation wurde ein experimentelles Programm zur Ermittlung der thermomechanischen Eigenschaften von  $\text{Nb}_3\text{Sn}$  Magnetspulen lanciert. Im speziellen wurden Messungen der thermischen Leitfaehigkeit von verkleinerten Spulenmodellen gemessen und theroretische Modelle enwtickelt die anhand der geometrischen Verhaeltnisse und der Materialien die diese Spulen bilden (Supraleiter, Glassfiberisolation, Epoxy) die Berechnung der

Leitfähigkeit ermöglicht. Messungen der thermischen Kontraktionskoeffizienten und der Elastizitätsmoduli wurden auch durchgeführt. Schliesslich wurden die wichtigsten Quenchprozessparameter, wie die Quenchausbreitungsgeschwindigkeit und die thermische Reaktionszeit der Quenchheizer in den Fermilab Nb<sub>3</sub>Sn Prototypmagneten gemessen und durch Modelle beschrieben. Kapitel 3 fasst die Resultate der Materialstudien zusammen.

Die experimentelle Ermittlung der Effekte von hohen Temperaturexkursionen auf den spröden Supraleiter verwendete den kritischen Strom als Mass für den erlittenen Schaden nach Erwärmung. Eine Serie von Kabelexperimenten, die in Kapitel 4 beschrieben werden, wurden am National High Magnetic Field Laboratory (NHMFL) durchgeführt, in der weltweit einzigen Testanlage für supraleitende Kabel mit ausreichenden starken Magnetfeldern (~10 T) und Stromquellen (>10 kA). Kapitel 5 beschreibt ähnliche Messungen die im Lawrence Berkeley National Laboratory (LBNL) an sogenannten racetrack Spulen durchgeführt wurden. Im Fall von Spulen ist es notwendig, dass die Spulen das von dem Supraleiter gesetzte Strom/Feld limit erreichen, was nur wenige Nb<sub>3</sub>Sn Magnete derzeit erreichen. Die LBNL Spulen erfüllten diese Bedingung und wurden daher für diese Experimente ausgewählt. Die Kabelmessungen beruhten auf der folgenden Anordnung: eine Scheife aus zwei, ~1m langen supraleitenden Kabel (aus ITER Nb<sub>3</sub>Sn Draht) wurde in einem für kritische Strommessungen üblichen Probenhalter eingebaut, in einem 8 T Feld unter Strom gesetzt und mit einem kleinen Heizer ge-quenched. Anstatt, wie in kritischen Strommessungen üblich, den Strom nach einem quench so schnell als möglich abzuschalten, wurde dieser gemäss einer zuvor definierten Verzögerung weiter in die Proben eingespeist um durch Jouleeffekt in dem nun normalleitenden Kabel die Erwärmung zu erzielen. Da dieser Prozess in Bruchteilen einer Sekunde verläuft entstehen thermomechanische Spannungen zwischen dem erhitzten Kabel und dem kryogenisch gekühlten Probenhalter. Der kritische Strom der Proben wurde nach jeder Temperaturexkursion gemessen um Schaden festzustellen. Spitzentemperaturen von 420 K wurden in diesen Experimenten erreicht, ohne eine merkliche Verringerung des kritischen Stroms im Supraleiter. Der Quenchprozess wurde mit numerischen Modellen und einem finite Elemente Code (ANSYS) simuliert. Die Modelle wurden an den Messungen kalibriert und ermöglichten ein detailliertes Aufzeichnen der zeitlichen und räumlichen Entwicklung der Temperaturen und Spannungen. Es zeigte sich, dass zwar die Deformationen im Supraleiter unter den bekannten Grenzwerten verblieb, jedoch in der Isolierschicht sehr hohe Scheerspannungen auftraten. Die Experimente wurden, gemäss demselben Verfahren, im LBNL fortgesetzt, wo, Nb<sub>3</sub>Sn Spulen aus dem sogenannten "small-magnet" Programm mit Heizern, Spannungs-abgriffen und Temperatursensoren ausgestattet wurden um Quenchmessungen (mit neuestem Nb<sub>3</sub>Sn Supraleiter) in einem mechanischen Umfeld, das dem eines Beschleunigermagneten ähnlich ist, durchzuführen. Der LBNL Testmagnet bestand aus zwei doppelagigen racetrack Spulen die übereinander in eine massive mechanische Halterung eingebaut wurden. Dieser Magnet, obwohl nur ~30 cm lang, erreichte ~11 T mit 9.1 kA. Wie im Kabel experiment wurden Spitzentemperaturen von bis zu 430 K ohne folgende Leistungseinbussen erreicht. Bei Temperaturen jenseits von 450 K trat sogenanntes detraining auf, d.h. der Quenchstrom im Magneten wurde verringert, konnte jedoch nach einigen Trainingsquenchen wieder auf den ursprünglichen Wert gebracht werden. Zeichen irreversiblen Schadens traten nach Temperaturen jenseits der 580 K auf. Analytische Modelle zeigen, dass die Spannungen im Supraleiter unter ~400 K innerhalb der bekannten Limitierungen verblieben.

Diese Dissertation hat die grundlegende Problematik im Hinblick auf die quench protection von Nb<sub>3</sub>Sn Hochfeldmagneten formuliert und es durch aufwendige Experimente ermöglicht die praktische Temperaturlimits in diesen Magneten festzustellen. In einem gut designten Nb<sub>3</sub>Sn Magnet sollte es, diesen Experimenten zufolge, möglich sein 400 K während eines quenchs zu erreichen ohne nachhaltige Schäden an Isolierung und Supraleiter.

# 1. Nb<sub>3</sub>Sn Superconducting Magnets for Particle Accelerators

Chapter 1 Table of Contents:	Page
1. Nb <sub>3</sub> Sn Superconducting Magnets for Particle Accelerators	1
1.1 Superconducting magnets for particle accelerators	2
1.2 Basic properties of Nb <sub>3</sub> Sn superconductor	3
1.3 Nb <sub>3</sub> Sn magnets for particle accelerators	6
1.3.a The Large Hadron Collider Upgrade	6
1.3.b The Very Large Hadron Collider (VLHC)	7
1.3.c VLHC-2 FNAL magnets	8
1.3.d Nb <sub>3</sub> Sn high field magnet models at Fermilab	10
1.3.e Nb <sub>3</sub> Sn high field magnets around the world	11
1.4 Conclusions	15
References	15

## 1.1 Superconducting magnets for particle accelerators

The first particle accelerator based on superconducting magnets was the Tevatron at Fermilab, which began operation in 1983. Today, the use of superconducting magnets, allows the machine to accelerate protons to an energy of almost 1 TeV, in a ring of about 2 km radius. The kinetic energy  $E_k$  of a relativistic particle with charge  $e$ , which moves on a circular orbit with radius  $R$ , is proportional to the radius and to the dipole magnetic field intensity  $B_0$  needed to steer it

$$E_k = e \cdot B_0 \cdot R \cdot c, \quad (1.1)$$

where  $c$  is the velocity of light. Therefore, higher energies can be reached in circular accelerators by increasing the radius of the machine, or by increasing the dipole field. The radius of the machine is often restricted by available space or by tunneling costs, while the field intensity of conventional electromagnets is practically restricted to the iron saturation value of 1-2 T, without incurring enormous power consumption levels during operation. The first particle accelerator to overcome this limit by the extensive use of the superconducting technology was the Tevatron at Fermilab [1.1], where about 1000 superconducting dipole and quadrupole magnets and hundreds of other small magnets have been developed, built, tested, installed, and operated at 4 - 5 K.

The chosen superconducting material was NbTi. Also the conductor fabrication for the accelerator led to a great improvement of the NbTi conductor, with a current density capability in the superconductor improving from 1800 A/mm<sup>2</sup> at 5 T/4.2 K, to about 2500 A/mm<sup>2</sup>. Later on, several other accelerators were built using NbTi superconducting magnets, as shown in Table 1.1. NbTi superconductors can carry 3000 A/mm<sup>2</sup> nowadays, thanks to the efforts made for the construction of these particle accelerators.

Accelerator	Organization	Radius (km)	Bore field (T)	Magnet temperature (K)	Year		Energy (TeV)	
Tevatron	Fermilab	1	4.5	4	LHe	1983	Operating	2 c.m. p-pbar
HERA	DESY	1	5.5	4.5	LHe	1991	Prot.-elect.	0.92 p to target
RHIC	BNL	1.2	3.5	4.6	LHe	1999	Heavy ions	0.2 c.m.
SSC	SSCL	14	6.6	4.35	LHe	1993	Dismissed	40 c.m. p-p
LHC	CERN	4	8.3	1.9	LHe II	2007	Scheduled	14 c.m. p-p
VLHC-1	Fermilab	35	2	4.5	LHe	2015	HEPAP recc.	40 c.m. p-p
VLHC-2	Fermilab	35	11	4.5	LHe	2030	?	175 c.m. p-p

Table 1.1: Superconducting magnets for accelerators survey.

Nowadays, the NbTi superconductor is in a mature state, reaching its maximum limits as stated in Table 1.2. Even though the current density could further improve, the maximum field cannot increase substantially for NbTi based superconductors. The Large Hadron Collider (LHC) is designed to operate at 1.8 K to be able to reach 8.4 T operating field. To further increase the dipole field intensity for a next generation hadron collider, it is necessary to use a different superconducting material. Although there are other promising materials, such as Nb<sub>3</sub>Al, and high  $T_c$  superconductors, Nb<sub>3</sub>Sn seems to be the only available superconductor that meets the essential requirements for high field superconducting magnets for the next generation hadron collider after the LHC. In fact, Nb<sub>3</sub>Sn is the only conductor available in multifilamentary and stabilized

strands, made in long pieces, and carrying high current densities at 10-12 T fields. Fig. 1.1 shows a comparison between NbTi, Nb<sub>3</sub>Sn and BSSCO critical currents. Table 1.2 lists the critical parameters of NbTi and Nb<sub>3</sub>Sn.

		NbTi	Nb <sub>3</sub> Sn	Unit
Critical temperature	$T_c$	9.4	18	K
Critical magnetic field	$B_{c2}$	14.5	~28	T
Critical magnetic field at 4.2 K	$B_c(4.2K)$	11	24	T
Non-copper critical current density	$J_c(4.2K)$	3000 @5 T	2400 @12 T	A/mm <sup>2</sup>

Table 1.2: Typical critical parameters of the most practical superconductors for high field magnets.

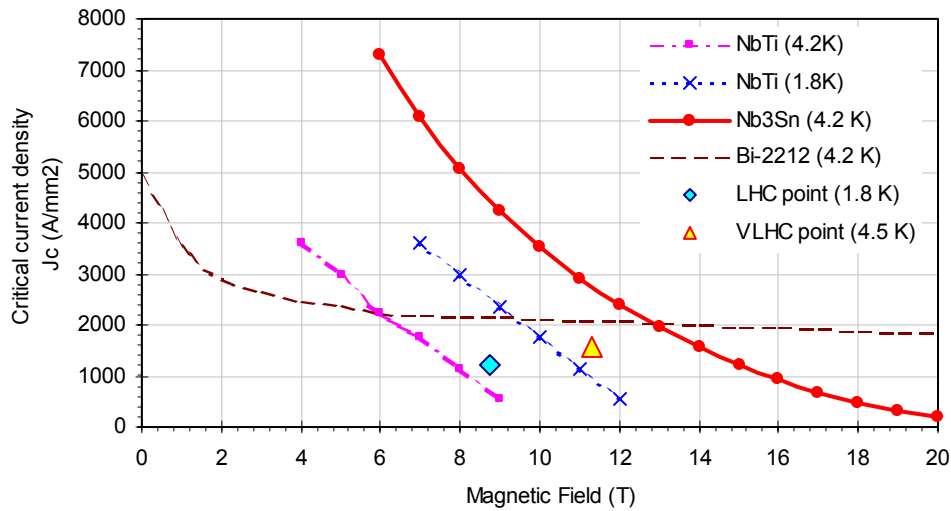


Fig. 1.1: Critical current density vs. magnetic field for different superconductors [1.2].

On the other hand, Nb<sub>3</sub>Sn is not as versatile a material as NbTi, because it cannot be drawn into strands and cabled after the heat treatment at 650-700°C, which creates the brittle superconductor. The next paragraph describes the basic characteristics of Nb<sub>3</sub>Sn superconductor. For a description of the critical surface, see chapter 3.

## 1.2 Basic properties of Nb<sub>3</sub>Sn superconductor

Nb<sub>3</sub>Sn is an intermetallic compound with a cubic A-15 structure. More precisely, it consists of a body-centered lattice of Sn atoms, with two Nb atoms on each face of the cube. Many of the A-15 materials are known to be superconductive, and they have very good superconducting properties, i.e. high critical temperature ( $T_c$ ), critical field ( $B_{c2}$ ) and critical current density ( $J_c$ ). Among the A-15 superconductors, Nb<sub>3</sub>Sn is the most commonly used because it is the easiest to be produced in a form suitable for large magnets. From the mechanical point of view, Nb<sub>3</sub>Sn is not as easy to handle as NbTi, because of its brittleness, after reaction. Bulk samples of Nb<sub>3</sub>Sn fracture at elongations of only 0.3 %. Conductors for magnet fabrication are made in the form of multi-filamentary composites, for stability and protection purposes. The form of this conductor has also the advantage that the fine filaments of Nb<sub>3</sub>Sn, embedded in the copper-bronze matrix, have higher strain limits, up to about 0.7 % applied strain.



Different manufacturing processes have been tested and developed in the last years by different companies. The most important ones are the bronze process, the internal tin process (IT), the modified jelly roll process (MJR), and the powder in tube process (PIT). Fig. 1.2 shows cross-sections of examples of conductors made with these processes.

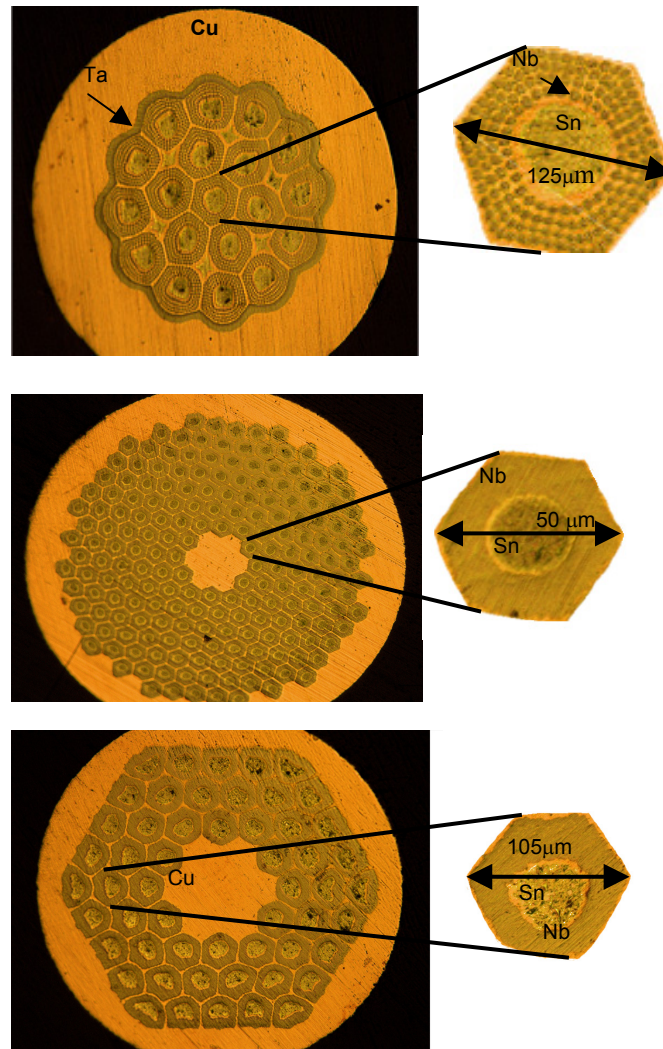


Fig. 1.2: Cross-section of untreated 1 mm Ø Nb<sub>3</sub>Sn strands fabricated using different processes [1.3].  
 (top) Internal Tin (IT) process by Intermagnetic General Corporation (IGC, now Outokumpo).  
 (medium) Powder in Tube (PIT) by Shape Metal Innovation Company (SMI).  
 (bottom) Modified Jelly Roll (MJR) by Oxford Superconducting Technology (OST).

To avoid conductor damage, the conductor is first prepared in the form of wire and Rutherford cable, with un-reacted strands, in which the components in the strands (niobium, copper, and bronze or tin), are compacted together, but still un-reacted. After the conductor is prepared, there are two possible techniques to build a Nb<sub>3</sub>Sn magnet, “Wind and React” or “React and Wind”.

The most commonly used technique is that of “Wind and React”: after the conductor is insulated, the coils are wound into their final shape, and heat treated for about two weeks, at high temperatures (of about 700 K). During the heat treatment, the Nb<sub>3</sub>Sn is formed by solid diffusion of Sn into Nb, through the copper matrix. This technique is best when the magnet design

includes small radius windings, but has the disadvantage of having to heat-treat the whole magnet, which requires large ovens in case of several meter long full-scale accelerator dipole magnets. Another disadvantage is the use of expensive inorganic insulation, that can withstand the heat treatment.

When the magnet design does not include small winding radii, then it is possible to use the “React and Wind” technique. In this case, the conductor is first heat treated on spools, and then wound to form the coils. The radius of the reaction spool is chosen in order to minimize the bending degradation of the conductor in the magnet. A common coil dipole magnet has a suitable design for the use of this technique. The common coil dipole magnet designed at Fermilab foresees a degradation of the critical current ( $I_c$ ) of less than 20% due to the bending [1.4].

Despite the problems arising from its strain sensitivity,  $\text{Nb}_3\text{Sn}$  remains the most promising superconductor for the next generation accelerator after the LHC, not only because of its remarkable properties today, but also because of the large potential for improvements of the material in the future. Fig. 1.3 shows how the  $\text{Nb}_3\text{Sn}$  conductor critical current density,  $J_c$ , was advanced since 1984. The improvement was driven throughout the 1980’s by the efforts to build the international fusion program (ITER) [1.5]. The conductor requirements for ITER were mostly small filament diameter to reduce AC loss for 50-60 Hz operation, while the accelerator magnets mostly require high  $J_c$  (and to a lesser degree low magnetization and therefore small effective filament diameters). Efforts are underway to develop strands for high field magnets. A US conductor development program for HEP started in 2000, with the goal to reach the following target specifications: a  $J_c$  (non-copper, at 12 T, 4.2 K) of 3000  $\text{A}/\text{mm}^2$ , an effective filament size of 40  $\mu\text{m}$  or less, a piece length greater than 10 km for wire diameters in the range of 0.3-1.0 mm, heat treatment times less than 200 h; target is 50 h for wind-and-react, and a wire cost of less than  $\$1.5/\text{kA}\cdot\text{m}$  (12 T, 4.2 K) [1.2].

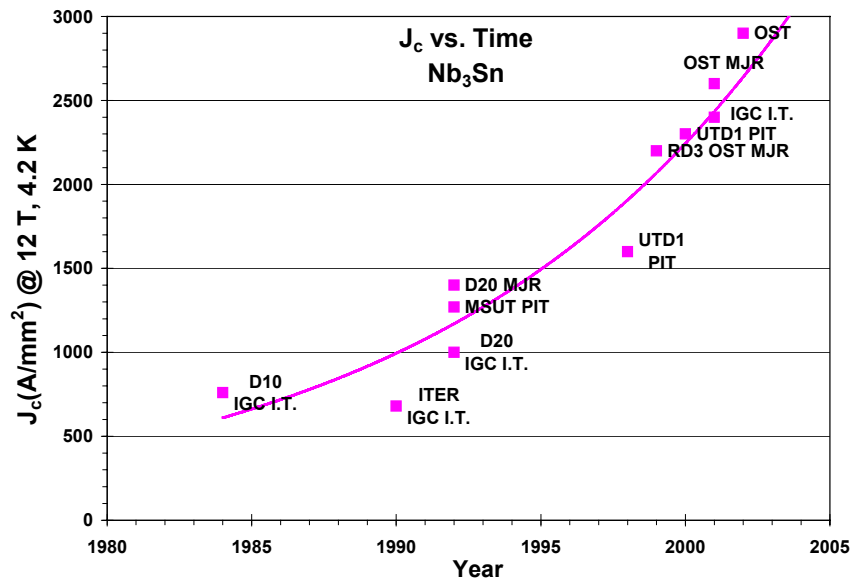


Fig. 1.3: Improvement in the (non-copper) critical current density of  $\text{Nb}_3\text{Sn}$  since 1984 up to date. In figure, “UT” stands for University of Twente [1.6].

## 1.3 Nb<sub>3</sub>Sn magnets for particle accelerators

### 1.3.a The Large Hadron Collider Upgrade

The state-of-the-art of superconducting magnets for particle accelerator is given by the LHC magnets. As an example, Table 1.3 lists the main magnet the high gradient quadrupoles (HGQ) at the high-luminosity interaction region (IRs), which are being developed and built at Fermilab and at KEK in collaboration with CERN. The quadrupoles in the IR regions will receive so high radiation doses that their lifetime is estimated to be about five years. Several plans on how to replace these magnets have been proposed. In order to allow a further increase in luminosity, Fermilab proposes to replace the 70-mm bore NbTi quadrupoles with 90-mm bore Nb<sub>3</sub>Sn quadrupoles, which will also provide a higher temperature margin to withstand the increased radiation levels resulting from the increased luminosity [1.7]. The parameters of these magnets are also listed in Table 1.3, denoted as HGQ-upgrade.

Parameter	HGQ (MQXB)	HGQ- upgrade
Yoke outer diam. (mm)	200	200
Aperture diameter (mm)	70	90
Nominal gradient $G$ (T/m)	205	205
Nominal current $I$ (kA)	11.33	14.5
$G$ max (T/m)	-	240
$I$ max (kA)	-	16.5
$G/I$ nominal (T/m/kA)	18.09	15.00
Inductance (mH/m)	3.5	4.72
Stored energy (kJ/m)	224.6	488.6

Table 1.3: Main design parameters for HGQ magnets.

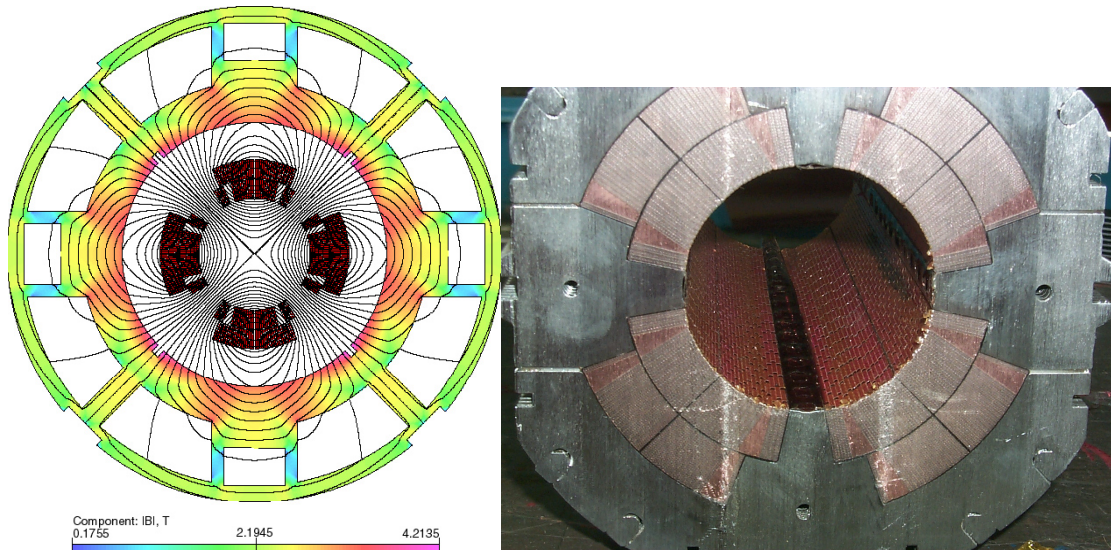


Fig. 1.4: Fermilab design for future Nb<sub>3</sub>Sn LHC high gradient quadrupole [1.8], and collared coils cross-section of HGQ NbTi model at Fermilab.

The design constraints for the magnet are that it must operate in 4.5 K Helium or superfluid Helium and have an outer diameter and operation current compatible with the existing LHC IR system and have a 90-mm bore with 250 T/m peak gradient. The proposed cross section is shown

in Fig. 1.4. One interesting feature of this design are the large cut outs in the cold iron which on the one hand provide cooling and still provide suppression of the iron saturation effect. Note that LBNL is also working on designs for this upgrade [1.9].

### 1.3.b The Very Large Hadron Collider (VLHC)

This paragraph summarizes the results of a design study for a new collider at Fermilab, which presented a two-stage very large hadron collider [1.10]. This accelerator was recommended by the High Energy Physics Advisory Panel to commence construction in 2015, “since a VLHC is so central to the long-term goals of our field, we strongly support R&D toward such a machine and recommend that it be continued at about the current level of effort. We also suggest that the research take a long-term perspective toward developing new technologies and techniques relevant to such a machine. High-field magnet research is particularly important. This work is essential for upgrading the LHC, and has considerable potential for applications in high-energy physics and other fields, including industry.” [1.11]

The Stage-1 VLHC features are a large circumference tunnel (233 km) using 2 T superferric dipole magnets, to reach a collision energy of 40 TeV and a luminosity comparable to that of the LHC. The high-gradient quadrupoles, needed for the collision optics, are high-field magnets similar to those under development at Fermilab and in other laboratories.

The VLHC in the second-stage, aims to reach a collision energy of at least 175 TeV in the center of mass, with high-field magnets in the same tunnel (Fig. 1.5). The proposal includes the existing Fermilab accelerator complex as the injector for stage-1, and stage-1 accelerator as the injector for stage-2.

		Stage 1	Stage 2
Total Circumference	(km)	233	233
Center-of-Mass Energy	(TeV)	40	175
Number of interaction regions		2	2
Peak luminosity	( $\text{cm}^{-2}\text{s}^{-1}$ )	$1 \times 10^{34}$	$2 \times 10^{34}$
Luminosity lifetime	(hrs)	24	8
Injection energy	(TeV)	0.9	10
Dipole field at collision energy	(T)	2	9.8
Average arc bend radius	(km)	35	35
Synchrotron radiation power per meter	(W/m/beam)	0.03	4.7
Average power use for collider ring	(MW)	25	100
Total installed power for collider ring	(MW)	35	250

Table 1.4: VLHC parameters for both stages [1.10].

Quoting [1.10]: “The very-large-circumference tunnel is an advantage to the Stage-2 VLHC, where the high beam energy makes synchrotron radiation significant. The design energy is 175 TeV, but the study concludes that reaching 200 TeV with a luminosity greater than  $2 \cdot 10^{34} \text{ cm}^{-2}\text{s}^{-1}$  will not be difficult, particularly if R&D can show that synchrotron radiation masks are effective in intercepting the radiation at ambient temperature. The power required for cryogenic refrigeration for the Stage-2 VLHC operating at 200 TeV is about 100 MW, which would decrease by 20 percent with the use of the masks. The major R&D for the Stage-2 machine is the development and commercialization of cost-effective high-field magnets. The large tunnel



permits 200 TeV operation with 12 T magnets, within reach of present-day materials.” ... “The VLHC proposal foresees an existing large accelerator laboratory as construction site, in order to reduce the initial investment in injectors and to take advantage of the existing intellectual and management infrastructure, by an international collaboration effort. This study assumes construction at Fermilab, and shows that Fermilab would be an excellent site. In reality, the VLHC could be built at any large laboratory with extensive hadron accelerator infrastructure. This facility would fit well within a worldwide plan that includes the Tevatron, followed by the LHC and a linear electron collider, and then a VLHC. The staged VLHC would take us quickly to the energy frontier; an upgrade in the same tunnel offers a straightforward path to the high-energy future” [1.10].

Collision	Energy (TeV)	Magnetic Field (T)	Leveled Luminosity Optimum ( $\times 10^{34} \text{ cm}^{-2} \text{ s}^{-1}$ )
Stage 1	40	2	1
Stage 2	125	7.1	5.1
Stage 3	150	8.6	3.6
Stage 4	175	10	2.7
Stage 5	200	11.4	2.1

Table 1.5: Properties of the Stage-2 VLHC at various energies [1.10].

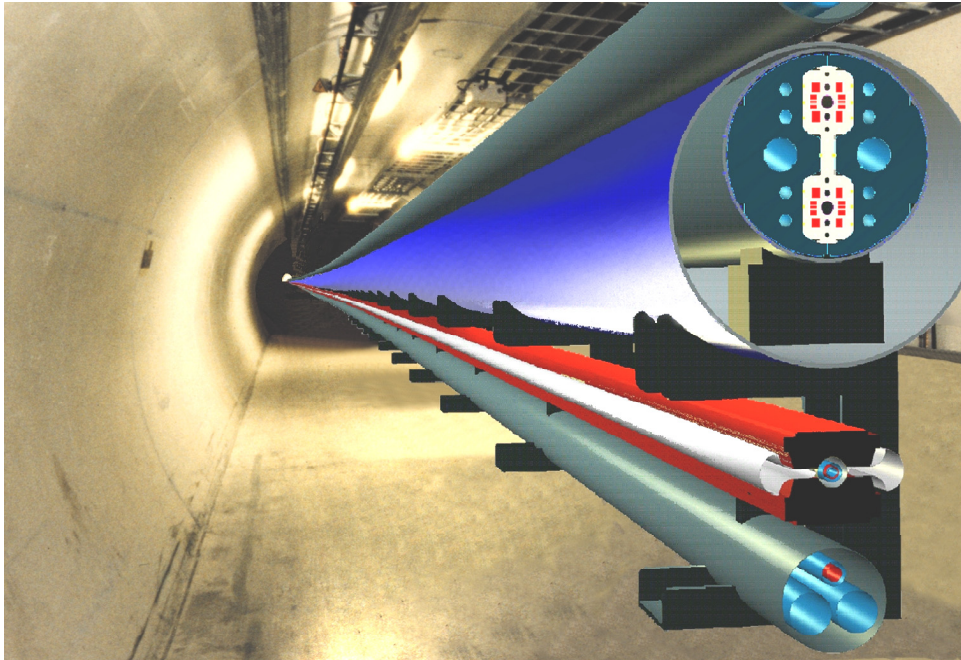


Fig. 1.5: Artist view of the tunnel layout for VLHC, with stage 1 magnet below, and high field  $\text{Nb}_3\text{Sn}$  dipoles above [1.10].

### 1.3.c VLHC-2 FNAL magnets

The main dipole magnet for the VLHC-2 study is based on the common coil design [1.12]. There are, however, several other dipole designs being studied at Fermilab for a future hadron collider like the second stage VLHC, including shell type ( $\cos\theta$ ) designs. Fig. 1.6 shows the

dipole model of the  $\cos\theta$  type magnet that is being developed at Fermilab [1.13] and the common coil model proposed for the VLHC-2.

Table 1.6 lists the main design parameters for the two dipole magnet types used as baseline for the VLHC quench protection study, namely the warm-yoke, horizontally separated configuration for the  $\cos\theta$  dipole, and the cold yoke configuration of the single layer common coil dipole, as in [1.10].

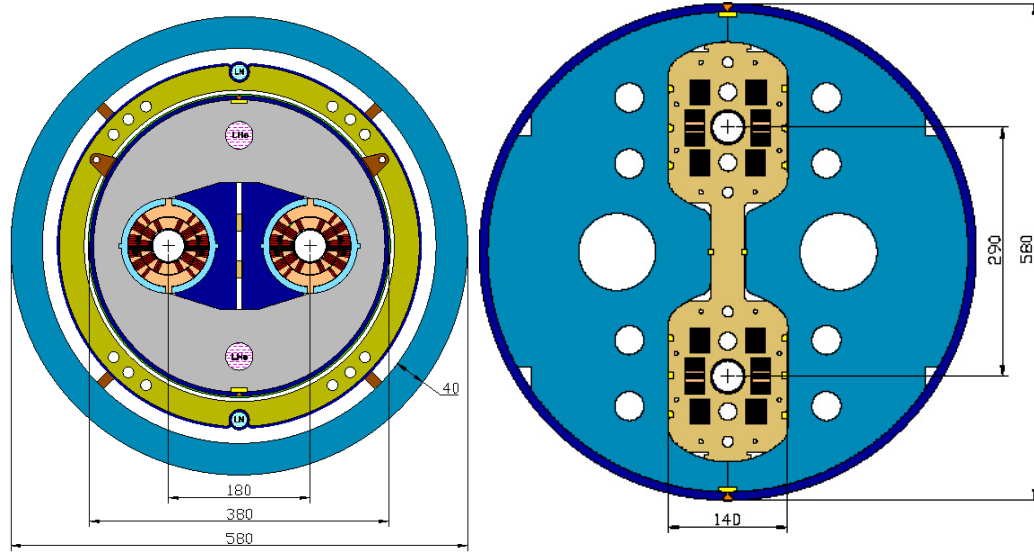


Fig. 1.6:  $\cos\theta$  dipole with warm yoke for minimized size and weight, and common coil, used in the VLHC-2 quench protection study.

Magnet	$\cos\theta$ warm-yoke	Common coil-cold yoke	LHC- main dipole
T (K)	4.5	4.5	1.9
Aperture (mm)	43	40	57
Aperture separation (mm)	180	290	194
Operating current $I_0$ (kA)	21.3	23.5	11.8
Bore field $B_0$ (T)	10	10	8.4
Peak field (T)	10.5	11.3	9.2
Inductance $L @ B_0$ (mH/m)	$2 \times 1.07$	$2 \times 1.5$	$2 \times 3.7$
Energy stored $E @ B_0$ (kJ/m)	$2 \times 243$	$2 \times 414$	$2 \times 245$
Length (m)	16	16	14.5
Iron yoke OD (mm)	580/380	560	550

Table 1.6: VLHC main magnet parameters. LHC dipole parameters are listed for comparison.

Magnet Conductor	$\cos\theta$	Common coil	LHC- main dipole (inner/outer coils)
Wire diam. (mm)	1	0.7	1.06/0.8
N. strands	28	60	28/36
Cable cross-sectional area $A_{cable}$ (mm <sup>2</sup> )	29.3	31.02	24/28
Current density in copper $J_{Cu}$ (A/mm <sup>2</sup> )	1734	1987	709
Copper/non copper ratio $Cu/NCu$	1.2	1.05	1.6/1.9
Copper RRR	$\sim 50$	$\sim 50$	$\sim 100$

Table 1.7: Conductor parameters for VLHC and LHC dipole magnets for comparison.

### 1.3.d Nb<sub>3</sub>Sn high field magnet models at Fermilab

Several short Nb<sub>3</sub>Sn high field magnet models are under development at Fermilab, including a one-aperture cos $\theta$  model, a short common coil model, and a “racetrack” magnet for R&D purposes.

The two-layer cos $\theta$  design dipole is shown in Fig. 1.7-left, and Fig. 1.8-left. It utilizes a keystoneed Rutherford cable of 28 one mm-diameter strands. The cable is wound with a stainless steel core to minimize the cross-over resistance between the strands. The two layers are wound and reacted together eliminating the need for the inner/outer coil splice. Mechanical support of the impregnated coils is provided by a stainless steel skin. Aluminum spacers are used to prevent excessive pre-stress at room temperature. Several models have been built and tested [1.14]. Most model magnets have not yet reached the expected short sample limit. The magnet program has been very successful in achieving its goals for field quality. The harmonics for the models are low, and consistent with expected coil displacements [1.15]. In addition, passive correctors were successfully used to reduce in great part the low current magnetization effects. Despite not reaching full fields, heater efficiencies have been studied and applied to the quench models. Some of these measurements are reported in chapter 3. A cos(2 $\theta$ ) version of this magnet is being considered as a possible candidate for an LHC IR upgrade, presented in the previous section.

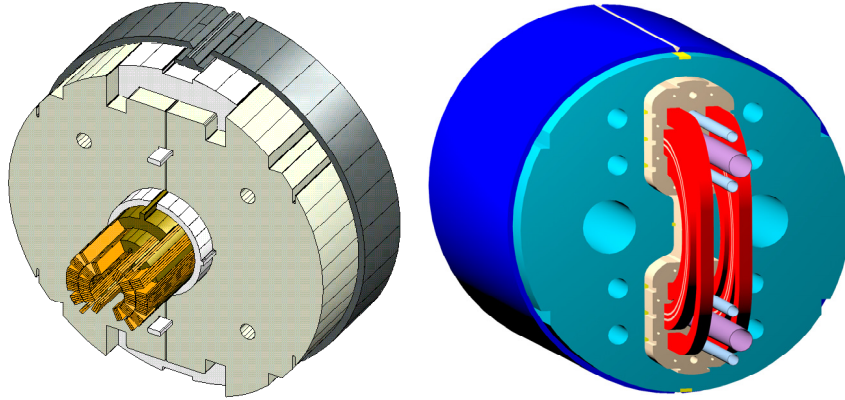


Fig. 1.7: Nb<sub>3</sub>Sn high field dipole magnets at Fermilab: cos $\theta$  and common coil respectively.

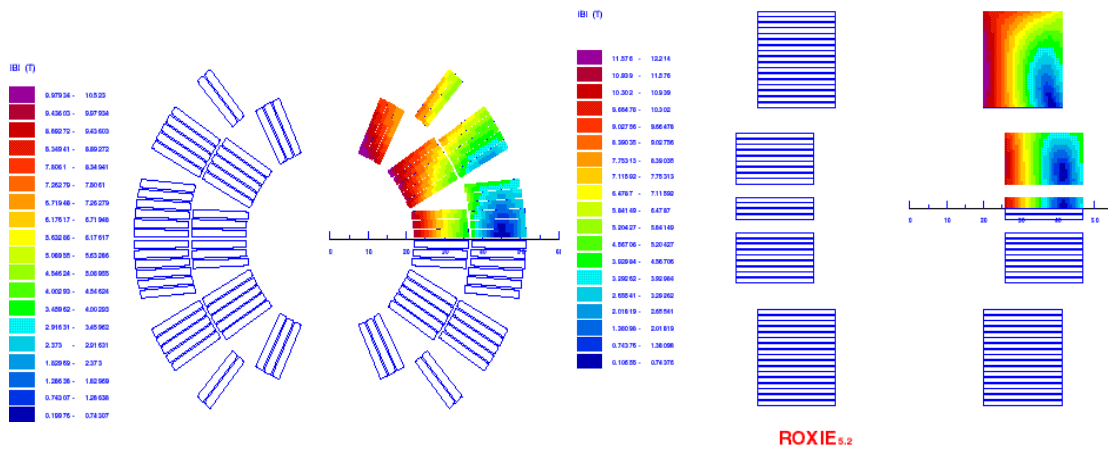


Fig. 1.8: Coil cross section of cos $\theta$  and common coil dipole magnets (one aperture) and field distribution on the coils, calculated with Roxie [1.16, 17].

A parallel approach has been to develop a common coil dipole, as shown in Fig. 1.7-right. This magnet has a maximum nominal field of 11 T at 4.5 K with a 40 mm aperture (Fig. 1.8-right). The coils are single layer, enclosed in a laminated collar structure. The “bridge” piece between the apertures is designed to accommodate the expected 750 MPa peak pressure during excitation. The wide separation of the two apertures allows for a wide bends in the ends thus making it possible to consider a conductor with the react-and-wind approach. In order to achieve the necessary amp-turns for a single layer magnet, a cable with a large width to thickness aspect ratio is required. This 60-strand cable has been constructed from MJR conductor produced by OST and cabled at Berkeley. After construction and test of a mechanical model, a 1-meter model was built, and the test is expected shortly [1.18].

Supporting the react-and-wind approach is the “racetrack” coil magnet [1.19]. Two layers of impregnated react-and-wind coils were tested together in a bolted mechanical structure (Fig. 1.9). This structure is very useful for studying mechanical coil support, insulation schemes, and quench heater efficiency. Each coil, 0.73 m long, has 28 turns. There is one spacer in the ends and no spacers in the straight section. The coils are separated by a 5 mm thick G10 plate. The conductor is a flat Rutherford cable made of 41 0.7 mm-diameter strands.

HFDB02

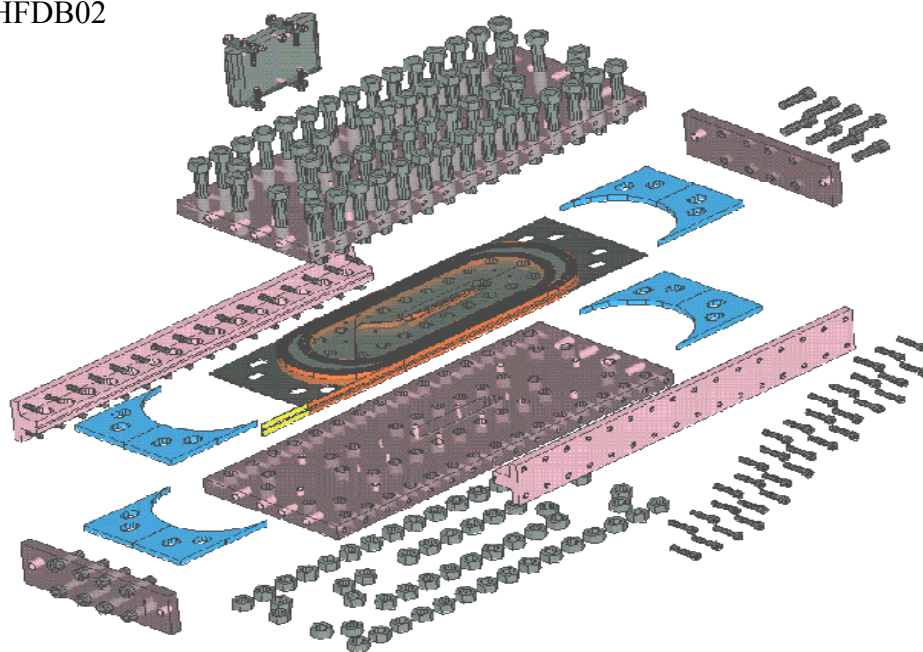


Fig. 1.9: Racetrack magnet HFDB02, exploded view.

### 1.3.e Nb<sub>3</sub>Sn high field magnets around the world

#### History

A review of the almost 40-year long history of Nb<sub>3</sub>Sn superconducting magnets can be found in [1.20, 21]. In 1962, Nb<sub>3</sub>Sn could achieve a  $J_c$  of 100 A/mm<sup>2</sup> in an external field of 2.5 T [1.22]. A rapid improvement of type II superconducting materials followed throughout the 1960's



allowing development of NbTi as well as Nb<sub>3</sub>Sn magnet models. A 20 cm-long Nb<sub>3</sub>Sn quadrupole magnet was built and tested at BNL in 1967, using Nb<sub>3</sub>Sn react and wind tape. The magnet had a wide 70 cm bore and achieved a gradient of 85 T/m, with 3 T peak field in the conductor and 400 A/mm<sup>2</sup> critical current [1.23]. Later in 1979, 80 mm-aperture dipoles were made with react-and-wind cable of the Isabelle-type, achieving bore fields comparable to Tevatron NbTi dipoles (4.8 T at 4.6 K), and could operate in helium gas at lower fields up to 17 K [1.24]. At CEA/Saclay, a two-layer dipole, similar in design to the Tevatron arc dipole achieved 6 Tesla [1.25]. Despite these Nb<sub>3</sub>Sn magnets achievements, NbTi magnets with comparable or better field and quench performance were chosen for large-scale projects [1.26,27].

In the 1980's interest in Nb<sub>3</sub>Sn magnets was renewed with the proposal to replace the LEP electron/positron ring with a hadron collider. There were two competing ideas for the upgrade, one was to make Nb<sub>3</sub>Sn magnets operating at 4.2 K, the other was to make NbTi magnets operating in superfluid Helium at 1.9 K. The former involved continue R&D in Nb<sub>3</sub>Sn while the latter required a significant cryogenic upgrade for CERN. A collaboration of ELIN and CERN, culminated in the successful construction of a 10.5 T dipole model, using the wind-and-react technology [1.28]. Despite these successes, the decision was made to adopt the NbTi at 1.9 K approach [1.29].

In the 1990s, Nb<sub>3</sub>Sn research in LHC-type dipoles was largely centered at Twente and LBNL, with significant progress made in quench and mechanical performance. Both programs utilized a “cosine  $\theta$ ” design with wind-and-react Rutherford cables (Fig. 1.10). In 1997 Twente reported a record field of 11 T [1.30,31,32] followed later that year by a 12.8 T at 4.4 K and 13.5 T at 1.8 K in LBNL's D20 dipole model [1.33].

Perhaps bolstered by these results as well as in view of future accelerator projects, several institutions started or rejoined their efforts in the Nb<sub>3</sub>Sn magnet technology towards the end of the decade and into the present, including Fermilab, TAMU, BNL, while LBNL, Saclay and the University of Twente continued to pursue their efforts.

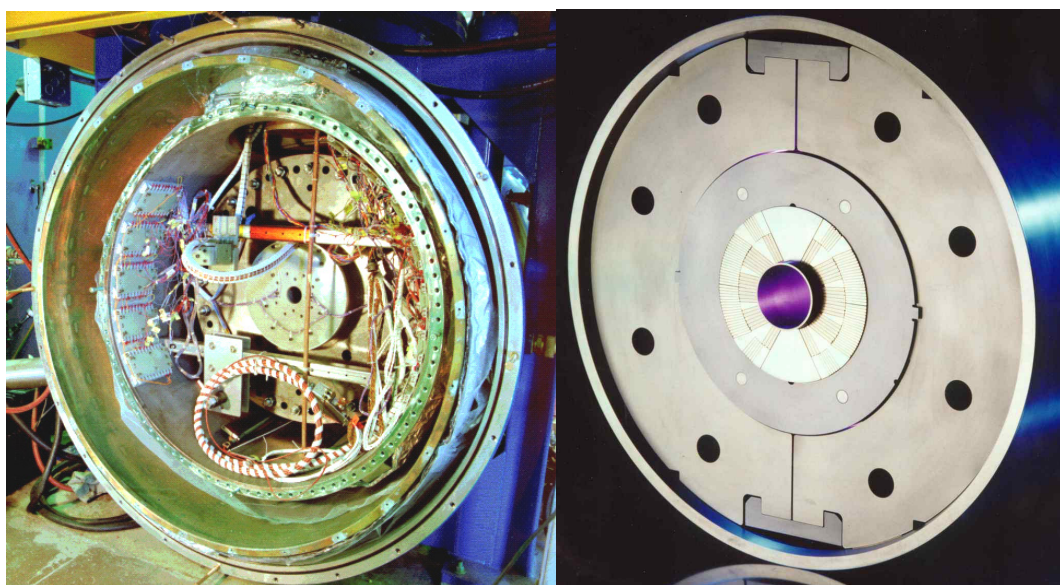


Fig. 1.10: D20 magnet, built at LBNL, and Twente Nb<sub>3</sub>Sn dipole magnet (A. den Ouden)

## Present programs

The Fermilab program, essentially presented in 1.3.d, is oriented towards magnet mass production, following its tradition, with the goal of developing “accelerator quality” magnets. “Accelerator quality” means magnets that are cost effective, robust in design, and with uniform bore fields that are reproducible throughout a large production series. The main line of developments is 10-12 T and wide aperture quadrupoles in the range of 200-300 T/m, operating in 4.3-4.5 K, with large critical temperature margin for use in high heat load environments.

The high field magnet program at the Lawrence Berkeley National Laboratory (LBNL) has centered on the common coil approach, after a very successful  $\cos\theta$  program, as mentioned above [1.33]. The program is divided into three lines: the “RD” program, which is geared towards accelerator field quality dipoles, the “HD” program whose goal is to build the highest field dipoles using simple coil designs and with reduced emphasis on field quality, and the “SM” program, which produces short racetrack coils to address R&D issues. The RD program is geared towards accelerator quality common coil dipoles. The magnets are characterized by one or more pancake coils. Last year, the RD3b, a three-layer coil, reached a field of 14.7 T a new record for accelerator dipoles. The most recent RD3c is shown in Fig. 1.11. It consists of a double layer pancake with a set of auxiliary coils for improved field quality [1.34].

The SM and HD programs support the main program. The SM program developed 1/3 scale magnets, with a field range of 9-12 T, which allowed test of new ideas such as new fabrication and cabling techniques. The SM program is briefly described also in chapter 5, in the frame of a quench experiment conducted in the context of this thesis. The HD program idea is to make flat coils with very simple geometries to push the limits of conductors and materials. The first HD magnet, set for construction and test in 2003 has an expected short sample limit of 15 T. Future magnets are proposed, in line with the main goal of LBNL program, to push accelerator magnet technology towards the highest fields.

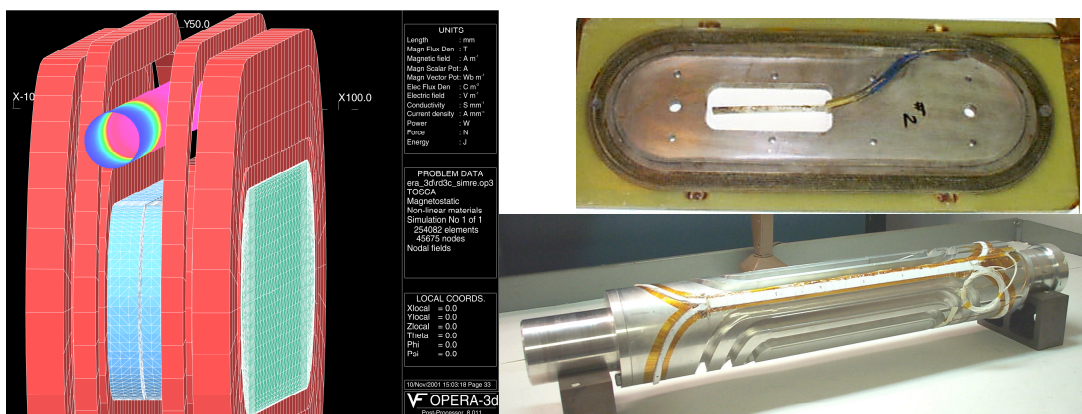


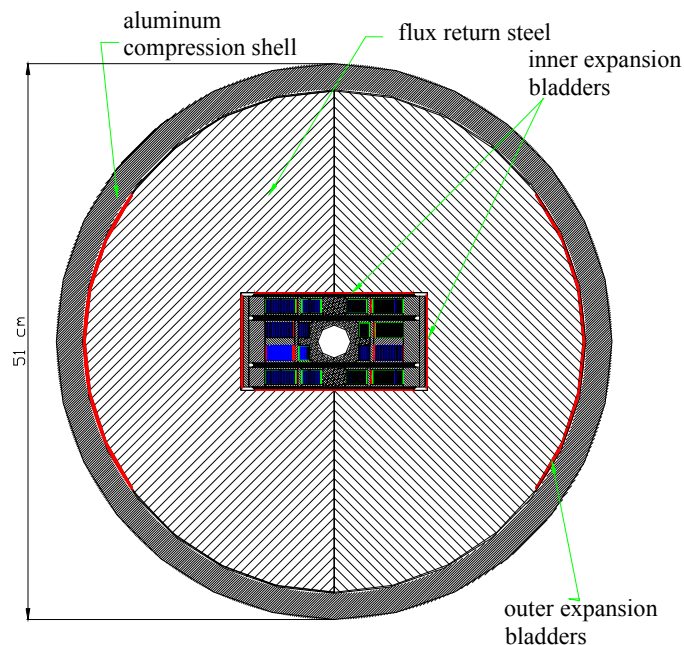
Fig. 1.11: LBNL RD3c (Courtesy of S. Gourlay), BNL slotted collar dipole design (Courtesy of E. Willen), and BNL 10-turn coil for react-and-wind studies [1.35].

BNL, with its long tradition of  $\text{Nb}_3\text{Sn}$  development has embarked on a program to build high field magnets out of new high field materials. The central approach has been to use the “react-and-wind” cable technology outlined above and to incorporate innovative magnet designs to fit the conductor capabilities [1.22]. There are two parallel magnet programs. The first relies on the so-called “6 around 1” flexible cable using the slotted magnet developed for the RHIC spin polarization program. This construction technique relies on a slotted collar structure, which

divides the coil into many independently supported sectors, each sector participating in the control of the Lorentz forces [1.36].

The second program is ultimately geared toward HTS materials but the same principles apply to  $\text{Nb}_3\text{Sn}$ . The design is similar to those used at LBNL, with simple 10-turn “racetrack” coils (as in Fig. 1.11). Innovative ideas for coils include a very high gradient flat coil quadrupole. Like the LBNL “SM” program, they have initiated a short model test coil program to conductor, cable and insulation scheme. As part of this process, a 12 T common coil react and wind  $\text{Nb}_3\text{Sn}$  dipole is being designed and built to provide a background field to test the HTS coils. This  $\text{Nb}_3\text{Sn}$  magnet is expected to be built and tested this year [1.37].

The block design is a feature of a single aperture dipole design that is being developed at the Texas A&M University (Fig. 1.12). The goal of this project is to build a 12 T dipole with 30 mm



aperture, using wind-and-react conductor. The magnet consists of four pancake coils arranged in approximately a  $\cos(\theta)$  geometry. A unique feature of this magnet is the support structure. Each coil has its own support system so that stress cannot accumulate between blocks. Progress towards building this magnet is reported in [1.38].

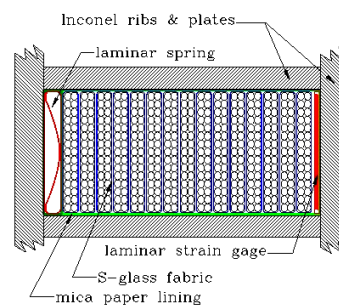


Fig. 1.12: The 12 T dipole magnet being developed at TAMU, using block type stress management.

The University of Twente is also heavily engaged in a program of developing high field dipoles. Following their success with the 11 T wind-and-react MSUT dipole (Fig. 1.10), their goal since 1998 has been to build a 10 T 88 mm dipole that could be used as a future upgrade to the LHC D1 separation dipole. Much of the effort up to this point has been in developing the conductor for this magnet that utilizes the powder in tube technology. The magnet is under construction and should be available for test this year [1.5].

Finally, work continues on  $\text{Nb}_3\text{Sn}$  quadrupoles at Saclay. Their proposed magnet has the same cross section as the LHC arc quadrupoles but with  $\text{Nb}_3\text{Sn}$  conductor. This magnet can be used for diverse applications, such as low  $\beta$  quadrupoles or for the final focus of Tesla [1.39].

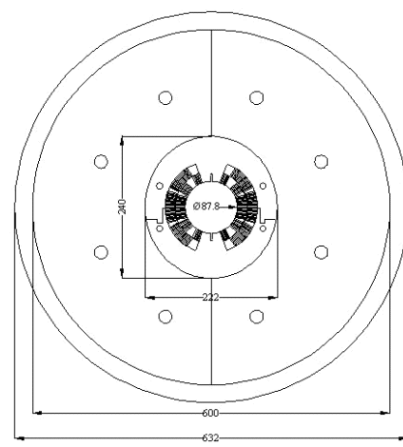


Fig. 1.13: CERN-UT magnet for LHC upgrade.

## 1.4 Conclusions

Accelerator magnets utilizing Nb<sub>3</sub>Sn have been studied for the last 40 years and have never been overshadowed by their NbTi counterparts. Future accelerator applications are beyond the field reach of NbTi, thus making Nb<sub>3</sub>Sn attractive. There has been significant progress in the past years in all phases of conductor development. Cabling techniques and coil designs take advantage of these innovations to create magnet designs with high fields with accelerator quality field homogeneity. The next test is to produce magnets suitable for use in an actual accelerator. This requires improvements in conductor costs, ease of manufacturing and reproducibility of the high field quality. This also requires an investigation of the effect of quenching on the brittle Nb<sub>3</sub>Sn superconductor, which is the subject of this thesis.

## References

- 
- [1.1] R.W. Seidel, "The First Large-Scale Application of Superconductivity: The Fermilab Energy Doubler, 1972-1983," *Historical Studies in the Physical Sciences*, 18:1, 25-54, 1987
  - [1.2] R.M. Scanlan, D.R. Dietderich, and H.C. Higley, "Conductor Development for High Field Dipole Magnets," *Proceedings of MT16*, September 1999
  - [1.3] S. Mattafirri, "Kinetics of phase growth during the Cu-Sn diffusion process and the Nb<sub>3</sub>Sn formation. Optimization of superconducting properties," *Laurea thesis* Pisa University, also TD-02-21, May 2002
  - [3.4] P. Bauer et al., "Fabrication and Testing of Rutherford-type Cables for React and Wind Accelerator Magnets," *IEEE Trans. App. Superc.*, Vol. 11/1, March 2001;
  - [3.5] N. Mitchell et al, "Conductor Designs for the ITER Toroidal and Poloidal Magnet Systems," *IEEE Trans on Mag.* V. 30, p. 1602-7, 1994
  - [1.6] E. Barzi et al., "Progress Report on Superconducting Strand and Cable R&D", Fermilab TD-01-013, February 2001
  - [1.7] A.V. Zlobin et al., "Large-Aperture Nb<sub>3</sub>Sn Quadrupoles for 2nd generation LHC Irs," *proceedings of EPAC 02*
  - [1.8] A. Zlobin et al., "Conceptual Design Study of Nb<sub>3</sub>Sn Low-beta Quadrupoles for 2nd generation LHC IRs", *IEEE Trans. App. Superc.*, ASC 2002 proceedings
  - [1.9] S. Caspi et al., "Nb<sub>3</sub>Sn Quadrupole Magnets for the LHC IR," *IEEE Trans. App. Superc.*, ASC 2002 proceedings
  - [1.10] P. Limon et al., "Design Study for a Staged Very Large Hadron Collider", Fermilab TM-2149, June 2001
  - [1.11] DOE/NSF High-Energy Physics Advisory Panel, Subpanel on Long Range Planning for U.S. High-Energy Physics Presented to HEPAP, Draft report, October 2001
  - [1.12] G. Ambrosio et al., "Development of the 11 T Nb<sub>3</sub>Sn Dipole Model at Fermilab," *proceedings of MT-16, IEEE Trans. on Applied Superc.*, v. 10, No. 1, March 2000, p.298
  - [1.13] A.V. Zlobin et al., "Development of Cos-theta Nb<sub>3</sub>Sn Dipole Magnets for VLHC", *proceedings of PAC 01*, Chicago, IL, June 2001

- 
- [1.14] N. Andreev et al., "Development and Test of Single-Bore cos-theta Nb<sub>3</sub>Sn Dipole Models," *proceedings* of MT17, Geneva, CH, Sept. 2002
  - [1.15] E. Barzi et al., "Field Quality of Fermilab Nb<sub>3</sub>Sn cos-theta Dipole Models With Cold Iron Yoke," *proceedings* of EPAC2002, Paris, France
  - [1.16] V.V. Kashikin, "Design and Optimization of Superconducting Accelerator Magnets," *Ph.D. Thesis* and Fermilab TD note, TD-02-001, 2002
  - [1.17] S. Russenschuck, "A Computer Program for the Design of Superconducting Accelerator Magnets", CERN AC/95-05 (MA), Sept. 1995.
  - [1.18] I. Novitski et al., "Development and Test of a Single-Layer Nb<sub>3</sub>Sn Common Coil Dipole Model," *IEEE Trans. App. Superc.*, ASC 2002 proceedings
  - [1.19] G. Ambrosio et al., "Fabrication and Test of a Racetrack Magnet using Pre-reacted Nb<sub>3</sub>Sn Cable," *IEEE Trans. App. Superc.*, ASC 2002 proceedings
  - [1.20] M.J. Lamm, "Nb<sub>3</sub>Sn Accelerator Magnet Development Around the world", *IEEE Trans. App. Superc.*, ASC 2002 proceedings
  - [1.21] G.L. Sabbi, "Status of Nb<sub>3</sub>Sn Accelerator Magnet R&D", *proceedings* of MT17, Geneva, CH, Sept. 2002
  - [1.22] J.E. Kunzler and M. Tanenbaum, "Superconducting Magnets", *Scientific American*, V. 206, N. 6, pp.60-67, New York, 1962.
  - [1.23] W.B. Sampson, "Superconducting Magnets for Beam Handling and Accelerators," *Proceedings for the Second International Conference on Magnet Technology*, H. Hadley, Ed. Oxford, 1967, pp. 575-578
  - [1.24] W.B. Sampson et al., "Nb<sub>3</sub>Sn Dipole Magnets", *IEEE Trans. Magnetics*, vol. Mag-15, N. 1, p. 117-118, Jan. 1979
  - [1.25] J. Perot, "Construction and Test of a Synchrotron Dipole Model Using Nb<sub>3</sub>Sn Cable", *IEEE Trans. Magnetics*, vol. Mag-19 no. 3, pp.1378-1380, May 1983.
  - [1.26] "Superconducting Accelerator Design Report", Fermi National Accelerator Laboratory, 1979
  - [1.27] "HERA, A proposal for a large electron proton colliding beam facility at DESY", *DESY Hera 81-10*, 1981
  - [1.28] A. Asner, R. Perin, et al., "First Nb<sub>3</sub>Sn 1 m long superconducting dipole magnet for LHC break the 10 Tesla field threshold", *Proceedings* of the 11<sup>th</sup> Intl. Conf. on Magnet Technology, p. 36-41, Tsukuba, Japan, 1989
  - [1.29] LHC Conceptual Design Report, LHC Study Group 2000-11-01
  - [1.30] H.H.J. ten Kate et al., "Development of an experimental 10 T Nb<sub>3</sub>Sn Dipole Magnet for the CERN LHC", *IEEE Trans on Mag.*, V. 27, N 2., p. 1996-1999, Mar. 1991
  - [1.31] A. den Ouden et al., "An experimental 11.5 T Nb<sub>3</sub>Sn LHC type of dipole magnet", *IEEE Trans on Mag.*, V. 30, N. 4, pp. 2320-3, July 1994
  - [1.32] A. den Ouden et al., "Application of Nb<sub>3</sub>Sn superconductors in accelerator magnets", *IEEE Trans. Appl. Superc.*, V. 7, 1997
  - [1.33] A.D. McInturff, "Test Results for a high field (13T) Nb<sub>3</sub>Sn Dipole", *proceedings* of PAC-97, Vancouver, May 1997
  - [1.34] A.F. Lietzke et al., "Test Results for RD3c, a Nb<sub>3</sub>Sn Racetrack Dipole Magnet", *IEEE Trans. App. Superc.*, ASC 2002 proceedings
  - [1.35] J. Escallier, "Technology Development for React and Wind Common Coil Magnets", *proceedings* of PAC-2001, Chicago, IL, June 2001.

- 
- [1.36] E. Willen, "Construction and Test of Nb<sub>3</sub>Sn Coil MCA003", BNL SC Div. Note, MDN-612-32 (AM-MD-313) Jan. 2002
  - [1.37] R. Gupta, private communication
  - [1.38] P.M. McIntyre et al., "Construction and Testing of Block-coil High-field Dipoles for Future Hadron Colliders", *IEEE Trans. App. Superc.*, ASC 2002 proceedings
  - [1.39] A. Devred et al., "Development of a Nb<sub>3</sub>Sn quadrupole magnet model", *IEEE Trans. Appl. Supercond.*, Vol 11(1), March 2001 p. 2184



## 2. Quench Protection Calculations for Nb<sub>3</sub>Sn Accelerator Magnets

Chapter 2 Table of Contents:	Page
2. Quench protection calculations for Nb <sub>3</sub> Sn accelerator magnets	1
2.1 Basics of the quench process	2
2.1.a Quench causes and stabilization	2
2.1.b Consequences of the quench	3
2.1.c Common quench protection strategies	5
2.1.d Calculation of the main quench parameters	10
2.2 Quench simulations	14
2.2.a Common quench simulation programs	15
2.2.b QLASA	16
2.2.c Quenchpro	20
2.2.d Contribution of the insulation to the adiabatic quench process	22
2.2.e Parametric quench studies for VLHC dipole magnets	23
2.2.f Summary of VLHC parametric studies	27
2.3 General quench study	28
2.3.a Analytical model	28
2.3.b Peak temperature analytic calculations results	34
2.3.c Summary of the general quench study	36
2.4 Conclusions of quench protection studies	37
References	39

## 2.1 Basics of the quench process

### 2.1.a Quench causes and stabilization

In applied superconductivity, the term “quench” is generally used to indicate the sudden transition from the superconducting to the normal, resistive state. This process occurs when one of the variables characterizing the superconducting state (temperature, magnetic field, and transport current density) exceeds the critical value. Suppose, for example, that a magnet is being operated at temperature  $T_0$ , with a transport current density  $J_0$  in the conductor, and being in a magnetic field of  $B_0$  intensity, given by the self-field, and the field produced by other turns in the magnet. If a perturbation occurs in the magnet, which increases locally the temperature, of even few degrees, the state of the superconductor will now correspond to a point above the critical surface (Fig 2.1). From that moment on, heat will be generated by the transport current, which starts sharing between the superconductor -now in the normal state- and the stabilizer. This temperature is therefore called generation temperature ( $T_g$ ), or current sharing temperature. If the heat generated exceeds the heat conducted away, the temperature will further increase, starting an irreversible process. When the quench process runs to completion, all the energy that was stored in the magnet as electromagnetic energy will be released inside the magnet as heat, dissipated in the normal conductor by the Joule effect. Because of the high current and the high stored energies in these magnets, the quench process can produce violent effects.

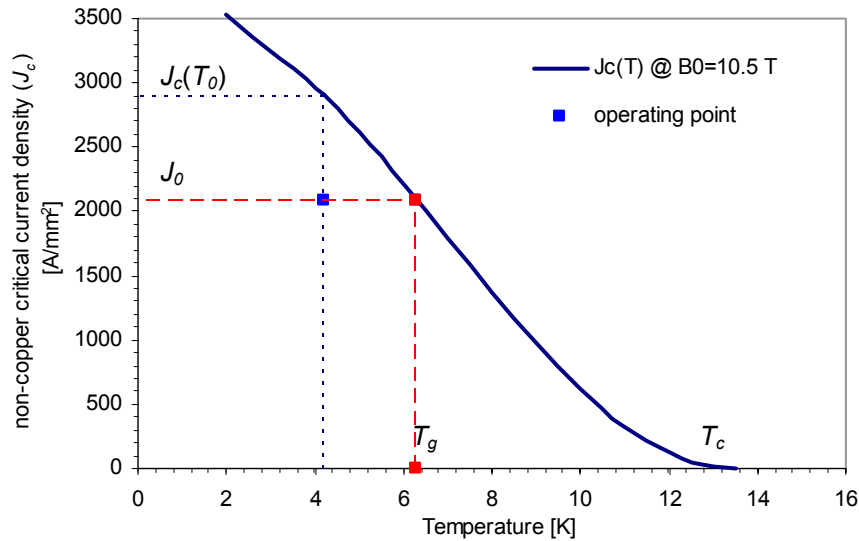


Fig. 2.1: Schematic of the quench start (Nb<sub>3</sub>Sn critical current for VLHC cos $\theta$  magnet).

Since the heat capacities of all materials are very small at low temperature, decreasing with the third power of the temperature according to Debye’s law, very small perturbations can initiate a quench. According to the simplest, adiabatic model, the temperature increase  $\Delta T$  is proportional to the energy deposition  $\Delta E$ , and inversely proportional to the heat capacity. In adiabatic conditions  $\Delta E$  as little as 10-100 mJ/cm<sup>3</sup> can generate a  $\Delta T$ , sufficient to bring the magnet operating point beyond the critical surface, and initiate the quenching process in state of the art Nb<sub>3</sub>Sn conductor.



To improve the stability of the superconductor, and to protect the magnet during quench, practical superconductors are made in the form of multifilamentary composites wires, where the superconducting filaments are embedded in a good (normal-) conducting metal, such as copper or Aluminum, the so-called stabilizer. The stabilizer provides:

- 1- a low resistance path for the current to reduce dissipation in the normal zone,
- 2- a contribution to the overall heat capacity,
- 3- a heat conduction path to remove the heat from the superconductor (which is typically a material with a low thermal conductivity).

It has to be noted that NbTi superconductors now routinely achieve filament diameters of 5  $\mu\text{m}$ , while the less developed Nb<sub>3</sub>Sn superconductors today have larger effective filament sizes of the order of 50-100  $\mu\text{m}$ .

Several kinds of predictable disturbances can release these small energies in a superconducting magnet. These are continuous disturbances such as AC losses (hysteretic losses, eddy currents), thermal loads (for example radiation load in an accelerator magnet), heating coming from the leads and from the splices, and so called “index losses” due to flux flow close to the critical surface (especially for high  $T_c$  superconductors). Other transient disturbances (like conductor movements, cracking of epoxy resin, and sudden heat loads like beam loss in an accelerator) are hardly predictable and difficult to avoid. In addition, as a result of larger filament diameters, flux jumps can occur in today’s Nb<sub>3</sub>Sn conductors. Large voltage spikes have been registered in Nb<sub>3</sub>Sn magnets built and tested at various laboratories, which are interpreted as flux motion [2.1, 2.2, 2.3]. Therefore, although the conductor is stabilized, a quench is an event that can always occur, and must be taken into account in all aspects of the accelerator magnet design.

### 2.1.b Consequences of the quench

To have an idea of the possible temperature rise in a superconducting magnet after a quench, we can calculate the power dissipated in a typical conductor without any active protection measure. The power dissipated by Joule heating in a strand is determined by the current density in the stabilizer, defined as the current over the cross-sectional area of the copper in the strand ( $J_{Cu}$ ). In fact, the resistivity of the other materials composing the conductor is much higher (two orders of magnitude higher for the Nb<sub>3</sub>Sn itself, for example). Assuming that a strand has been provided with sufficient stabilizing copper to limit the current density in the copper ( $J_{Cu}$ ) to 1000  $\text{Amm}^{-2}$ , the power dissipated by Joule heating in the strand initially (at low temperatures) is:

$$\text{Power/volume} = \rho \cdot J_{Cu}^2 \cong 6 \cdot 10^{-10} (\Omega\text{m}) \cdot 10^{18} (\text{A}^2/\text{m}^4) = 600 \text{ MW/m}^3, \quad (2.1)$$

certainly a power that can melt a metal in a few seconds! To avoid such high temperatures, protection measures have to be taken, both at the design level and during operation. The active protection measures to be taken during operation can be divided into the following categories:

1. Quench detection;
2. Current supply disconnection;
3. Extraction of as much stored energy as possible from the coils;
4. Spreading of the remaining stored energy in the coils to avoid heat concentration.

The quench protection methods will be described in further detail in the next paragraph. Here, the possible effects of a quench if the protection measures are not adequate, or in case of a failure in the protection system, are briefly described.

- Excessive temperature: first possible damage is in the insulation system. For example, epoxy resins have a glass transition point at about 400 K. Weakening of the insulation can result in an electrical short with the high voltage that develops during a quench. In addition, since the quench process is very fast, high temperature gradients can develop between the hot spot where the quench started and the parts of the magnet that are still cold. Therefore, the risk arises that thermo-mechanical stresses damage magnet components, in particular the insulation. The insulation sees the highest temperature gradients, and typically has low shear strength. In addition, thermo-mechanical stresses can cause critical current degradation (especially in the strain sensitive Nb<sub>3</sub>Sn). The study of these problems is the subject of this thesis.

- High voltages, to ground and between turns, can create short circuits and arcing.

The main cause of failure reported in an extensive survey of failures having occurred in superconducting magnets [2.4] is an operation error, such as wrong wiring, or wrong coil energization sequence. The second most important cause of failures is related to voltage problems (see example in Fig 2.2).

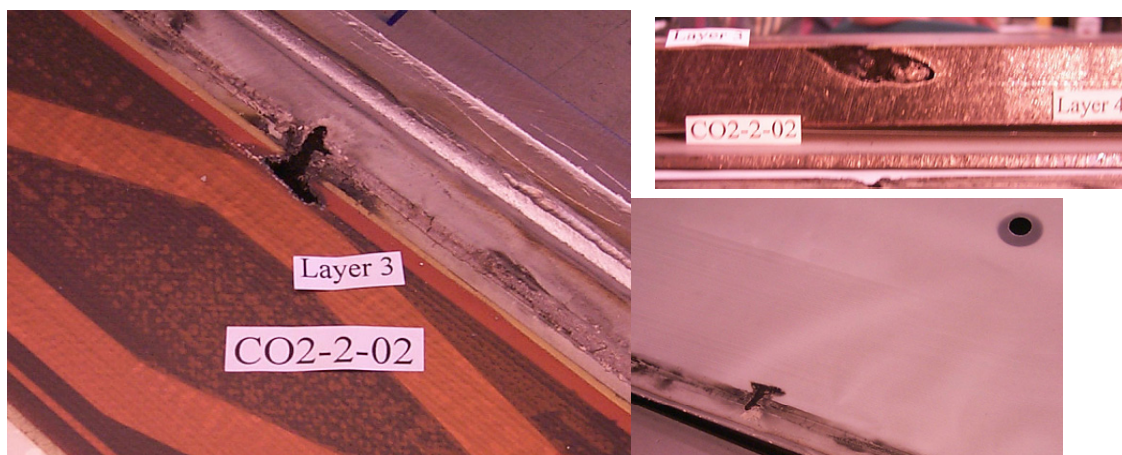


Fig. 2.2: Damage caused by an electrical short between coil and case in magnet RD3a (courtesy of LBNL magnet group); the arc melted the metal of the coil case producing a visible hole.

[2.4] therefore concludes that although the most common source of failures is not a design error, the reliability of the magnet operation can be improved by larger safety margins, especially in designing the insulation scheme. In fact, a common problem seems to be damage to the insulation, which can occur during assembly, transportation, or just because of a finite lifetime, and the lack of inspection and replacement (for example because of tear and wear or radiation dose). Another common cause of magnet failure is due to neglecting the low dielectric strength of low pressure Helium in stray magnetic field. Also the electrical protection circuit might be improved by redundancy, in order to avoid that an error in the system logic, or that a hardware problem might cause permanent damage to the magnet.

- Helium blow off after the quench: sudden helium blow-off can cause a large pressure rise, especially in single cryostats containing a string of magnets. Helium pressure waves can also propagate the quench to other magnets.

### 2.1.c Common quench protection strategies

Small magnets, such as 1 m accelerator magnet models and small bore laboratory solenoids, might not require an active protection system, if the conductor is well stabilized (sufficiently low  $J_{Cu}$ ), and the magnet is permanently connected with a parallel dump resistor. For example, the LBNL small magnets, described in chapter 5, are protected in this way, except for the use of a switch to connect the dump. In this case,  $J_{Cu}$  is high, but the fast quench propagation and the small inductance lead to a fast current decay. In addition, there is quench-back, which is the fast spread of the quench throughout the coils as a results of inductive voltages caused by the fast decay of the magnet current. Quench-back helps dumping the stored energy even faster.

Other passive protection techniques are 1- coupling the superconducting magnet with a short-circuited secondary winding, where the secondary circuit extracts part of the stored energy, and 2- shunt resistors across sections of the magnet. Unfortunately, the use of passive protection techniques is not suitable for accelerator magnets. In fact, most accelerator magnet designs require strong fields, long lengths, and small radius cryostats, in order to obtain high efficiency and reduce the overall costs of the accelerator construction and operation. Therefore, accelerator magnets are characterized by high overall current densities, high stored energy densities, and high inductances, which demand a fast and reliable active quench protection system.

As a concrete example of a typical quench protection system, we will describe the system used at the Magnet Test Facility (MTF) at Fermilab's Technical Division [2.5].

#### 1) Quench detection

The first action of the quench protection system is to detect the quench. The most common quench detection technique for accelerator magnets is based on detection of voltage rise. Voltage taps are attached to the conductor, usually in a few points in the magnet, for example at the ends of each coil, or at more locations in a prototype model. Subtracting the voltage signals coming from two equivalent sections of the magnets (for example the two half coils or poles of a dipole magnet) is a common method to reduce the noise caused by inductive pick up of external disturbances, such as power supply ripple. A common method to balance the two signals is to connect the voltage taps to a bridge circuit. Other analog or digital devices can be used to improve the noise rejection.

At the Magnet Test Facility (MTF), the quench management system includes a Digital Quench Detection system (DQD), and an Analog Quench Detection System (AQD). Both systems are used simultaneously for redundancy. [2.6]. The signals coming from the magnet are amplified and then distributed to the AQD and DQD systems. At the AQD level, after amplification and further subtraction of the signals, if the voltage threshold is exceeded, the system is set to the “tripped” status. The status is monitored by the quench logic system, which triggers the protection actions. The DQD system, based on a 16-bit analog to digital converter, samples the voltage signal from the magnet at a very high frequency. The digitized signal rate after filtering, is ~2400 Hz, and with a delay of ~1.9 ms. The resulting maximum quench

decision time is therefore  $\sim 2.4$  ms. The DQD allows a lower user-defined threshold voltage, by bucking of the digital signals. On the other hand, the AQD system is considered more reliable, since it has been used for years.

Other quench detection techniques are based on sensors for other kinds of signals, such as, inductive signals, temperature variations, and sounds.

Inductive signals are caused in quenching magnets, by the current redistribution inside a cable, associated with the transition from the SC to the normal state. These signals can be detected by means of small pick up coils placed close to the conductor at different locations along the windings (see for example ATLAS model coil quench velocities measurements [2.7]).

A technique that is used sometimes for accelerator magnet models is based on the reception of inductive signals by the so-called quench antenna [2.8, 2.9]. A quench antenna consists of an array of pick-up coils positioned at given angles in the bore of the magnet, in a similar way as for magnetic measurements. To increase the sensitivity to the small flux variations associated with the current rearrangement at the quench front, the main signal coming from the change in the total magnet current must be compensated. In a dipole model, for example, the antenna has to measure the quadrupole component, and in a quadrupole magnet the sextupole component. Consecutive sets of coils along the magnet can be used to complete the localization of the quench origin and to determine longitudinal quench velocities. [2.10]

A quench antenna was built recently at Fermilab for quench studies of  $\text{Nb}_3\text{Sn}$  dipole magnets, and it will be used during next magnet tests [2.11]. A quench antenna could also be used in replacement of voltage taps, since their installation on the brittle conductor is a difficult operation, which can even compromise the magnet performance.

## 2) Current supply disconnection

As soon as the quench is detected, the first action to be taken is to disconnect the current supply, and to reduce the current in the magnet. For this purpose, the magnet circuit usually includes a resistor, in parallel to the magnet, and a switch (Fig. 2.3). The resistor is usually outside the cryostat, and is called dump resistor. When the quench is detected, the quench protection system opens the switch (after a programmable delay time).

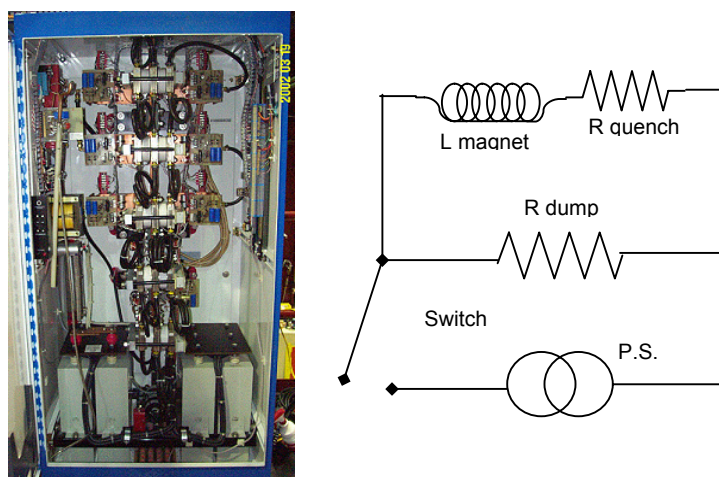


Fig. 2.3: MTF 10 kA dump resistor switch (one of the two at MTF) and schematic of magnet protection with dump resistor.

### 3) Extract stored energy

Once the switch is open, the current decay is determined solely by the magnet inductance, the resistance of the dump, and the resistance developed inside the magnet.

$$I = I_0 \cdot e^{-t/\tau}, \tau = L/(R_{Dump} + R_{quench}) \quad (A) \quad (2.2)$$

If the dump resistance  $R_{Dump}$  is much greater than the resistance of the normal zone in the magnet,  $R_{quench}$ , and the decay time  $\tau$  is small, then a large fraction of the stored energy will be dissipated in the dump, outside the cryostat. It is therefore a very common protection method for small magnets. The size of the magnet in fact determines its inductance  $L$ , which in turn drives the current decay, according to (2.2). The decay time can remain constant as long as the dump resistance is increased proportionally to the inductance. On the other hand, also the voltage at the magnet leads (equal to the voltage across the dump resistor) is proportional to the resistance.

$$V_{max} \cong I_0 \cdot R_{Dump} \quad (V) \quad (2.3)$$

The dump resistance  $R_{Dump}$  is then chosen in order to have  $V_{max} < 1\text{-}2$  kV. Therefore, the dump resistance is fixed with the current, and cannot be increased with magnet inductance. This means that the fraction of energy extracted by the dump resistor is not constant as the magnet size increases, and therefore, other protection measures must be taken.

### 4) Spread energy into the winding

If the stored energy of the magnet cannot be extracted, then it has to be dissipated into the windings as uniformly as possible, in order to avoid overheating of the location where the quench started (therefore called “hot spot”). In fact, if the energy distribution was uniform than the magnet would be safe. The case of the Common Coil magnet designed at Fermilab illustrated this point (see Fig. 2.4).

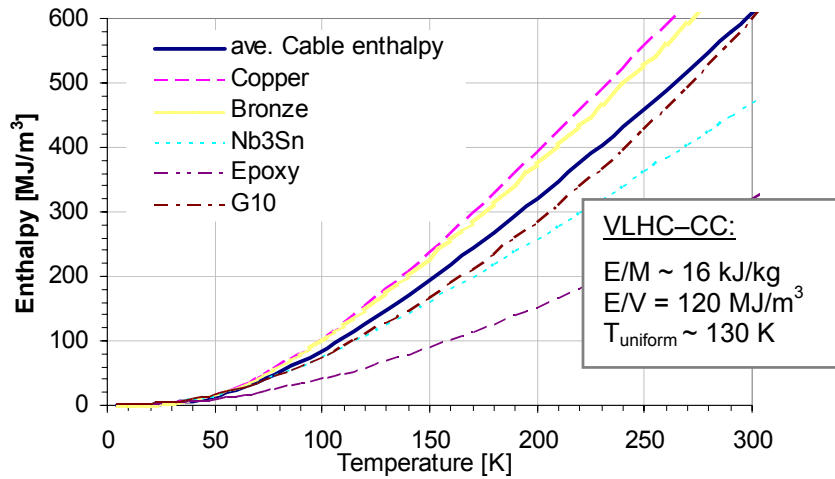


Fig. 2.4: Enthalpy per unit volume (case for the VLHC-2 common coil magnet)

From the plot in Fig. 2.4, we can see that if the total energy stored in the magnet at nominal operating condition ( $120 \text{ MJ/m}^3$ ) was released uniformly in the entire coil volume the resulting temperature would be 130 K. If the same energy was released in only half the conductor volume, the temperature would rise to 190 K, for a quarter of the volume 250 K, and so on.

Fig. 2.5 shows the energy per mass of big-size superconducting magnets for detectors; we can see that the energy per mass is usually kept constant, even when increasing the total mass. These magnets in fact have a high ratio of stabilizer vs. superconductor, while the conductor for accelerator magnets (also shown in Fig. 2.5) is designed usually in order to have high overall current density, and therefore high conductor efficiency, in terms of field intensity in the bore. We can see that the dipole magnets for the LHC and for the VLHC, as described in chapter 1, have a stored energy close to many detectors magnets, but a much higher stored energy per unit volume.

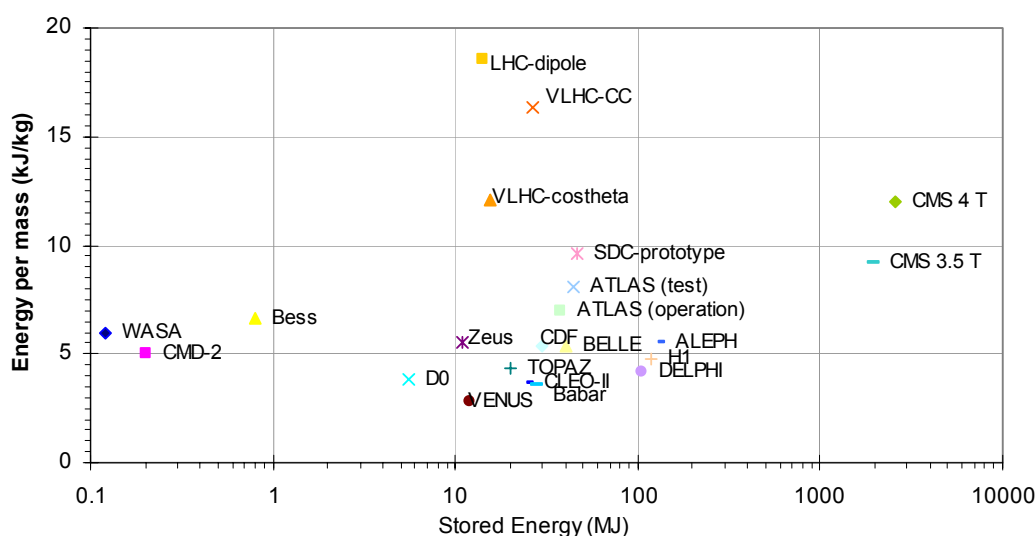


Fig. 2.5: Stored energy per mass vs. stored energy for solenoid magnets in detectors (A. Yamamoto), compared to state of the art accelerator dipole magnets.

In order to spread the energy into the winding, the normal zone has to propagate as fast as possible. The quench can diffuse in different ways:

- Natural quench propagation (longitudinally along turns, and transversely turn-to-turn, across the insulation)
- Quench-back (quench induced by fast current decay)
- Quench heaters

In a long magnet, such as an accelerator magnet, the first two ways of quench propagation are not usually enough to protect the magnet from overheating, and therefore the magnets are equipped with so-called quench heaters.

Quench heaters consist typically of stainless steel strips sandwiched between two layers of insulation. Fig. 2.6 shows the quench heaters used in Fermilab magnets HFDA03 (a  $\cos\theta$  magnet) and HFDB02 (a racetrack magnet).

The strip heater geometries are also typical: the strip dimensions are chosen in order to have a resistance per length of  $\sim 2\text{-}3 \text{ ohm/m}$  at LHe or room temperature. In addition, the strip geometry is designed such as to generate a low self inductance, in order to avoid inductive noise in the quench protection system and allow for a fast discharge of the capacitors into the quench



heaters. Heater strips in long magnets usually have additional copper plating, as, for example, for the LHC dipole magnets [2.12]. Copper-coated sections are alternated with non-coated sections of appropriate length. The copper cladding of the strip allows a faster and more effective energy discharge of the heater power supply, by reducing the resistance per length, and by concentrating the given power over a smaller area. The parts of the cable under the non-plated steel will quench first, and the parts under the copper plated areas will be reached shortly thereafter by natural quench propagation.

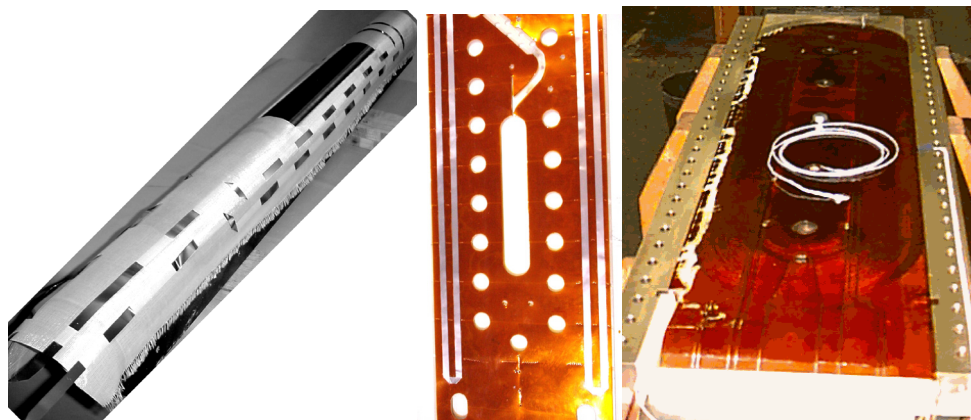


Fig. 2.6: Quench heaters of  $\cos\theta$  magnet HFDA03 and racetrack magnet HFDB02 and in RD2 (LBNL).

In the  $\cos\theta$  magnet, the strips are waived into a ceramic cloth, and in the racetrack magnet, the strips are glued to a Kapton foil; in both cases, the heaters are then sandwiched between two additional layers of the same material. The insulating layers are cut into the desired shape to fit into the magnet assembly; additional cuts were made in the Kapton foils to facilitate the epoxy flow in the magnet structure (Fig. 2.6). The ceramic insulation for the  $\cos\theta$  magnet was chosen because it can maintain good electrical and mechanical properties during and after the high temperature reaction cycle [2.13]. The insulating material for the racetrack magnet does not have to withstand the reaction cycle, because the magnet is built utilizing the react & wind technique.

All the heaters were tested and proved efficient. Reliability has still to be improved, because the connections between the strips and the copper wires are delicate and should be protected from strain occurring during fabrication, cool-down and quench. Additional heaters have to be added for redundancy in case the magnet protection relies entirely on the quench heaters (as in long magnets). Also critical is a symmetric distribution of the heaters over the coils. In fact, asymmetric heating of the coils inside the magnet can cause high thermal strain within the coils, which can result for example, in detraining [2.14]. Therefore quench heater failures should be avoided.

### 5) Quench protection systems for particle accelerators

In a particle accelerator, magnets are connected in series and form long strings. The LHC quench protection scheme is shown in Fig. 2.7, as an example. The LHC has 154 dipole magnets connected in series, for each string or octant of the ring. Since each magnet has an inductance ( $L_I$ ) of 0.102 H, the total inductance of the circuit ( $L_{oct}$ ) is 15.7 H [2.15]. The current is provided by one power supply. Two 75 m $\Omega$ -dump resistors can be switched into the string. One is shunting the power supply; the other is placed in the center of the magnet string. The use of two

dump resistors in different locations helps distributing the resistive and inductive voltage over the circuit. The total time constant of the magnet string is then given by  $L_{oct}/R_{tot} \sim 15 \text{ H}/150 \text{ m}\Omega = 100 \text{ s}$ . This is a very long time for a conductor with a copper cross section of  $\sim 10 \text{ mm}^2$ , carrying 12 kA. To avoid such long decay times and to avoid the entire magnet string discharging its energy in one single magnet, each magnet is connected in parallel with a cold diode. The Fermilab accelerator system uses external thyristors. Through external thyristors or cold diodes, the current can bypass the quenching magnet, and decouple the two current circuits:

- One circuit consists of the quenched magnet and the diode, with a current decay time constant of  $\sim 100 \text{ ms}$ ;
- The rest of the magnet string, including the dump resistors, constitutes the second circuit, with a current decay time constant of  $\sim 100 \text{ s}$ .

As a result, the quenching magnet will absorb only its own stored energy, and by distributing this energy with the quench heaters, overheating can be avoided.

The energy stored in the rest of the circuit will be dissipated in the external dump resistors.

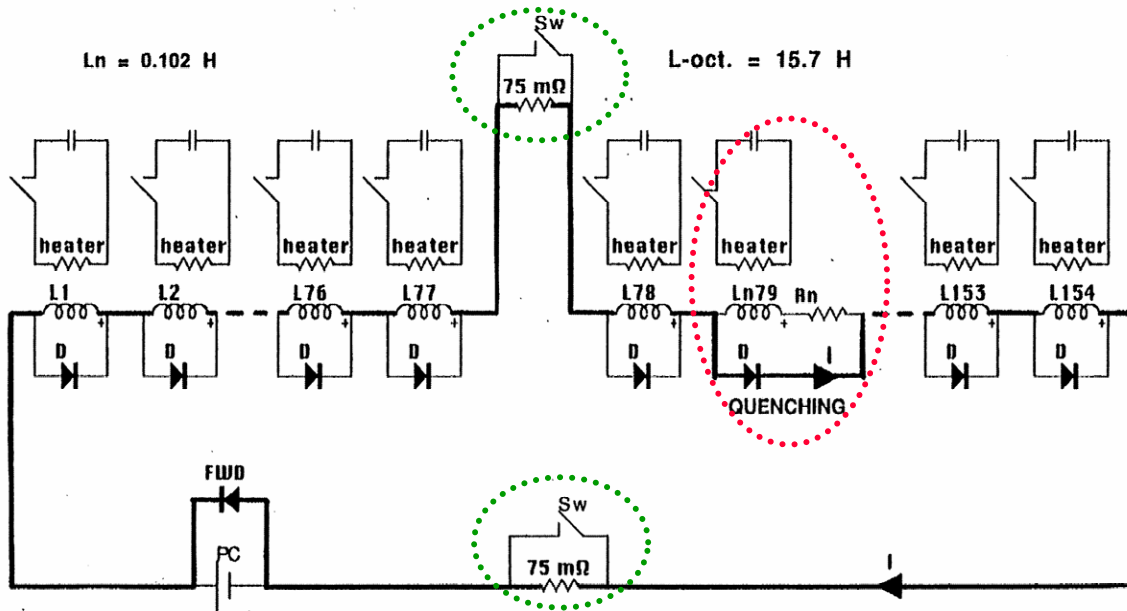


Fig. 2.7: Quench protection circuit for an octant of the LHC [Courtesy of F.Rodríguez Mateos/CERN].

#### 2.1.d Calculation of the main quench parameters

In the last paragraph, we have seen that to protect an accelerator magnet in a string of magnets, it is necessary to use diodes (or thyristors), and quench heaters. Consequently, we can study the quench protection for just a single magnet, as a first step, to have an estimation of the temperature and voltage distribution that can develop after a quench.

Detailed simulations of the quench process will be presented later in this chapter, together with the description of simulation programs and the discussion of the results. Here, we present the basics of any quench protection calculation, such as the quench-integral calculation, which can provide a first estimate of the main quench parameters.



Hot spot temperature estimation

To have a conservative estimate of the peak temperature, we can consider the adiabatic heat balance equation at time  $t$  of the quench process:

$$\frac{R(T)I(t)^2}{Vol} dt = c_p(T) dT \quad (\text{J/m}^3), \quad (2.4)$$

where the Joule heating per unit volume, given by the resistance of the conductor  $R$ , multiplied by the current ( $I$ ) square in the time step  $dt$  is completely absorbed by the heat capacity ( $c_p$ ) of the materials in that volume ( $Vol$ ), which results in a temperature increase by  $dT$ . Considering that the resistance per unit length  $l$ , is  $R/l = \rho/A$ , where  $A$  is the cross section of the conductor and  $\rho$  is the overall resistivity of the conductor, we can rewrite (2.4) as

$$\rho(T) \left( \frac{I(t)}{A} \right)^2 dt = c_p(T) dT \quad (\text{J/m}^3). \quad (2.5)$$

Dividing (2.5) by the resistivity, and multiplying by  $A^2$ , we obtain:

$$I(t)^2 dt = A^2 \frac{c_p(T)}{\rho(T)} dT \quad (\text{A}^2\text{s}) \quad (2.6)$$

The term on the right side of (2.6) contains only material properties and geometrical factors, which depend directly only from temperature, and the left term of (2.6) depends directly only on time. By integration over time/temperature, from zero/ $T_0$  to infinite/ $T_{peak}$ , we can now obtain the so-called Quench Integral ( $QI$ ), a function of the final temperature ( $T_{peak}$ ), which is also the maximum temperature in the adiabatic approximation,

$$QI(T_{peak}) = \int_0^\infty I^2(t) dt = A^2 \int_{T_0}^{T_{peak}} \frac{c_p(T)}{\rho(T)} dT \quad (\text{A}^2\text{s}) \quad (2.7)$$

The  $QI$  is commonly measured in  $\text{MA}^2\text{s}$ , also known as MIIts (“mites”), which means  $10^6$  (M), squared  $I$  (I·I), integrated in time (t).

From equation (2.7) we can see why the  $QI$  is a very convenient way to obtain a peak temperature estimation. In fact, because the right side of (2.7) contains only material properties and geometrical factors of the conductor, magnets with the same conductor, refer to the same MIIts curve. Therefore, measurement or simulation of the current decay can provide an estimation of the peak temperature, by comparing the accumulated MIIts with the curve calculated from the right side of (2.7).

Note that the adiabatic equation yields a conservative peak temperature estimate (no heat exchange with the helium, nor heat conduction are considered)!

$\text{Nb}_3\text{Sn}$  magnets are usually impregnated with epoxy resin in order to increase the overall coil stiffness and to protect the brittle conductor from stress concentration. Therefore, the adiabatic assumption is usually considered a good approximation. The question is, however, how much of

the insulating material should be included in the heat balance equation, and therefore in the quench integral.

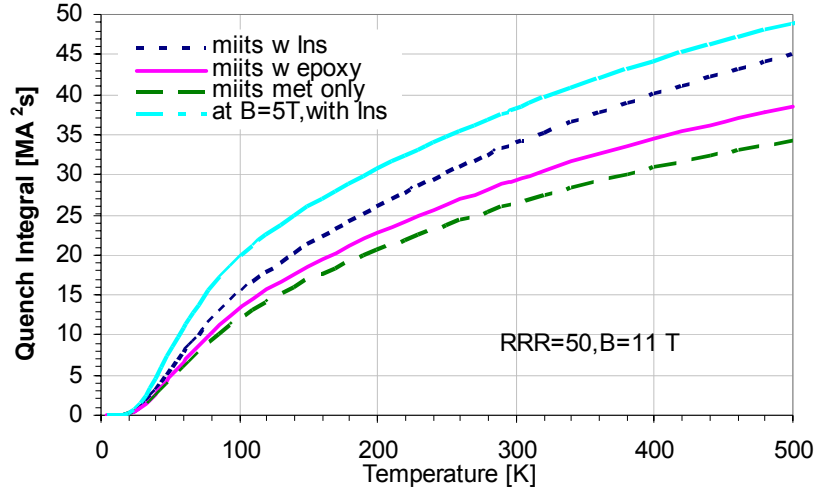


Fig. 2.8: Quench integral for common coil magnet for VLHC-2 for conductor with (w ins) and without insulation (met only) as well as without insulation but including epoxy in the voids of the cable. The material properties are as discussed in chapter 3.

Equations (2.5-7) point out clearly the most important conductor parameters affecting the temperature after a quench:  $A$ ,  $\rho$ , and  $c_p$ .

The following summarizes the most important ways to reduce the peak temperature:

- Decrease of the cable current density (larger cable, more copper)
- Use of lower resistivity materials (for example high RRR)
- Fast current ramp down (early quench detection, fast heater action, fast resistance rise: low RRR)

To exemplify the last point, we can rewrite the  $QI$  as the sum of two parts, by dividing the integral before and after the heaters become effective ( $\tau_d$ ):

$$QI(T_{peak}) = \int_0^{\infty} I^2(t) dt = I_o^2 \tau_d + \int_{\tau_d}^{\infty} I^2(t) dt \quad (A^2 s) \quad (2.8)$$

where  $\tau_d$  is the total heater delay time, that is given by the quench detection time plus the quench heaters activation time (basically, the time it takes for the heat transfer from the strip to the conductor, through the layers of insulation). The first term of (2.8) is trivial. The second term, in case of a magnet protected by a dump resistor, is given by the exponential decay (2.2) with  $\tau = L/R_{Dump}$ . In the case the protection relies on quench heaters, the resistance determining the current decay is a function of time, since it depends on the normal zone volume, the temperature distribution and also the magnetic field. In this case, the prediction of the peak temperature is more difficult. An evaluation of the second term in (2.8) can be obtained in this case from the following procedure. First, we have to consider the average temperature reached by the coils quenched by the heaters, using the average enthalpy function and the stored magnetic energy. For example, in case of the common coil with 100% heater coverage, the average temperature in the coils is 130 K (Fig. 2.4). Now, from the  $QI$  function with an average field, it is possible to

evaluate the necessary MIIs to reach such a temperature, and therefore the last term of equation (2.8). In the Common Coil example, we can see from the curve at 5 T in Fig 2.8, that 130 K corresponds to 18 MA<sup>2</sup>s. The hot spot temperature is found from the total  $QI$  function at the peak field in the coil where the quench originally started (11 T in this example). This model has produced good agreement with the results from the simulations of the common coil magnet proposed for the VLHC-2 [2.16].

### Calculation of voltage distribution

In the case of short dipole models or other small magnets, which are protected by discharging most of the energy into the dump resistor, the largest voltage drop ( $V_{max}$ ) occurs across the dump resistor ( $R_{Dump}$ ) itself, that is between the magnet leads. In this case we have seen in (2.3) that  $V_{max} \sim I \cdot R_{Dump}$ . It is common practice to keep the maximum voltage below 1 kV, and therefore to choose  $R_{Dump}$  such that  $I_{SS} \cdot R_{Dump} < 1$  kV, where  $I_{SS}$  is the expected maximum current (so called short sample limit). The example of the common coil magnet shown in Fig 2.9 reveals the functional dependencies which are at the basis of the compromise between peak voltage and temperature. The choice of 1 kV is somewhat arbitrary, and in fact depends on the insulation, the geometry of the leads, and other conditions such as vapor or liquid cooling, etc.

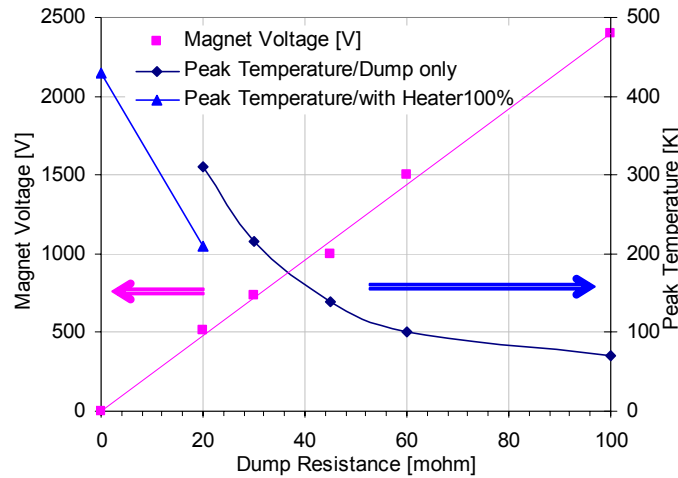


Fig. 2.9: Peak voltage across magnet leads and peak temperature vs. dump resistance in quench simulation for short model (1 m) of the common coil magnet [2.16].

In the case the magnet is not connected to an external dump resistor, such as for a magnet in an accelerator string, the voltage across each magnet ( $V_{tot}$ ) is due to the diodes or thyristor voltage, which is usually negligible in this context. We have therefore:

$$V_{tot} = R_{quench}(t) \cdot I - L_{tot} \cdot dI/dt \cong 0 \quad (\text{V}) \quad (2.9)$$

Equation (2.9) shows how the resistive voltage, due to the resistance developed inside the magnet ( $R_{quench}$ ), and the inductive voltage, given by the total magnet inductance  $L_{tot}$  times the current derivative  $dI/dt$ , compensate over the whole magnet, reducing therefore the possibility for high voltages to ground.

On the other hand, in the case of long magnets, both the resistive and the inductive terms of (2.9) are usually higher than for a short magnet protected by a dump resistor. Therefore, high voltages to ground can occur inside the coils, and, with higher peak temperatures, the turn-to-turn voltage between the hot spot and the surrounding cold zones can also be higher than for a short magnet protected by a dump resistor. Fig. 2.10 shows the voltage distribution in the case of Fermilab's common coil magnet proposed for the second stage of the VLHC [2.16]. We can see that the voltage to ground starts at zero, rises following the inductance pattern particular to this magnet, and has a sudden increase at turn N. 40, where the quench started (hot spot).

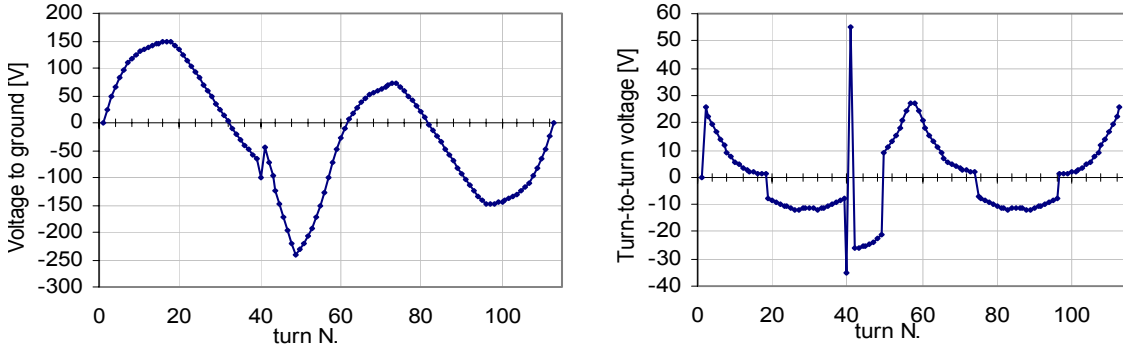


Fig. 2.10: Voltage to ground and turn-to-turn voltage vs. turn number, in quench simulation for long model (10 m) of the Common Coil magnet [2.16]. Calculation performed with Quenchpro (see 2.2.c)

## 2.2 Quench simulations

As described previously in this chapter, the quench process is a thermo-electrical problem, determined by the heat balance equation and by the electro-magnetic laws governing the current decay in the magnet circuit. The thermal and electrical problems are coupled through the temperature and field dependence of the resistance, and the active protection measures (PS regulation, quench heaters, diodes etc.). It is not possible to solve the problem analytically, not even the heat balance equation, because of the non-linearity of the material properties and the complex geometry.

Several numerical codes have been developed in the superconducting magnet community to simulate the quench in a superconducting magnet. Here we present briefly some commonly used programs, and a more detailed description of the programs used in this thesis work, which were specialized to treat Nb<sub>3</sub>Sn magnets.

In order to study the thermo-mechanical effects of the quench, another quench simulation method was used, utilizing the Finite Element program ANSYS<sup>TM\*</sup>, with the advantage of a very fine temperature distribution even in the insulation. The results of the quench simulation are then available for a thermo-mechanical analysis. The ANSYS simulations are described in chapters 4.

---

\* Trademark of SAS IP

### 2.2.a Common quench simulation programs

The program QUENCH [2.17], developed in 1968 at DRAL, is one of the first programs to calculate the quench propagation in a superconducting magnet, and is widely used, even if in the form of modified versions. The original program is a simple numerical solution of the adiabatic heat balance equation. The winding is considered as a “bulk” with non-isotropic properties, which determine the quench propagation velocities in all directions.

The program is designed in particular for impregnated solenoids and does not include quench protection heaters, but provides the possibility to include coupled secondary circuits or dump resistors as means of quench protection.

The basics of the QUENCH program are described in the following, since they are also the basics of the QLASA program, used for simulating the quench of Nb<sub>3</sub>Sn magnets in this thesis work. The convention for the symbols used in the following model description can be found in the appendix.

At time  $t = 0$  a quench is initiated in the coil and starts to propagate with different velocities in longitudinal (that is parallel to the conductor) and transverse directions, so that at time  $dt$  the normal zone will be an ellipsoid. At each subsequent temporal step, a layer is added to the surface of the normal zone, like the skin of an onion. In each layer, the temperature is uniform and is updated at each time step. The temperature rise is found from the adiabatic heat balance equation (therefore, neither cooling effects nor conducted heat are considered) for each particular layer (2.5).

The current decay is given at each time step  $dt$  by:

$$dI = I \cdot (R/L) \cdot dt \quad (\text{A}) \quad (2.10)$$

where the resistance  $R$  is the sum of a possible external resistance ( $R_{Dump}$ ) and the total resistance of the coil ( $R_{coil}$ ):

$$R = \sum_{coil} R_{coil} + R_{dump}, \text{ with } R_{coil} = \sum_{layer} \rho(T_l) V_l / A_{cable}^2 \quad (\Omega) \quad (2.11)$$

$R_{coil}$  is the sum of the resistance of each layer given by the cable resistivity ( $\rho_{cable}$ ) at the temperature ( $T_l$ ) of the layer, multiplied by the volume ( $V_l$ ) of the layer, and divided by the total cable cross-sectional area ( $A_{cable}$ ).

The program QUABER [2.18] was developed at CERN for the design of the quench protection system of the LHC magnets. It uses a commercial network solver (SABER<sup>TM†</sup>) to simulate the electrical circuit. Embedded in a time loop, QUABER calculates the temperature distribution in the magnets at each time step from the adiabatic quench integral, accounting for transverse heat propagation as well as longitudinal heat conduction. The resistance distribution in the conductor array is then used to solve the transient electrical problem with SABER<sup>TM</sup>, and so on. QUABER takes into account the magnetic field distribution in the magnet cross-section (specified in input, as provided by ROXIE) and the decay of the magnetic field together with the current (using an input transfer function). The repartition of quench protection heaters over the coils and the heater delay time are input parameters. The ability to solve complex electrical

---

<sup>†</sup> Trademark of Analogy Inc.

problems, like calculating the current sharing between all the components of a magnet string circuit, including parallel diodes, dump resistors, etc, makes QUABER a widely used quench protection package.

Another program developed at CERN, called SPQR (Simulation Program for Quench Research) [2.19], was successfully used to simulate the effect of the heat transfer to the Helium, the effect of quench heaters, and eddy current heating. It was also designed to be interfaced with QUABER.

## 2.2.b QLASA

At the LASA<sup>‡</sup> laboratory, the original QUENCH program has been revised and developed through the years. The main structure of the program was changed, in order to make it simpler and more versatile. Other changes regarding the physics model and the calculation of quench parameters were also introduced [2.20].

One of the first improvements was the introduction of a material properties library that is independent and can be called from any part of the program.

In addition, the possibility to simulate a larger system of magnets, electrically independent, each consisting of multiple coils with different materials and different features was implemented. It is also possible to simulate voltage taps inside each coil, in order to have a voltage distribution inside the coils.

The program offers the choice between various magnet circuitries. One of the simplest consists of one or more coils driven by a power supply and connected to an external dumping resistor by a switch, as in Fig. 2.11. The dump might be connected in parallel only after switch activation (as in MTF), or be always connected in parallel, as an additional safety measure.

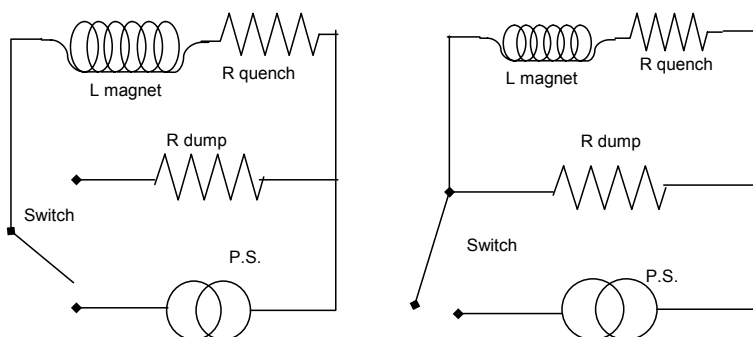
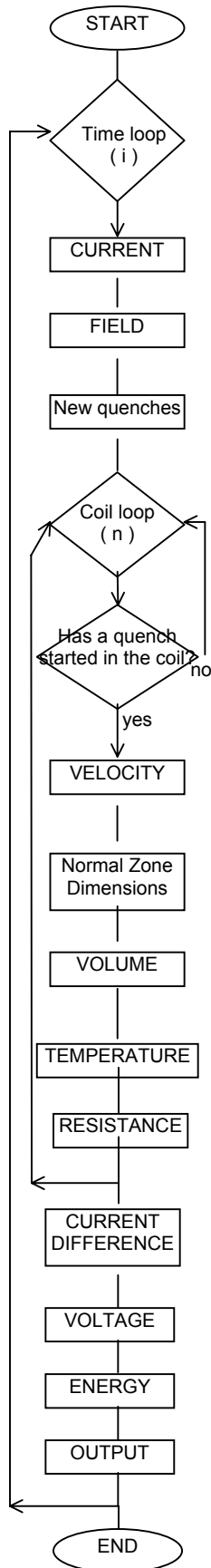


Fig. 2.11: Simple circuit with dumping resistor (dump connected as at VMTF) and in other possible configurations.

Some further developments, subsequent to [2.20], include a persistent mode operation option, and recently the implementation of more accurate scaling laws for the critical surface of Nb<sub>3</sub>Sn.

The following block diagram outlines the structure of the QLASA program:

<sup>‡</sup> Laboratorio Acceleratori e Superconduttività Applicata of the INFN in Milan



The program begins reading the input file, calculates some constants, and initializes the variables.

The time loop starts, and for each time step the variables are updated.

The current changes according to the current difference calculated in the preceding time step.

The field is then updated (proportionally to the current).

Quenches may start at a time and at a point given in the input or because the current in a coil exceeds the critical current.

For every coil the main parameters are computed if a quench occurred in the coil, otherwise the coil remains at bath temperature and has zero resistance.

The quench propagation velocities are calculated with (2.12), (2.13). The specific heats and the thermal conductivities are computed with subroutines, which use values from the material property library.

The lengths of the semi-axes of the ellipse describing the normal zone can be calculated...

... and the volume of the new layer added to the normal zone.

For each layer (or shell) added at a certain time step, the temperature is found from the adiabatic heat balance equation (2.5).

The resistance of each coil is the sum of the resistance of the zones between voltage taps (2.11).

When the parameters for each coil are calculated, the current change is found from (2.11).

Voltage between voltage taps is the sum of resistive and inductive voltages:  $V_{zone} = I \cdot R + L \cdot dI/dt$

The energy fractions, dissipated in the coils and in the dump resistor, are reported at the end of the run.

For each time step, all the above-mentioned parameters are written to files.

The program ends when it has reached the maximum number of steps given in the input, and writes the final output file, summarizing the main results.

An important aspect of QLASA (as well as of QUENCH) is the quench propagation velocity. The quench spreads non-isotropically. The direction along the conductor, so called longitudinal direction, is indicated by the subscript  $l$ , and the transverse direction (radial and axial referred to the solenoid geometry), by the subscript  $t$ .

Here is a list of symbols used in the following model description.

$C_p^{met,Av}$	is the specific heat averaged over the metal components and over temperature, between bath ( $T_b$ ) and critical temperature ( $T_c$ ).
$T_M$	is the transition temperature, taken as the average of critical and generation temperature ( $T_g$ , also known as current sharing temperature).
$C_p^{met}(T_M)$	is the specific heat averaged only over the metal components
$\lambda$	is the conductivity
$L_0$	Lorentz number ( $2.45 \cdot 10^{-8} \text{ W} \cdot \text{ohm} \cdot \text{K}^{-2}$ ); from the Wiedemann-Franz law: $\lambda \cdot \rho = L_0 T$ .

The longitudinal velocity ( $v_l$ ) is found analytically from the heat balance equation in one dimension. The formula used in QLASA is

$$v_l = \frac{I/A_{met}}{C_p^{met,Av}} \sqrt{\frac{L_0 T_M}{T_M - T_b}} \text{corr}_l \quad (\text{m/s}) \quad (2.12)$$

where  $\text{corr}_l$  is a correction factor to adjust the calculation to experimental data. The correction factor can also be used to simulate the effect of heaters, as explained later.

In the transverse directions, the quench diffuses more slowly because of the insulating barriers:

$$v_t = v_l \frac{C_p^{met}(T_M)}{C_p(T_M)} \sqrt{\frac{\lambda_t}{\lambda_l}} \text{corr}_t \quad (\text{m/s}) \quad (2.13)$$

Quench simulations have been compared with experimental data from several magnets. Quench studies have been performed for multi-coil magnets, wound from NbTi and/or Nb<sub>3</sub>Sn conductors, driven by a power supply or in persistent mode [2.21]. Good agreement was found between simulation results and experimental data for NbTi magnets. For Nb<sub>3</sub>Sn magnets, it was found that in order to match the experimental values the velocities needed small correction factors, from 1.15 to 1.5. Similar correction factors were found during quench velocity studies performed at Fermilab (see chapter 3.6.a).

### Coil arrangement and field map

Before running a quench simulation, it is necessary to create a model of an accelerator dipole magnet adapted to the program characteristics, because QLASA was created mainly for solenoids. Here, the model for racetrack geometries is described, as an example. While the main features of the magnet and of the cable are kept unchanged, racetrack coils have to be transformed into solenoids.



The radius of the solenoid is found, keeping the cross section and the volume of the winding constant. To obtain a field profile most similar to that of the real model (Fig. 2.12), it is necessary to rotate the circular coils by 90°, from the common coil configuration to the solenoid configuration. The peak field is then at the inner radius in the middle plane, where it is often in solenoids.

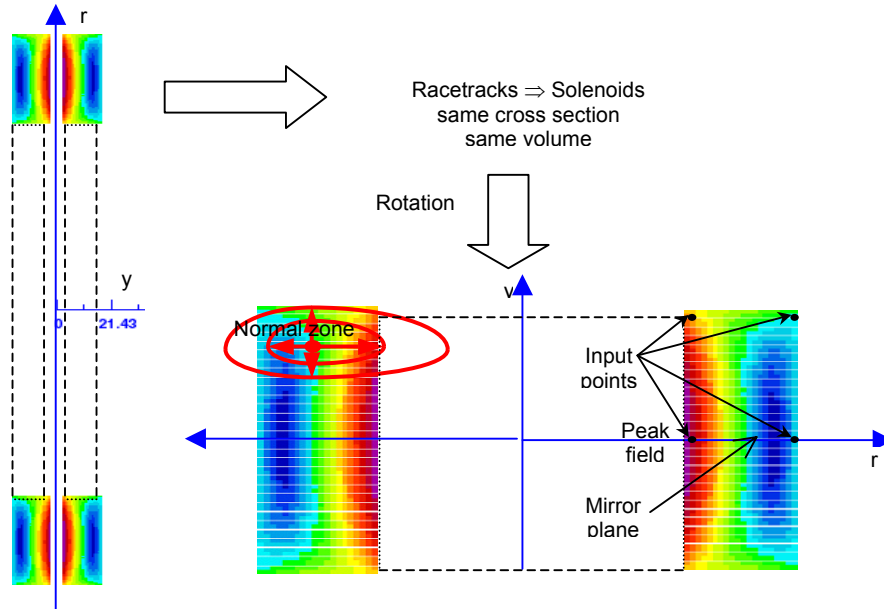


Fig. 2.12: Transformation of racetrack coils into solenoids. Colors refer to the field strength.

The field distribution in each coil is calculated by the QLASA program by interpolating values given in the input in four points: at inner radius, outer radius, in the middle plane and upper plane (with respect of the solenoid geometry). Below the mid plane, the field is calculated with mirror symmetry (mirror in mid plane). Another way to describe more accurately the field profile is to subdivide each coil into more coils (up to 16 coils were used in this work). Another advantage of the 16 coils model is to have the voltage at the ends of each sub-coil, without additional voltage taps. Its disadvantage is that the sub-coils become thermally independent, i.e. the normal zone cannot propagate across coil boundaries. This can affect the quality of the temperature calculation.

To better simulate the effect of the heaters it is necessary to subdivide the coil, so the 16 coil-model was often used. In this model it is possible to initiate the quench in a point in the  $n^{\text{th}}$  sub-coil at time zero, and let the program simulate the normal quench propagation in that coil (small correction factors to the quench velocities are applied).

The quench is initiated in all the coils covered by quench heaters, after the quench detection time, plus the quench heater time delay. Very high correction factors for the quench propagation velocities (of the order of 10-100) are used to spread the quench over several turns and over the length covered by the heaters in the short time estimated by heaters parameters (such as geometry, copper plating, etc.) and quench propagation times. The heater delay time is a key parameter of the quench simulation, as parametric studies show (see chapters 2.2.d and 2.3.a). The values used in the simulations were taken from measurements, when possible (see 3.6.b).

### 2.2.c Quenchpro

The program Quenchpro [2.22], presently in the form of a MCAD<sup>®</sup> spreadsheet, is divided into two parts. In the first part, the magnet is defined as a series circuit of 16 sub-coils. After the definition of the magnet parameters, preliminary calculations of the material properties, and definition of the quench protection system parameters, the program calculates the current, the temperatures, and resistances of the 16 coils during the quench. In the second part of the program, the coordinates of all turns in the magnet are defined, so that the turn-to-turn inductance matrix can be calculated. Based on the resistance, temperature, and current decay calculation of the first part and the inductance matrix, the program then calculates the turn to ground and turn-to-turn voltages.

#### Calculation of Temperature and Current Decay

In the first part, which is described in detail in the following, the current, temperatures and resistances of all 16 sub-coils are grouped into a vector, whose time-dependence is iteratively calculated from the preceding time-step, after the initial value of all parameters at quench-time ( $t = 0$  sec) have been defined. There are two MIIts-clocks in the vector: one that starts accumulating quench integral at  $t = 0$  and the other that starts accumulating  $QI$  after the start of heater action (given by the sum of quench-detection time and heater delay time). Each coil group is assigned to one of the MIIts clocks (or none) depending on its mode of quench (initial spontaneous or heater induced).

Using the adiabatic approximation, the maximal temperature  $T_{max}$  of the quenched superconductor is calculated from the quench integral ( $QI$ ). Quenchpro calculates the peak temperature as a function of  $QI$  from the material properties prior to the quench process calculation. In the course of the quench process calculation Quenchpro calculates the  $QI$  from the current decay profile and retrieves the temperature from the pre-established  $T_{max}(QI)$  correlation mentioned above. Quenchpro uses a constant (average) field in the calculation of the material properties, thus it only weakly approximates the real case, where the field varies through space and time. Then, as the program computes the quench process, the maximum temperature of the conductor for each time step is obtained with the  $QI$  calculated from the time integration of the square of the simulated current decay profile. It is important to note that the  $QI$  integration starts at quench time, thus each coil-part is related to a different “MIIts-clock” by its own time of quenching.

The  $QI$  function can be defined over the entire cable cross section, including not only superconductor, copper and bronze, but also the epoxy filling the voids in and on the cable, as well as the epoxy-impregnated cable insulation. The program has a library of the material properties for these materials, in the temperature range of interest.

The program assumes that the entire normal zone in each coil is at the one momentary temperature given by the quench integral accumulated in the coil at that time. In case a spontaneous and a heater induced quench occur in the same coil, the coil temperature is therefore assumed to be the temperature of the initially quenched turn. This leads to an overestimation of the resistance of this particular coil. It is therefore advisable to set the initial quench in a small coil with a small number of turns, and to refrain from using heaters in this particular coil.

The calculation of the normal zone length requires information about the nature of the quench (spontaneous, through heaters or through quench propagation) and the time when the

quench occurs. The quench starts spontaneously at  $t = 0$ , typically in one turn of one of the 16 coil parts, and spreads via longitudinal propagation. After quench detection and heater delay time all turns covered by active heaters are quenched over their full length. The heater induced quenches also propagate longitudinally. The longitudinal heat propagation is fully described with the quench propagation velocity (which is constant in Quenchpro). A so-called end-of-propagation time is defined to account for the decrease of propagation velocity in the real case. After that time, the program suppresses the propagation of the normal zone.

The program assumes that the magnet power supply is disconnected from the magnet after quench detection time and the so-called switch time. If required, a dump resistance can be specified to simulate dump-supported quenches. If the dump resistance is set to zero the magnet leads are considered short-circuited. After that, the current decay is calculated from the time constant at each time, calculated from the total magnet resistance (the sum of the resistance of all sub-coils and the dump) and the total (constant) inductance  $L$ . The time constant is used to calculate the new current from the old current. With the new current, the increase of quench integral is found and thus the new temperature of the coils, giving a new resistance and so forth - until the current has dropped to zero.

Quenchpro and QLASA simulations results were compared during the quench protection studies of the racetrack magnet and differences were pointed out [2.23]. The normal zone propagates with constant velocity along the conductor in Quenchpro, while in QLASA it propagates in all the directions with velocities decreasing with the current. The temperature is assumed to be equal to the peak temperature in the entire normal zone and the field equal to an initial value in Quenchpro, while there is a temperature profile from the point where the quench originally started to the edge of the normal zone in QLASA. The field value affecting the resistivity is calculated as an average over the total normal zone, and decreases with the current in QLASA. The simplifications in temperature and field in Quenchpro resulted in an overestimation of the resistance, and therefore in faster current decay. For a better estimation of the resistance, it was found that instead of giving the peak field, a low field value could be used, and used as a “tuning” parameter, in a similar manner as the correction factors for the velocities in QLASA. Using an “effective field” value of 1-2 T, QLASA and Quenchpro give similar results, with peak temperature differences of about 10 %.

### Calculation of Voltage Distribution

In the second part of Quenchpro the inductance matrix of the magnet is calculated on a turn-to-turn basis. Therefore, the mid-points of all turns have to be specified. The mutual inductance between two turns is calculated from the current and the magnetic flux originating in one turn and enclosed by the surface of the other turn. In addition, all inductances are multiplied by an “iron-enhancement” factor to account for the effect of iron yoke. The iron-enhancement factor is chosen such that the total calculated inductance (the sum of all mutual and self-inductances) agrees with the total inductance calculated by other magnetic design programs such as Opera<sup>®</sup> or Roxie. The iron enhancement factor is typically 1.1 in the magnets regarded here.

The voltage to ground is calculated from the current, the resistances of each turn (calculated from the resistances of the respective sub-coil), the temporal current derivative, and the self and mutual inductances of the turns. The calculation proceeds as a running sum of resistive and inductive voltages through the magnet parts following the exact electrical sequence of the turns in the magnet. The inductance matrix ( $L_{j,k}$ ) has to be built according to the same electrical

sequence. The maximum voltage to ground is occurring most likely at the time at which the total resistive voltage of the coil is biggest. The voltages shown in the output are therefore calculated at that particular time.

The turn-to-turn voltage for a chosen time-step and a given turn can be calculated from the difference in coil to ground voltage to the turn before (referring to the turn sequence in the electrical scheme of the magnet). Similarly to the case of the turn to ground voltages the turn-to-turn voltage is calculated at the time at which the total resistive voltage of the coil reaches its maximum.

## 2.2.d Contribution of the insulation to the adiabatic quench process

Studies performed for LHC magnets revealed that heat transferred to the helium bath has to be included in the quench simulations [2.19]. For impregnated magnets, as usual for Nb<sub>3</sub>Sn magnets, the helium fraction in the coils is negligible, and therefore was not considered in the quench simulations presented here, and the adiabatic assumption is considered to be a good approximation for epoxy-impregnated coils.

On the other hand, the question arose whether the epoxy within the cable voids and the external insulation contribute to the thermal balance during the quench process. In fact, the impregnation provides a close contact between the external insulation and the strands. To answer this question, we looked at the thermal diffusion times of the insulating materials. The thermal diffusivity of epoxy and G10 are indicated in Table 2.1, together with the heat diffusion time for a 0.1 mm-thick insulating layer. From these data we concluded that the insulation plays an important role in the thermal balance equation and should be included in the quench integral of the conductor.

Material	Diffusivity (m <sup>2</sup> /s) at 4 K	Diffusivity (m <sup>2</sup> /s) at 300 K	Time (ms) at 4 K	Time (ms) at 300 K
G10	9·10 <sup>-5</sup>	3·10 <sup>-7</sup>	0.1	33
Epoxy	6·10 <sup>-5</sup>	10 <sup>-6</sup>	0.2	10

Table 2.1: Thermal diffusivity of epoxy and G10, and relative heat diffusion times for a 0.1 mm-thick insulating layer [2.24].

On the other hand, since the diffusion time is proportional to the square of the heat transfer length, the temperature over a thick insulating layer will not be uniform in the time range of the diffusivity, but strong gradients will establish between the “hot spot” and the cold environment. The quench integrals, used in Quenchpro, consider a uniform temperature over the cable cross-section, therefore, in some cases, depending on the materials involved and the time scale of the quench process, the insulating thickness considered in the quench integrals was less than the actual thickness (see a discussion of this issue in the context of measurements in chapter 4 and 5). The quench simulations in the following, however, were performed on the basis of quench integrals that included the conductor insulation (which in the case of the cos $\theta$  / common coil magnets was 0.15 mm / 0.1 mm thick ceramic-fiber / epoxy impregnated fiber-glass). A collection of the material properties used in the simulations of the quench processes discussed in the following is presented in detail in chapter 3.

### 2.2.e Parametric quench studies for VLHC dipole magnets

Quench simulation programs have been used to study the quench protection requirements of several magnets. First, quench studies were performed to find the requirements for the protection of the short model magnets built and tested at Fermilab. During testing, these magnets can be protected just with the parallel dump resistor, but for R&D purposes, the magnets were also equipped with quench heaters and, in some cases, also with spot heaters, voltage taps, and temperature sensors. Although these quench protection studies are on-going, the results obtained thus far were useful to tune the model parameters (see chapter 3.4 for a discussion of the measurements obtained thus far, and for the comparison with the QLASA model).

Quench simulation studies have been performed, not only for Fermilab's short model magnets, but also for theoretical long versions of these, in view of a future hadron collider using Nb<sub>3</sub>Sn magnets. The main magnet parameters of the full-scale version of Fermilab's magnets are reported in Table 1.6-7 in chapter 1 for the VLHC design study [1.22]. The main results of this study were also compared to the results of analytical calculations that are independent of the particular design of the magnets. The results of the generic study are reported in section 2.3.

This section reports the results of parametric studies, performed with Quenchpro and QLASA, varying the heater coverage, the total heater delay time, the copper to non-copper ratio, and the copper RRR. The studies performed for the common coil model are described in further detail in [2.16]. The parametric studies aimed at finding the appropriate conductor and quench-heater parameters to limit the temperatures to ~400 K and voltages to 1 kV.

Table 2.2 reports the main magnet parameters relevant for quench protection, and Table 2.3 reports the main conductor parameters of the same magnets. The magnet cross-sections were presented in chapter 1 (Fig. 1.7, Fig. 1.8).

Magnet	Cosθ warm-yoke	Common coil-cold yoke	LHC- main dipole
T (K)	4.5	4.5	1.9
B (T)	10	10	8
I (kA)	21.3	23.5	11.8
Peak field (T)	10.5	11.3	9.2
L (mH/m)	2×1.07	2×1.5	2×3.8
E (kJ/m)	2×486	2×828	2×490
e (MJ/m <sup>3</sup> )	86.2	119.8	117
Length (m)	16	16	14.5
# of turns	96	112	164

Table 2.2: VLHC magnet parameters relevant to quench protection. LHC dipole parameters are listed for comparison (the superconductor for LHC is NbTi). All magnets have two apertures.

Magnet	Cosθ warm-yoke	Common coil-cold yoke	LHC- main dipole
A <sub>cable</sub> (mm <sup>2</sup> )	29.3	31.02	25.5
J <sub>Cu</sub> (A/mm <sup>2</sup> )	1734	1987	709
Cu/NCu	1.2	1.05	1.6/1.9
RRR	50	50	100

Table 2.3: Conductor parameters of VLHC magnets relevant to quench protection. LHC dipole parameters are listed for comparison (the superconductor for LHC is NbTi).

The working assumption for the current carrying capacity of the conductor is a non-copper critical current density ( $J_c$ ) of ~3 kA/mm<sup>2</sup> (at 12T, 4.2K). All magnets are 2-in-1, double aperture magnets.

These tables show that the Nb<sub>3</sub>Sn magnets carry almost double the current of the LHC dipole magnets, in a conductor that is only marginally larger than that of the LHC dipole. Both Nb<sub>3</sub>Sn magnets have approximately the same total conductor cross-sectional area of ~30 mm<sup>2</sup> including insulation and voids. The cos $\theta$  magnets use larger strands, and the common coil dipole has a wider cable. The Cu/NCu ratios listed in the table provide the best possible compromise between sufficient field margin and realistic quench protection parameters. Especially in the case of the common coil dipole, a lower Cu/NCu ratio had to be chosen to obtain sufficient field margin for state of the art conductor. The resulting copper current densities in the Nb<sub>3</sub>Sn magnets are therefore much higher than for the LHC main dipole magnets.

The common coil dipole has an inductance higher than the VLHC cos $\theta$  magnet, but lower than the LHC dipole. The common coil dipole has also a stored energy of almost twice that of the VLHC cos $\theta$  magnet, due to a higher inductance and a higher current. The magnet length indicated in Table 1.6 corresponds to the preliminary estimate from the accelerator design viewpoint. The length parameter has no impact on the peak temperature, but it affects the magnet voltage and the size and cost of the quench protection hardware. The RRR of 50 listed in Table 2.4 represents a realistic estimate for available Nb<sub>3</sub>Sn conductors at the present.

When fixed, the quench protection parameters varied in this study are as in the following table:

Fixed parameters	Abbreviations	Common Coil	Cos $\theta$
Copper to non-copper ratio	Cu/NCu	1.0	1.2
Copper RRR	RRR	50	50
Heater coverage (%)	HC	100	50
Total heater delay time (ms)	$\tau_H$	40	40

Table 2.4: Quench protection parameters for VLHC magnet study.

The total heater delay time shown in Table 2.4 includes the quench detection time plus the heater delay time. The choice of 40 ms was based on heater delay time studies performed for LHC dipole magnets [2.15], and on measurements performed on Nb<sub>3</sub>Sn magnets at Fermilab (chapter 3.6.b).

### Conductor parameters

As described above, the copper current density is the conductor parameter that affects quench protection the most. Fig. 2.13-left shows the hot spot temperature vs. copper content (at fixed wire diameter and fixed current), from 50 % of the strand area (corresponding to Cu/NCu = 1) to ~62 % of the strand area (corresponding to Cu/NCu = 1.6).

For the common coil magnet, the peak temperature changes from 390 K to 330 K with a copper content increase of ~11 %. Similarly, for the cos $\theta$  magnet, the peak temperature changes from 400 K to 350 K with a copper content increase of ~12 %. We can see therefore, that a large increase in copper content is required to decrease the peak temperature. In fact, the resistance affects the quench process in two antagonistic ways: on one hand, the lower the resistance, the lower the heat generation at the hot spot; on the other hand, the lower the overall resistance of the magnet, the longer the decay time, which raises the peak temperature.

Fig. 2.13-right shows the hot spot temperature vs. copper RRR (at fixed copper content as in Table 2.4).

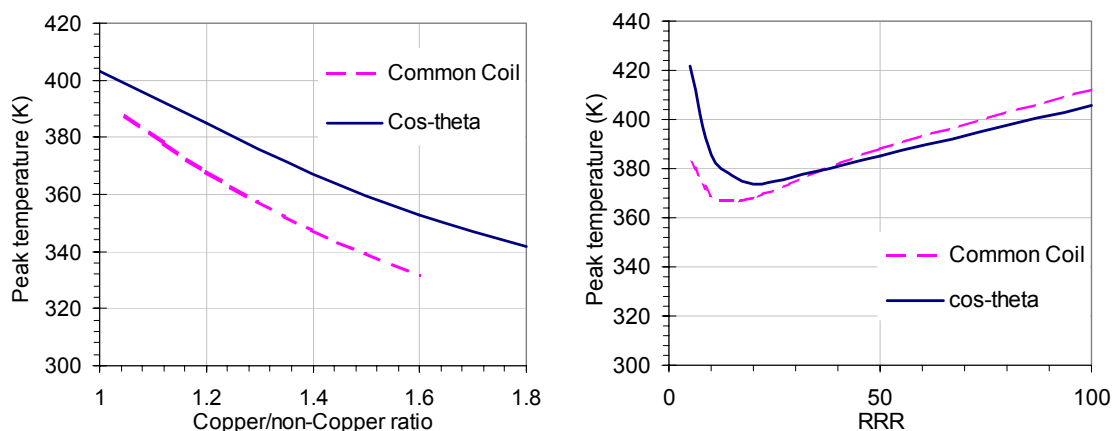


Fig. 2.13: (left) Peak temperature vs. copper content with RRR = 50; and (right) Peak temperature vs. RRR with Cu/NCu = 1.2/1.05 for cos $\theta$ /CC.

The peak temperature initially decreases, from a RRR of 5 to about 15, where the curve has a minimum. Above RRRs of 15-20, the peak temperature increases with growing RRR. In fact, the slowed current decay, due to the lowered matrix resistance, ultimately leads to higher peak temperatures.

On the other hand, it has to be noted that the peak voltages increase with lower RRR. To limit the peak temperature to 400K, the Cu/NCu has to be larger than 1.0 for both magnet types. The RRR has to be in the range of 10-70.

### Heater Coverage and Heater Delay Time

As mentioned earlier, the quench protection of long accelerator magnets relies on the use of quench heaters. The two main parameters describing the quench heater system are the percentage of coil surface covered by the heaters ( $HC$ ), and the heater delay time ( $\tau_H$ ), that is the time from the quench start, to the time when the heaters become effective in quenching the coils.

Fig. 2.14 (left) shows how a decrease in heater coverage raises the peak temperature. To maintain the peak temperature below the 400 K limitation, the common coil magnet requires 100% heater coverage and the cos $\theta$  magnet requires a minimum of 50% heater coverage.

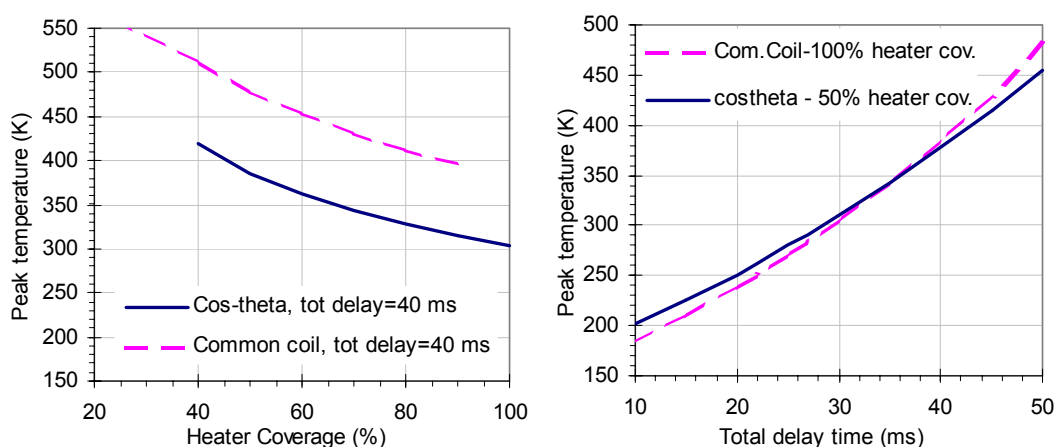


Fig. 2.14: Peak temperature vs. heater coverage (left), and peak temperature vs. total delay time (right).



The effect of the delay time ( $\tau_H$  = quench detection time + heater delay time) on peak temperature is shown in Fig. 2.14 (right). With  $\tau_H \leq 40$  ms the peak temperature remains within the 400 K limitation.

The voltages depend not only on the percentage of heater coverage, but also on the position of the heater strips. The voltages reported in Table 2.5 were calculated for heaters distributed symmetrically over both apertures. In case of a non-symmetric heater distribution, as in the case of heater failure, larger voltages arise [2.25]. The cos $\theta$ /common-coil magnets require a minimum of 50/70% heater coverage to limit the peak voltage to 1 kV.

Model	Heater position	Heater coverage (turn %)	$V_{\text{peak}}$ (kV)
cos $\theta$	all 48 turns	100	0.30
	outer layer only	54	0.91
	inner layer only	46	1.36
CC	all 52 turns	100	0.24
	36 mid-plane turns	71	0.98
	18 mid-plane turns	35	1.87

Table 2.5: Peak voltage to ground vs. heater coverage.

### Heater studies

As shown in Fig. 2.14, the total heater delay time is a parameter that greatly affects the peak temperature. Therefore several studies regarding the heater efficiency were performed, both theoretically and experimentally. Fig. 2.14 shows that the total heater delay time has to be less than 40 ms, to remain within the temperature limit. Reserving 10 ms for quench detection, the heater delay time has to be restricted to 30 ms. An additional problem stems from the fact that the critical temperature of Nb<sub>3</sub>Sn is higher than that of NbTi used in the LHC magnets, and requires therefore a larger amount of heat to start the transition. The quench heater performance has been studied first with a finite element (FE) model [2.26]. The model represents a cross section of the magnet (2D model), including the cable, the insulation, the heater strip, and the collar.

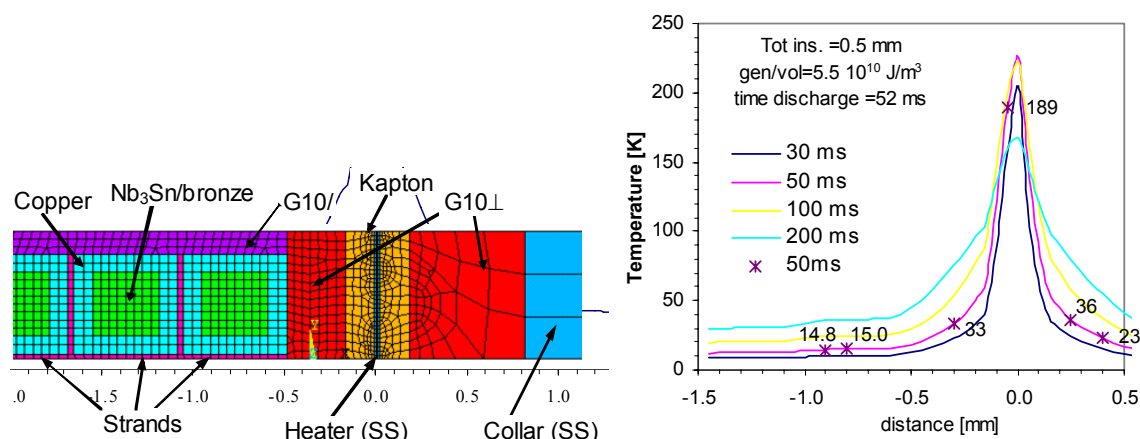


Fig. 2.15: FE model for heater study (dimensions in mm and temperatures in K). Insulation assumed: 0.1 mm coil insulation (G10), 0.3 mm ground insulation (G10) and 0.1 mm of Kapton insulation as part of the strip heater. Heater discharge time constant assumed: 52 ms, total energy deposited in heater: 55 kW/cm<sup>3</sup>.

Fig. 2.15 shows the central parts of the meshed 2D model and the materials. As an insulation the model leading to the results presented in Fig. 2.15 assumed 0.1 mm coil insulation (G10), 0.3 mm ground insulation (G10) and 0.1 mm of Kapton insulation as part of the strip heater.

At time zero, the heat generation starts in the heater strip region. The stainless steel strip heats quickly. The insulation slows down the heat transfer to the cable. Once through the insulation barrier, the heat propagates faster and the temperature profile becomes relatively flat inside the cable.

Fig. 2.16 shows the resulting temperature in the strand closest to the heater, 30 ms after the heaters are fired, for varying heater power and insulation thickness. At higher heater powers, the peak temperatures in the heater increases and, in turn, the thermal diffusivity of the insulation decreases, eventually counteracting the larger temperature gradients between heater and cable. The results clearly show that the most important parameter for the heater efficiency is the insulation layer thickness (dashed line in Fig. 2.16). The generation temperature at nominal current is  $\sim 11$  K on the outside of the  $\cos\theta$  outer layer and on the outside surface of the common coil magnet (average field  $\sim 4$  T). To reach this temperature within 30 ms, the power per coil area must be  $\geq 130$  W/cm<sup>2</sup> in both the  $\cos\theta$  and the common coil magnet, at a total insulation thickness of 0.5 mm. Using 70 W/cm<sup>2</sup> heater power, the insulation thickness has to be less than 0.48 mm, which seems enough for electrical insulation purposes. Additional insulation can be put between the heaters and the mechanical structure to prevent shorts to ground.

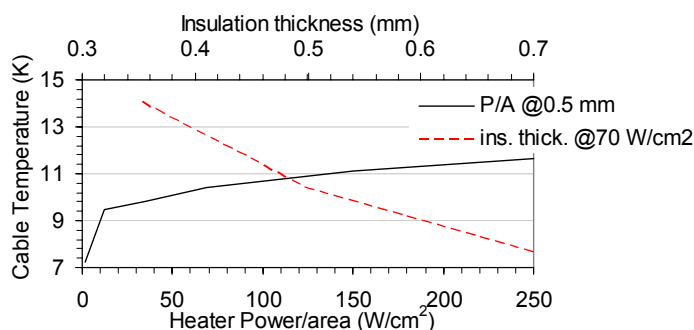


Fig. 2.16: Cable temperature after 30 ms, vs. power per unit area and insulation thickness.

## 2.2.f Summary of VLHC parametric studies

A possible set of quench protection system parameters for the VLHC dipole magnets was proposed (they are summarized in Table 2.6). A  $\text{Cu}/\text{NCu} = 1$  for the common coil and a  $\text{Cu}/\text{NCu} = 1.2$  for the  $\cos\theta$  magnet were chosen, to satisfy not only quench-protection but also bore-field requirements. In the case of the Common Coil magnet, assuming 20 % total critical current degradation,  $\text{Cu}/\text{NCu} = 1$  gives a 15 % bore field margin. A RRR value of 50 is expected to meet the quench protection requirements. It was not chosen as the optimum solution, but it corresponds to the average RRR of commercially available Nb<sub>3</sub>Sn conductor today.

	VLHC $\cos\theta$	VLHC CC
Cu/Ncu	1.2	1.05
RRR	50	50
Heater Coverage (%)	>50	100
Total Heater Delay Time (ms)	<10+30	<10+30
$QI$ @ 400 K ( $\text{MA}^2\text{s}$ )	43	42
$QI$ @ 40 ms ( $I=I_0$ ) ( $\text{MA}^2\text{s}$ )	18	22
Heater insulation (mm)	<0.5	<0.5
Heater Power ( $\text{W}/\text{cm}^2$ )	>130	>130
Peak Temperature (K)	380	390
Bulk Temperature (K)	140	120
Max Volt to Ground (V)	900	255
Current Decay Time (ms)	120	100

Table 2.6: Quench Parameters of FNAL VLHC Magnets

With a heater coverage of 100% for the Common Coil, and  $\sim 50\%$  for the  $\cos\theta$  (heaters on the outer layer), and a total heater delay time of 40 ms, the peak temperature remains below 400 K and the peak voltage below 1 kV. To better understand why these magnets need so extensive and effective heaters, it is interesting to compare the resulting quench integrals to those of the LHC dipoles. For the VLHC magnets, the  $QI$  at 40 ms (the heater activation time) is about half the  $QI$  budget for 400 K, while the LHC dipoles at 40 ms are at only 8% of the 400 K value. Therefore VLHC magnets have a smaller margin for current ramp down.

The magnet parameters were chosen such as to limit the peak temperatures to  $\sim 400$  K and the peak voltages to ground to 1 kV. Understanding if these limits are a safe choice for high field accelerator magnets, based on experiments and on theoretical investigations of the thermo-mechanical stresses generated in the magnets during a quench, is the motivation for this thesis work.

## 2.3 General quench study

The results of the study of the quench protection parameters for the VLHC main magnets have raised questions about the general trends of quench protection parameters in  $\text{Nb}_3\text{Sn}$  high field magnets. Given the high heater coverage requirements in the VLHC magnets, for example, it is questionable if even higher levels of stored energy are compatible with the standard quench protection approach. For this purpose an analytical approach for the peak temperature calculation was developed. The analytical peak temperature calculation allows a direct estimate of the effect of the various conductor and magnet parameters (such as current, stored energy ...) on the peak temperature.

### 2.3.a Analytical model

The peak temperature calculations presented in this section, are based on the adiabatic heat balance equation (2.5), as for the numerical models, but with an analytical approach. In this model [2.27], the material properties defining the quench integral ( $QI$ ), specific heat and

resistivity, are expressed in the simplest possible form to find an analytical expression for the peak temperature, as a function of quench integral, cable design parameters, and other important quench protection parameters, such as heater coverage, copper current density, heater delay time, magnet aperture, operating field, and current. Given the simplified laws for the specific heat and resistivity, the quench integral is expressed as a rational equation in the peak temperature, so that the peak temperature can then be obtained analytically from the  $QI$  equation.

The specific heat of the materials involved (copper, Nb<sub>3</sub>Sn, bronze, G10) can be approximated with the following phenomenological law (2.14), in the 50-500 K temperature range. The material constants  $A$  and  $B$  are listed in Table 2.7. Fig. 2.17 shows how the simplified specific heat model compares to the data from literature (see e.g. chapter 3.4).

$$c_p(T) = A_{cp}T - B_{cp}T^{1.5} \quad (\text{J} \cdot \text{m}^{-3} \text{K}^{-1}) \quad (2.14)$$

Material	$A_{cp}$	Unit	$B_{cp}$	Unit
G10	30000	J/K <sup>2</sup> /m <sup>3</sup>	1000	J/K <sup>2.5</sup> /m <sup>3</sup>
Copper	28500	J/K <sup>2</sup> /m <sup>3</sup>	950	J/K <sup>2.5</sup> /m <sup>3</sup>
Bronze	28500	J/K <sup>2</sup> /m <sup>3</sup>	950	J/K <sup>2.5</sup> /m <sup>3</sup>
Nb <sub>3</sub> Sn	16000	J/K <sup>2</sup> /m <sup>3</sup>	610	J/K <sup>2.5</sup> /m <sup>3</sup>

Table 2.7: Specific heat parameters of materials used in magnet coils (valid only for T<500 K).

The specific heat of the composite cable is calculated with the “rule of mixture”. The weighting factors in the specific heat of the composite are the respective cross-sectional areas of the components divided by the total cable surface  $A_{cable}$ . The total cable surface includes not only the metal area, but also the area in the cross-section covered by insulation and epoxy (assuming 25 % insulation fraction over the total, insulated cable cross-sectional area). Note that this implies that the specific heats of the cable-insulation as well as the epoxy-impregnation are taken into account in the conductor temperature calculation (as discussed in 2.2.d).

$$c_{pcable}(T, j_{Cu}, B, I) = \frac{1}{A_{cable}(j_{Cu}, B, I)} \sum_i A_i(j_{Cu}, B, I) c_{pi}(T) \left( \frac{\text{J}}{\text{m}^3 \text{K}} \right) \quad (2.15)$$

The specific heat of the composite cable is expressed in (2.15), as a function of  $j_{Cu}$ , the bore-field  $B$  and cable-current  $I$ , which are treated as the main variables of the analytical equation, by determining the cross-sectional area of the components ( $A_i$ ) and the total cross-sectional area of the cable  $A_{cable}$ . The introduction of the current density in the copper stabilizer,  $J_{Cu}$ , as a variable requires a change of strand copper cross-sectional area according to the magnet current. The magnet current, together with the superconductor critical current (which depends on the peak magnetic field) determine the non-Cu cross-sectional area. The resulting  $c_p$  constants  $A_{cp}$  and  $B_{cp}$  of the composite cable are defined as ( $n$  is 2 for  $A_{cp}$  and 2.5 for  $B_{cp}$ ):

$$A_{cp}^{cable} = \sum_i \frac{A_i}{A_{cable}} A_{cp}^i; B_{cp}^{cable} = \sum_i \frac{A_i}{A_{cable}} B_{cp}^i \left( \frac{\text{J}}{\text{K}^{1+n} \text{m}^3} \right) \quad (2.16)$$

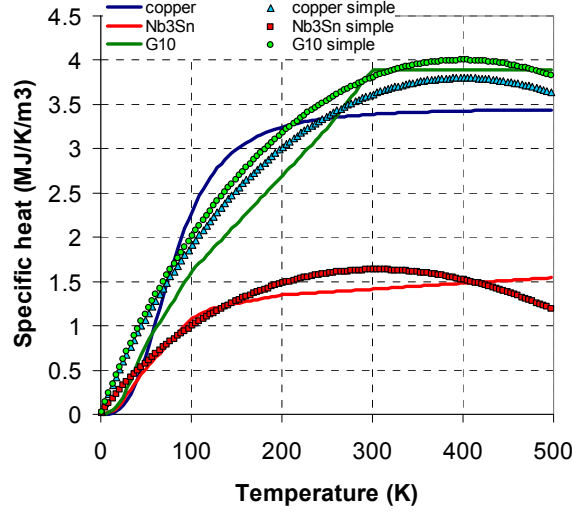


Fig. 2.17: Comparison of simplified specific heat model (calculated with (2.14) with parameters from Table 2.7) with data from literature for copper, Nb3Sn and G10 (chapter 3.4).

The average normal state resistivity of the cable is calculated from the electrical resistivity of copper only, which can be approximated as a linear function of temperature:

$$\rho_{cable}(j_{Cu}, B, I, T) = X_{Cu} \frac{A_{cable}(j_{Cu}, B, I)}{A_{Cu}(j_{Cu}, B, I)} T \quad (\Omega m) \quad (2.17)$$

Given the simplified laws for the specific heat and resistivity the adiabatic quench integral becomes:

$$\begin{aligned} QI(j_{Cu}, B, I, T) &= A_{cable}^2 \int_{T_b}^T dT \left[ \frac{c_{pcable}}{\rho_{cable}} \right] = \\ &= A_{qi}(j_{Cu}, B, I) [T - T_b] - B_{qi}(j_{Cu}, B, I) [T^{1.5} - T_b^{1.5}] \quad (A^2 s) \end{aligned} \quad (2.18)$$

where  $A_{qi}$  and  $B_{qi}$  are ( $n=2$  for  $A_{qi}$  and  $n=2.5$  for  $B_{qi}$ ):

$$A_{qi}(j_{Cu}, B, I) = \frac{A_{cable} A_{Cu} A_{cp}^{cable}}{X_{Cu}}; \quad B_{qi}(j_{Cu}, B, I) = \frac{A_{cable} A_{Cu} B_{cp}^{cable}}{X_{Cu}} \quad \left( \frac{A^2 s}{K^{n-1}} \right) \quad (2.19)$$

Equation (2.18) can be brought into the form (2.20) and (2.21), where the parameters are defined in equations (2.22) to (2.24). The peak temperature  $T$  can then be obtained from the known solution of equation (2.21).

$$A_{qi}T - B_{qi}T^{1.5} = QI + A_{qi}T_b - B_{qi}T_b^{1.5} \quad (2.20)$$

$$T^3 + aT^2 + bT + c = 0 \quad (2.21)$$

$$a(j_{Cu}, B, I) = - \left( \frac{A_{qi}(j_{Cu}, B, I)}{(-B_{qi}(j_{Cu}, B, I))} \right)^2 \quad (2.22)$$

$$b(j_{Cu}, B, I, QI) = 2 \left( \frac{A_{qi}(j_{Cu}, B, I) (QI + A_{qi}(j_{Cu}, B, I) T_b - B_{qi}(j_{Cu}, B, I) T_b^{1.5})}{(-B_{qi}(j_{Cu}, B, I))} \right) \quad (2.23)$$

$$c(j_{Cu}, B, I, QI) = - \left( \frac{(QI + A_{qi}(j_{Cu}, B, I) T_b - B_{qi}(j_{Cu}, B, I) T_b^{1.5})}{(-B_{qi}(j_{Cu}, B, I))} \right) \quad (2.24)$$

There are three known solutions of (2.21), but only one is a real positive number in the range of interest ( $T < 500$  K):

$$T = - \frac{A(a, b, c) + B(a, b, c)}{2} - i \frac{A(a, b, c) - B(a, b, c)}{2} \sqrt{3} - \frac{a}{3} \quad (\text{K}) \quad (2.25)$$

where  $A, B$  are defined in equations (2.26) to (2.28), and  $i = \sqrt{-1}$ .

$$A(a, b, c) = \left( \frac{-q(a, b, c)}{2} + \sqrt{Q(p, q)} \right)^{3/2}; B(a, b, c) = \left( \frac{-q(a, b, c)}{2} - \sqrt{Q(p, q)} \right)^{3/2} \quad (2.26)$$

$$Q(p, q) = \left( \frac{p(a, b)}{3} \right)^3 + \left( \frac{q(a, b, c)}{2} \right)^2 \quad (2.27)$$

$$p(a, b) = -\frac{a^2}{3} + b; q(a, b, c) = 2 \left( \frac{a}{3} \right)^3 - \frac{ab}{3} + c \quad (2.28)$$

### Calculation of the auxiliary quench parameters

This section presents the trends of the parameters that most affect the peak temperature. Table 2.8 reports the main magnet parameters. The left part includes the parameters that were fixed in the model. The part on the right includes the parameters that were fixed when not explicitly varied.

The Cu/NCu ratio of the conductor is defined via the operational current density in the non-Cu area (NCu) and the maximum stipulated current density in the copper. Therefore, the copper current density depends on the cable current and the bore field, when all the other parameters are fixed. For larger fields, the superconductor current density drops such that, at a fixed copper current density, the NCu area will be increased. Therefore, the Cu/NCu ratio shown in Fig 2.18 decreases as the field becomes larger.

Constant Parameters	Value	Unit	Occasionally fixed Parameter	Value	Unit
Bath temperature	4.5	K	Bore field (dipole)	10	T
Apertures per magnet	2		Magnet operational current	20	kA
Bronze in non-Cu area	25	%	Total delay time	40	ms
Insulation fraction in cable	25	%	Coil bore diameter	40	mm
RRR in copper matrix	50		Copper current density	2	kA/mm <sup>2</sup>
Peak field/bore field ratio	1.2		Effective $J_{non-Cu}$ @12 T, 4.2 K	2.3	kA/mm <sup>2</sup>
Operating margin ( $J/J_c(B)$ )	60	%	Magnet length	15	m
Quench velocity	1	m/s	Heater coverage, coil surface	50	%

Table 2.8: Parameters for general quench calculations.

The non-copper (NCu) cable cross-section was derived from the operational superconductor current density (which is usually defined in terms of the non-copper area in the conductor cross-section) and the stipulated cable current. The bronze fraction determines the bronze part in the NCu fraction, which can be as high as 50% depending on the conductor fabrication route (it was assumed to be 25% here). The total cross-sectional area of the cables is the sum of the Cu and NCu parts as well as the insulation (and impregnation), specified via the insulation fraction in the total cable cross-section.

The total cable cross-sectional area depends primarily on the operational conductor current density and the chosen cable current, which together, determine the non-copper area. Secondly it depends on the choice of the copper current density and the bronze- and insulation-fractions.

Fig. 2.19 shows how the total cable cross-section increases with bore-field, for different cable currents, at a fixed Cu current density of 2 kA/mm<sup>2</sup>, and the bronze- and insulator-fractions specified in Table 2.8. The increase in cable cross-section with field is caused by the decrease of the critical current density in the superconductor at higher fields.

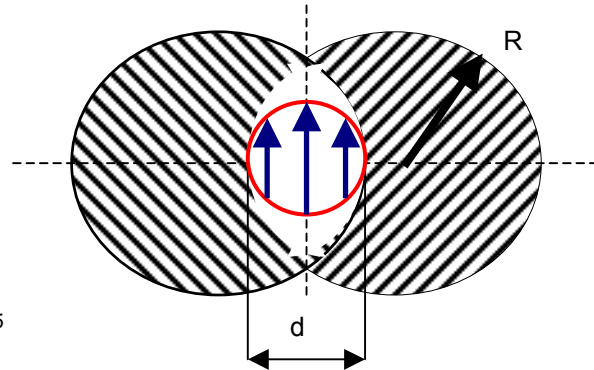
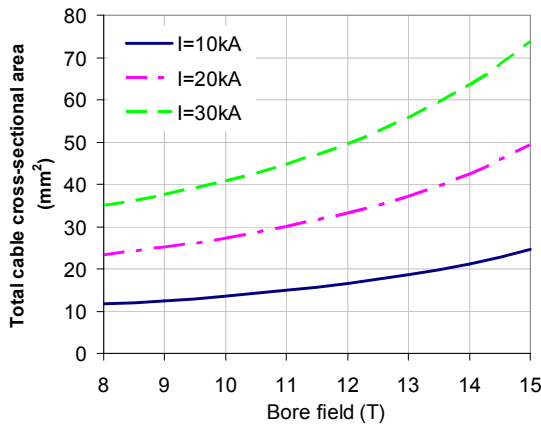


Fig. 2.19: Cable cross-section as a function of field for different currents, and intersecting circles model used for the coil area calculation.

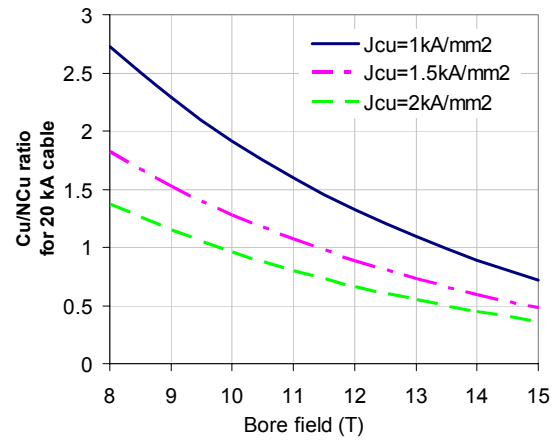


Fig. 2.18: Cu/NCu ratio vs. bore-field.



In order to estimate the inductance of the magnet an approximate calculation of the number of turns, given by the coil cross-sectional area divided by the total cable cross-section, is required. The simplest model used to estimate the required coil surface area for a given aperture and bore field is that of the intersecting-circles (Fig. 2.19), the simplest case of the intersecting ellipses model. This model stipulates that a bore-field  $B$  is produced by a coil-surface carrying the current density  $j_{tot}$  (in opposite directions left and right from the bore). The model therefore does not account for wedges, intra-layer ground-insulation or mechanical stabilizers within the coil. The intersecting circles model yields an analytical expression for the coil radius as a function of the bore field and average conductor current density. The coil area, calculated with the “intersecting circles” model divided by the cable cross-section gives the number of turns of the magnet. It is independent of the magnet (or more precisely, “cable”) current, since it is only determined by the total current (number of cables times cable current) in the coil. The coil-area grows with bore field and gives an idea of the effect of cable current on the turn-number (i.e. the higher the cable current, the smaller the number of turns).

The increase in coil size (or number of turns) with increasing field results in an increased magnet inductance. Fig. 2.20 shows the increase in magnet inductance with field for different cable currents and magnet apertures. The smaller the cable current (the larger the number of turns) and the larger the aperture, the larger the inductance. Therefore, large, high-current cables and small apertures are strategies used to reduce the magnet inductance.

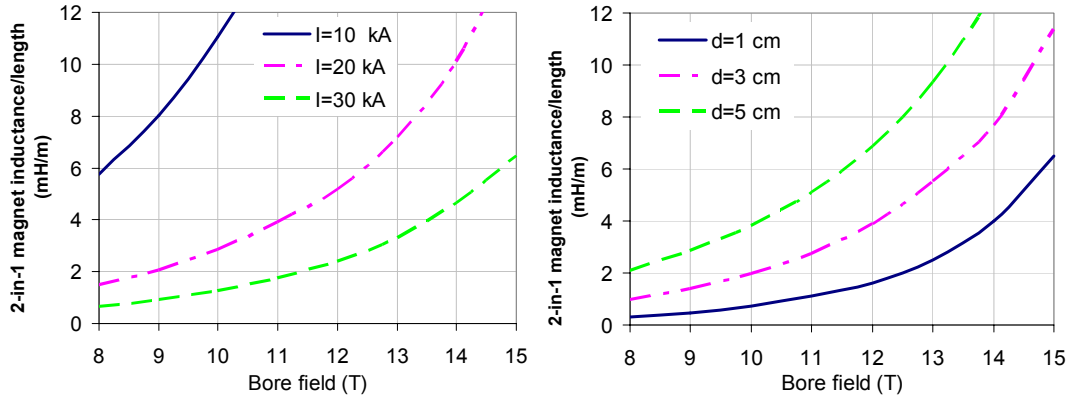


Fig. 2.20: Magnet inductance as function of bore-field, current (left) and aperture (right).

An estimate of the current decay time constant can be made based on the coil inductance and the coil resistance after the quench. The coil resistance is calculated as the resistance of the coil fraction covered by the quench heaters at  $T_{bulk}$ , that is the temperature at the end of the current decay.  $T_{bulk}$  is obtained from the enthalpy function. A multiplicative factor of 1.5 is applied to the decay time constant to account for the overall overestimation of the resistance over time. The current decay time is strongly determined by the heater coverage and is independent of current. This is related to the fact that the number of turns or coil size appears both in the magnet inductance and magnet resistance and that the cable cross-section scales with the cable current. The inductance drops as the cables are made larger to carry more current. At the same time the magnet resistance decreases because of the increase in cable cross-section ( $R_{mag} \sim N_{turn}$ ). The decay time increases with smaller heater fractions, and thus smaller magnet resistance.

The quench integral ( $QI$ ) is calculated from the time-integrated square of the magnet current. In the adiabatic model used here this quench integral can be equated to the quench integral as calculated from the material properties, which allows the estimation of the peak temperature by comparison. The  $QI$  accumulated during the current decay process is  $(\tau/2) \cdot I^2$  in the case of an exponential decay, in addition to the quench integral of the current decay the quench integral accumulated during the delay time (as in equation 2.8).

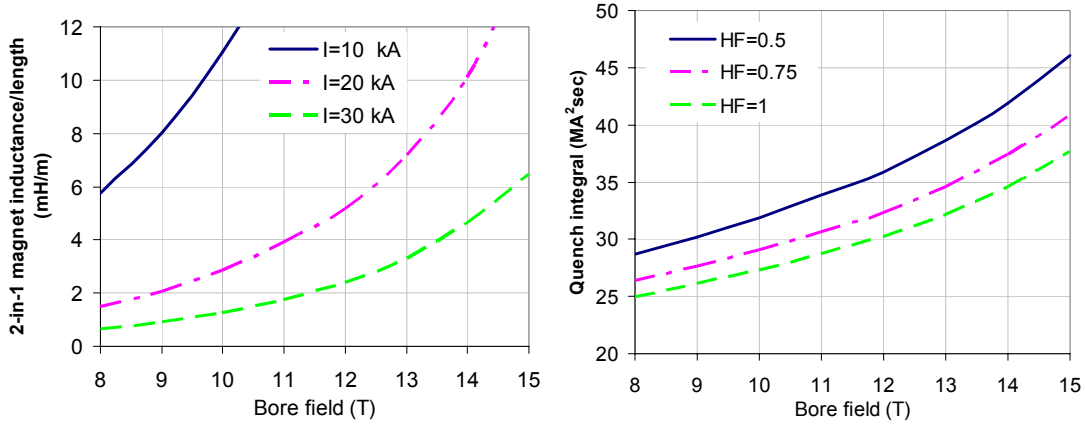


Fig. 2.21: Quench integral as a function of bore field for different currents, and heater fractions (right).

Fig. 2.21 shows that the quench integral generally rises with bore field due to the increase in decay time, because of larger magnet inductance. The quench integral dependence on the current is strong. This strong dependence is not propagated to the peak temperature calculation, since the cable cross-section and cable enthalpy are raised accordingly to keep the normal matrix current density  $j_{Cu}$  constant.

### 2.3.b Peak temperature analytic calculations results

As mentioned before, copper current density, heater coverage and heater time delay are the most influential quench protection parameters (Fig. 2.22-23).

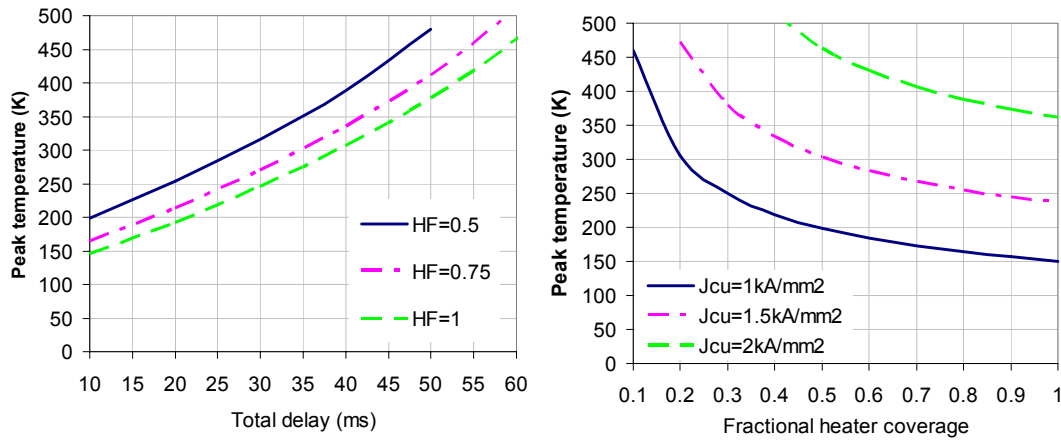


Fig. 2.22: Peak temperature as a function of heater time delay for different heater coverage (left) and peak temperature as a function of heater coverage for different copper current densities (right).

Fig. 2.22 (left) shows the increase in peak temperature with heater time delay for varying heater coverage (heater fraction  $HF$ ). We can see that a 10 ms increase in time delay results in a  $\sim 25\%$  increase in peak temperature. Fig. 2.22 (right) shows the peak temperature as a function of heater coverage for different copper current densities. The effect of the heater coverage is very strong at small heater fractions, and over 50% coverage, the effect is reduced to a “10% - effect” (and therefore more pronounced for high copper current density).

Fig. 2.23 shows that the peak temperature drops with bore field, due to the considerable increase in the cable cross-section toward higher fields, because of the loss in critical current density in the superconductor. On the other hand, higher field magnets have higher inductance due to an increased number of turns. The increase in inductance affects the current decay time constant, and therefore the quench integral, but only a fraction ( $\sim$ half) of the total quench integral. Therefore, as the bore field rises, the inductance and decay time constant as well as the quench integral increase, but at the same time, the coil volume increases! The increase in specific heat of the conductor weighs more on the resulting peak temperature than the increase in inductance, ultimately leading to slightly lower peak temperatures.

Fig. 2.23 (left) also shows also that the peak temperature does not depend on the magnet current. In fact, several other parameters are independent from the current (the decay time constant, the joule energy density in the coils, etc.). For example, the coil energy product, i.e. the Joule energy density in the coils, is a function of  $j_{Cu}$ . It is, however, current independent because the cable size increases with the current at a constant copper current density. Therefore, increasing the cable size to keep the inductance low, is recommended because it does not result in an increased peak temperature and helps in reducing the voltages (via the reduced inductance).

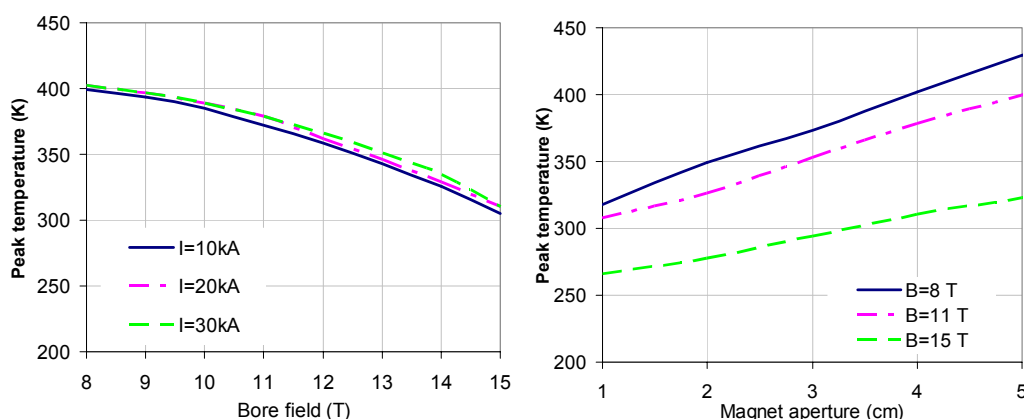


Fig. 2.23: Peak temperature after a quench as a function of field and current, and magnet aperture.

Fig. 2.23 (right) shows how the peak temperature increases with magnet aperture, due to the increase in number of turns and thus in inductance (Fig. 2.21), and decay time.

The calculations presented here assumed a critical current density in  $\text{Nb}_3\text{Sn}$  virgin strands of  $3\text{ kA/mm}^2$  in the non-copper area, at 4.2 K and 12 T. Although today's  $\text{Nb}_3\text{Sn}$  superconductor achieves  $\sim 2.4\text{ kA/mm}^2$  current density over the non-Cu area, realistic predictions for the near future indicate a current density as large as  $3\text{ kA/mm}^2$  (Fig. 1.2). Fig. 2.24 shows the effect of even larger critical current densities on the magnet peak temperatures after a quench.

The results in Fig. 2.24 show an increase in peak temperature for increased critical current densities. The increase is more pronounced at high copper current density. The increase can be explained by the “loss” of  $c_p$  of  $\text{Nb}_3\text{Sn}$  caused by the improved superconductor performance. On the other hand the higher  $j_c$  results in a reduced magnet inductance (less turns), which partly counteracts the loss of  $c_p$ .

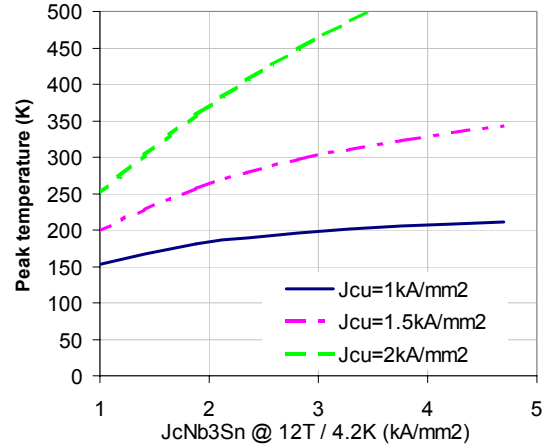


Fig. 2.24: Peak temperature as a function of superconductor current density ( $J_{\text{non-Cu}}$ ) for different copper current densities.

### 2.3.c Summary of the general quench study

Table 2.9 compares the main quench simulation results of the two main VLHC dipole magnets studied at Fermilab (presented in chapter 1.3.d and also discussed in chapter 2.2), with results from the analytical model described here for the same magnets, and for the generic magnet described in previous plots. The results were obtained based on the same set of input parameters listed in the first part of the table. The second part of the table lists the parameters that were different in the analytical model from the magnet designs, studied with the numerical quench simulation programs.

In addition, we recall here some parameters that were kept constant in all the calculations, including the bath temperature at 4.5 K, the bore field at 10 T, the magnet length at 17 m, the total heater delay time at 40 ms (10 ms quench detection time plus 30 ms heater time), and the copper RRR at 50. The last part of the table reports the result of the quench calculation with the different methods. Note that to account for the fact that the common-coil dipole is of the “block-type” and therefore less “efficient”, an additional multiplicative factor of 1.5 was applied to the coil cross-sectional area (calculated from the intersecting circles model).

Table 2.9 shows that the decay times resulting from the analytical models are smaller than the values obtained with the numerical quench simulations. The discrepancy comes from the fact, that the resistance of the coil affecting the decay time is calculated in the analytical model, at the end of the quench process, at the so-called  $T_{\text{bulk}}$ . In reality, the resistance varies during the quench process, reaching its maximum at the end. Therefore the decay time is overestimated (and not representative) when calculated from the final, maximum resistance. The resulting quench integrals and peak temperature are also underestimated to some extent. The peak temperature resulting from the analytical model agrees with the numerical calculations within 10 % for both magnet types.

Magnet Simulation model	Cos $\theta$ Numerical	Cos $\theta$ Analytical	Common coil Numerical	Common coil Analytical
I (kA)	21.3	21.3	23.5	23.5
$J_{Cu}$ (A/mm <sup>2</sup> )	1734	1734	1987	1987
Aperture (mm)	43	43	40	40
Heater coverage (%)	50	50	100	100
Inductance (mH/m)	2.14	2.7	3	2.9
Energy (kJ/m)	485	618	828	801
En./heated coil vol. (MJ/m <sup>3</sup> )	172	227	119.8	115
N. of turns	96	94	112	119
$A_{cable}$ (mm <sup>2</sup> )	29.3	28.4	31.02	29.1
Cu/NCu	1.2	1.2	1.05	1.05
$T_{peak}$ (K)	380	386	390	366
$T_{bulk}$ (K)	140	125	120	88.7
Decay time (ms)	120	84	100	48
$QI$ (MA <sup>2</sup> s)	43	37.2	42	35.5

Table 2.9: Comparison of magnet parameters relevant to quench protection, and quench simulation results, calculated with numerical models and the analytical model.

From this study we can derive the following trends regarding the peak temperature in existing and future Nb<sub>3</sub>Sn high field magnet designs:

- Heater coverage and copper current density are the major quench protection design parameters.
- The use of larger cables and currents is recommended since it does not result in an increase in peak temperatures, but helps to reduce inductive voltages.
- Nb<sub>3</sub>Sn high field magnets most likely operate with high copper current densities to increase coil efficiency. They will therefore have to deal with high heater coverage, even though, coverages larger than 50% bring about a conflict with heater redundancy requirements.
- Higher fields do not result in increased peak temperatures, on the contrary, the temperature decreases with bore field, for fixed conductor parameters.
- Smaller apertures and shorter heater delays are of course beneficial for quench protection purposes.
- As the critical current density of the superconductor improves with time, the peak temperature will also tend to rise without an increase in copper content or heater coverage.

## 2.4 Conclusions of quench protection studies

This chapter presented quench protection studies for Nb<sub>3</sub>Sn magnets for particle accelerators, from the basics, to simulations of the quench process. The numerical codes developed and used to find the requirements to protect Fermilab's dipole magnets were described. Parametric quench protection studies for the VLHC magnets were performed using the numerical models, varying quench protection parameters such as heater coverage, heater delay time, Cu/NCu ratio, and copper RRR. The results show that a heater coverage of ~100% of the turns for the common coil, and ~50% for the cos $\theta$  magnet (heaters on the outer layer), and a total heater delay time of 40 ms or less are necessary to limit the peak temperature to 400 K and the peak voltage to 1 kV.

To understand if these results are particular to the specific designs, and to obtain general trends of quench protection parameters in Nb<sub>3</sub>Sn high field magnets, an analytical approach to calculate the peak temperature was developed.

Summarizing the results from the parametric quench protection study for the VLHC magnets using numerical models, and the general quench protection study using the analytical model, it emerged, that heater coverage and copper current density are most influential parameters of the quench protection design. Taking into account that Nb<sub>3</sub>Sn high field magnets most likely operate with high copper current densities to increase coil efficiency, quench protection will have to rely mostly on quench heaters. In addition, as the critical current density of the superconductor improves with time, the peak temperature will also tend to rise without an increase in heater coverage or heater efficiency. Since for example, heater coverage larger than 50% conflicts with the heater redundancy requirement, it is questionable if this or even higher levels of current density and stored energy are compatible with standard quench protection methods.

Present R&D to improve heater efficiency includes insulation material studies. A promising material is ceramic gel, under development at Global Research and Development, NHMFL and Ohio State University [2.28]. Coating of the stainless strips with this gel may reduce the insulation thickness between the conductor and the heater strip, and therefore reduce heater time delays. Material properties studies affecting the quench process and essential for the design of superconducting magnets are presented in the next chapter.

In designing efficient quench protection systems, it is necessary to define the maximum temperatures that can be attained in the coils during a quench. Although critical current versus strain data are well known for Nb<sub>3</sub>Sn, little is known about how these limitations apply to the case of a cable thermally expanding in a magnet during a quench. To investigate the effect of the thermo-mechanical shock exerted on the coil during a quench, an experimental and computational program was launched. These studies are presented in Chapter 4 and 5.

## References

- 
- [2.1] L. Chiesa, et al., "Performance Comparison of Nb<sub>3</sub>Sn Magnets at LBNL," *IEEE Trans. App. Supercond.*, June 2003, ASC02 proceedings
  - [2.2] G. Ambrosio et al., "Development and Test of a Nb<sub>3</sub>Sn Racetrack Magnet Using the React and Wind Technology," *Adv. Cryog. Engineering*, Vol. 613, 47B, p.329
  - [2.3] V.V. Kashikhin, "Flux Jumps in Nb<sub>3</sub>Sn Magnets," Fermilab, Technical Division Note, TD-03-05, Jan. 2003
  - [2.4] J.H. Schultz, "Protection of Superconducting Magnets," PAC01 *proceedings*, Chicago, June 2001
  - [2.5] M.J. Lamm et al., "A New Facility to Test Superconducting Accelerator Magnets," *proceedings* of PAC-97, Vancouver, Canada, 1997
  - [2.6] D.F. Orris, et al., "A Quench Management System for Testing Superconducting Magnets," *IEEE Trans. App. Supercond.*, June 2003, ASC02 proceedings
  - [2.7] E.W. Boxman et al., "Current Diffusion and Normal Zone Propagation Inside the Aluminum Stabilized Superconductor of ATLAS Model Coil," *IEEE Trans. App. Supercond.*, June 2003, ASC02 proceedings
  - [2.8] K.-H. Mess, P. Schmüser, S. Wolf, "Superconducting Accelerator Magnets," World Scientific Publishing, 1996
  - [2.9] D. Leroy et al., *IEEE Trans. App. Supercond.*, V. 3, p. 781, 1993
  - [2.10] T. Ogitsu et al., *IEEE Trans. Magn.*, V. 30, N. 4, p. 2773, 1993
  - [2.11] P. Schlabach, J. Sim, "Feasibility Study of a "Next Generation" Rotating Coil DAQ System," Fermilab, Technical Division Note TD-98-32, 1998
  - [2.12] F. Rodriguez-Mateos, et al., "Quench Process and Protection of LHC Dipole Magnets", LHC Project Note 184, July 1999
  - [2.13] N.I. Andreev, D.R. Chichili, I.M. Terechkine, A.V. Zlobin "Development and Study of Insulation Systems for Nb<sub>3</sub>Sn Accelerator Magnets," *proceedings* of MT17, Geneva, Sept. '01
  - [2.14] J. Billan, et al., "Test Results on the Long Models and Full Scale Prototypes of the Second Generation LHC Arc Dipoles," *IEEE Trans. App. Supercond.*, V. 9, N. 2, June '99
  - [2.15] F. Rodriguez-Mateos, P Pognat, S. Sanfilippo, et al. "Quench Heater Experiments on the LHC Main Superconducting Magnets," LHC report 418, CERN, Sept. 2000
  - [2.16] L. Imbasciati, G. Ambrosio, P. Bauer, V. Kashikhin, S.W. Kim, A.V. Zlobin, "Quench Protection Study of the Single Layer Common Coil Dipole Magnet," Fermilab, Technical Division Note TD-00-57, Nov. 2000
  - [2.17] M. N. Wilson, "Superconducting Magnets," Clarendon Press Oxford, 1983
  - [2.18] D. Hagedorn, F. Rodriguez-Mateos, "Modeling of the Quenching Process in Complex Superconducting Magnet Systems," *IEEE trans. Magn.*, 28, 1992
  - [2.19] F. Sonnemann, "Resistive Transition and Protection of LHC Superconducting Cables and Magnets," *Ph.D. Thesis*, University of Aachen-CERN, 2001
  - [2.20] M. Canali, L. Rossi, "DYNQUE: a Computer Code for Quench Simulation in Adiabatic Multicoil Superconducting Solenoids", INFN/TC-93/06, 1993
  - [2.21] M. Sorbi, "Studio della Propagazione del Quench e Misure su Avvolgimenti Superconduttori Adiabatici," Milan University *Thesis*, 1993



- 
- [2.22] P. Bauer et al., “Concept for a Quench Calculation Program for the Analysis of Quench Protection Systems for Superconducting High Field Magnets”, Fermilab, Fermilab, Technical Division Note TD-00-027, April 2000
  - [2.23] L. Imbasciati, G. Ambrosio, P. Bauer, V. Kashikin, A.V. Zlobin, “Quench Protection of the Common Coil Racetrack (CCRT-1) – Results of Adiabatic Model Calculations,” Fermilab, Technical Division Note TD-00-56, Sep. 2000
  - [2.24] Cryocomp v 2.0, Eckels Engineering and Cryodata Inc.
  - [2.25] P. Bauer, L. Imbasciati, G. Ambrosio, V. Kashikin, M. Lamm, A.V. Zlobin, “Quench Protection Calculations for Fermilab’s Nb<sub>3</sub>Sn High Field Magnets for VLHC – Part 2,” Fermilab, Technical Division Note TD-01-04, Mar. ‘01
  - [2.26] L. Imbasciati, G. Ambrosio, P. Bauer, “Quench Heater Design Considerations for VLHC Magnets”, Fermilab, Technical Division Note TD-01-022, April 2001
  - [2.27] P. Bauer, L. Imbasciati, V.V. Kashikhin, M. Lamm, A.V. Zlobin, “General Quench Protection Calculations for Nb<sub>3</sub>Sn High Field Dipole Magnets Part 1 – Peak Temperature,” Fermilab, Technical Division Note TD-01-71, Dec. ‘01
  - [2.28] I.H. Mutlu, E. Celik, Y.S. Hascicek “High temperature insulation coatings and their electrical properties for HTS/LTS conductors”, *Physica C*, 370 (2002) 113-124

# 3. Material Properties and Quench Parameters

Table of contents chapter 3	page
3. Material Properties and Quench Parameters	1
3.1 Scaling laws of Nb <sub>3</sub> Sn superconductor	2
3.1.a Relation between critical current density and field	2
3.1.b Temperature dependence	2
3.1.c Strain dependence	4
3.2 Thermal conductivity measurements of Nb <sub>3</sub> Sn cable stacks	7
3.2.a Description of the samples	8
3.2.b Apparatus description	8
3.2.c Experimental results	10
3.3 Thermal conductivity modeling	11
3.3.a Thermal conductivity of the insulating layer of sample # 2	12
3.3.b Thermal conductivity of the bare sample (# 3)	12
3.3.c Overall thermal conductivity of sample 1 (with e-glass insulation)	18
3.3.d Summary of thermal conductivity study	20
3.4 Material properties for quench integrals	20
3.4.a Specific heat and density	21
3.4.b Resistivity	22
3.4.c Conductivity	22
3.5 Thermo-mechanical properties	23
3.5.a Elasticity modulus	23
3.5.b Thermal contraction	25
3.6 Measurements of quench parameters	26
3.6.a Quench velocities	27
3.6.b Experimental quench heater study	28
References	31

### 3.1 Scaling laws of Nb<sub>3</sub>Sn superconductor

The superconducting state is a thermodynamic state determined by four variables: transport current density ( $J_c$ ), temperature ( $T$ ), magnetic field ( $B$ ), and strain ( $\varepsilon$ ). The superconducting state is found below the critical surface defined by the critical current density, as a function of temperature, field, and strain. The critical surface of Nb<sub>3</sub>Sn superconductor is described briefly in this paragraph.

#### 3.1.a Relation between critical current density and field

The critical current as function of the magnetic field can be derived by the equation describing the critical state, that is given when the Lorentz force on the fluxoids is exactly balanced by the pinning force  $F_p$  [3.1] and [3.2]:

$$J_c(B) \times B = -F_p(B) \cdot \quad (\text{N/m}^3) \quad (3.1)$$

Experimental studies showed that the pinning force follows the so-called Kramer law [3.3]:

$$F_p(B) = C \cdot b^p \cdot (1-b)^q = C \cdot f(b) \quad , \quad (\text{N/m}^3) \quad (3.2)$$

where  $C$  is a constant independent from  $B$ ,  $f$  is a function of the reduced field  $b = B/B_{c2}$ , with  $B_{c2}$ , the upper critical field of a type II superconductor. The exponents are specific for each superconductor. Typical values for Nb<sub>3</sub>Sn are  $p = 0.5$ , and  $q = 2$ . The pinning force relation (3.2) was confirmed for  $0.3 < b < 0.9$ , and for fixed temperature, by numerous experimental studies. Microscopic models of the pinning force, such as [3.3-4], attempt to describe the basic mechanisms underlying the empirical law (3.2). [3.4] presents a model based on anisotropic flux pinning by grain boundaries, which can account for the observed scaling behavior over the field range for both NbTi and Nb<sub>3</sub>Sn superconductors. The attractive force close to the grain boundaries provides the “transverse” pinning mechanism of intra-granular vortices. This is also the main pinning mechanism for NbTi. When a vortex falls into the boundary (inter-granular vortices), then the normal core disappears, and the vortex can slide along the boundary, and is pinned only by inhomogeneities, such as boundary intersections. While NbTi filaments consist mainly of long grains, Nb<sub>3</sub>Sn structure consists of an array of  $\sim 0.2 \mu\text{m}$ -long grains, separated by  $\sim 2 \text{ nm}$ -thick layers. These grain boundaries can therefore be considered superconducting-normal-superconducting Josephson junctions. The force in this case is much weaker than in the Abrikosov vortex case. Therefore, two different scaling laws for the critical current were derived from this model, one for the transverse pinning and one for the longitudinal pinning. The limiting current density is determined by the weaker longitudinal pinning for fields above  $\sim 2 \text{ T}$ . Improvements of the pinning mechanism by further engineering of the Nb<sub>3</sub>Sn superconductor could be the way leading to larger critical current densities, as suggested by the latest development (Fig. 1.2).

#### 3.1.b Temperature dependence

The temperature dependence of the pinning force can be introduced in (3.2) via the critical field as a function of temperature, and introducing  $\kappa(T)$ , the Ginzburg-Landau parameter,

$$F_p(B, T) = C \cdot \kappa(T)^{-g} \cdot B_{c2}(T)^n \cdot f(B/B_{c2}(T)), \quad (\text{N/m}^3) \quad (3.3)$$

where the exponents  $g$  and  $n$  are used to fit the experimental data [3.5]. The more general expression of the current density (3.1), which includes (3.3) is then

$$J_c(B, T) = C \cdot (1-t^2)^2 \cdot B_{c2}(T)^{-1/2} b^{-1/2} (1-b)^2, \quad (\text{A/m}^2) \quad (3.4)$$

where  $t = T/T_{c0}$  is the temperature normalized over the critical temperature at zero field  $T_{c0}$ . The constants  $T_{c0}$  and  $C$  are independent of temperature and field, but dependent on strain. The critical field can be expressed as a function of temperature introducing the following empirical law [3.6]

$$B_{c2}(T) = \kappa(T) \cdot \alpha \cdot T_{c0} \cdot (1-t^2), \quad (\text{T}) \quad (3.5)$$

where  $\alpha$  is a coefficient independent of  $B$  and  $T$ . Approximating  $\kappa(T)$  by an empirical law [3.7]

$$\kappa(T) = \kappa(0) \cdot [1 - 0.31 \cdot t^2 \cdot (1 - 1.77 \cdot \ln(t))], \quad (3.6)$$

and using  $B_{c20}$  as a parameter dependent on the specific material, the fabrication process and strain, the critical field as a function of temperature becomes

$$B_{c2}(T) = B_{c20} \cdot (1-t^2) \cdot [1 - 0.31 \cdot t^2 \cdot (1 - 1.77 \cdot \ln(t))]^2. \quad (\text{T}) \quad (3.7)$$

Using  $K(T) = \kappa(T)/\kappa(0)$ , the temperature dependence of the critical current density can also be found in literature [3.8], [3.9], expressed by

$$J_c(B, T) = C^{[\text{UT}]} \cdot S^n \cdot \frac{\beta(T)^v}{[K(T)]^v} \cdot \frac{f(b)}{B} \quad (\text{A/m}^2) \quad (3.8)$$

where  $C^{[\text{UT}]}$  and  $S$  are field and temperature independent. The field dependence of the critical current ( $f(b)/B$ ) is as in Kramer's law (3.2). The temperature dependence is in the dependence of  $B_{c2}(T)$ , given by (3.7), and in

$$\beta(T) = [1 - (t)^2] \cdot K(T), \quad (3.9)$$

The critical current constants  $C$ , used in Summers model, and  $C^{[\text{UT}]}$  of the University of Twente model, are different. They are related through (3.10).

$$C = \frac{C^{[\text{UT}]}}{\sqrt{B_{c20m}}} \left( \frac{\text{A} \cdot \text{T}^{1/2}}{\text{m}^2} \right) \quad (3.10)$$

Rewriting (3.8) using Summers' notation we have the explicit relation between critical current density and temperature:

$$J_c(B, T) = C(1-t^2)^2 \left(1 - \frac{B}{B_{c2}(T)}\right)^2 \frac{1}{B^{1/2} B_{c2}(T)^{1/2}} [1 - 0.31 t^2 (1 - 1.77 \cdot \ln(t))], \quad (\text{A/m}^2) \quad (3.11)$$

### Error estimation

The scaling laws just described here fit several kinds of Nb<sub>3</sub>Sn superconductors, which can be very different at microscopic levels, because of different fabrication processes. When using these laws for general studies such as quench protection, we must be aware of possible deviations from these laws for particular conductors. Such estimation can be found in [3.10]. The article compares the Summers model with data measured on two typical conductors,

- Cable 1: *bronze route* (Vacuumschmelze-ITER)
- Cable 2: *internal tin diffusion* (Europa Metalli)

The method used to determine the critical parameters was the following: first, the critical field as a function of temperature was measured, and  $B_{c20}$  and  $T_{c0}$  are found from the data fit. Secondly, the critical current is measured as a function of field at 4.2 K, and the data were fit using only the parameter  $C$ . Using these three parameters, the critical current dependence at different temperatures are compared with new data up to 11 K and 20 T. The model shows that around 8 K / 13 T, the error is about 10%, while at higher temperatures and fields the error is about 30%.

### 3.1.c Strain dependence

As mentioned before, all parameters describing the critical surface (critical current density  $J_c$ , critical field  $B_{c2}$ , and critical temperature  $T_c$ ) depend on the strain conditions of the Nb<sub>3</sub>Sn filaments inside the strands. Measurements show that the critical parameters initially increase with applied strain  $\epsilon_a$ , have a maximum at  $\epsilon_m$ , and then decrease (Fig. 3.1).

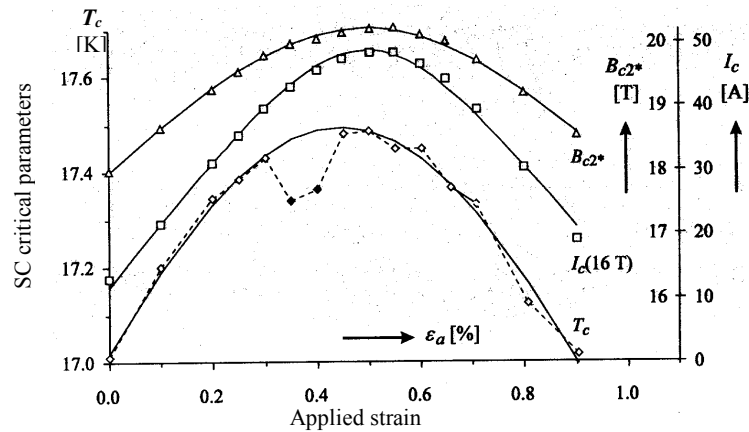


Fig. 3.1: Degradation of the critical parameters with applied strain for ITER type strands ([1.11] A. den Ouden, Twente Univ.).

Measurements such as in Fig. 3.1 show that the Nb<sub>3</sub>Sn filaments are under compression at zero applied strain due to different thermal contractions, from the reaction temperature to liquid helium temperature, between the Nb<sub>3</sub>Sn and the bronze/copper matrix. The maximum of the critical surface corresponds to the intrinsic strain minimum ( $\epsilon_a = \epsilon_m$ ). Naming the intrinsic strain  $\epsilon_i = \epsilon_a - \epsilon_m$ , we can complete the scaling laws with the following relations describing the critical surface as a function of the intrinsic strain [3.12],

$$B_{c20}(\varepsilon) = B_{c20m} \cdot (1-a \cdot |\varepsilon_i|^u), \quad (T) \quad (3.12)$$

$$T_{c0m}(\varepsilon) = T_{c0m} \cdot (1-a \cdot |\varepsilon_i|^u)^{1/w}, \quad (K) \quad (3.13)$$

$$C(\varepsilon) = C_0 \cdot (1-a \cdot |\varepsilon_i|^u)^{1/2}, \quad (A/mm^2, \text{ or } A \cdot T^{1/2}/mm^2) \quad (3.14)$$

where  $a$ ,  $u$  and  $w$  are fit parameters:  $a \sim 900$  for compressive intrinsic strain ( $\varepsilon_i < 0$ ) and  $a \sim 1250$  for the tensile part of the curve ( $\varepsilon_i > 0$ ),  $u \sim 1.7$ , and  $w \sim 3$ .

The general strain laws expressed in (3.12-14) are valid only for reversible strain conditions. Increasing the applied strain above the minimum strain condition for Nb<sub>3</sub>Sn can induce plastic deformations in the copper/bronze matrix, since their tensile yielding point is close to 0.5 % strain. At this strain level or higher, cracks in the Nb<sub>3</sub>Sn filaments may also appear, causing irreversible critical current degradation (such as suggested by some of the measurement points in Fig. 3.2). Measurements performed with a compressive applied strain show that the reversible degradation is less pronounced. In fact, it is known that materials are less sensitive to compressive than to tensile stresses.

### Deviatoric strain model

A more general scaling law based on a three-dimensional strain model is more appropriate when dealing with the strain in a conductor under the mechanical stresses present in a superconducting magnet. For this reason, it is more correct to express the critical parameters as a function of the deviatoric strain [3.13] instead of the axial strain, as used to model pure elongation experiments. This approach explains why even at the maximum of the critical parameters, the Nb<sub>3</sub>Sn is not in a stress-free state, but only in a state of minimum stress, because even if the axial strain is zero, the other components contribute to the overall state of stress.

The critical current density of Nb<sub>3</sub>Sn as a function of magnetic field  $B$ , temperature  $T$  and strain  $\varepsilon$  can be expressed with (3.8),

$$J_c(B, T, \varepsilon) = \frac{C(\varepsilon)\beta(T, \varepsilon)^v}{BK(T, \varepsilon)^v} S(\varepsilon)^n f\left(\frac{B}{B_{c2}(T, \varepsilon)}\right) \left(\frac{A}{m^2}\right), \quad (3.15)$$

where the strain dependent parameters were explicitly stated.

The strain dependence of the critical temperature  $T_c$ , critical field  $B_c$  and the current gauge constant  $C$  is usually written in terms of the strain function  $S(\varepsilon)$ , as  $B_{c2}(T) = B_{c02m} S(\varepsilon)$ , and  $C(\varepsilon) = C_0 S(\varepsilon)^n$ . Using Ekin's model (3.12-14), the strain function can be written as  $S(\varepsilon) = (1-a \cdot |\varepsilon|^u)$ . Using the deviatoric strain model, the strain function is described by

$$S(\varepsilon) = \frac{1 - C_a \sqrt{(\varepsilon_a - \varepsilon_m)^2 + (\varepsilon_{0,a})^2}}{1 - C_a \varepsilon_{0,a}} \quad (3.16)$$

where  $C_a$  the strain sensitivity, and  $\varepsilon_{0,a}$  is the small strain that remains at minimum intrinsic strain ( $\varepsilon_a = \varepsilon_m$ ), because of the contributions of the other components to the overall state of stress. This strain model converges to the Ekin/Summers model (3.12-14), in the limit of large uniaxial strain.

In the most general case, the strain in the conductor is represented by a 3x3 matrix. The axial strain  $\varepsilon$  in (3.16), however, can be derived from the 3D strain matrix using the deviatoric strain function defined in (3.17).

$$\varepsilon_{dev} = \frac{2}{3} \sqrt{(\varepsilon_x - \varepsilon_y)^2 + (\varepsilon_y - \varepsilon_z)^2 + (\varepsilon_z - \varepsilon_x)^2} \quad (3.17)$$

Table 3.1-2 give a summary of the material and conductor parameters for state of the art wires. In some cases values measured on strands of the type used in the racetrack magnet (OST) are reported.

n	p	q	v	$\gamma$	u	w	a
1	0.5	2	2.5 / 2	2 / 1	1.7	3	900

Table 3.1: Material parameters for Nb<sub>3</sub>Sn. Where two numbers are quoted, the first number refers to the Ekin/Summers model, while the second number refers to the Twente model.

$B_{c20m}$	$T_{c0m}$	$C_0$	$\varepsilon_m$	$C_a$	$\varepsilon_{0,a}$
27.4	16.7	33500* / 185000*	-0.0029*	39.12	0.0017

Table 3.2: Parameters for the conductor used in racetrack magnet HFDB02. Values measured on strands used for HFDB02 are indicated with an asterisk. The strain  $\varepsilon_m$  is the axial, intrinsic strain.  $C_0$  was found via a fit of measured critical currents (Fig. 3.3); the first  $C_0$  value refers to the Ekin/Summers model ( $AT^{0.5}/mm^2$ ), the second to the Twente model ( $AT/mm^2$ ). They are related with (3.10).

Fig. 3.2 shows a measurement of the critical current of an OST strand (of the type used in the racetrack magnet HFDB02) as a function of axial strain. This measurement, performed at NIST, indicates that the filaments are in a state of intrinsic pre-compression of 0.29%. The intrinsic pre-compression of the filaments is the result of differential thermal contraction between filaments and matrix during cool-down from the reaction temperature to the operating temperature of 4.2 K.

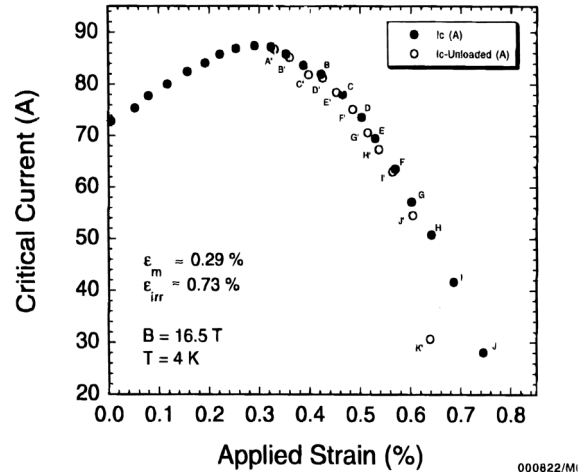


Fig. 3.2: Critical current vs. axial applied strain [courtesy of J. Ekin, N. Cheggour/NIST]. Measurement performed on billet OST/ORE/130 (thin barrier, 0.6 mm strand diameter).

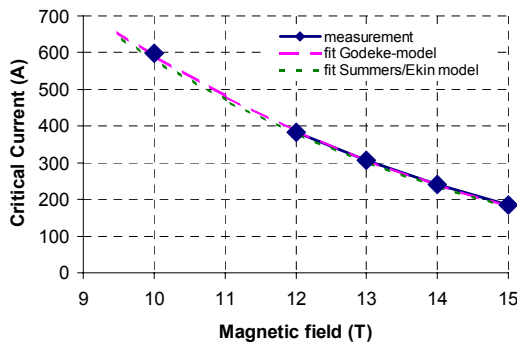


Fig. 3.3: Fit of experimental critical current data (at 4.22K) measured on a strand sample for racetrack magnet HFDB02 (billet: OST/ORE-151). No self-field correction included.

With a choice of constants such as those stated in Table 3.1, the critical current density of an OST, MJR-process strand (strand diameter = 0.7 mm, Cu/non-Cu = 0.87) can be estimated. In Fig. 3.3 the calculation with both parameterizations (equations 3.11 and 3.15) and the experimental data are being compared.

### Cable strain dependence

The extrapolation of the dependence on axial applied strain of strands to the strain dependence of cables is difficult, because of several factors that affect the strain, such as strand twist, transposition, compaction, key-stoning, and eventual defects such as sharp edges. Attempts of modeling the filaments inside strands have been made; in particular cable-in-conduit conductor models succeeded in predicting the minimum strain level [3.14]. Rutherford cable models appear to be more difficult. On the other hand, there are several experiments on Rutherford cables, where the critical current was measured while applying pressure on the broad face of the cable. These measurements indicate that if the cable samples are well impregnated, and the pressure is applied uniformly during the test, they can withstand 150 MPa without permanent degradation [3.15]. On the other hand, when the impregnated sample contains voids or defects, or the pressure is not uniformly distributed on the cable, stress concentration causes immediate large degradation as pressure is applied, and large permanent degradation after the pressure is released. Therefore magnet fabrication has to be careful in avoiding these problems.

Other sets of measurements of critical current degradations under transverse applied pressure were performed on impregnated cables [3.16], confirming that up to 150 MPa there is no permanent degradation, and also indicate that even under 210 MPa, the permanent degradation is only few percent. Several other measurements including react & wind samples indicate that these samples have the same sensitivity to transverse pressure, as straight samples [3.17].

On top of the previously mentioned factors that affect the strain of the  $\text{Nb}_3\text{Sn}$  filaments (thermal pre-compression due to thermal contraction differences of the strand components, cable fabrication, winding after reaction, and any applied strain, such as due to pre-stress and Lorentz forces) we have also to consider the strain that is induced by non-isotropic thermal expansion of the conductor during the quench process. This problem will be addressed in chapter 4.

## **3.2 Thermal conductivity measurements of $\text{Nb}_3\text{Sn}$ cable stacks**

The knowledge of the thermal properties of the impregnated coils is of crucial importance for the design of  $\text{Nb}_3\text{Sn}$  magnets. In fact, the performance of epoxy-impregnated coils, which are cooled indirectly, is sensitive to the value of the thermal conductivity. This is particularly true in the case of heating caused by hysteretic losses, which are usually relevant in  $\text{Nb}_3\text{Sn}$  magnets because of their large effective filament diameter, and in the case of continuous heat deposition, such as in magnets near the interaction regions of a collider [3.18]. Although the thermal properties of the individual materials forming the coils are well known, the resulting overall properties can hardly be predicted with a good accuracy. The calculation of the thermal conductivity along the cable (longitudinal) and across the cable (horizontal/radial in common coil/ $\cos\theta$  magnet frames) is straightforward. The most difficult to estimate is the vertical/azimuthal thermal conductivity from cable to cable, across the insulation.

The vertical thermal conductivity at cryogenic temperatures of stacks of reacted  $\text{Nb}_3\text{Sn}$  Rutherford cables, with different insulations, and vacuum impregnated with epoxy resin was measured at the INFN Laboratory for Applied Superconductivity and Accelerator (LASA) in Milan (Italy), in collaboration with the University of Milan and Fermilab [3.19].



### 3.2.a Description of the samples

The samples are stacks of reacted Rutherford cables, vacuum impregnated with epoxy resin (CTD-101K) [3.34], under a pressure of 15 MPa. The sample characteristics are listed in Table 3.3. The first sample is a 13 cables-stack, 86 mm long. All the other samples are ten-stacks, 25.4 mm long.

The cables are insulated with some of the different materials under study at Fermilab in the frame of the Nb<sub>3</sub>Sn magnet program. An insulation scheme based on ceramic-fiber tape with ceramic binder [3.20] is a key element of the production of the FNAL cos $\theta$  dipole. E-glass, Kapton® and pre-impregnated fiberglass (pre-preg) tapes [3.21] have been studied during the R&D for FNAL single-layer common coil and racetrack magnets.

Sample#		1	2	3	4 & 5
Insulation material		Fiberglass (E-glass)	Kapton+ Pre-preg	Only epoxy	Ceramic fibers + binder
Ins. thickness	(mm)	0.2	0.23	-	0.35
Strand diameter	(mm)	0.7	0.7	0.7	1
Cu/non-Cu		1.4	0.87	0.87	0.92
Packing factor		0.87	0.87	0.87	0.9
Cable thickness	(mm)	1.2	1.2	1.2	1.8
Cable width	(mm)	14.5	14.5	14.5	14

Table 3.3: Main parameters of cable stacks for the conductivity measurements.

The first three samples are stacks of cables with the same design (41 strands of 0.7 mm diameter). Similar cables were used for the construction of two racetrack magnets at Fermilab [3.22]. In the first sample, a fiberglass tape is wrapped around each cable with 30% overlap. In the second sample, the turn-to-turn insulation consists of a layer of Kapton® (76  $\mu$ m-thick), and a layer of pre-impregnated fiberglass tape. The final average thickness of the insulating layer, after impregnation, is 0.23 mm. The third sample is a stack of the same cable as in sample # 2, but it is epoxy-impregnated without any other insulating material. In this sample, the cables are in direct thermal contact. Therefore, the measure of the thermal conductivity of this sample, allowed the direct measure of the impregnated cable, and the comparison with the other samples allowed estimating the contribution of the insulating layer to the overall coil thermal conductivity.

The last two samples in Table 3.3 are ten-stacks of a cable with 28 strands, 1 mm in diameter, as the cable used in the Fermilab cos $\theta$  dipole magnets. This cable has a higher compaction and higher copper content than the cable of samples # 2 and # 3. Samples # 4 and # 5, are prepared following the same procedure used for the production of the coils of the cos $\theta$  dipole models. Each cable is wrapped with ceramic fiber tape, with 40 % overlap, then it is wetted with a ceramic binder (CTD-1002x), and cured at 80 °C for 20 minutes. The samples are then heat treated to form the Nb<sub>3</sub>Sn composite. Analysis at the SEM show that, after the heat treatment, the cable strands are coated with a thin layer of a material with a high content of oxygen and silica [3.23]. The effect of this coating on the contact electrical resistance between the strands is under investigation at Fermilab.

### 3.2.b Apparatus description

The experimental setup, described in detail in [3.24] is briefly presented here. The conductivity measurement was performed using a steady-state method, described in the following: the sample is placed between two heat sinks, providing a constant heat flux in one

(axial) dimension, when thermal equilibrium is reached. The cold sink is in direct contact with the cryogen, and the warm sink is heated through an electrical resistance. The measures of the current and of the voltage across the resistor provide a precise value of the input power. The heat flux is then given by the power divided by the area of the cross section of the sample. The temperature is measured at several points along the sample and on the two sinks, through Au-Fe (0.07 % at w.) – Chromel-P thermo-couples. The system is enclosed in a vacuum chamber in which the pressure is maintained at about  $10^{-6}$  mbar, to avoid convective losses. The vacuum chamber is made of stainless steel, and is gold plated to reduce radiation losses. The main parts of the apparatus are shown in Fig. 3.4.

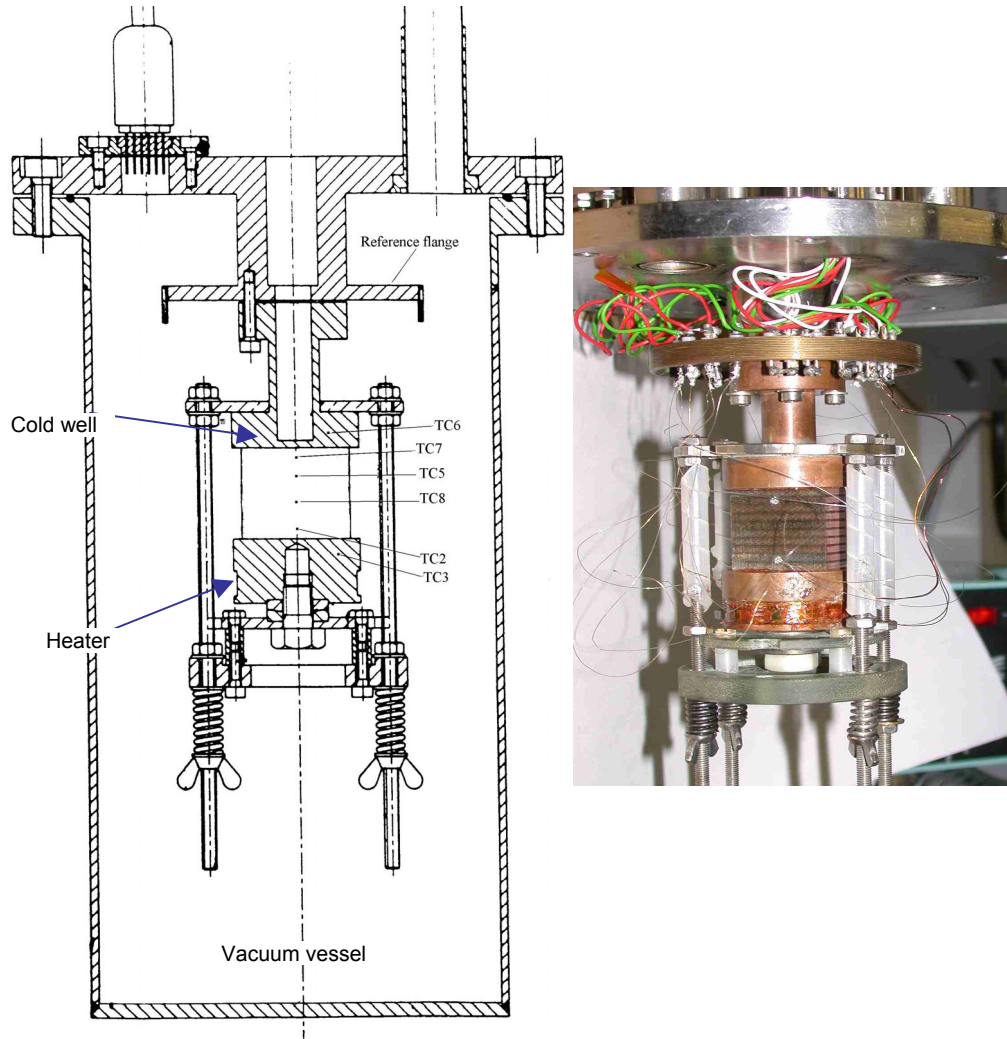


Fig. 3.4: Schematic drawing of the conductivity measurement apparatus.

The Fourier-Biot law determines the thermal conductivity:

$$\dot{Q} = -k \cdot S \cdot dT/dl \quad (\text{W}), \quad (3.18)$$

where  $\dot{Q} = -P$  is the heat flowing in the sample (equal to the input power  $P$ , but in opposite direction with respect to the temperature differential  $dT/dl$ );  $k$  is the thermal conductivity (which is temperature dependent); and  $S$  is the cross-sectional area of the sample. Considering  $S$  a constant, and approximating  $k$  to be a linear function of temperature, we can calculate the thermal conductivity at an average temperature with:

$$k(\bar{T}) = P \cdot l / (S \cdot \Delta T) \quad \left( \frac{\text{W}}{\text{K} \cdot \text{m}} \right), \quad (3.19)$$

with  $\Delta T = T_1 - T_2$ , and  $\bar{T} = (T_1 + T_2) / 2$ .

The approximation of  $k(T)$  as a linear function is a good approximation for metals at low temperature, or if the conductivity dependence on temperature is a slowly varying function. The conductivity of the insulating materials typically has a steep increase at low temperature. In the case of our composite samples, at temperatures close to liquid helium temperature, the error due to this approximation is small for temperature differences of a few Kelvin (Fig. 3.5).

Another source of error is the power loss, due to heat dissipated by convection through the supporting system, convective losses through residual gas, and radiation from the warm sample and from the heater to the vacuum vessel at bath temperature. The setup is designed and tested to have very low power losses, estimated to be about 3 % of the input power, in most of the temperature range of operation with liquid helium [3.24]. A maximum dissipation of 10 % is possible using liquid nitrogen, due to larger temperature differences.

### 3.2.c Experimental results

Fig. 3.5 shows the results of the conductivity measurements performed using liquid helium as cryogen.

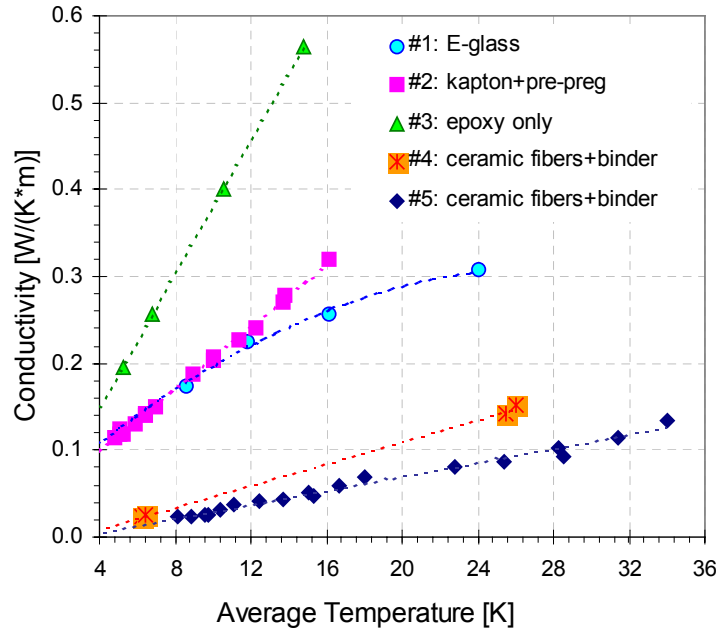


Fig. 3.5: Results of the conductivity measurements with liquid helium: experimental data (points) and interpolating functions (dashed lines).

The measured data from sample # 1 (E-glass insulation) can be interpolated using a quadratic function, while all the other data of Fig. 3.5 can be interpolated using linear functions. The conductivity values of sample # 1 and sample # 2 are close at temperatures below 12 K. The extrapolated value at 4.2 K is 0.1 W/(K-m). Sample # 3 (epoxy impregnated without insulation) has a higher thermal conductivity, than the insulated samples, with an

extrapolated value at 4.2 K of 0.16 W/(K-m). Samples # 4 and # 5 (ceramic insulation) have a very low thermal conductivity of 0.03 W/(K-m), at 6 and 8 K respectively. Extrapolation to lower temperatures might result in an underestimation of the real conductivity, since the linear interpolating functions have a small, but negative value at zero Kelvin.

Fig. 3.6 shows the data of the first three samples, including measurements performed with liquid nitrogen.

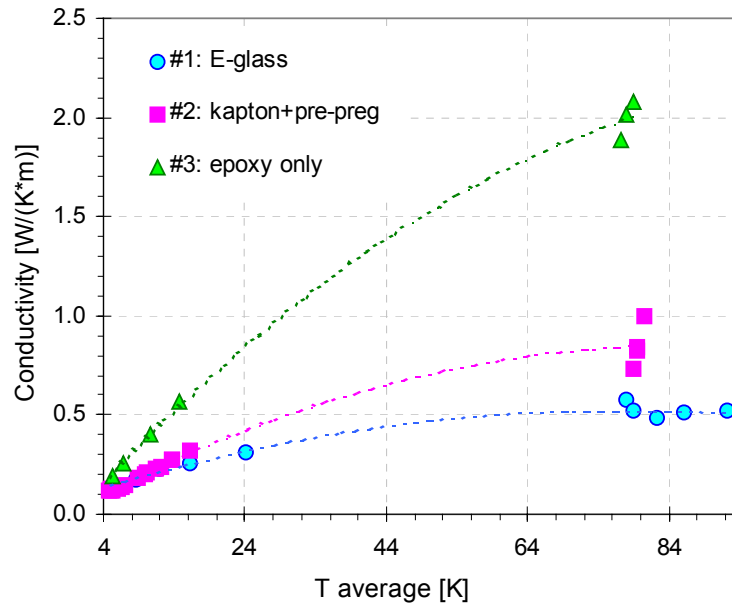


Fig. 3.6: Results of the conductivity measurements with liquid nitrogen: experimental data (points) and a quadratic interpolation of the experimental data (dashed lines).

### 3.3 Thermal conductivity modeling

The measured data of thermal conductivity of the Nb<sub>3</sub>Sn cable stacks were also compared with calculated values, obtained on the basis of the components' material properties and the cable stack geometry. The comparison can not only be a useful check of the measurement procedure, but can also provide a useful tool to predict the thermal properties of a coil with different conductor or insulation characteristics than those tested. Therefore, chapter 3.3 presents:

First, the thermal conductivity of the insulating layer of sample 2, extracted from the measurement data of sample 2 and 3. The results are compared with data from literature to validate the measurement procedure (section 3.3.a).

Second, the thermal conductivity of the metal part of a cable is considered. Measured data from sample 3 (bare sample) are compared with a detailed model of a Rutherford cable (section 3.3.b). The model results were successfully used in the FE model of the quench experiment presented in chapter 4.

Third, the thermal conductivity data are compared with the calculation results from the QLASA program (based on a simple model), in order to validate the procedure used in the quench simulation program (section 3.3.c).

### 3.3.a Thermal conductivity of the insulating layer of sample # 2

The thermal conductivity of the insulating layer of sample # 2 (insulated stack) was calculated from the thermal resistance of the sample, subtracting the contribution of the impregnated cable, using the thermal resistance from sample # 3 (bare stack), according to (3.20):

$$R_{th}(\text{ins. layer}) = R_{th}(\text{ins. stack}) - R_{th}(\text{bare stack}) \quad (1/W). \quad (3.20)$$

The resulting thermal conductivity is indicated by the red continuous line in Fig. 3.7. In the same graph, the thermal conductivity of other insulations are also indicated for comparison: G10 (from Cryocomp [3.25]), Kapton [3.26], epoxy impregnated fiberglass, IVA-type [3.27, 28], and the resulting thermal conductivity of 76  $\mu\text{m}$  Kapton and 0.154 mm pre-preg (from above data), indicated by the black dashed line.

The difference between the thermal conductivity of the insulating layer of sample #2 and the conductivity from the data from literature is about 10%. This difference could be due to slight differences in thickness and/or in the epoxy used in the fabrication of the pre-preg tape.

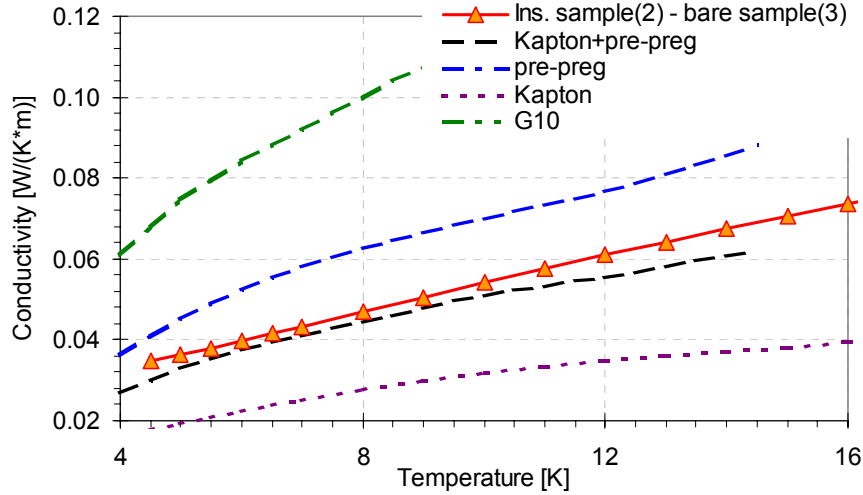


Fig. 3.7: Thermal conductivity of the insulating material of sample 2, consisting of Kapton and pre-preg tapes, derived from insulated sample and bare sample, and compared to other insulations.

### 3.3.b Thermal conductivity of the bare sample (# 3)

In the following we present a detailed model of the thermal conductivity of a Rutherford cable in the transverse direction (Fig. 3.8), that is vertical direction in a CC magnet frame, and azimuthal direction in a  $\cos\theta$  magnet design.

The overall thermal conductivity is determined by the heat conducted in each strand in the transverse direction and the thermal contact resistance between the two layers of strands, and by the heat conducted along the strands due to their transposition. The results of the calculations are compared with the experimental data of the sample impregnated without insulation.

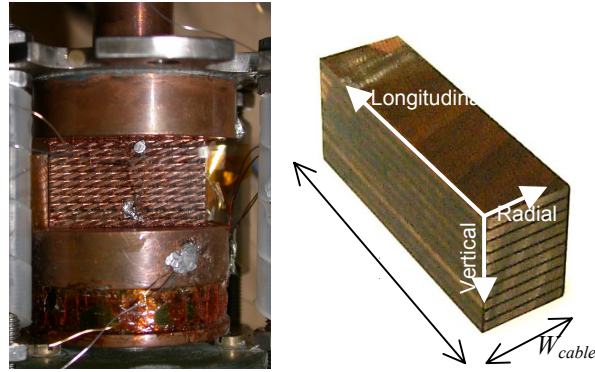


Fig. 3.8: Sample without insulation (left), and convention for axis labeling, and dimensions (right).

### Single strand

To calculate the thermal conductivity in the transverse direction of a Rutherford cable, we first consider the heat flow inside each single strand, without considering the transposition. In this case (see Fig. 3.9), the heat flux goes from  $T_2$  to  $T_1$  (with  $T_2 > T_1$ ), mainly through the copper matrix surrounding the superconducting core. In fact,  $\text{Nb}_3\text{Sn}$ , Tin, Bronze and other materials inside the core, have a much lower conductivity (Fig. 3.10), even for low RRRs of copper. The RRR of the same conductor was measured for short samples and for the racetrack magnet HFDB02.

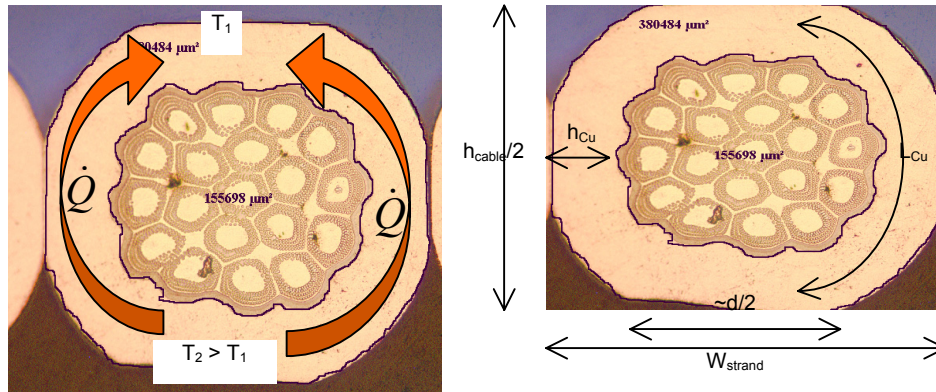


Fig. 3.9: Picture of a strand in a cable and schematic of heat flow (ITER strand is used just as example), and geometrical parameters determining the axial thermal conductance in a strand.

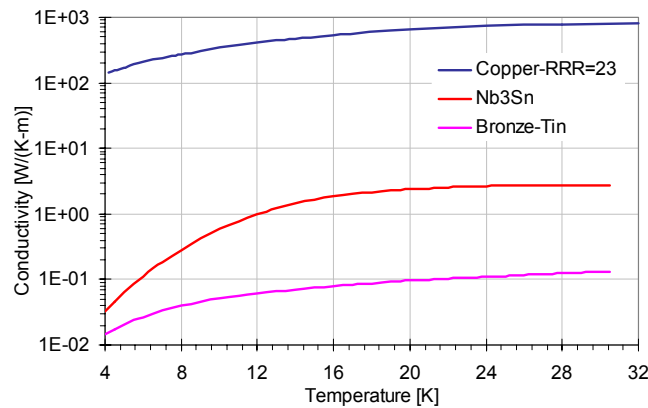


Fig. 3.10: Conductivity of copper with RRR=23 and  $B=0$  T, from [3.29];  $\text{Nb}_3\text{Sn}$  [3.30], and bronze contained in the superconducting core of a strand, which is contaminated by tin (estimation from Wiedeman-Franz law and measured electrical resistivity)

Hence the strand transverse conductance  $C_{strand}$  can be expressed as

$$C_{strand} = 2 \cdot k_{Cu} \cdot \frac{h_{Cu} \cdot l}{L_{Cu}} \quad (\text{W/K}) \quad (3.21)$$

where the parameters to be used in (3.21) are given in Table 3.4. Looking at the cable cross-section in Fig. 3.9, we can approximate  $L_{Cu} \sim d$ , and  $h_{Cu}$  as:

$$h_{Cu} \approx \frac{W_{strand}}{2} - \sqrt{\frac{A_{non-Cu}}{N_{strand} \cdot \pi}} \quad (\text{m}) \quad (3.22)$$

Symbol	Model parameter	Value
$k_{Cu}$	Copper thermal conductivity (with RRR = 23, B = 0 T)	See Fig. 3.10
$h_{Cu}$	width of the heat flow path through the copper matrix branches	0.12 mm
$l$	sample length ( $\sim$ the length of the strand)	25 mm
$L_{Cu} \sim d$	length of the heat flow path through the copper matrix branches	0.7 mm
$d$	strand diameter	0.7 mm
$W_{strand}$	strand width = $W_{cable}/(N_{strand}/2)$	0.76 mm
$A_{non-Cu}$	non copper area in the cable cross-section, from Cu/non-Cu = 0.87	8.52 mm <sup>2</sup>
$N_{strand}$	number of strands in the cable	41
$h_{cable}$	cable thickness	1.3 mm
$W_{cable}$	cable width	15.14 mm

Table 3.4: Parameters used to model thermal conductivity in a strand.

Therefore, from  $C_{strand} \sim k_{strand} \cdot W_{strand} \cdot l / (h_{cable}/2)$ , we obtain the contribution of each strand to the thermal conductivity in transverse direction, as:

$$k_{strand} = k_{Cu} \cdot \frac{h_{cable} / 2}{W_{strand}} \cdot \left( \frac{2h_{Cu}d}{2h_{Cu}^2 + L_{Cu}d} \right) \left( \frac{\text{W}}{\text{K} \cdot \text{m}} \right) \quad (3.23)$$

### Contact between strands

The thermal conductivity of a cable in axial direction is reduced drastically when we consider the thermal resistance due to the contact between the two layers of strands. This thermal resistance is difficult to predict, because it depends strongly from the surface characteristics. In particular, for copper, the thermal resistance depends on the oxidation level. This explains why in literature there is a wide range of data values, varying from source to source [3.31].

“Thermal contact resistance is attributable to several factors, the most notable being that contact between two surfaces is made only at a few discrete locations rather than over the entire surface area. A close examination of even the smoothest surfaces reveals an asperity, which limits the actual area of contact to as few as three discrete locations, irrespective of the dimensions of the sample. This is supported empirically by findings that the thermal conductance of pressed contacts is dependent upon the applied force and not on the area of contact or on the apparent contact pressure. As the applied force is increased, surface deformation of the material occurs. The initial area of contact increases and, as the material deforms further, contact occurs at new locations. The heat flow is constricted in the vicinity of the contact locations because of the narrowness of the effective areas of contact. This constriction is, in large part, responsible for contact resistance. Additionally, the presence of



surface films or oxides contributes to the phenomenon. The thickness of these layers adds an additional variable to the conductance. At low temperatures, each oxide layer acts as an additional boundary resistance, and the problem is compounded because of the acoustic mismatch between the layers (Kapitza resistance). Thermal conductance increases asymptotically with increasing applied force. As the applied force increases, the actual area of contact approaches the apparent area. For uncoated samples at liquid helium temperature, it has also been found that thermal conductance is related to the surface finish of the samples.

Experimental data has shown that the thermal conductance of metallic pressed contacts increases according to a simple power law function of temperature, under a given applied force” (quoted from [3.31]) at LHe temperature.

With increasing temperature from the LHe temperature, the conductance becomes linear with  $T$ , and above  $\sim 200$  K, tends to a temperature independent value. Nilles and Van Sciver [3.32] performed measurements up to room temperature, of oxidized and non-oxidized samples, with accurate cleaning procedures, and using  $N_2$  atmosphere (Fig. 3.11). The non-oxidized sample has a conductance that is proportional to the copper conductivity taking into account the geometrical factor (area of the sample and surface roughness) and dividing by a factor of 25. The oxidized sample has a lower conductance at low temperature, and strangely, a higher conductance than the non-oxidized sample at room temperature.

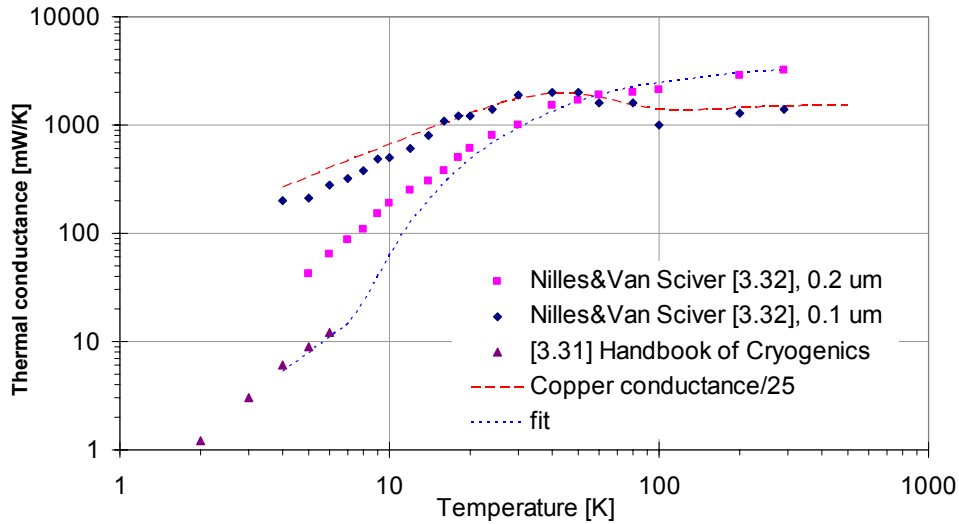


Fig. 3.11: Thermal conductance of copper sample pairs vs. temperature from different references, and simple models to fit the data.

Since the properties of our samples are not measured, and since there is such a large difference in different samples according to their preparation, a simple model was used to fit the data (dashed line in Fig. 3.11), in which the conductance follows the power law, at low temperature, and an exponential law up to high temperature. The parameters describing this function are chosen in order to fit the conductivity of the cable sample.

During impregnation of our samples, the pressure was estimated to be about 15 MPa. To obtain the force on the contact area, it is necessary to estimate the actual contact area. If the total area ( $A_{tot} = l \cdot W_{cable}$ ) is reduced by a factor eight, ( $A_c = A_{tot}/8$ ), the resulting force over the contact surface is 735 N. Since it is difficult to measure the exact value of the contact area, this value can be considered a free parameter to fit the experimental data (varying it within a reasonable range [3.33]).

We considered in the following, the data of copper-to-copper contact with oxide surfaces. The temperature dependence of the contact conductance ( $C_{contact}$ ) is approximated by:



$$\begin{cases} C_{contact}(T) = \alpha \cdot T^n & \text{for } T < T_r = 16 \text{ K} \quad (\text{W/K}) \\ C_{contact}(T) = C_{300} \cdot e^{-1/(\beta \cdot T)} & \text{for } T > T_r \quad (\text{W/K}) \end{cases} \quad (3.24)$$

with  $n = 1.8$ ,  $\alpha = 0.43 \cdot 10^{-3} \text{ W/K}^{n+1}$ ,  $C_{300} = 2.7 \cdot 10^{-3} \text{ W/K}$ , and  $\beta$  is a function of the other parameters, since it is determined by the condition of continuity between the high temperature curve and the low temperature one:

$$\beta = -(T_r^n \cdot \ln(\alpha \cdot T_r^n / C_{300}))^{-1} = 0.017 \quad (\text{K}^{-1}) \quad (3.25)$$

The fraction of volume that is not occupied by the metal in a cable stack is filled with epoxy resin. The area occupied by epoxy ( $A_{epoxy}$ ), in the cable cross-section, can be found by considering the strand area ( $A_{met} = N_{strand} \cdot A_{strand}$ ) and the area of the rectangular cable envelope containing the strands ( $A_{cable} = h_{cable} \cdot W_{cable}$ ). Then  $A_{epoxy} = A_{cable} - A_{met}$ . Considering a contact area between the strands  $W_{cable}/2$  wide, then we obtain an effective thickness of  $h_{epoxy} = 2 \cdot A_{epoxy} / W_{cable}$ . The resulting contribution of the epoxy to the total conductivity is almost negligible.

The formula that describes the conductance of the middle layer (contact conductance plus epoxy conductance) is

$$C_{midplane}(T) = C_{contact}(T) + k_{epoxy} \cdot l \cdot (W_{cable}/2) / h_{epoxy} \quad (\text{W/K}) \quad (3.26)$$

The total conductance of the cable stack in transverse direction, without considering the transposition of the strands, is given by the series of thermal resistance of the strand layers and of the contact planes:

$$C_{cable} = \left( \frac{2}{C_{strand} \cdot (N_{strand}/2)} + \frac{2}{C_{midplane}} \right)^{-1} \quad (\text{W/K}) \quad (3.27)$$

where we have considered that in a cable stack, there are two contact planes (“mid-plane”) for cable, on average.

The total conductivity of the cable stack in axial direction, without considering the transposition of the strands, is given by:

$$k_{cable} = \left( \frac{1}{k_{strand}} + \frac{W_{cable} \cdot l}{h_{cable}} \cdot \frac{2}{C_{midplane}} \right)^{-1} \quad (\text{W/m/K}) \quad (3.28)$$

### Strand transposition effect on the thermal conductivity

To calculate the effect of the transposition (Fig. 3.12) on the transverse thermal conductivity we first have to calculate the thermal conductivity along the strands ( $k_{long}$ ):

$$k_{long} = \sum_i f_i \cdot k_i \quad (\text{W/m/K}) \quad (3.29)$$

where  $f_i = A_i / A_{Xsection}$  are the fractions of the different components of thermal conductivity  $k_i$ , over the cable cross-section area  $A_{Xsection}$ .

Since the measurements were performed in stationary conditions, let us consider uniform temperatures on planes normal to the axial direction, along which we measured the temperature gradient. This is a good approximation only if we can consider the sample to be homogenous and the heat source to be uniform. In reality, the sample is not homogeneous, and we will discuss this approximation in the next paragraph. This case is of interest for the study of a quench in a magnet, where the temperature distribution is not uniform, especially close to the hot spot. In the case of uniform temperature on the planes normal to the axial direction, the heat flow involves only the region of the transposition of the strands, at the edge of the cable. This length ( $L_{transp}$ ) is few millimeters. Since it is difficult to have an exact measure, we used this parameter to fit the experimental data. We have to notice also that the resulting effective thermal conductivity is very sensitive to this value.

If the sample were half pitch long ( $l=L_{pitch}$ ), then the contribution to thermal conductance in the axial direction due to the strand transposition (length) would be  $C_{pitch}$ :

$$C_{pitch} = k_{long} \frac{A_{X section}}{L_{pitch}} = k_{pitch} \frac{L_{transp} \cdot W_{cable}}{h_{cable}} \quad (W/K) \quad (3.30)$$

Giving an effective thermal conductivity  $k_{pitch}$

$$k_{pitch} = k_{long} \frac{h_{cable}^2}{L_{pitch} \cdot L_{transp}} \quad (W/(Km)) \quad (3.31)$$

Since the measured sample was shorter than half the transposition length, not all the strands were transposed from one layer to the other. The total sample transverse thermal conductivity  $k_{sample}$  can be approximated by (3.32)

$$k_{sample} = k_{cable} + k_{pitch} \cdot l/L_{pitch} \quad (W/(Km)) \quad (3.32)$$

Since not all the strands are transposed (with  $l < L_{pitch}$ ), thermal gradients can establish within the planes normal to the axial direction. In this case, and in case of transient heat diffusion like during a quench, the sample should be considered as inhomogeneous. The transposition length  $L_{transp}$  that affects the heat diffusion in (3.31) can then increase from few millimeters, as in the homogeneous case, to a transposition pitch. For  $L_{transp} = L_{pitch}$ , the contribution of the transposition  $k_{pitch}$  to the overall transverse conductivity is negligible, resulting in a thermal conductivity close to the model without transposition at all ( $k_{sample} = k_{cable}$ ) [3.34].

### Results of the calculations and comparison with experimental data

The following describes the results of the calculations, and the comparison with the experimental data.

The three main “free” parameters that affect the sample thermal conductivity are  $\alpha$  and  $C_{300}$  that determine the contact conductance, at LHe and LN temperatures respectively, and  $L_{transp}$  that determines the transposition effect. These parameters are varied together, in order

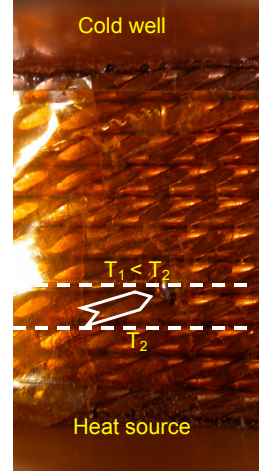


Fig. 3.12: Bare sample and schematic of the transposition effect.

to have  $k_{sample}$  (3.32) fitting the experimental data. The best fit is represented in Fig. 3.13 by the continuous line.

The best fit resulted to be that with a low value of contact thermal conductance at LHe temperature,  $\alpha=0.4 \cdot 10^{-3} \text{ W/K}^{2.8}$ , a short effective thermal transposition length,  $L_{transp}=5.3 \text{ mm}$ , and  $C_{300} = 4 \cdot 10^{-3} \text{ W/K}$  (Fig. 3.13 continuous line). A longer transposition length with higher contact conductance parameter resulted in a non-linear temperature dependence of the thermal conductivity at LHe temperatures, which is not supported by the measured data.

The dotted line in Fig. 3.13 represents  $k_{cable}$  without transposition effect (3.28), using the same contact thermal conductance parameters,  $\alpha=0.4 \cdot 10^{-3} \text{ W/K}^{2.8}$  and  $C_{300} = 4 \cdot 10^{-3} \text{ W/K}$ . The results are lower than the experimental data by about 25% at LN, and a factor 10 lower at LHe temperatures.

Using the best-fit values, and with  $l=L_{pitch}$  in (3.32), we obtain the thermal conductivity for a longer sample (Fig. 3.13 dashed line). We can see that longer samples have higher thermal conductivity, due to the contribution to  $k_{pitch}$  of all the strands, while in a sample shorter than half the transposition pitch, not all the strands are transposed to the second layer, and therefore cannot contribute to the heat transfer in transverse direction along the strands. This curve was successfully used for the thermal analysis of the cable quench experiment (see Chapter 4).

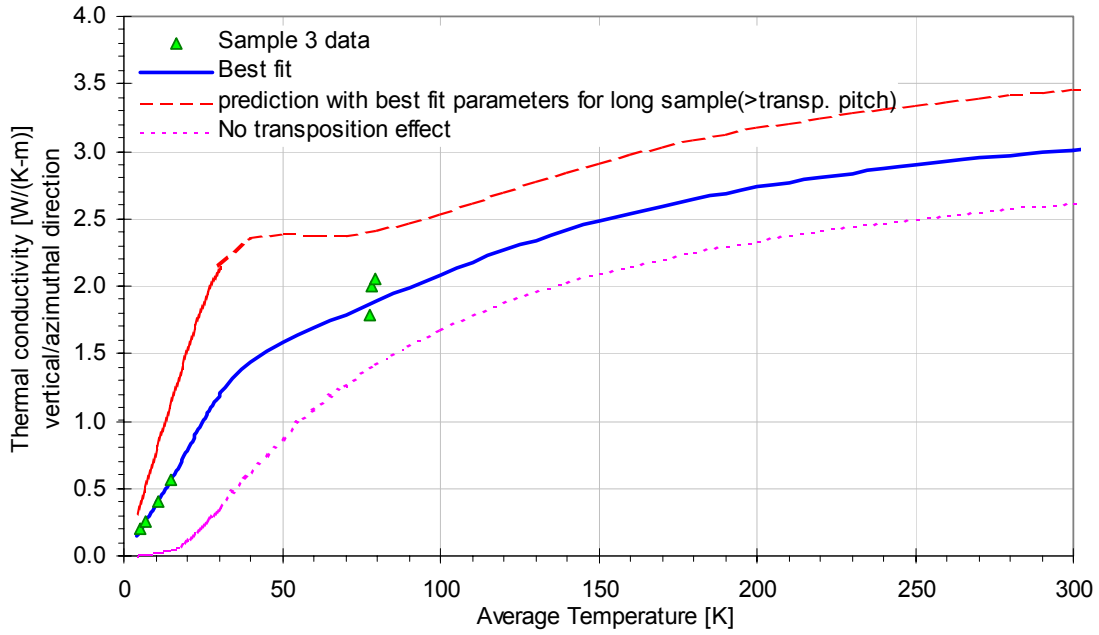


Fig. 3.13: Sample 3 thermal conductivity data compared to model results using  $\alpha=0.4 \cdot 10^{-3} \text{ W/K}^{2.8}$ ,  $L_{transp}=5.3 \text{ mm}$ , and  $C_{300} = 4 \cdot 10^{-3} \text{ W/K}$ .

### 3.3.c Overall thermal conductivity of sample 1 (with e-glass insulation)

The conductivity of the insulated cable stack can also be calculated with a simpler model, where the conductivity of the insulation layer is considered to be like that of pre-preg material (data from [3.27], [3.28]), and the conductivity of the bare cable is calculated from the conductivity of the components and their relative surface fraction over the cross section, as a series of thermal resistances (Fig. 3.14).

The simple model does not include the contact thermal resistance between strands, or the transposition effect. This model can successfully approximate the thermal conductivity in vertical direction because, in an insulated cable stack (or coil), the overall thermal resistance is essentially determined by the insulation.

This simple model is used in the QLASA program to simulate the quench process (see 2.2.b, and [2.20]).

The conductance of the sample using the QLASA simple model ( $C_{sample}^{QLASA}$ ) is the sum of the conductance of the side insulation ( $C_{insR}$  that is negligible) and the series of the thermal resistances of the components, as in (3.33). The height of each layer ( $h_i$ ) is calculated from the cross-sectional area of the component  $A_i$  divided by the cable width:  $h_i = A_i / W_{cable}$  (Fig. 3.14).

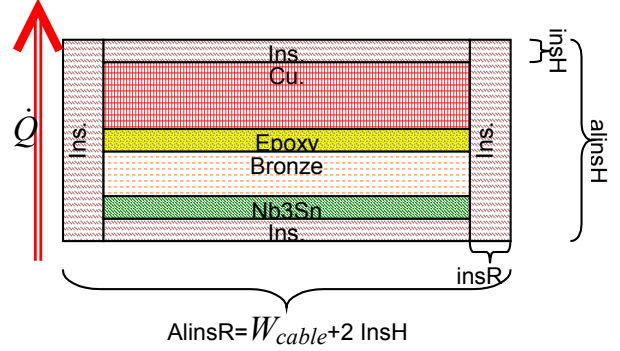


Fig. 3.14: Schematic of the simple thermal conductivity model used in QLASA for the transverse direction.

$$C_{sample}^{QLASA} = C_{insR} + \sum_i \frac{W_{cable} \cdot l}{h_i / k_i} \quad (\text{W/K}) \quad (3.33)$$

Fig. 3.15 presents a comparison between the simple model conductivity function, and the measured data for sample #1 (E-glass insulation). The two lines of Fig. 3.15 represent the calculated conductivity, including and not including the epoxy fraction (continuous and dashed lines respectively).

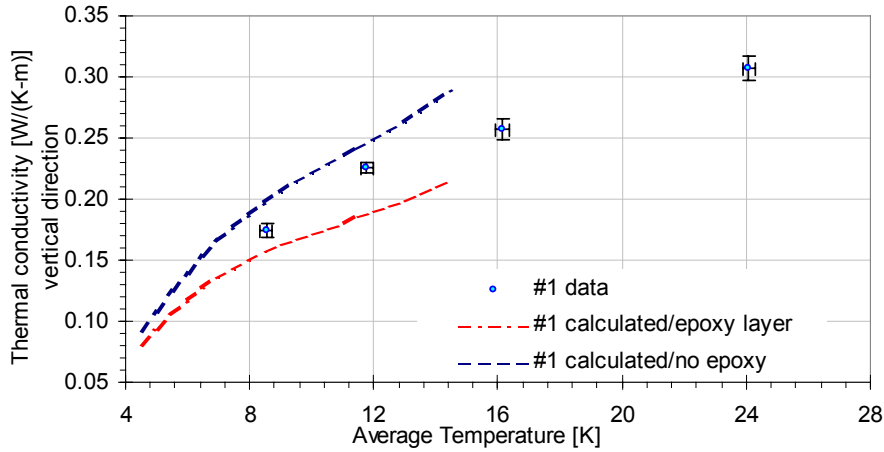


Fig. 3.15: Comparison of the measured thermal conductivity data with the thermal conductivity calculated from the material properties of the components, for sample #1 (E-glass insulation).

Fig. 3.15 shows that the thermal conductivity calculated without epoxy, is overestimating the thermal conductivity of sample 1, by a few percent. Including the epoxy, the thermal calculations resulted in an underestimation of the thermal conductivity of sample 1. In fact, the epoxy is included as a continuous layer between the strands while in reality the strands have some contact points. Therefore, the overall thermal conductivity of an insulated cable stack can be estimated, with good approximation, with this simple method, by taking into account only part of the epoxy fraction.

### 3.3.d Summary of thermal conductivity study

The thermal conductivity at cryogenic temperatures of stacks of reacted Nb<sub>3</sub>Sn Rutherford cables, with different insulations, and vacuum impregnated with epoxy resin was measured. The different insulation schemes, under study at Fermilab in the frame of Nb<sub>3</sub>Sn magnet program, include E-glass, Kapton and pre-preg tapes used for the react-and-wind common coil and racetrack magnets, and ceramic-fiber tape with ceramic binder used for the wind-and-react cos $\theta$  magnets.

Measurements of two samples, one insulated with Kapton and pre-preg, and another without cable insulation, but with otherwise identical characteristics (epoxy-impregnated, same strand parameters etc.) allowed determination of the contribution to the overall coil thermal conductivity of the insulating layer, and of the impregnated cable. The thermal conductivity of the insulating layer was in good agreement with data from literature.

Measured data from the so-called bare (un-insulated) sample were compared with calculations using a detailed model of a Rutherford cable. The analysis included the thermal contact resistance between the two layers of strands of the Rutherford cable, and the effect of the transposition pitch. The contact thermal resistance is difficult to predict, because it depends on the contact surface area and on other insulating materials that can cover the strands, such as oxides and epoxy. For example, the samples fabricated following the procedure of the racetrack magnet included synthetic oil, which was used to prevent sintering of the two layers of strands during reaction. The samples fabricated following the procedure for the cos $\theta$  magnet, are believed to have a similar surface contamination, related to the use of a synthetic binder in the insulation. In fact, the results show that even though the cable had a higher compaction and higher copper content than the cable of the other samples, the overall turn-to turn thermal conductivity is lower. The difference in the conductivity between the cos $\theta$  samples can be explained by a difference in the thickness of the coating or in the pressure during preparation. Measurements of the electrical contact resistance of Nb<sub>3</sub>Sn cables are under way at Fermilab [3.35].

Even though the transverse conductance of the measured cables through the contact thermal resistance were small, the transposition of the strands strongly dominates and increases the conductivity of the un-insulated cable, especially at low temperatures.

For an insulated cable stack, the overall thermal conductivity is mainly determined by the turn-to-turn insulation. This is the reason why a simple model (as used in QLASA) gives results that agree with the measured data to within 10%.

## 3.4 Material properties for quench integrals

Specific heat, density and resistivity are the material properties affecting the quench integrals. This section presents the material properties used in the quench process simulations presented in chapter 2, and in the analysis of the quench experiments described in chapters 4 and 5. In addition to the cable conductivity model described in chapter 3.3 describing measurements of the turn-to-turn conductivity, the conductivity in all directions, including radial and longitudinal, are discussed in chapter 3.4.d.

### 3.4.a Specific heat and density

The specific heat and density data refer to the material properties electronic library MATPRO, used in the QLASA program [3.36].

Fig. 3.16 and Fig. 3.17 show the specific heat per unit mass and per unit volume respectively. Note that the specific heat of the insulating materials was extrapolated from values at around room temperature to higher temperatures. Epoxy and epoxy-composites are not usually employed above the glass transition temperature (410 - 430 K).

Table 3.5 lists the density of component materials of the Nb<sub>3</sub>Sn coils used in the quench simulations.

Material	Density (Kg/m <sup>3</sup> )
Copper	8960
Bronze	8850
Nb <sub>3</sub> Sn	8040
Epoxy	1800
G10	1900

Table 3.5: Density of component materials of Nb<sub>3</sub>Sn

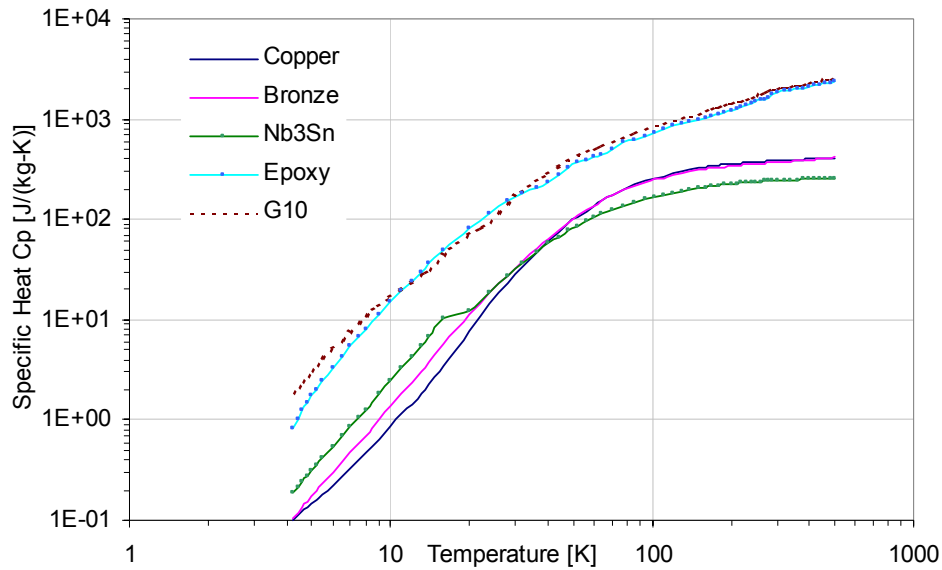


Fig. 3.16: Specific heat per unit mass, used in calculations, for materials commonly used in Nb<sub>3</sub>Sn magnets.

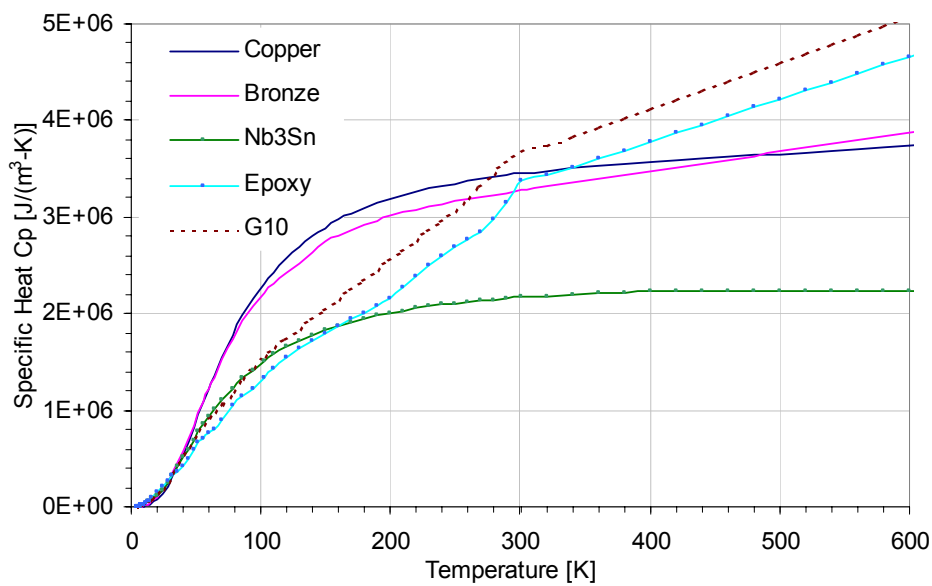


Fig. 3.17: Specific heat per unit volume, used in calculations, for materials commonly used in Nb<sub>3</sub>Sn magnets.

### 3.4.b Resistivity

The resistance of the cable is probably the most influential quench process parameter, as discussed in chapter 2. In the quench simulations, therefore, the copper resistivity must be accurately described as a function of temperature, RRR and magnetic field. Fig. 3.18 shows the resistivity of copper from liquid helium to 600 K. The resistivity functions used in the quench simulations, with QLASA [3.29] and Quenchpro, are similar up to 500 K, with only a few percent difference around 200 K. These resistivity functions are also compared to literature values and to the measurement performed on the small magnet described in chapter 5 (and [5.6]). The resistivity was calculated from resistance measurements, and geometrical factors, including the transposition pitch. We can notice that the resistivity of SC10 was slightly higher than the value expected for oxygen free high conductivity copper (OFHC [3.37]) at 293 K ( $\rho_{Cu}=1.69 \cdot 10^{-8} \Omega \cdot m$ ) by about 10%, and about 4% with respect to data from measurement on NbTi strands [3.38] ( $\rho_{Cu}=1.8 \cdot 10^{-8} \Omega \cdot m$ ). The parameterization of the copper resistivity from NIST [3.39], gives a room temperature value of  $\rho_{Cu}=1.76 \cdot 10^{-8} \Omega \cdot m$ .

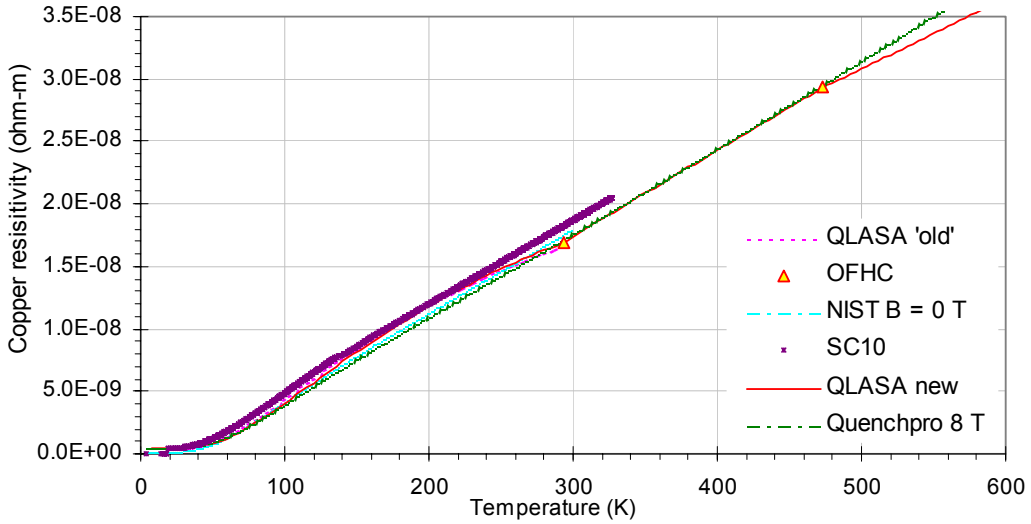


Fig. 3.18: Copper resistivity with RRR=100, B= 8 T.

### 3.4.c Conductivity

The conductivity of the cable in transverse direction (turn-to-turn) can be calculated according to the model described in 3.3. The radial and longitudinal thermal conductivity are mainly determined by the heat transferred along the strands, and the heat conducted through the contacts can be neglected.

In longitudinal direction the conductance ( $C_z$ ) is given by ( $\beta$  is the cable pitch angle)

$$C_z = k_{Cu} \frac{A_{Cu}}{\cos \beta \cdot l} = k_z \frac{A_{X section}}{l} \quad (\text{W/K}) \quad (3.34)$$

Therefore, the longitudinal conductivity  $k_z$  is

$$k_z = k_{Cu} \frac{A_{Cu}}{\cos \beta \cdot A_{X section}} \quad (\text{W/K/m}) \quad (3.35)$$

In the radial direction, a similar model can be applied. Equation (3.36) expresses the radial thermal conductivity  $k_x$  as a function of  $k_z$ :

$$k_x = k_z \cdot \text{tg}^2(\beta) \quad (\text{W/K/m}) \quad (3.36)$$

In the FE model described in chapter 4, where the bare cable and the external insulations are treated as different components, the conductivity is given by (3.35) (3.36) and (3.31). In the numerical code QLASA, the conductivity is used to calculate the quench propagation velocities, using the simple model described in 3.3.c, for the transverse conductivity in transverse and radial directions, just by changing the cable geometrical factors [2.20].

### 3.5 Thermo-mechanical properties

The Young modulus, the Poisson ratio, and the integrated thermal contraction, from  $T = 300$  K to  $T = 4.2$  K, of the epoxy impregnated ten-stack of insulated  $\text{Nb}_3\text{Sn}$  cable was studied at Fermilab as part of the high field magnet R&D program. These properties are not only essential to design a mechanical structure that complies with the coil mechanical properties during assembly, cooling, and excitation, but also for maintaining a precise coil geometry, which is essential for high field quality, and to estimate the stress redistributions during quench. In the context of quench protection, however, the mechanical properties of the coil are related to the thermal properties when estimating the thermo-mechanical stresses induced in the coils during the fast heating during the quench. The main thermo-mechanical properties relevant for this thesis work are reported in this chapter.

#### 3.5.a Elasticity modulus

Elasticity moduli of  $\text{Nb}_3\text{Sn}$  cable stacks with different cable and insulation characteristics were measured at Fermilab. We report here measurements performed with a biaxial fixture (Fig. 3.19).

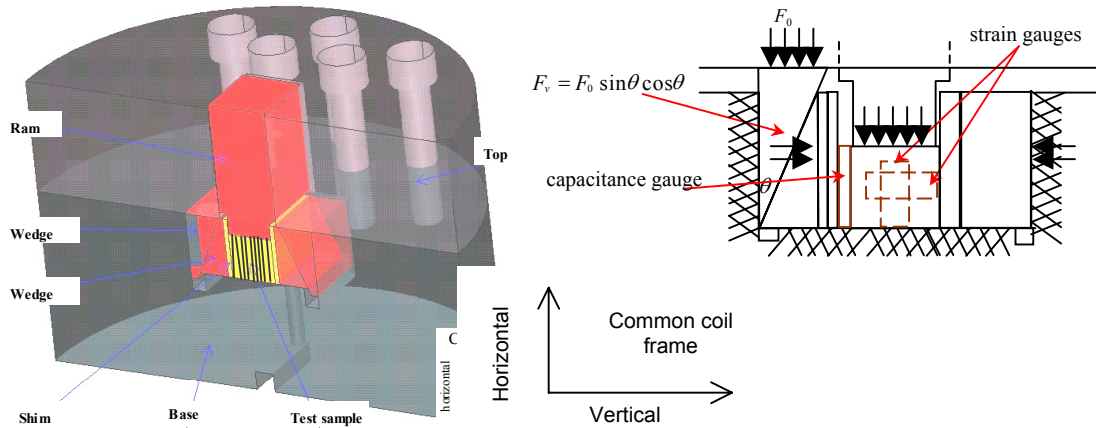


Fig. 3.19: Drawing of the test fixture. The test sample can be pre-stressed in the horizontal direction of the fixture (transverse direction for the sample – common coil magnet frame) while in the vertical direction the load can be varied (horizontal direction for the sample - common coil magnet frame) with a hydraulic pressure piston.



The calibration of the fixture, and the measurement procedure are described in detail in [3.40]. Note that before the measurements, a “massaging” sequence is performed in order to “train” the sample-and-gauge composite to respond consistently to the applied load. This massage sequence consisted of 5 cycles of loading and unloading the sample between zero and maximum load. The measured samples are listed in Table 3.6.

Sample	strand/cable	insulation	remark
Kapton wrap	ITER – reacted, 0.7 mm diameter, 41 strands (9-stack), flat	1 x 50 % + 1 butt-lap wrap of 2 mils Kapton tape = 6 mils Kapton	Samples made 2 years ago at start of the program
Cos $\theta$ standard	ITER – reacted, 1mm diameter, 28 strands (Cos $\theta$ cable), keystone	1 x 50 % overlap wrap of 125 $\mu$ m ceramic tape = 250 $\mu$ m Ceramic	Reference sample to compare with data for cos $\theta$ magnet [3.42]
Kapton sheet	OST – reacted, 0.7 mm diameter, 41 strands (racetrack 2 cable), flat	8 mils Kapton sheet	Test insulation schemes for common coil magnet
Kapton+E-glass	OST – reacted, 0.7 mm diameter, 41 strands (racetrack 2 cable), flat	5 mils Kapton sheet + 7 mils E-glass sheet	Test insulation schemes for common coil magnet
E-glass	OST – reacted, 0.7 mm diameter, 41 strands (racetrack 2 cable), flat	7 mils E-glass sheet	Test insulation schemes for common coil magnet

Table 3.6: Ten-stack measured with the bi-axial fixture. All samples were impregnated with CTD-101 epoxy and had approximately the same dimensions of 2 cm x 1.45 cm x 1.17 cm. The insulation thickness quoted here was measured without applied pressure. All stacks (except the first) were impregnated under a pressure of ~10 MPa.

The results of the 10-stack measurements are listed in Table 3.7. The measurement error associated with the modulus results is of the order of  $\pm 5$  GPa [3.40]. The uni-axial measurement of the sample for the cos $\theta$  agreed within this order with the previous measurements [3.42]. The vertical moduli of all other samples are relatively lower than reported in [3.42], which probably results from the larger insulator/metal ratio and different insulation schemes. The modulus of the Kapton wrap sample could not be measured because of systematic gauge breakage. These samples were impregnated under low pressure and therefore reveal a vertical modulus not much higher than that of epoxy.

Young's Modulus sample	Vertical Modulus (GPa)		Horizontal Modulus (GPa), constrained	
	300 K	4.2 K	300 K	4.2 K
Kapton old	<10	-	-	-
Cos- $\theta$ standard	35	-	-	-
Kapton sheet	14	-	-	-
Kapton E-glass	18	24	24	35
E-glass	20	25	-	-

Table 3.7: Ten-stack modulus measurement results. Vertical/Horizontal refer to the Common Coil magnet frame (see Fig. 3.). \* Calculated from a Poisson ratio of 0.33.

The results indicate that if the cable stack is impregnated under moderate pressure, the resulting modulus is about 22 GPa at 300 K, and 31 GPa at 4.2 K in longitudinal and horizontal-direction, and 18 GPa at 300 K, and 24 GPa at 4.2 K in vertical-direction.

The horizontal modulus appears to be softer (~30 GPa) than previously estimated on the basis of models (55 GPa at 4.2 K). This change had to be taken into account in the FE models of the racetrack and common coil magnets.

The measurement confirmed that the vertical modulus is sensitive to the insulation type and thickness. In addition, the measurement revealed that the modulus is also very sensitive to the amount of pressure applied during impregnation. These are the conditions chosen for the racetrack and common coil magnets (to prevent damage of the reacted conductor).

Furthermore, since massaging procedures are not foreseen for the wind-and-react magnets, the coils might be even softer in the actual magnets.

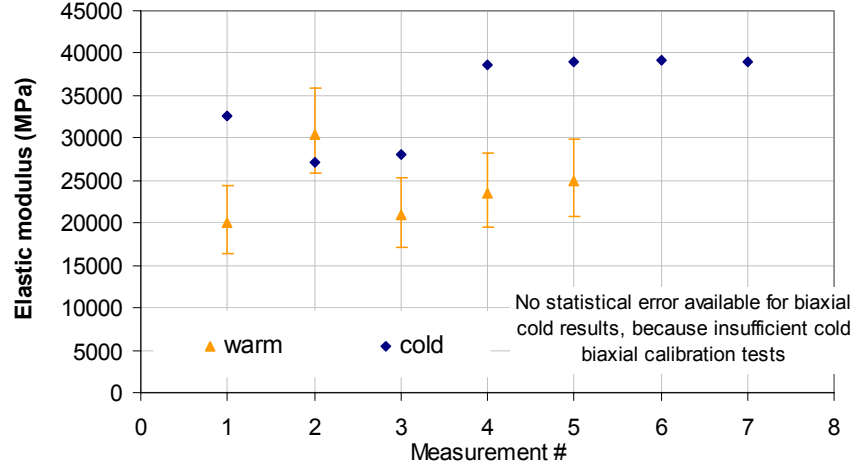


Fig. 3.19: Horizontal modulus distribution for Kapton+E-glass sample measured with bi-axial loading.

### 3.5.b Thermal contraction

Measurements of the integrated thermal contraction of Nb<sub>3</sub>Sn insulated cable stacks from 293 K to 77 K and to 4.2 K were performed at Fermilab. The technique, described in detail in [3.41], is based on the use of calibrated strain gauges. Measurements reported here were published in [3.42, 3.19].

A temperature change  $\Delta T$  induces a resistance change  $\Delta R$  in a strain gauge, due to

1. a change in the resistivity of the grid material, proportional to the gauge factor  $\beta_G$ ;
2. a difference in the thermal contraction coefficients between the sample and the grid,  $\alpha_S$  and  $\alpha_G$  respectively. The relative resistance change of the gauge on a sample is given by the sum of these two effects:

$$\Delta R_S / R = [\beta_G + (\alpha_S - \alpha_G) \cdot F_G] \cdot \Delta T = \varepsilon_S \cdot F_G, \quad (3.37)$$

where  $F_G$  is the gauge factor, a proportionality factor between the apparent strain  $\varepsilon$ , and the relative resistance change. If the same type of gauge is installed on a standard reference material with a known thermal coefficient  $\alpha_R$ , then

$$\Delta R_R / R = [\beta_G + (\alpha_R - \alpha_G) \cdot F_G] \cdot \Delta T = \varepsilon_R \cdot F_G, \quad (3.38)$$

Subtracting the above two equations and rearranging, we get

$$(\alpha_S - \alpha_R) = (\varepsilon_S - \varepsilon_R) / \Delta T. \quad (3.39)$$

Knowing  $\alpha_R$ ,  $\varepsilon_S$  and  $\varepsilon_R$  for a particular change in temperature, we can compute  $\alpha_S$ , the integrated thermal contraction coefficient of the sample.

The thermal contraction was measured in all three directions: vertical/azimuthal, horizontal/radial, and longitudinal direction (along the cable), referring to the common coil/cos $\theta$  type magnet. The thermal contraction coefficients along horizontal and longitudinal directions are very similar [3.42]. Two different types of gauges (Gauge-1 and Gauge-2 in [3.41]) of the WK Series from Micro Measurements Group were installed in each direction, to check for repeatability and for gauge-type errors. Measurement results are reported in Table 3.8. The first sample of the Table 3.8 is sample #2 of Table 3.3. Two other ten-stacks were made using the same cable, but with different insulation.

Vertical (Azimuthal) Thermal Contraction				
Insulation Pattern	Sample #	Gauge - 1	Gauge - 2	Average
Kapton + E-glass	2*	4.262	4.045	4.154
Kapton (0.2 mm)	6	4.419	4.606	4.513
E-glass (0.18 mm)	7	3.646	3.77	3.708
Ceramic-fibers	4*			3.22
Horizontal (Radial) Thermal Contraction				
Insulation Pattern	Sample #	Gauge - 1	Gauge - 2	Average
Kapton + E-glass	2*	3.000	2.966	2.983
Kapton (0.2 mm)	6	2.808	2.904	2.856
E-glass (0.18 mm)	7	2.970	2.996	2.983
Ceramic-fibers	4*			2.29

Table 3.8: Integrated thermal contraction data from 293 k to 77 k (mm/m). \* Samples 2 and 4 as in conductivity measurements (Table 3.3).

The readings of the two gauges were consistent. To confirm the technique adopted, one of the types of gauges used on the ten-stacks was used on a copper and a stainless steel sample, and the measured data were compared with published values. The measured integrated thermal coefficient (from 293 K to 77 K) of 304 stainless steel and copper samples, are 2.85 and 3.07 mm/m respectively, very close to the published values of 2.81 and 3.07 mm/m.

In the radial direction, as expected, the integrated thermal contraction coefficient does not depend on the insulation pattern. However, this value is higher than the previously measured value for the 28 strands, 1.0 mm diameter cos $\theta$  cable ( $\alpha_s = 2.29$  mm/m). In azimuthal direction, the integrated thermal contraction coefficient depends on the insulation pattern, varying from 3.2 to 4.5 mm/m. Measurements performed on similar cable stacks, insulated with quartz fibers, are within this range ( $\alpha = 3.9$  mm/m) [3.43].

### 3.6 Measurements of quench parameters

The effect of the material properties on quench parameters is difficult to predict, because of the composite nature of the materials involved, as we have seen in the case of thermo-mechanical properties of cable stacks. In addition, many other factors can affect quench parameters in a superconducting magnet, such as cooling and stress distribution, which may vary during operation and during the quench process. Therefore, measurements of quench velocities and quench heater delay time were performed on magnets built and tested at Fermilab.

The quench studies were performed in the current range of up to ~70 % of the expected short sample limit for the racetrack magnet (calculating the margin on the load line). The maximum current achieved during test of the racetrack magnet HFDB02 was 12675 A that is 78% of the short sample limit at 5.1 K (minimum temperature in the coil during 75 A/s ramp). The racetrack magnet HFDB02 is described in chapter 1 and [3.22].

### 3.6.a Quench velocities

The quench velocities in the simulations are critical parameters, because the rate of growth of the normal zone, and the final zone volume depends on them. The current decay is a strong function of the normal zone volume via the coil resistance.

To measure quench propagation velocities, the racetrack coils of HFDB02 were equipped with two spot heaters, one for each coil, with temperature sensors close to the spot heaters, and voltage taps across the spot heater regions. Since one voltage tap close to the spot heater of the top coil was damaged during fabrication, most of the studies were performed on the bottom coil. Few tests were also performed on the top coil and the results were found to be similar.

Quench velocity studies were performed measuring the “time of flight”, that is the time difference between the quench signals of two voltage taps at a known distance. First the velocities were calculated over the distance from the spot heater center to the closest voltage taps, in the two directions ( $v_{0R}$ : towards return end; and  $v_{0L}$ : towards lead end). These measurements are affected by uncertainty in the distance the quench traveled, because of the finite length of the spot heater (25 mm). Here we considered the distance from the center of the spot heater. In addition, the spot heater continues to heat the cable even after the quench start, which can significantly affect the resistance per length, in case the temperature rises above 20-30 K. To avoid the above-mentioned type of errors, the quench velocities were also measured with the time-of-flight method using voltage taps further away from the spot heater (labeled  $v_{1R}$  for return end; and  $v_{1L}$  for lead end). Finally, the transverse quench propagation (turn-to-turn), through the insulation, was measured when possible. The precision of the data analysis was affected by the inductive noise that arises when the quench starts. In fact, the lost voltage tap in the top coil jeopardized the possibility of reducing the noise by “bucking” the signal (that is subtracting the signal coming from voltage taps pairs in the same position in the two coils). This fact explains in part the large scattering of the results. The measured velocities are plotted in Fig. 3.20 vs. the reduced current, that is  $I/I_c(B(I_{magnet}))$ , where B is the peak field generated by the current  $I_{magnet}$ .

Fig. 3.20 also shows the quench velocities calculated with (2.12), with a correction factor of 1.5.

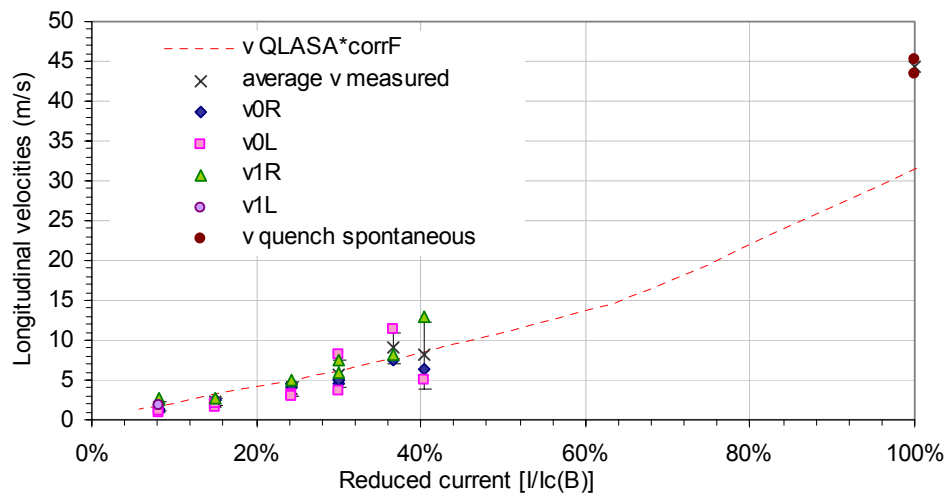


Fig. 3.20: Longitudinal quench propagation velocities vs. reduced current on the load line; bars represent standard deviation from the average measured velocity; dashed line represent velocities calculated with QLASA quench velocity routine (see 2.2.b).

The QLASA formula seems to underestimate the longitudinal quench propagation velocity by about 50 % up to 40 % of the critical current (which corresponds to 70% of the expected maximum current in the magnet). A factor 2 must be applied to simulate correctly the quench velocities close to the critical current.

The velocities calculated with the time of flight are also consistent with the velocities calculated utilizing the slope of the resistance rise.

The quench propagation velocity measured during spot heater tests were different from the velocity with which a “spontaneous” quench would propagate, because in this case, the voltage rise was much steeper. During spot heater tests an average  $dV/dt$  of about 14 V/s was measured, while during spontaneous quenches, voltage derivatives of 333 V/s were measured, for the single turn signal. The corresponding quench propagation velocities, in the case the quench is propagating in both directions is  $\sim 40$  m/s for the multi-turn signal, a voltage rise of two times 333 V/s was measured, indicating a quench propagating along two turns. These higher quench velocities might have been due to heating inside the magnet that raised the temperature above the bath temperature, in a large zone of the coil, where the quenches started. The heating source might have been the damage of the conductor in several points along the external turns, which caused the premature quenches in one of the coils. The spontaneous quenches were associated with a reduced current of 100% in Fig. 3.20.

Fig. 3.21 shows the transverse propagation time that is the time difference from the quench start in the spot heater segment and the quench start in the next turn. The data are also compared with the values calculated with (2.13), with a correction factor of one.

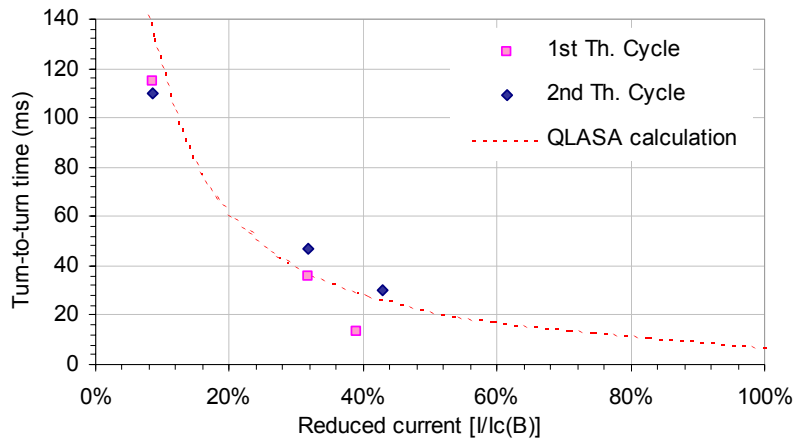


Fig. 3.21: Transverse quench propagation times vs. reduced current on the load line; squares refer to measurements taken during first thermal cycle, diamonds during the second thermal cycle, and dashed line QLASA quench velocity routine (see 2.2.b).

### 3.6.b Experimental quench heater study

Here we present the main results of the quench heater studies performed on the racetrack magnet HFDB02, at Fermilab [3.22], and on the  $\cos\theta$  type models HFDA02.

The quench heaters of HFDB02 consisted of four stainless steel strips: two strips for each coil, connected in series. The strips were glued on a 3 mil Kapton foil; another 3 mil Kapton foil, was put on the coil, with additional 5 mil adhesive Kapton strips with gaps for epoxy flow. The total coil-to-heater insulation therefore was a 0.3 mm-thick Kapton layer [3.44].

The quench heater for the bottom coil was placed on the inner side of the coil, close to the G10 middle plate. The heater is therefore close to the high field region. The quench heater for the top coil is placed on the outer side of the coil, close to stainless steel external structure,

and, therefore, in a low field region. On the other hand, when the magnet is excited, the Lorentz forces exert a pressure on the external heater that improves the thermal contact, and therefore the heater efficiency. This asymmetric position of the heaters allowed us to determine the outcome of the combined effect of magnetic field and pressure on the efficiency of the heaters, according to the different position. These measurements are especially important for the quench protection of the common coil magnet, given the similarities between the two cases. The two couples of heater strips for each layer were connected in series (Fig. 3. 22). Different electrical connection schemes between the heaters of each layer were used, a series and a parallel connection.

Measurements of minimum voltage and heater delay times were performed also for the  $\cos\theta$  type magnets. Different connection schemes were also tested (see Fig. 3.23 and [3.45]). The insulation cable-to-heater, in HFDA02 was a 0.4 mm-thick impregnated ceramic cloth (Fig. 2.6).

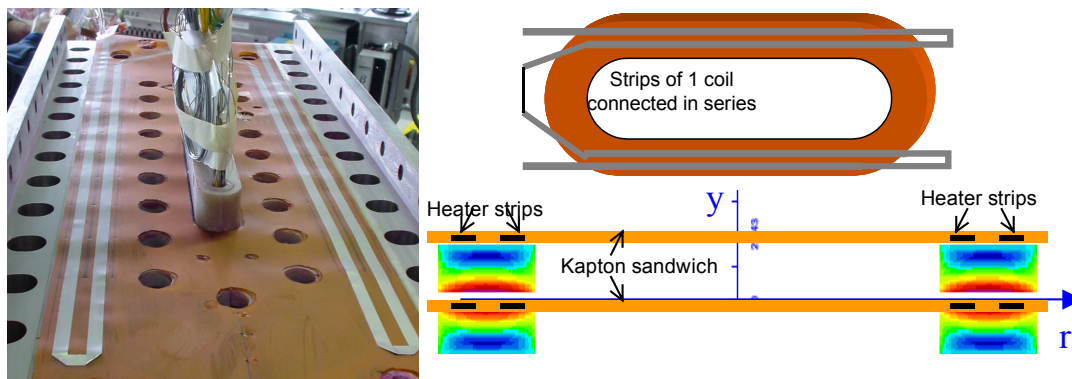


Fig. 3.22: Quench heaters on the top coil of the racetrack magnet HFDB02, and quench heater layers position on the racetrack coils. Note the asymmetry respect to the “bore”.

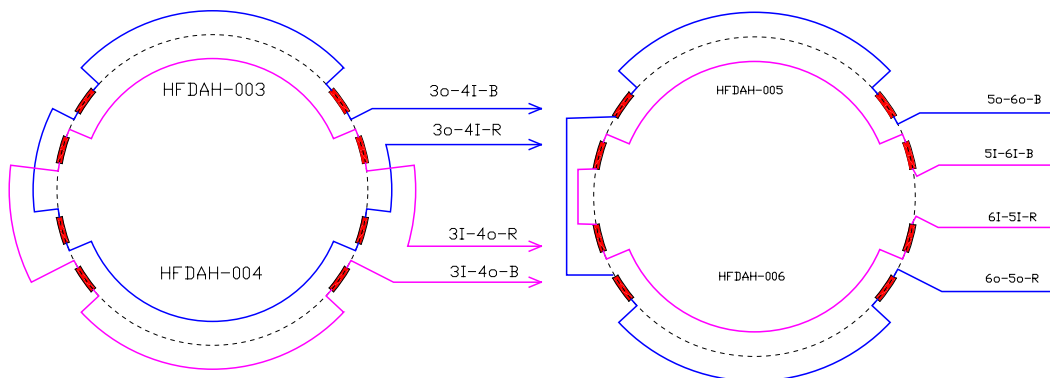


Fig. 3.23: Quench heaters wiring scheme for  $\cos\theta$  magnets HFDA02.

The collected data are reported in [3.45] and shown in Fig.3-24 and Fig. 3.35. Fig. 3.24 shows the heater delay time at different magnet currents and for different heater connection schemes, resulting in different heating rates per heater surface area. The heater delay time is measured from the heater firing to the first start of the quench. Therefore, it does not include the quench detection time.

We can see that, as in Fig. 2.24, the heater delay time decreases steeply with the power per area, below  $\sim 10 \text{ W/cm}^2$ , and becomes less sensitive for larger power.

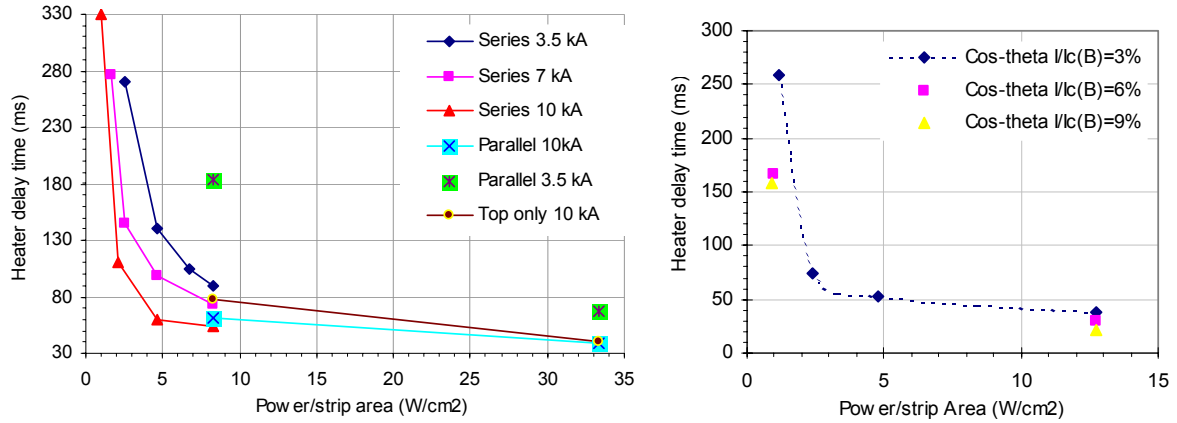


Fig. 3.24: heater time delay vs. power per strip area performed at 4.5 K for different electrical connections of the heaters for racetrack magnet HFDB02 (left). Quench heater delay time vs. power per area over the strip heaters for cosθ magnet HFDA02 (right)

Summarizing the quench heaters test results for the racetrack magnet:

- The minimum delay time of about 40 ms was reached at 10 kA / 33 W/cm<sup>2</sup> ( $I/I_c = 60\%$ ). This power per area of 33 W/cm<sup>2</sup> was possible with the parallel connection or with the top heater only, given the energy stored in the heater power supply.
- With series and parallel connections, the quench started first in the bottom coil (high field region).
- With the top coil heater only (low field region), the heater delay time was ~20 ms more than with both active heaters, at the same power per strip, at low power.
- At high power per strip, the time delay for bottom and top coil was at the same level.

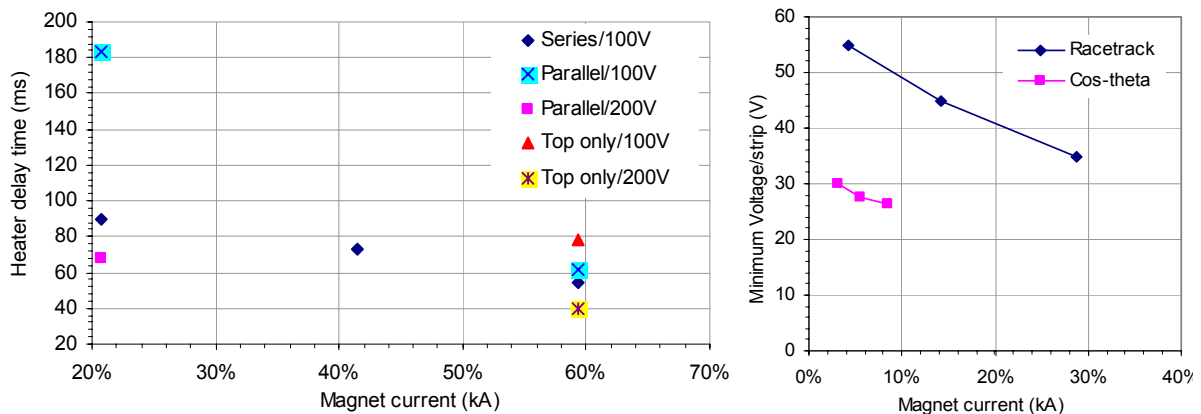


Fig. 3.25: Time delay study Quench heater delay time vs. power per area over the strip heaters for cosθ magnet HFDA02, and minimum voltage per strip vs.  $I/I_c(B(I))$ , compared with racetrack HFDB02 heaters.

The minimum heater delay time achieved in HFDA02 was 27 ms, at 7000 A, which is 9 % when calculated over the load line of the critical current calculated at an average field in the outer layer at the given current (corresponding to 40% of the expected short sample current). The low field in the outer layer explains this low reduced current.

Therefore, we can conclude from these measurements that the heater delay time of 40 ms, as suggested for the VLHC magnets quench protection, is feasible. Fig. 3.25-right shows the minimum voltage per heater strip for the cosθ and the racetrack magnet. The comparison shows that racetrack heaters are less efficient, because a higher power per area is required to attain the same heater time delays. Taking into account that the insulation layer between

heaters and conductor is 0.4 mm in the  $\cos\theta$  magnet, and 0.3 mm in the racetrack magnet, the difference in heater delay time might be attributed to the difference in diffusivity of Kapton and impregnated ceramic fibers. Other factors can contribute to the time delay of the heaters, such as pressure during impregnation and pressure during magnet excitation.

## References

- 
- [3.1] Y.B. Kim, C.F. Hempstead, A.R. Strnad, *Phys. Rev. Lett.*, V. 129, p. 528, '63
  - [3.2] C.P. Bean, *Phys. Rev. Lett.*, Vol. 8 p. 250, 1962
  - [3.3] E.J. Kramer, *J. Appl. Phys.*, Vol. 44, p. 1360, 1973
  - [3.4] J. McDonald, M. Barzi, "A Model for  $J_c$  in Granular A-15 Superconductors," *IEEE Trans. Appl. Supercond.*, Vol. 11/1, March 2001
  - [3.5] W.A. Fietz, W.W. Webb, *Phys. Rev.*, Vol. 178-2, p. 657, 1969
  - [3.6] D.P. Hampshire, H. Jones, and E.W.J. Mitchell, "An in-depth characterization of  $(\text{NbTa})_3\text{Sn}$  filamentary superconductor," *IEEE Trans. Mag.*, Vol 21, 289, '85.
  - [3.7] L.T. Summers, M.W. Guinan, J.R. Miller, P.A. Hahn, "A model for the prediction of  $\text{Nb}_3\text{Sn}$  critical current as a function of field, temperature, strain and radiation damage," *IEEE Trans. Mag.*, Vol 27-2, 2041, '91
  - [3.8] A. Godeke, B. ten Haken, H.J. ten Kate, "Scaling of the critical current in ITER type niobium-tin superconductors in relation to the applied field, temperature and uni-axial applied strain," *IEEE Trans. Appl. Supercond.*, Vol. 9, N. 2, June 1999
  - [3.9] A. Godeke, H.J.G. Krooshoop, H.G. Knoopers, B. ten Haken, H.J. ten Kate, "Experimental Verification of the Temperature and Strain Dependence of the Critical Properties in wires," *IEEE Trans. Appl. Supercond.*, Vol. 11, March 2001
  - [3.10] A. Martinez, J.L. Duchateau, "Field and temperature dependencies of critical current on industrial  $\text{Nb}_3\text{Sn}$  strands," *Cryogenics*, 37 ('97), pp. 865-875
  - [3.11] A. Den Ouden, *Ph.D. thesis*, Univ. of Twente
  - [3.12] J. Ekin, "Strain scaling law for flux pinning in practical superconductors. Part1: Basic relationship and application to  $\text{Nb}_3\text{Sn}$  conductors," *Cryogenics*, Nov.1980
  - [3.13] B. Ten Haken, A. Godeke, H.H.J. ten Kate, "The strain dependence of the critical properties of  $\text{Nb}_3\text{Sn}$  conductors," *Journal of Applied Phys.* Vol. 85, N. 6, '99
  - [3.14] N. Mitchell, "Analysis of the effect of  $\text{Nb}_3\text{Sn}$  strand bending on CICC superconductor performance," *Cryogenics*, Vol. 42, pp. 311-325, 2002
  - [3.15] J.M. van Oort, "Critical current degradation in  $\text{Nb}_3\text{Sn}$  superconductors in accelerator magnets," *Ph.D. Thesis*, Univ. of Twente, Netherlands, 2000
  - [3.16] D.R. Dietderich, R.M. Scanlan, R.P. Walsh, J.R. Miller, "Critical Current of Superconducting Rutherford Cable in High Magnetic Fields with Transverse Pressure," *IEEE Trans. Appl. Supercond.*, Vol. 9, N. 2, June 1999
  - [3.17] P. Bauer et al., "Fabrication and Testing of Rutherford-type Cables for React and Wind Accelerator Magnets," *IEEE Trans. Appl. Supercond.*, Vol. 11/1, March 2001
  - [3.18] V. Zlobin et al. "Conceptual Design Study of  $\text{Nb}_3\text{Sn}$  Low-Beta Quadrupoles for 2nd Generation LHC IRs", *IEEE Trans. Appl. Supercond.*, June 2003, proceedings of ASC02
  - [3.19] L. Imbasciati, G. Volpini, et al., "Thermo-Mechanical Characterization of Insulated and Epoxy-Impregnated  $\text{Nb}_3\text{Sn}$  Composites," *IEEE Trans. Appl. Supercond.*, June 2003, proceedings of ASC02



- 
- [3.20] D. R. Chichili et al., "Fabrication and testing of High Field Dipole Mechanical Model," *proceedings of MT-16*, Tallahassee, FL, 1999
  - [3.21] G. Ambrosio et al., "Study of insulating materials for HFDB-02 Racetrack Magnet using Nb<sub>3</sub>Sn and the react-and-wind technology," Fermilab TD note, TD-02-08, March 2002
  - [3.22] G. Ambrosio, et al., "Fabrication and Test of a Racetrack Magnet Using Pre-Reacted Nb<sub>3</sub>Sn Cable," *IEEE Trans. Appl. Supercond.*, June 2003, proceedings of ASC02
  - [3.23] M. Barzi et al., "Development and study of Rutherford-type Cables for Accelerators Magnets at Fermilab," *IEEE Trans. Appl. Supercond.*, June 2003, proceedings of ASC02
  - [3.24] F. Broggi, S. Piuri, L. Rossi, "An apparatus for thermal conductivity measurements at cryogenic temperature on coil blocks," INFN/TC-93/01, '3
  - [3.25] Cryocomp v 2.0, Eckels Engineering and Cryodata Inc., normal to cloth G10 properties
  - [3.26] Measurements at CERN, private communication
  - [3.27] F. Rondeaux, Ph. Bredy, J.M. Rey, CEA Saclay, "Thermal Conductivity Measurements of Epoxy Systems at Low Temperature," *Advances in Cryogenic Engineering Materials*, Vol. 48A, p.197
  - [3.28] M. Damasceni, L. Rossi, S. Visona, "Measurements at cryogenic Temperature of the Thermal Conductivity of the ground Insulation of a Model of the ATLAS BT coils," Techn. Rep. LASA/ATLAS/510, 1998
  - [3.29] MATPRO, electronic library of QLASA; copper conductivity calculated by F.M. Ametrano, F. Broggi
  - [3.30] MATPRO, electronic library of QLASA; Nb<sub>3</sub>Sn thermal conductivity from H.A. Brechna, *Supercond. Magnet Systems*, Springer Verlag, p. 424
  - [3.31] L. J. Salerno and P. Kittel, *Handbook of cryogenics*, Chapter 3, pp. 167, ...
  - [3.32] M. J. Nilles and S. W. Van Sciver, "Effects Of Oxidation And Roughness On Cu Contact Resistance From 4 K To 290 K", *Adv. in Cryog. Eng. Mat.*, V.34
  - [3.33] J-M. Depond, D. Leroy, L. Oberli, "superconducting cable topology," CERN-LHC Internal Note 97-09, LHC-MMS
  - [3.34] L. Imbasciati, G. Ambrosio, P. Bauer, D. Pedrini, V. Previstali, L. Rossi, G. Volpini, "Thermal Conductivity Measurements of Impregnated Nb<sub>3</sub>Sn Cable Stacks," Fermilab Technical Division Note TD-03-19, Apr. 2003
  - [3.35] B. Kaspar, G. Ambrosio, P. Bauer, L. Imbasciati, "Contact Resistance Measurement in Nb<sub>3</sub>Sn Rutherford Type Cables," Fermilab Technical Division Note, TD-02-39, Nov. 2002
  - [3.36] MATPRO, electronic library for material properties, used in QLASA program, courtesy of L. Rossi
  - [3.37] Smithells *Metals Reference Book*, 7th edition, Brandes and Brook
  - [3.38] S.S. Kozub, Y.V. Shpakovich, A.V. Zlobin, "Thermal Conductivity and Electric Resistance of Composite Wires," *Cryogenics*, V. 32, ICEC supplement, pp. 295-299
  - [3.39] N.J.Simon, E.S. Drexler, R.P. Reed "properties of copper and copper alloys at cryogenics temperatures", NIST Monograph 77
  - [3.40] R. Conway, G. Ambrosio, P. Bauer, D.R. Chichili, L. Elementi, J.-M. Rey, "Calibration of Fixture for Bi-axial Loading of Epoxy Impregnated Nb<sub>3</sub>Sn Cable Ten-Stack, using Epoxy, G10, and Aluminum Samples," Fermilab Technical Division Note TD-01-077, Dec. 01
  - [3.41] MICRO MEASUREMENTS GROUP, Strain Gage Technology: Thermal Expansion Measurement, Tech. Rep. TN-513

- 
- [3.42] D.R. Chichili, T.T. Arkan, J.P. Ozelis, I. Terechkine, "Investigation of cable insulation and thermo-mechanical properties of Nb<sub>3</sub>Sn composite," *IEEE Trans. Appl. Supercond.*, Vol. 10, N. 1, p. 1317-1320, 2000
  - [3.43] M. Reytier et al., "Characterization of the Thermo-Mechanical Behavior of Insulated Cable Stacks Representative of Accelerator Magnet Coils", *IEEE Trans. Appl. Supercond.*, Vol. 11, N. 1, 2001
  - [3.44] G. Ambrosio, N. Andreev, S. Bhashyam, I. Novitski, "HFDB-02 "2<sup>nd</sup> Racetrack" production report," Fermilab Technical Division Note TD-02-032, Aug. '02
  - [3.45] S. Feher, G. Ambrosio, P. Bauer, L. Imbasciati, J. Tompkins, A.V. Zlobin, "HFDB-02 '2<sup>nd</sup> Racetrack' Test Report," Fermilab Technical Division Note TD-02-33, July 2002

## 4. Quench experiment on cables

Chapter 4 Table of Contents:	Page
4. Quench experiment on cables	1
4.1 Cable quench experiment	2
4.1.a Measurement Set-Up	2
4.1.b Measurement results	6
4.2 Adiabatic quench process simulation	10
4.3 Finite element quench process simulation	11
4.1.c Finite element models	12
4.1.d Results and Comparison with the experiment	20
4.4 Mechanical analysis	26
4.1.a Analytical estimate	27
References	32

## 4.1 Cable quench experiment

As discussed in chapter 2 the study of quench protection issues in Nb<sub>3</sub>Sn magnets has raised the question of what peak temperatures can be tolerated before irreversible damage occurs in the brittle Nb<sub>3</sub>Sn. A series of measurements was conducted on Nb<sub>3</sub>Sn cable samples, in a setting similar to that of critical current measurements, to obtain a first answer. The basic measurement principle was to use heater induced quenches to heat the cables up to a chosen temperature, and to use subsequent measurements of the cable critical current, as a measure of the damage in the superconductor. To achieve the desired temperature, the current in the sample was not switched off immediately, as during critical current measurements, but maintained at the initial high level for a pre-defined time delay. The current in the normal-conducting matrix generated a well-defined amount of heating of the cable. Since the process is very fast (<0.5 sec), the metallic structure encasing the samples (i.e. the sample holder) remains at a lower temperature, inducing the sought thermo-mechanical stress. This process was repeated with increasing switch time delays, to increase the maximum temperature. Repeated measurements of the cable critical current after every excursion to high temperature allowed assessing the critical current degradation as a function of the peak temperature during a quench. The series of experiments described here followed the following experimental procedure:

- Critical current measurement at  $B = 8 \text{ T}$
- Current ramp to a constant current below the critical current
- Quench initiation with a spot heater
- PS ramps current to zero after a programmed delay time
- Analysis of the voltage data to estimate temperatures reached in the cable
- Critical current measurement.

This sequence was repeated, increasing the delay time in steps of 50 ms, until peak temperatures of the order of 400-500 K were reached.

A detailed report of the measurement can be found in [4.1]. The results of this test were also published in [4.2].

### 4.1.a Measurement Set-Up

The experiments were conducted at the conductor characterization facility at the National High Magnetic Field Laboratory (NHMFL) [4.3,4], which was used before for critical current measurements for Fermilab's react & wind Nb<sub>3</sub>Sn conductor study [4.5]. The test-station was originally designed for testing the effect of strain on the  $I_c$  of strands and cable-in-conduit samples, for the 45 T hybrid magnet, which was built and operates at NHMFL.

#### *Magnet*

The test facility at NHMFL consists of a 12 T split solenoid with a radial access port for the sample (Fig. 4.1). The high field region is about 15 cm long (the diameter of the solenoid bore), located approximately in the middle of the sample holder. The field drops sharply at the edge of the solenoid bore.

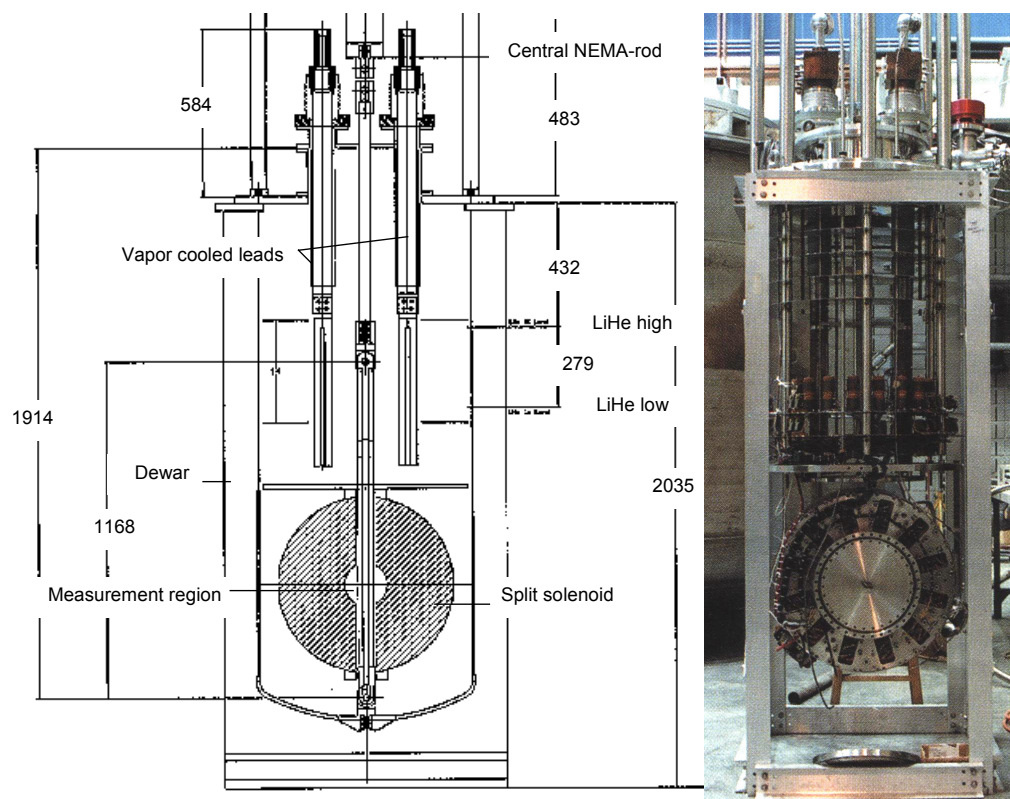


Fig. 4.1: The 12 T split solenoid, schematic and picture.

A pressure piston, acting through the bore of the magnet, gives the sample mechanical support and allows the application of transverse pressure on the sample in the high field region. In this test-series, the pressure system was used only to support the sample against the Lorentz forces (applying  $\sim 20$  MPa). Fig. 4.2 shows a sketch of the magnet and the sample clamping system.

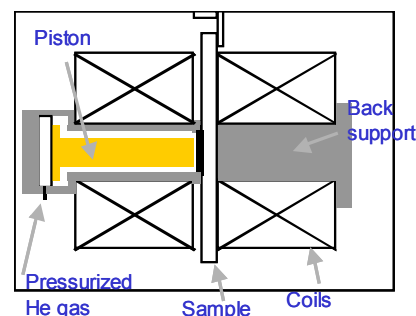


Fig. 4.2: Schematic of the magnet and the pressure piston supporting the sample against Lorentz-forces.

### Sample holder

The cable holder consists of a stainless steel "U" channel base containing two insulated  $\text{Nb}_3\text{Sn}$  cables (Fig. 4.4) [4.6]. The cables are spliced together in a copper case at the lower end to provide a continuous current path, and are soldered to copper bus plates at the upper end where the connections to the test system current leads are made. Fig. 4.3 shows the sample holder ready for testing with the characteristic "cold fingers" that allow operating the  $\text{NbTi}$  current leads above the liquid helium level.



Fig. 4.3: Leads connected to the cable sample holder prior to testing.

Additional insulated Nb<sub>3</sub>Sn cables, that are not electrically part of the circuit, are placed above and below the Nb<sub>3</sub>Sn cable pair under test to replicate the coil environment. The cable samples are vacuum impregnated with epoxy in situ, as in the magnet. Voltage taps are soldered to the samples, to the left and right of the high field region (20 cm spacing), to measure the critical current and the peak temperature via the resistance. Spot heaters are glued to the cables in the middle of the high field region to induce the quench.

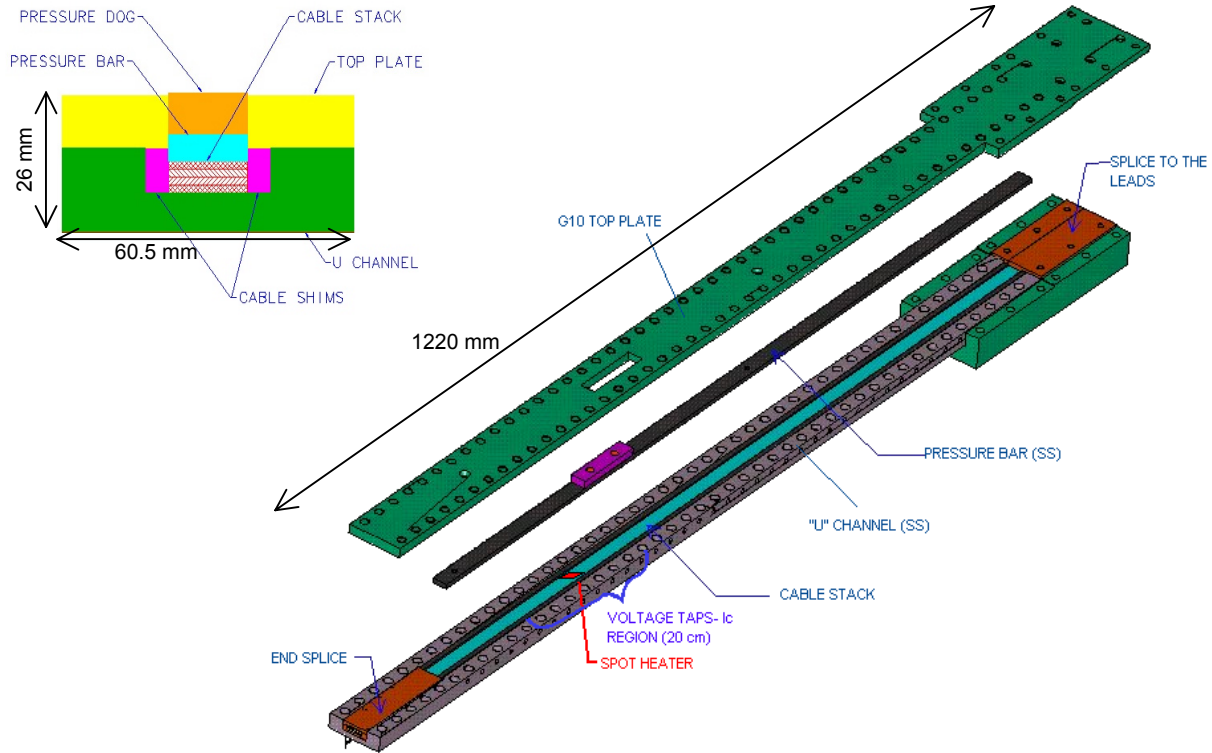


Fig. 4.4: Drawing of the cable sample holder: cross section (on top) and assembly.

### Samples

The samples tested in these measurements were ITER-type Nb<sub>3</sub>Sn/Cu cables, produced by IGC (Table 4.1). The cables were reacted at 600°C for 250 hrs.

Cable type	Flat, Rutherford
Strand diameter	0.7 mm
Number of strands in cable	41
Cu/non-Cu ratio	1.42
Packing factor	87 %
Length	1 m
Insulation thickness	~0.1 mm
Bronze fraction in non-Cu part	35 %
Critical current at 8 T, 4.5 K	~ 8000 A

Table 4.1: Strand parameters.

The insulation consisted of a 0.1 mm thick fiber-glass (E-glass) sleeve, which was glued to the cable with a matrix. The actual insulation thickness after curing was 0.15 mm. Additional 0.3 mm Kapton tape was placed on the cable, close to the spot heater, to avoid discontinuity in the high field region, where the pressure is applied.

Fig. 4.5 shows the cross section of a reacted strand. The measured total area and the non-copper area of the strand are indicated. The bronze cross sectional area inside and in between every sub-element was also measured.

Table 4.2 contains the list of samples that were tested in this measurement series. Samples 1a and 1b, measured in sample holder 1, were reacted straight. Samples 2a and 2b, measured in sample holder 2, were reacted in the bent state (on a spool with 290 mm diameter) and straightened before measurement to induce a bending strain (of 0.18 %). All samples had no core. Critical current measurements of sample 2b indicated that the cable was damaged during preparation.

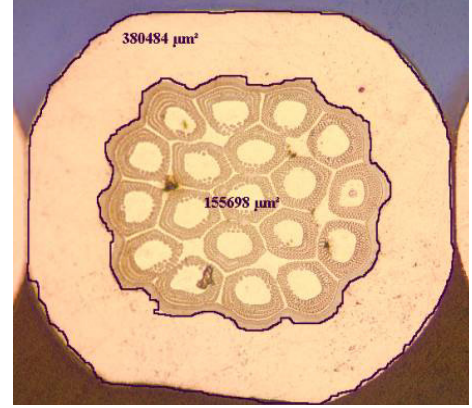


Fig. 4.5: Cross section of a reacted strand. Indicated are the total area and the non-copper area.

#	SH	Characteristics	Comment
1a	1	0.7 mm ITER strand cable, without core, reacted straight	OK
1b	1	0.7 mm ITER strand cable, without core, reacted straight	OK
2a	2	0.7 mm ITER strand cable, without core, reacted bent	OK
2b	2	0.7 mm ITER strand cable, without core, reacted bent	Damage?

Table 4.2: Samples tested for the quench study.

### Power supply

Fig. 4.6 shows a sketch of the sample power supply network. It should be noted that the DCCT read the total bus-current. To obtain the actual current in the sample, the current through the parallel protection resistor ( $R_D=22.3\text{ m}\Omega$ ) had to be subtracted from the total power supply current. The power-supply voltage limit was 50 V. The spot heaters were connected to a manually ramped DC current supply.

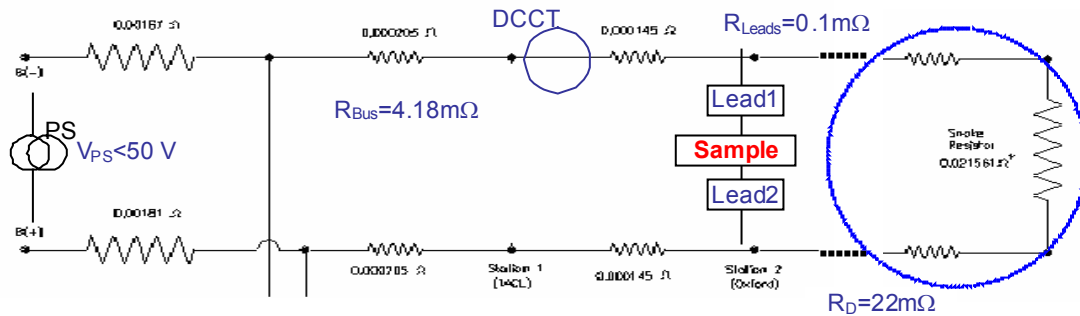


Fig. 4.6: Sketch of sample powering system in the NHMFL cable test facility

### Quench detection system

The quench detection was performed using a 4-channel quench detection unit, with variable detection threshold voltage ( $0.5\text{ mV} \div 7\text{ V}$ ). Voltage taps, covering the high field region ( $I_c$  taps), and the two branches of the sample between the splices, were connected to the quench detection

unit. When a quench was detected, the signal from the quench detection unit was intercepted by an analog RC circuit, which delayed the signal to trigger the power supply ramp-down, for a programmable duration. The delays were varied between 50 ms and 0.5 s.

#### *Data acquisition system*

Critical current measurements were performed using the slow (1-2 Hz), but highly filtered, data acquisition system, using a Labview based acquisition software in conjunction with Keithley Nanovoltmeters (linked via GPIB).

For the quench tests a fast data acquisition system (1 kHz), based on a 16-bit AD converter card with a voltage resolution of  $\sim 0.3$  mV (in the  $\pm 10$  V range) was used. Since the data acquired with this system were not filtered, the noise level, with activated power supply, was  $\pm 2$  mV. This noise level was sufficiently low for measurements of 2-10 V signals, as during quench tests (see Fig. 4.7).

### **4.1.b Measurement results**

#### - Data analysis description

In this paragraph, a quench test is described in detail to exemplify the data analysis method. The test described was performed on sample 2, at 7.5 kA, with a programmed delay time of 300 ms. The voltage signal nomenclature is given in Table 4.3.

Name	Description: Voltage between taps ...	Length between taps
Totloop	... covering entire sample loop incl. splices to leads	$\sim 2$ m
Toplc	... high field region of top sample (a)	0.2 m
Botlc	... high field region of bottom sample (b)	0.2 m
Tottop	... over the whole top sample (a)	$\sim 1$ m
Totbot	... over the whole bottom sample (b)	$\sim 1$ m

Table 4.3: Voltage tap nomenclature description.

As shown in Fig. 4.7, the quench starts in the bottom sample at  $t = 115$  ms. The voltage rises almost linearly in the first 20 ms, and then reaches a plateau before continuing to increase steeply shortly thereafter. The initial rise of the voltage corresponds to the quench propagation in the high field region, from the spot heater towards the voltage taps in both directions. When the entire high field region is driven normal, the voltage stays more or less flat because the resistivity function is almost flat at low temperatures. Above 20-30 K, the voltage slope starts to increase fast again, until the current starts ramping down, after the pre-defined delay. During the whole quench duration, the current in the sample remains almost constant, decreasing only to  $\sim 7$  kA at  $t = 500$  ms (in fact, the current in the parallel protection resistor remained below 430 A).

At  $t = 150$  ms, the voltage signal of the top sample starts to increase also, indicating that the quench has now spread to the other sample via heat transfer through the insulation. From the zoom into the initial 100 ms following the quench (Fig. 4.7-right), the quench propagation time from one cable to the other, which corresponds to the turn-to-turn propagation time in a magnet, can be derived to be  $\sim 35$  ms.



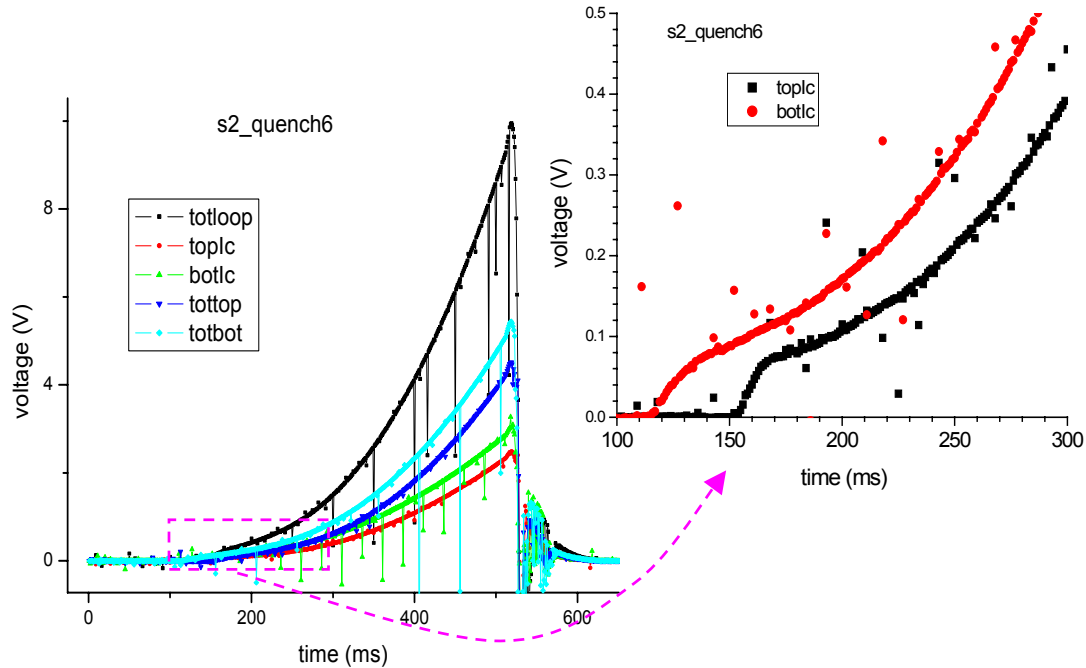


Fig. 4.7: Voltage signals and zoom into the signal at the quench beginning, for sample 2, at 7.5 kA.

From the same plot, the RRR of the conductor can be estimated from the voltage at the plateau, which corresponds to a resistivity of  $4.3 \cdot 10^{-10} \Omega \cdot \text{m}$  in the top sample, resulting in a RRR of  $\sim 140$  (taking into account the effect of the 8 T magnetic field, and assuming a resistivity of  $1.53 \cdot 10^{-10} \Omega \cdot \text{m}$  at 273 K). The RRR of the bottom sample was  $\sim 150$ , while the cables in sample holder 1 had a RRR of  $\sim 100$ .

To calculate the peak temperature, the measured resistance was compared to the conductor resistance as a function of temperature, calculated from tabulated material properties (chapter 3.4) and the conductor geometry (see Table 4.1). It sufficed to consider only the copper fraction, in order to match the room temperature resistivity value. The temperatures derived from the experimental data were compared to quench integral calculations, based on equation (2.7) and the material properties discussed in chapter 3.4. A summary of the main results of the experiment and the model are presented in Table 4.4 and Fig. 4.9.

#### - Summary of results

The major results of the cable quench tests were:

- The peak temperature (calculated via the resistivity) reached  $\sim 470$  K in the straight sample, and 310 K in the other
- There was no sign of critical current degradation up to 420 K, in the straight sample
- There was no sign of critical current degradation up to 300 K, in the bent sample
- The peak temperature estimated via the quench integral ( $T_{peak-MII}$  in the table) agreed with the temperature measured via the resistivity within 10-15%, after including 0.1 mm of insulation.

During the last critical current measurement of sample 1, after the 470 K temperature excursion, a premature quench occurred, at 8820 A, followed by a quench of the background magnet. It was therefore not possible to estimate the critical current value for the last temperature excursion.

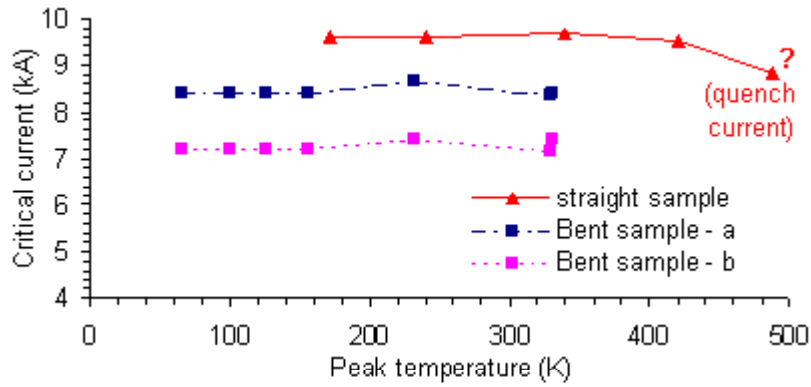


Fig. 4.8: Critical current vs. peak temperature.

Sample1_8T_8kA	1	2	3	4	5	6	7	Ave	$\sigma$
Programmed delay (ms)	100	100	150	200	250	300	350		
Measured delay (ms)	-	200	240	287	350	400	430		
$T_{\text{peak-V}}$ (exp) (K)	-	132	168	232	332	408	472		
$T_{\text{peak-MIIt}}$ (calc) (K)	-	102	140	200	300	400	480		
T difference MIIt-V (%)	-	-23	-17	-14	-10	-2	+2		
$I_c$ (A)	9800	-	9580	9600	9660	9500	>8820	9628	112
Sample2_8T_7.5kA	1 (7kA)	2	3	4	5	6	7	Ave	$\sigma$
Programmed delay (ms)	50	100	150	200	250	300	300		
Effective delay (ms)	140	200	240	284	344	400	405		
$T_{\text{peak-V}}$ (K)	68	100	124	156	224	312	312		
$T_{\text{peak-MIIt}}$ (K)	60	86	110	150	220	300	300		
T difference MIIt-V (%)	-12	-14	-11	-4	-2	-4	-4		
$I_{c\text{-top}}$ (A)	8400	8400	8400	8400	8650	8350	>8400	8433	108
$I_{c\text{-bottom}}$ (A)	7200	7200	7200	7200	7400	7150	7400	7250	104

Table 4.4: Main results of cable quench experiment.

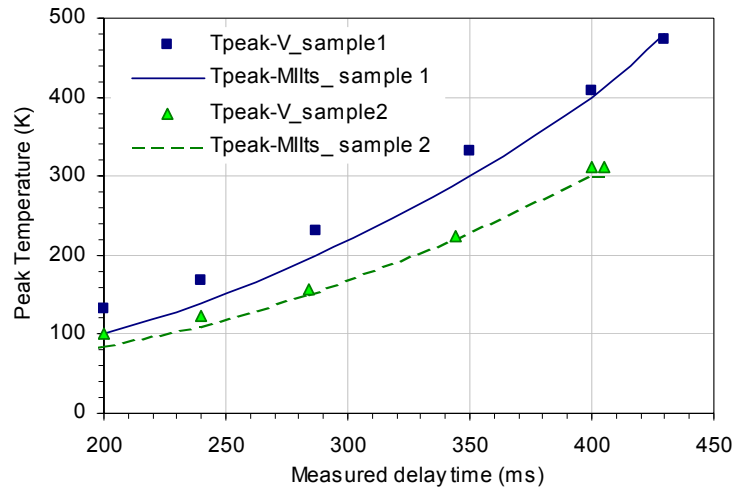


Fig. 4.9: Peak temperature vs. effective time delay. Continuous lines represent temperatures measured through the voltage data, and dotted lines represent temperatures computed from the quench integral.

### - Magnet quenches

Quenching of the background solenoid interrupted the quench test series for both samples. In the case of the first (straight) sample, the quench occurred just after the  $I_c$ -measurement, corresponding to the last point in Fig. 4.9 during which the temperature reached  $\sim 470$  K. The sample was then extracted from the magnet, and burnt black epoxy appeared on the outside of the sample holder (see Fig. 4.10). The traces of burning were located at the  $I_c$ -voltage taps. The insulation near the spot heater appeared to be intact. The G10-top plate also showed burn marks all along the sample holder. The burn marks could indicate that the steel case reached high temperatures. The peak power dissipated during the quench test in the 20 cm central region was  $\sim 42$  kW, which integrated over time, corresponds to an energy deposition of 5.2 kJ or 133 MJ/m<sup>3</sup>. If this energy was distributed over the entire sample-holder cross-section (in this 20 cm length segment, the peak temperature would be  $\sim 130$  K. The estimated sample to magnet heat transfer time, through  $\sim 1$  cm of stainless steel sample holder, is 4 to 20 seconds in the temperature range of 4 to 100 K. Therefore the quench process duration (maximum 400 ms) was smaller than the heat diffusion time, such that the sample-holder remains colder than the sample creating the sought compression of the cables. On the other hand, the estimated peak temperature in the sample holder of 130 K was well below the glass transition of the epoxy and, therefore, cannot explain the burn marks on the G10 top plate. In addition, the insulation damage appeared in the regions left and right from the spot-heater, where the temperature gradients were highest. That hints towards an insulation failure, due to temperature gradient induced shear stress together with high temperatures, leading to an electrical short.

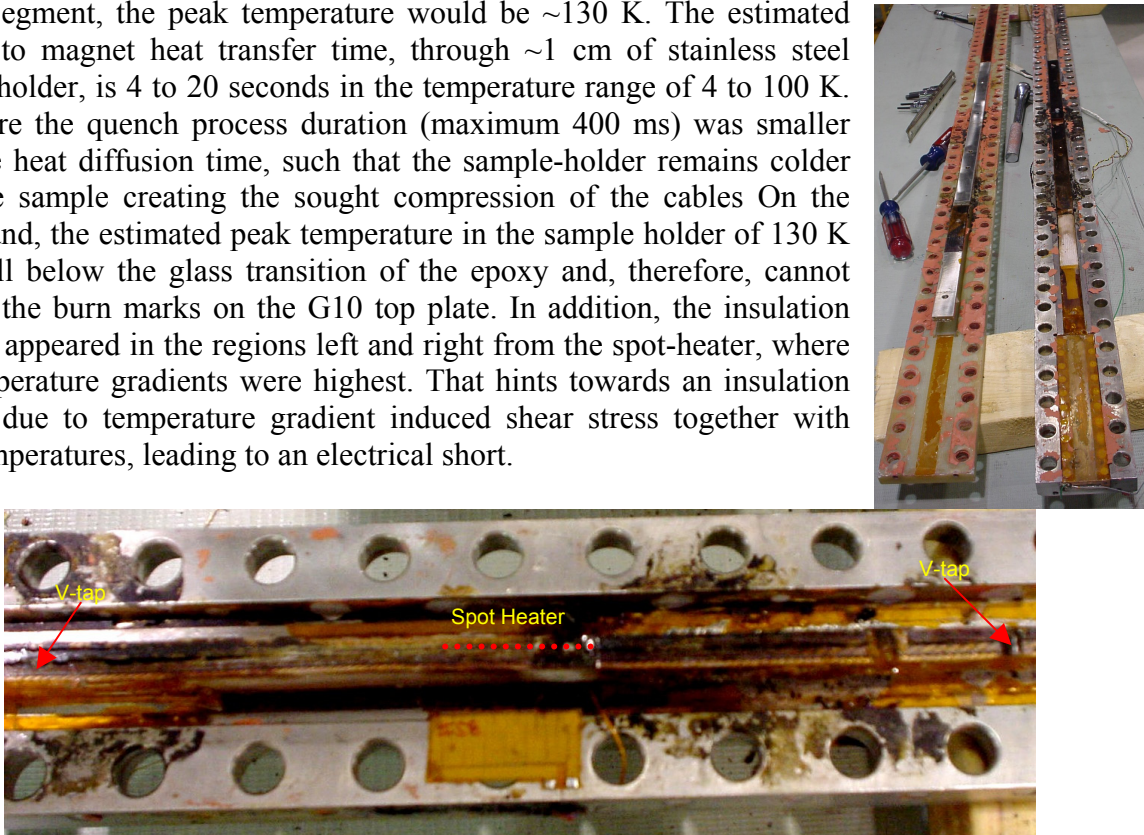


Fig. 4.10: Sample 1 after the quench tests.

It is also possible that mechanical movement of the sample caused the magnet quenches. The estimated mechanical moment on the sample in a perpendicular magnetic field of 8 T, is  $\sim 20$  N·m. The force applied at the edge of the sample holder ( $d = 3$  cm) against the pressure piston is  $\sim 600$  N. This considerable force is applied slowly as the current ramps up, and is suddenly released during the fast current ramp down during the quench. This fast movement can be transferred to the magnet through the piston housing. There are, therefore, several indications that the quench in the sample 1 following the 470 K temperature excursion was not related to conductor damage, but to thermal, electrical or mechanical problems.

## 4.2 Adiabatic quench process simulation

A numerical model was used to calculate the voltages and temperatures in the sample during a quench test based on the quench integral ( $QI$ ) calculation, as described in chapter 2.2.c (the model is very similar to Quenchpro). The material properties are as reported in chapter 3. A cable insulation thickness of 0.1 mm was included in the conductor cross-section for the quench integral calculation.

The electrical simulation of the quench assumed a quench starting at  $t = 0$  in the center of the high field region of one cable. The quench is then spread with a propagation velocity of 10 m/s over the whole high-field, center-region (and stops propagating thereafter). After 35 ms the quench propagates to the second cable. The resistance of the sample is calculated as the resistance of the normal region ( $< 0.3$  m) at peak temperature. The step function approximation of the temperature profile, with uniform high temperature in a 30 cm region, and bath temperature outside, resulted in a good estimate of the measured resistance of the sample, and of the current profile. The model included the effect of the protection resistor, in parallel to the sample, on the current in the sample. Fig. 4.11 and Fig. 4.12 show temperature, resistance, and current as a function of time during a quench at 7500 A, calculated with the model described above, and compared to the experimental results.

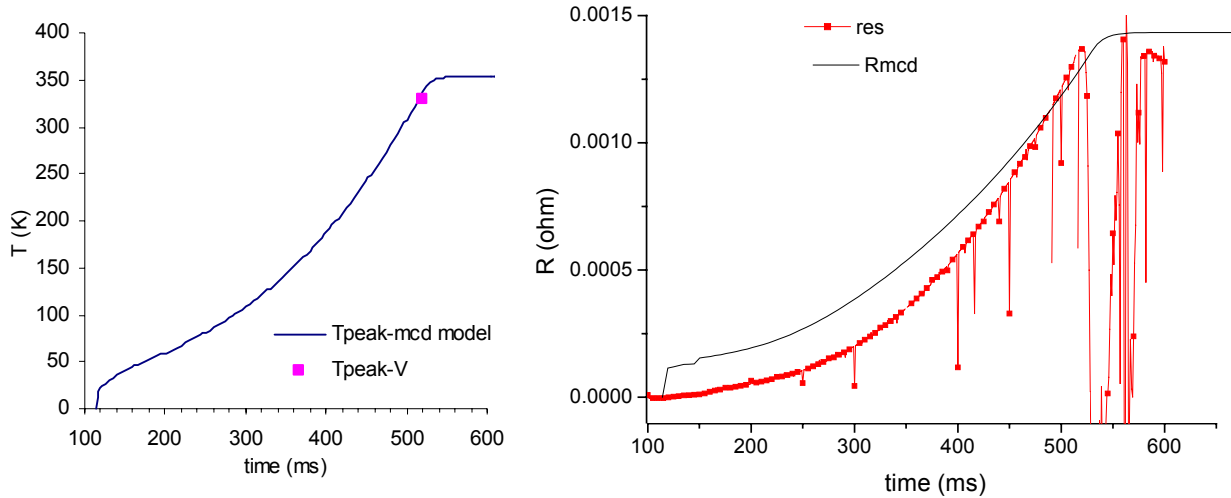


Fig. 4.11: Peak Temperature and total resistance of the sample-loop vs. time, comparison between model (mcd in the legend) and experimental data;  $t=115$  ms is the quench starting time.

The good agreement between the experimental data and the quench simulation using the quench integral approach is an indication that the model parameters are sound.

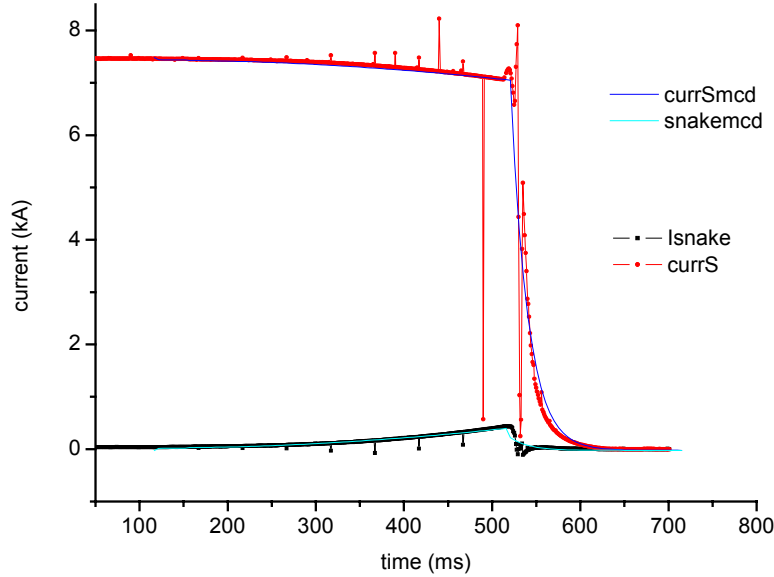


Fig. 4.12: Current in the sample and in the snake vs. time, comparison between model (mcd in the legend) and experimental data.

### 4.3 Finite element quench process simulation

The main goal of this theoretical investigation was to study the thermo-mechanical stress during the quench in a high field, high current density  $\text{Nb}_3\text{Sn}$  magnets using a thermo-mechanical finite element (FE) model (using ANSYS<sup>(TM)†</sup>). The cable quench test offered the unique opportunity to calibrate the FE model on a simple and straightforward sample geometry and stress distribution. Therefore the thermo-electrical calculations obtained with the FE model were compared to the experimental data of the cable experiment described in this chapter. One of the procedures to be tested was the quench process simulation, which requires coupling of the electrical and thermal variables. This can be done in ANSYS, utilizing the solid element SOLID69 with voltage and temperature as the degrees of freedom. The following discusses the FE model simulation of the cable quench test.

The advantage of a completely integrated solution using ANSYS is that the heat conduction from the cable to the environment is automatically accounted for. The temperature gradient between the coil and the surroundings is the most important contributor to the thermal stress on the cable. The stress in the insulation layer is also of particular interest, because the temperature gradients are the highest. Epoxy cracking in the insulation is one of the concerns that have to be addressed in magnets. Therefore the model must distinguish bare cable and insulation, and the mesh must be accordingly fine. The quench propagation is determined by a resistivity function of the superconductor, varying from a very low value to the normal state value, with a fast rise at the generation temperature. The stress analysis can be done at the end, on the basis of the temperature profile obtained.

<sup>†</sup> Trademark of SAS IP, Inc.

#### 4.1.c Finite element models

Two finite element models of the cable quench test were generated. The first model has a very simple geometry, representing just a single cable. The simplicity of this model was useful for learning how to simulate the quench exploiting ANSYS capabilities. It is also useful to compare the results of the analytic quench integral model with the results of the quench simulation with this FE model. The results should agree because the quench process in both models is adiabatic since there is no heat transferred to other cables, the structure or the helium. On the other hand, the hot spot temperature resulting from the FE model cannot be higher than that resulting from the quench integral calculations, because heat transfer in longitudinal direction is included in the ANSYS model. The second so-called complete model represents the entire sample holder.

##### - Geometry

##### *Single cable model*

The cross-section (in the x-y plane) corresponds to the cable area (parameters are listed in Table 4.5), including 0.1 mm of G10 type insulation. The length is the so-called “active length” of the cable that is the cable length between the splices. The mesh is finer in the high field region between the voltage taps.

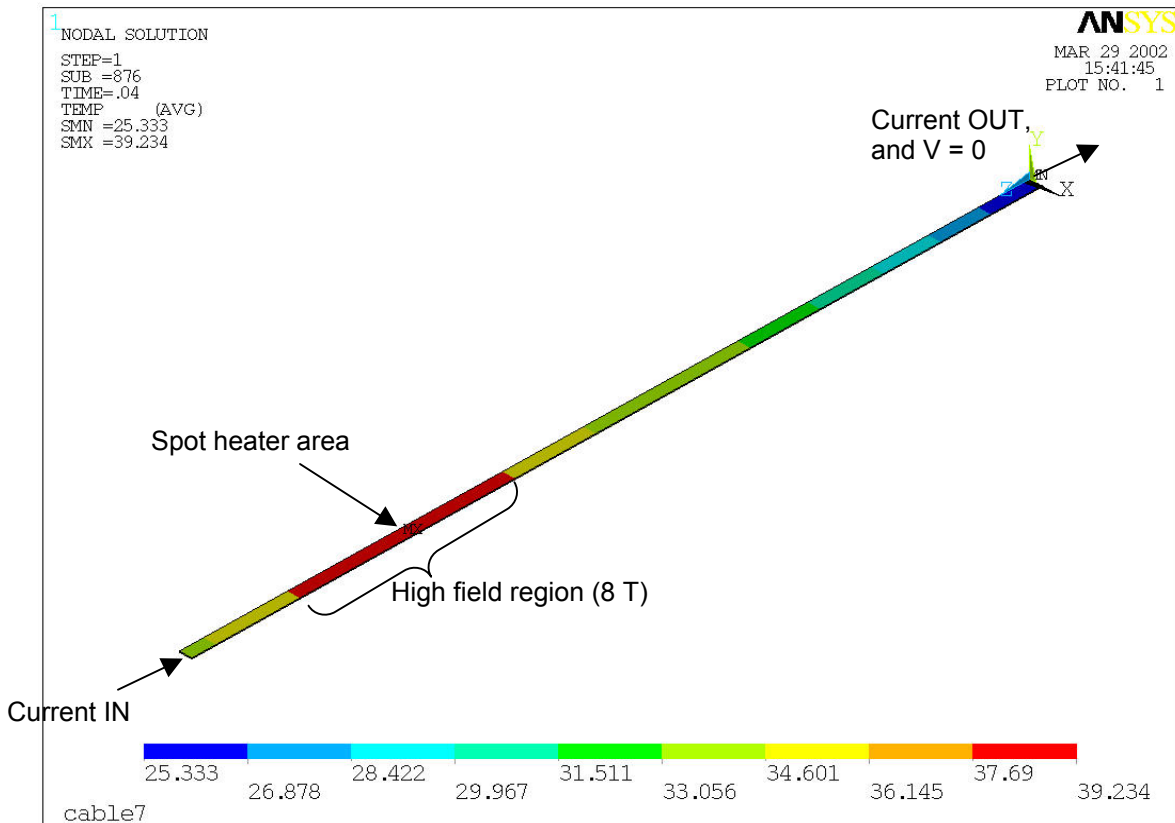


Fig. 4.13: Single cable model with initial temperature distribution (in K), and applied boundary conditions.

Model parameter	Label	Value	Dimension
Cable width	cabw	15.16	mm
Cable thickness	cabt	1.44	mm
Cable length (w/o splices)	actl	0.97	m
Voltage tap 1 (distance from lead splice)	zvt1	0.594	m
Spot heater (distance from lead splice)	zsh1	0.705	m
Spot heater end (distance from lead splice)	zsh2	0.734	m
Voltage tap 2 (distance from lead splice)	zvt2	0.794	m
mesh size – x direction		cabw/2	mm
mesh size – y direction		cabt	mm
mesh size – z direction		2 – 5	mm

Table 4.5: Single cable FE model parameters.

*Complete sample holder model*

The model differentiates between the two active cables (bare dimensions), the two “dummies”, the stainless steel u-channel, the G10 top plate, the stainless steel pusher, sidebars and pressure-bar, and the insulation. The main cross-section (in the x-y plane) is shown in Fig. 4.14. Given the symmetry of the problem, only half the cross-section is simulated. The main geometrical model parameters are listed in Table 4.6. The active length of the cable, the voltage taps and spot heater positions are the same as in the single cable model. Since the complete model includes the copper splices it is longer than the single cable model.

Model parameter	Name	Value	Dimension
Cable width	wcab	7.48	mm
Cable thickness	cabth	1.24	mm
Baseline insulation thickness	insth	0.3	mm
Bottom splice position	zbot	.97+.125	m
Lead splice position	zlead	-0.125	m
mesh size – x direction	cabw/4		
mesh size – y direction	cabth		
mesh size – z direction		2 – 5	mm

Table 4.6: parameters of complete FE model.

**- Elements***Single cable model*

The element chosen to simulate the quench is the 3-D solid element called SOLID69, characterized by 8 nodes, and two Degrees Of Freedom (DOF). Each node is associated with a temperature DOF and a voltage DOF. The thermal and electrical problems are coupled by the resistivity function, since the Joule-heating affects the temperature, and the temperature affects the voltage level.

*Sample holder model*

The element SOLID69 is chosen for the two active cables. The rest of the model is made of SOLID70 elements, to simulate the thermal problem. These elements have only one DOF (temperature) at their eight nodes.



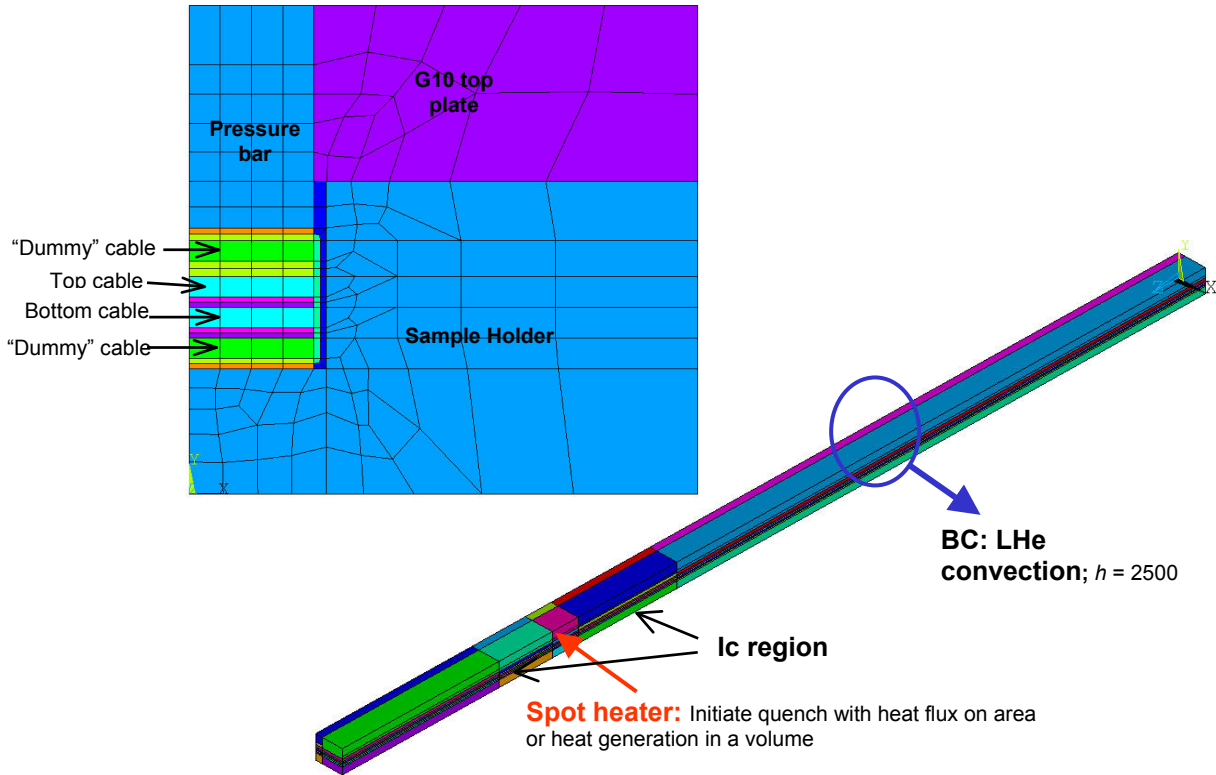


Fig. 4.14: Sample holder model cross-section.

#### - Material properties

All material properties are input as tables, as a function of temperature (with the exception of the densities, which are constant). More precisely, the ANSYS program requires input in the form of vectors with a maximum of 100 components (ANSYS command: MPTEMP). Besides the temperature vector, there are input vectors for the material properties in all directions C, KXX, KYY, KZZ, RSVX, RSVY, RSVZ. A minimum number of temperature points is required for accuracy in the computation. With 66 points we estimated an accuracy level of about 2 %, which is within the accuracy of the material property data themselves.

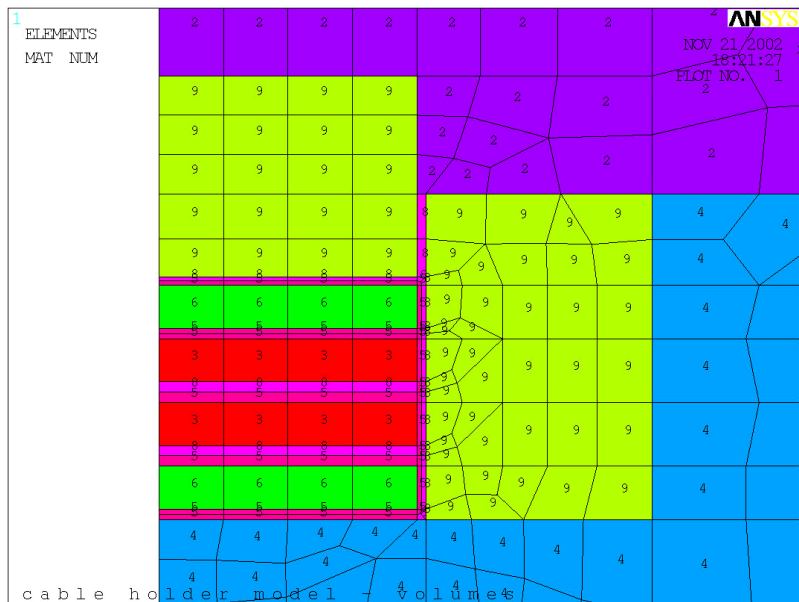


Fig. 4.15: Sample holder model cross-section: enlargement of the cable region to show the different materials (numbers refers to Table 4.7).



ANSYS calculations are based on elements with the shape of solid bricks, while in reality the conductor is a Rutherford cable with a composite structure. It is therefore necessary to obtain the average material properties from the properties of the components, weighted over the geometrical factors. The cable geometry is outlined in Tables 4.5 and 4.6. All materials are listed in Table 4.7. For the single cable model, only materials 1 and 3 were used. The material property calculations are discussed next.

Parameter	Mat N.	Density (kg/m <sup>3</sup> )	Description
		Sample holder / Single cable	
matcab	1	7843 / 6935	Cable; Cu RRR = 100, B = 8 T; T <sub>g</sub> = 5.5 K
matg10z	2	1900	G10 cover plate; z    to fibers
matlow	3	7843/ 6935	Low field cable; Cu RRR = 100, B = 1 T; T <sub>g</sub> = 12.5 K
matsteel	4	7800	Stainless steel sample holder U-channel
matepo	5	1600	Fiber-glass, epoxy impregnated = 1150·0.4+1900·0.6
matdum	6	7843	Dummy cable
matkap	8	1420	Kapton insulation
matssc	9	7800	Steel - sidebars, reduced (1/4) to account for loose contact
matcu	13	8960	Copper for splices: RRR = 100, B = 1 T

Table 4.7: Material numbers in finite element models and densities. Single cable model sample densities are lower because they include 0.1 mm of G10 insulation, whereas in the complete model the insulation is modeled separately.

### Specific heat and density

The specific heat and density of the cables were obtained by averaging the components weighted over the cable cross-section (which included the 0.1 mm G10 insulation in the case of the single cable model) using the relative fractions listed in Table 4.8. Fig. 4.16 shows the thus obtained specific heat of the cable (and that of the components, see chapter 3.4.a for the details).

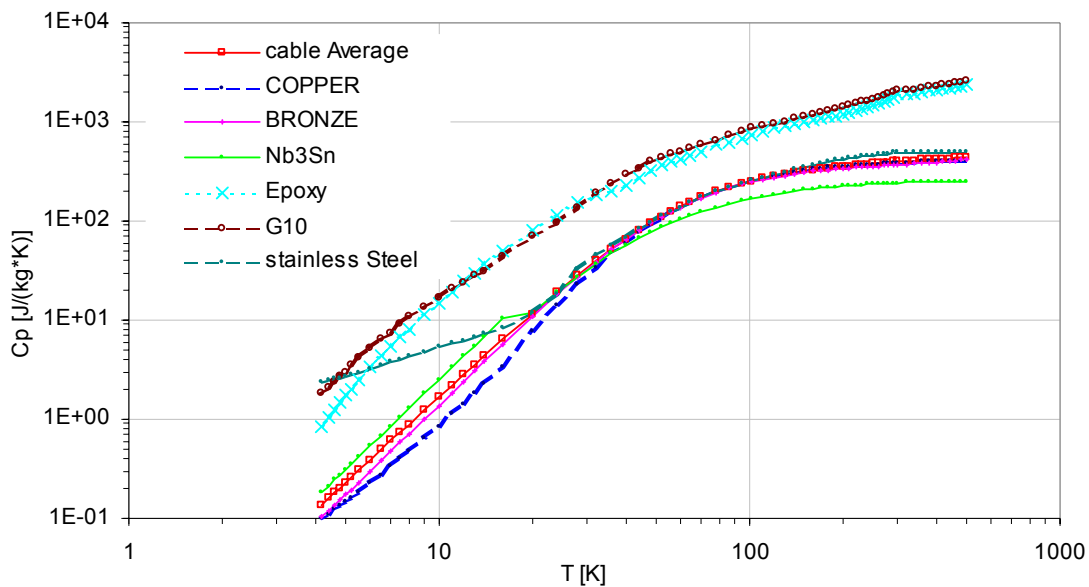


Fig. 4.16: FE model specific heat data as a function of temperature; Nb<sub>3</sub>Sn specific heat as in superconducting state up to fixed critical temperature of 18 K. The average cable specific heat was derived from the different materials in the cable composite weighted with the geometry factors specified in Table 4.8.

Material	Density (Kg/m3)	Fraction Sample holder	Fraction Single cable	Comment
Copper	8960	0.51	0.424	Cu/non-Cu = 1.42
Bronze	8850	0.18	0.153	SC/bronze = 0.5
Nb <sub>3</sub> Sn	8040	0.18	0.153	SC/bronze = 0.5
Epoxy	1800	0.13	0.110	Packing factor = 0.87
G10	1900	-	0.150	0.1 mm insulation

Table 4.8: Weighting factors of cable components for specific heat calculation used in FE models.

#### - Resistivity

At low temperatures the superconductor has zero resistivity, but in order not to incur in computational errors, the resistivity in the superconducting state was set to  $10^{-14}$  ohm-m. Above the critical temperature ( $\sim 14$  K at 8 T), the copper determines the resistance per unit length ( $R/l$ ) and the average resistivity over the cable envelope  $\rho_{ANSYS}$  becomes:

$$\frac{R}{l} = \frac{\rho_{Cu}}{A_{Cu}} = \frac{\rho_{ANSYS}}{A_{env}} \Rightarrow \rho_{ANSYS} = \frac{A_{env}\rho_{Cu}}{A_{Cu}} = \frac{\rho_{Cu}}{f_{Cu}} \quad (4.1)$$

Below the critical temperature, and above generation temperature –or current sharing temperature- Joule heating is determined by current sharing between Nb<sub>3</sub>Sn and copper (following [4.7]). The calculated generation temperature of sample 1, at 8000 A and 8 T is 5.5 K and 12.5 K in the rest of the cable (assumed to be at 1 T). In the current sharing regime between the generation and critical temperatures, the resistivity for the ANSYS elements ( $\rho_{ANSYS}$ ) is derived from the following calculation: assuming that the voltage is determined by the current and resistance in the copper stabilizer, the heat generation in the conductor can be written with (4.2). The current in the stabilizer,  $I_{Cu}$ , is given by the total current minus the temperature dependent critical current in the superconductor. By analogy with the average heat generation per unit volume,  $G_{ANSYS}$ , in the composite conductor,  $\rho_{ANSYS}$  can be written with (4.3).

$$G_{cable}(T) = \frac{V \cdot I}{l \cdot A_{env}} = \frac{\rho_{Cu} I_{Cu}}{A_{Cu}} \cdot \frac{I}{A_{env}} = I \cdot (I - I_c(T)) \frac{\rho_{Cu}}{A_{Cu} A_{env}} \quad (4.2)$$

$$G_{ANSYS}(T) = I^2 \frac{\rho_{ANSYS}(T)}{A_{env}^2} \Rightarrow$$

$$\rho_{ANSYS}(T) = \frac{\rho_{Cu} A_{env}}{A_{Cu}} \frac{(I - I_c(T))}{I} = \frac{\rho_{Cu}}{f_{Cu}} \left( 1 - \frac{I_c(T)}{I} \right) \quad (4.3)$$

Below the current sharing temperature, the resistivity function assumed was that of a power law  $\sim T/T_c^n$  ( $n = 40$ ). Table 4.11 summarizes the main parameters of the heat generation calculation in the different models used.

Symbol	Description	Equation	Unit	Single cable ANSYS model	Sample-holder ANSYS model	Mathcad
$A_{env}$	Cable envelope area		mm <sup>2</sup>	21.84	18.55/2	21.64
$A_{Cu}$	Cable copper area		mm <sup>2</sup>	9.26	9.26/2	9.26
$f_{Cu}$	Copper fraction	$= A_{Cu}/A_{env}$		0.424	0.51	0.431
$\rho_{Cu}(300\text{ K})$	Copper resistivity		ohm-m	$1.72 \cdot 10^{-8}$		
$\rho_{Cu}(14\text{ K})$	with RRR=100, 8 T		ohm-m	$4.73 \cdot 10^{-10}$		
$\rho_{ANSYS}(300\text{ K})$	Cable tot. resistivity	(4.1)	ohm-m	$4.06 \cdot 10^{-8}$	$3.37 \cdot 10^{-8}$	$4.06 \cdot 10^{-8}$
$\rho_{ANSYS}(14\text{ K})$	Cable tot. resistivity	(4.1)=(4.3)	ohm-m	$1.116 \cdot 10^{-9}$	$9.48 \cdot 10^{-10}$	$1.154 \cdot 10^{-9}$
$I$	Total current		A	8000	8000/2	8000
$J_{env}$	Total current density		A/mm <sup>2</sup>	366	431	372
$I_c(4.2\text{ K})$	Critical current		A	9600	9600	
$G(14\text{ K})$	Heat generat. per vol.	(4.2)	J/m <sup>3</sup>	$1.5 \cdot 10^8$	$1.76 \cdot 10^8$	$1.6 \cdot 10^8$
$R/l(300\text{ K})$	Resistance per length	$= \rho/A_{env}$	ohm/m	$1.86 \cdot 10^{-3}$	$1.82 \cdot 10^{-3} \cdot 2$	$1.89 \cdot 10^{-3}$

Table 4.9: Symbols for resistivity calculations, and main parameters for the different models. The sample holder ANSYS model includes only half of the area considering the symmetry.

Fig. 4.17 shows the temperature dependent resistivity used in the ANSYS model for different magnetic fields (and therefore different current sharing temperatures). The function is a linear interpolation between tabulated input values, calculated with equation (4.1), (4.3) and the power-law.

The resistivity data in x and y direction are calculated from the resistivity in z direction multiplied by two constant factors ( $f_x$  and  $f_y$  respectively) obtained simply by consideration of the cable twist ( $\beta$  = cable pitch).

$$f_x = 0.5/\text{tg}(\beta)^2 = 8 ; f_y = 0.5/[\text{tg}(\beta) \cdot t/w]^2 = 1160 \quad (4.4)$$

These factors, however, are not relevant to the final outcome of the calculations, since the problem is determined mainly by the resistivity along the cables. On the other hand, there is a small temperature gradient in x and y directions, which creates an electrical gradient, which in turn affects the current distribution. Therefore, the current distribution is determined by the transverse thermal conductivity inside the cable and the resistivity as in (4.4). The resulting current variation inside the cable is only a few percent.

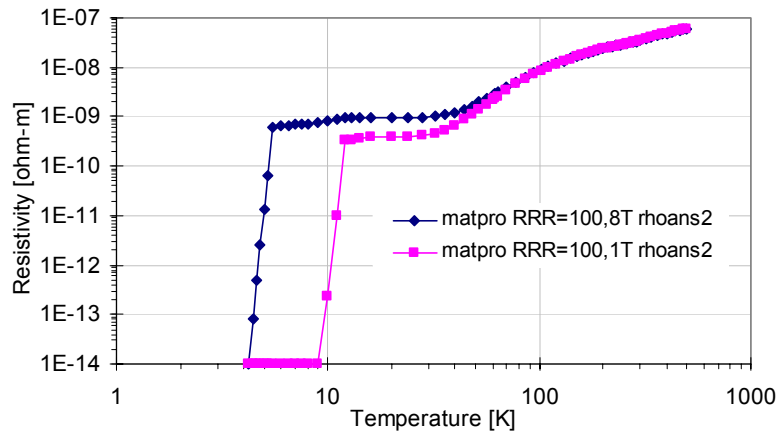


Fig. 4.17: Resistivity data as a function of temperature for the sample holder ANSYS model (bare cable); RRR = 100, B = 8 and 1 T.

### - Quench integral

The quench integrals calculated with (2.7) and the material properties (specific heat and resistivity) as discussed above are shown in Fig. 4.18. Fig. 4.18 clearly shows that the insulation, if included in the thermal balance, can strongly affect the quench integral. The issue of how much of the insulation material contributes with its specific heat to the quench process was introduced in chapter 2. The cable quench test offered the possibility to quantify this contribution. As can be seen clearly in Fig. 4.19, the experimental data support the contribution of 0.1 mm of insulation to the process.

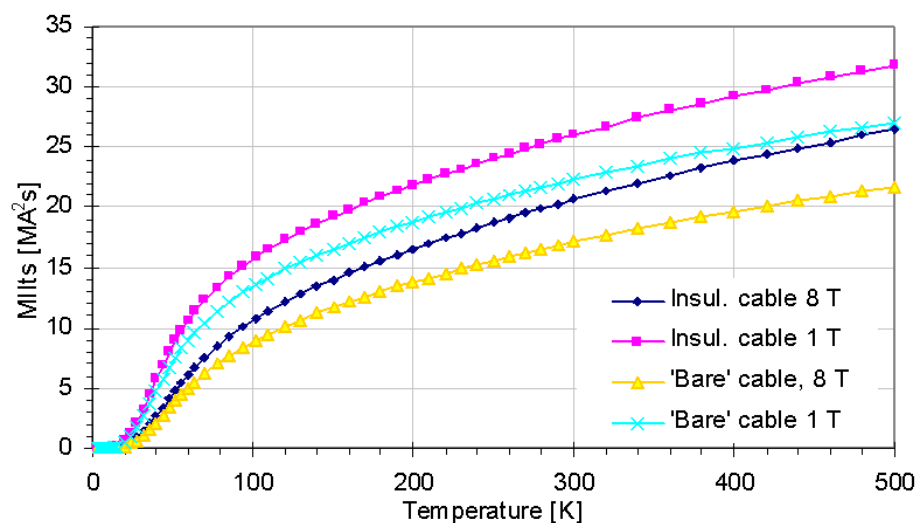


Fig. 4.18: Quench integral for cable quench test FE model: including 0.1 mm of insulation - left / w/out insulation - right; RRR = 100, B = 8 and 1 T.

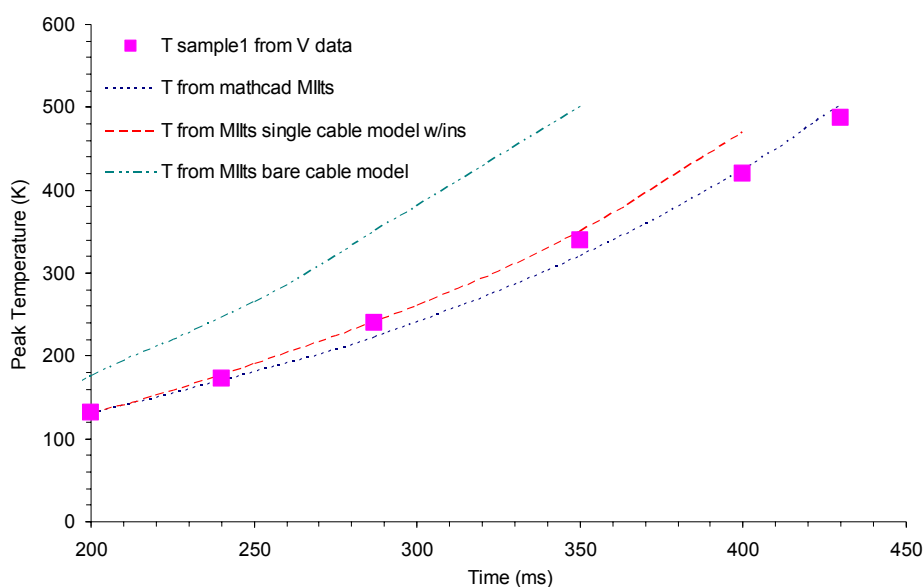


Fig. 4.19: Peak temperature as a function of time (from quench start). Comparison of experimental data with expected temperature from the quench integral calculation.

## Conductivity

The conductivity of the cable was calculated according to the model discussed in chapter 3.3. Fig. 4.20 shows the conductivity of the different materials involved and the conductivities calculated for all directions from the conductivities of the components.

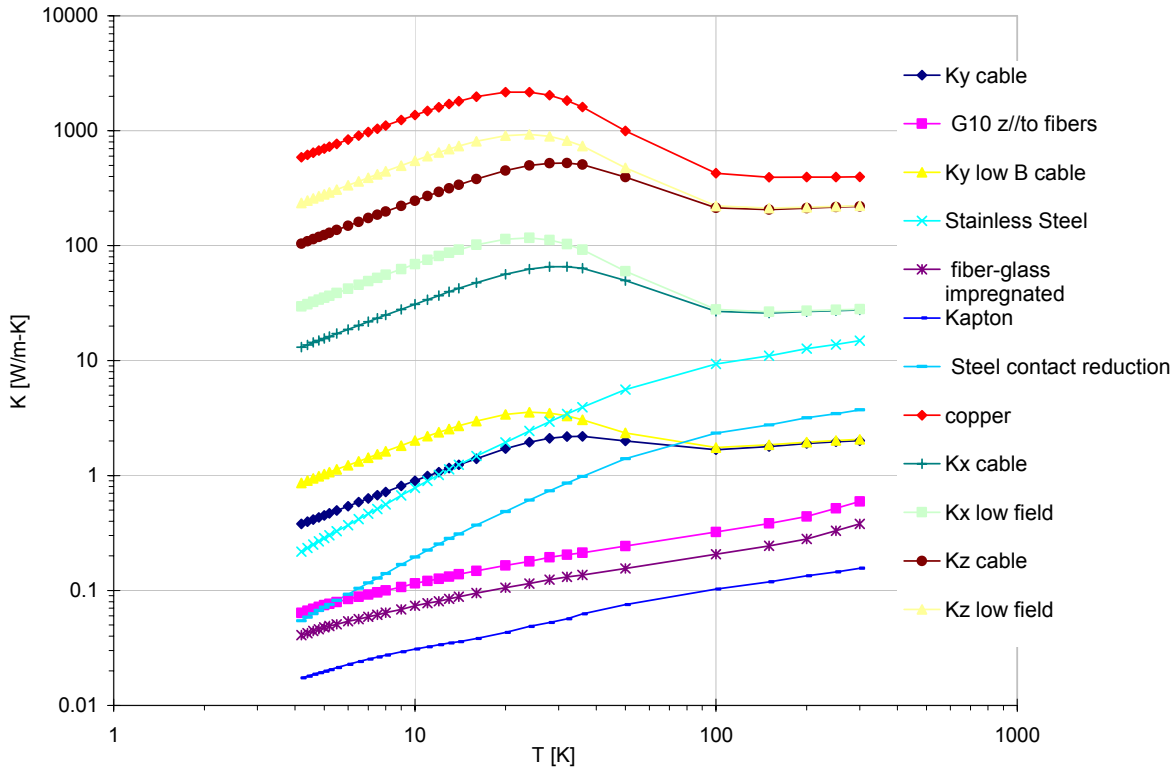


Fig. 4.20: Conductivity of all the materials in the model.

## Initial and Boundary Conditions and Solution:

### Single cable model

The initial condition of the thermal problem is a uniform temperature of 4.2 K ( $T_{bath}$ ). For the single cable model, no boundary conditions are applied, with the exception of convective transfer to liquid Helium at the ends. A small heat convection coefficient ( $h$ ) of 1000 W/(K·m<sup>2</sup>) and a small surface make this a negligible contribution. A heat flux of 7000 W/m<sup>2</sup> is applied on the spot heater surface, for about 30 ms, to initiate the quench. The heat from the heater is very small compared with the electrical power dissipated during the quench process.

Electrically, the problem is determined by the voltage at the extremities of the cable and the current. At each end, the nodes of the cable are coupled in the electrical DOF. In other words, the cable surfaces are at the same potential. One set of nodes, at  $z = 0$ , is taken as reference voltage, imposing  $V = 0$ .

The current is imposed on one node at each set of coupled nodes. ANSYS automatically equally distributes the current at the eight nodes. The ANSYS command is the same as for imposing a force (F,...,amps,...).

The program writes current and heat flux as function of time to tables.

### Sample holder model

A 4.2 K uniform temperature is given as initial condition. Convective cooling with liquid helium occurs at the ends and all around the sample holder, with a convection coefficient  $h = 1000 \text{ W/(K}\cdot\text{m}^2)$ . The outer surface of the sample holder remains at bath temperature and the resulting heat flux is small.

The same electrical conditions as for the single cable model were applied to both cables, which are not electrically in contact. The simulation of the electrical and thermal problem at the splices is outside the main purpose of this study. To obtain a solution it is necessary to ramp up the current before quench start, in a finite time (here 2 seconds). For the sample holder model, the maximum current is 4000 A, because of the symmetry we have used.

The same method as in the single cable case is applied for the simulation of the spot heater firing, defining a “heater” table, except that the heat flux was imposed on the surface insulation layer just under the cable region heated by the spot heater and that the heater pulse was shorter (15  $\mu\text{s}$ ). Consequently, the time between the quench start in the two cables is very short ( $\sim 5 \text{ ms}$ ).

A very small minimum time step of  $\sim 10^{-6} \text{ s}$  is necessary for the solution to converge. The simulations typically covered times of up to 450 ms.

### 4.1.d Results and Comparison with the experiment

#### - Simple FE model results

The peak temperature, which is the temperature at the center of the sample under the spot heater, calculated with the simple FE model as a function of time agrees well with the measurement (Fig. 4.21).

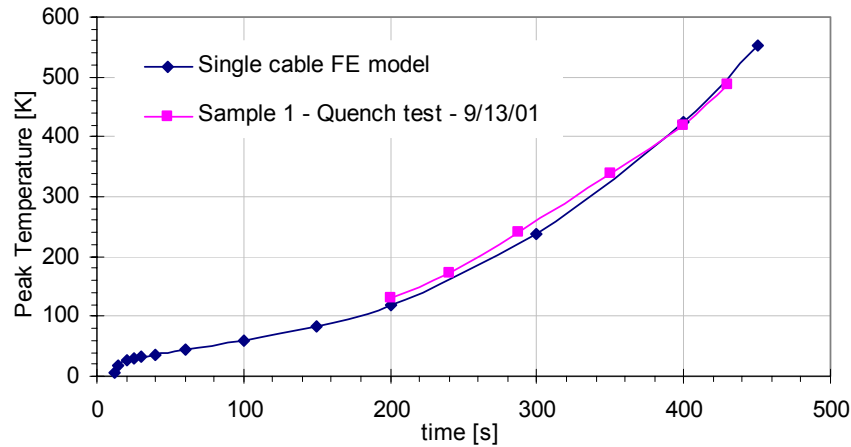


Fig. 4.21: Single cable model resulting peak temperature and comparison with experimental data.

This agreement indicates that the 0.1 mm insulation layer has in fact contributed with its specific heat in the quench process. The temperature profiles along the samples and as a function of time are shown in Fig. 4.22 and 4.24. At 10 ms, the temperature is still at 4.2 K, because the quench has not yet occurred. At 10 ms the spot heater begins rising in temperature. The quench happens quickly. In fact, almost the entire high field region is normal conducting at 15 ms. This very fast propagation leads to a uniform temperature in the high field region (Fig. 4.22).

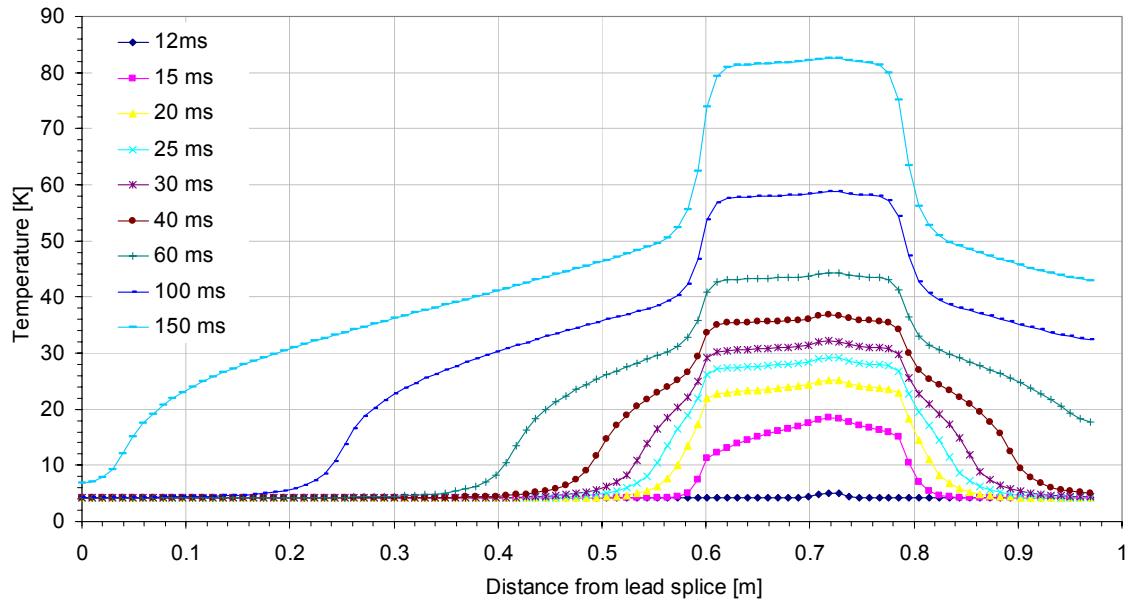


Fig. 4.22: Single cable model resulting temperature profile up to 200 ms.

The quench propagation velocity can be estimated to  $\sim 30$  m/s (Fig. 4.23). The measured quench propagation velocity was a factor 2 lower. This discrepancy, however, is not important for the peak temperature at later times. As soon as the quench reaches the low field region, the quench propagation is slowed down to  $\sim 4$  m/s. The quench velocity outside the high field region was not measured in the experiments. This sudden reduction of the velocities of the quench propagation is due to the transition from high to low magnetic field. The velocity profile might be steeper in the model than in reality due to the step-function field profile in the model. Implementing a more accurate field profile in the FE model is difficult, since it would require a larger number of materials and material property files.

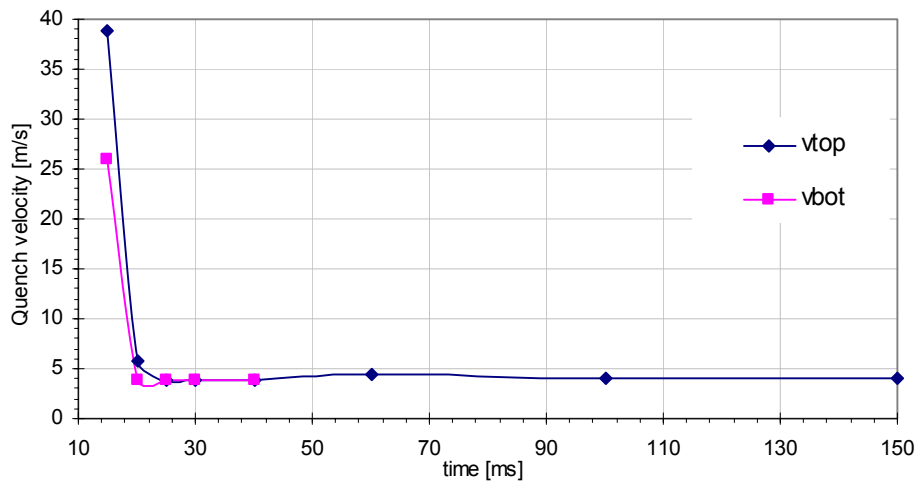


Fig. 4.23: Single cable model calculation of quench propagation velocities towards bottom and top splices ( $v_{bot}$  and  $v_{top}$  respectively).

In Fig. 4.24, the temperature profile at different times up to 450 ms is shown. At 450 ms, the temperature drops from the high field region at uniform temperature of  $\sim 550$  K, to 330 K just outside the high field region, and then decreases almost linearly towards the ends at 140 K and 170 K at the top and bottom respectively. The temperature at the ends is probably overestimated, since the heat conducted to the copper splice boxes and to the lead on the upper part is not included in the model (almost adiabatic except for some small convective cooling). The cooling effect is more accurately represented in the complete sample holder model.

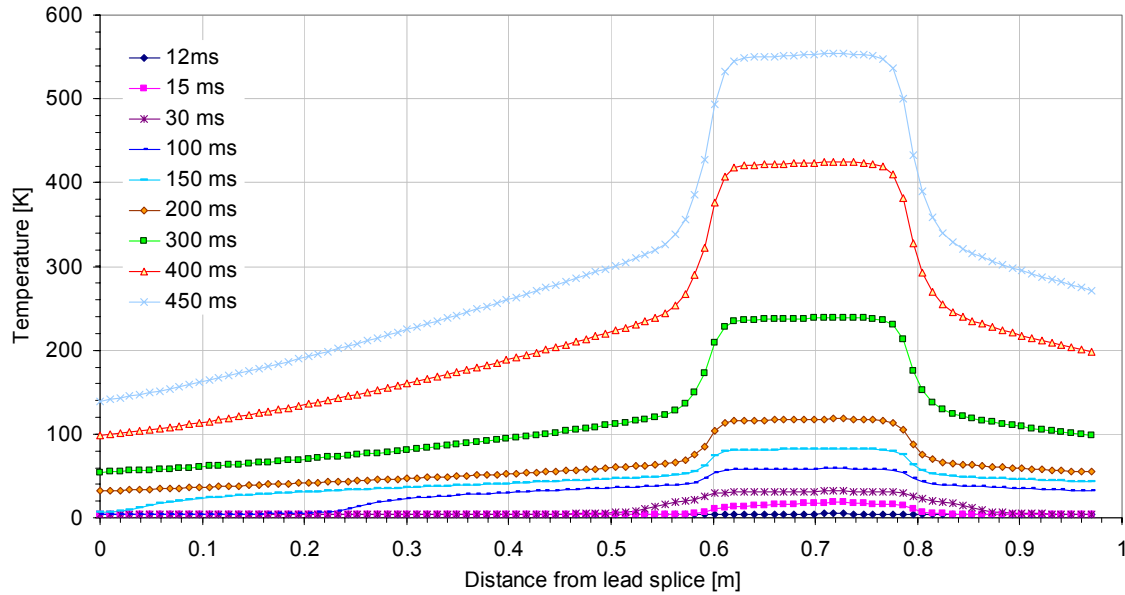


Fig. 4.24: Single cable model resulting temperature profile up to 450 ms.

### Voltage

Comparing the voltage resulting from the ANSYS model we also find good agreement with the experimental data (Fig. 4.25). Unfortunately, the voltage over the whole cable was not recorded above 5 V, because the channel was saturated.

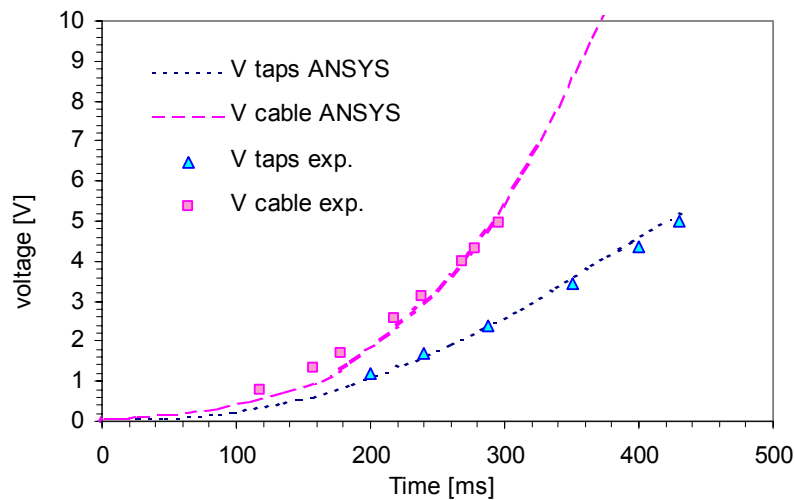


Fig. 4.25: Single cable model calculation of sample voltage up to 450 ms.



### - Sample holder model results

The peak temperature resulting from the quench simulation with the sample holder model is shown in Fig. 4.26, as a function of time. To compare it with experiment results, the time of the quench start was chosen as the time in which the hot spot reached the critical temperature of the conductor at 8 T (14.5 K). This temperature is reached 31.5 ms after the heat generation starts in the spot heater location. The temperature values are reported in Table 4.12.

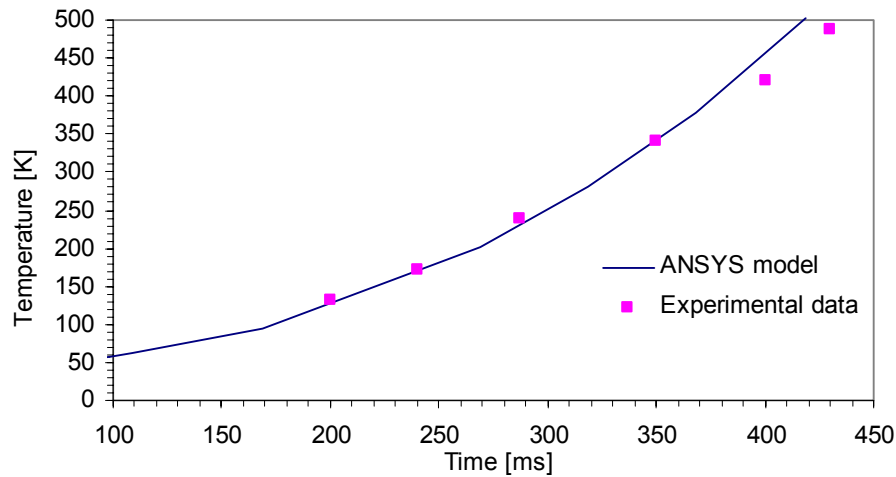


Fig. 4.26: Sample holder FE model results: peak temperature and comparison with experimental data.

We see from this plot that there is also a good agreement between the peak temperature resulting from the FE simulation and the experiment. A 10 % temperature overestimation occurs at 400 ms and later. This small discrepancy might be due to an underestimation of the cooling effect in the ends, or to inaccuracies in the material conductivities. As described in chapter 3, it is difficult to predict with good accuracy the thermal impedances at the contact surfaces between the components of the sample holder assembly. The contact impedance was taken into account, for example, in the calculation of the conductivity of the cable in y-direction (see chapter 3), and in the x-direction conductivity of the steel sidebars lining the sample. The latter was obtained by lowering the conductivity of the material (steel) by a factor 4.

Time (ms)	-21.5	58	68	78	88	98	108	168	268	318	368	378	418
Lead	4.21	4.21	4.21	4.21	4.21	4.21	4.22	28	35	40	41	46	52
Lead splice	4.21	4.21	4.21	4.22	4.22	4.22	4.29	35	42	49	51	58	71
SH center	43	46	50	54	58	62	95	201	281	378	403	504	647
Bot. splice	4.96	9	13	16	18	20	28	38	44	53	56	67	89
Bottom end	4.21	4.21	4.27	4.51	5.0	5.8	19	27	29	30	31	32	34

Table 4.10: Sample holder FE model results: temperature [K] at the hot spot (SH center), and at the splices, at different times after the quench.

Fig. 4.27 shows the temperature profiles obtained with the complete sample holder model at different times, up to 200 ms. As can be seen the profiles match those obtained with the simpler model. The initial quench propagation is very fast, producing a flat temperature profile in the high field region. The quench propagation velocities in the low field region are about 3 m/s, for the quench that propagates toward the lead end. Towards the bottom splice, the quench in the

low field region has also a 3 m/s speed in the beginning, and then it slows down to about 0.6 m/s as it reaches the splice region. This effect is probably due to the heat conduction that occurs at the copper splice box, when the quench reaches the splice the temperature cable model. At the top splice, the temperature rises up to 46 K at 380 ms. This temperature might be overestimated because the model does not include the heat conducted through the leads, which are very well stabilized with the cold fingers (see Fig. 4.3). The temperature distribution in the splice region is shown in Fig. 4.29 and Fig. 4.30.

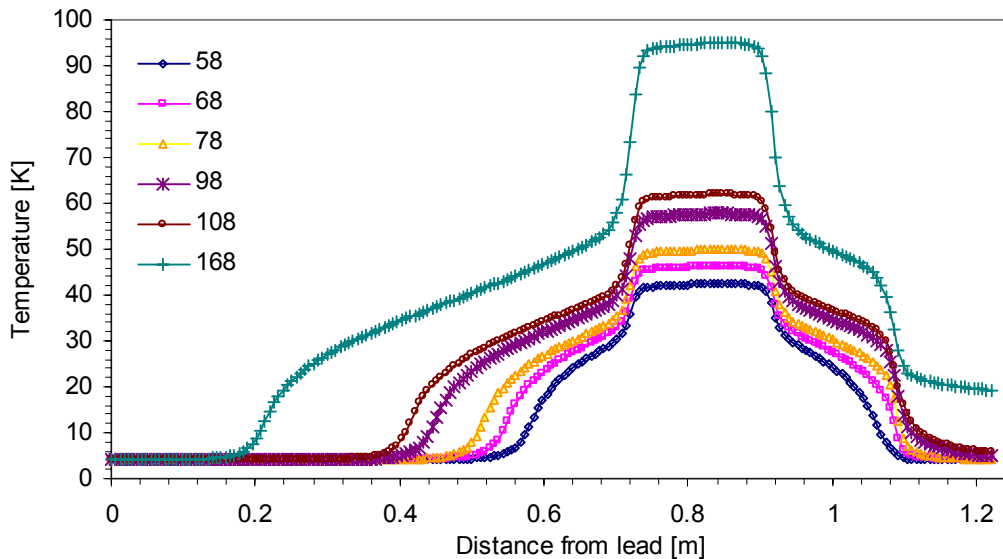


Fig. 4.27: Temperature profile up to 200 ms calculated with sample holder model.

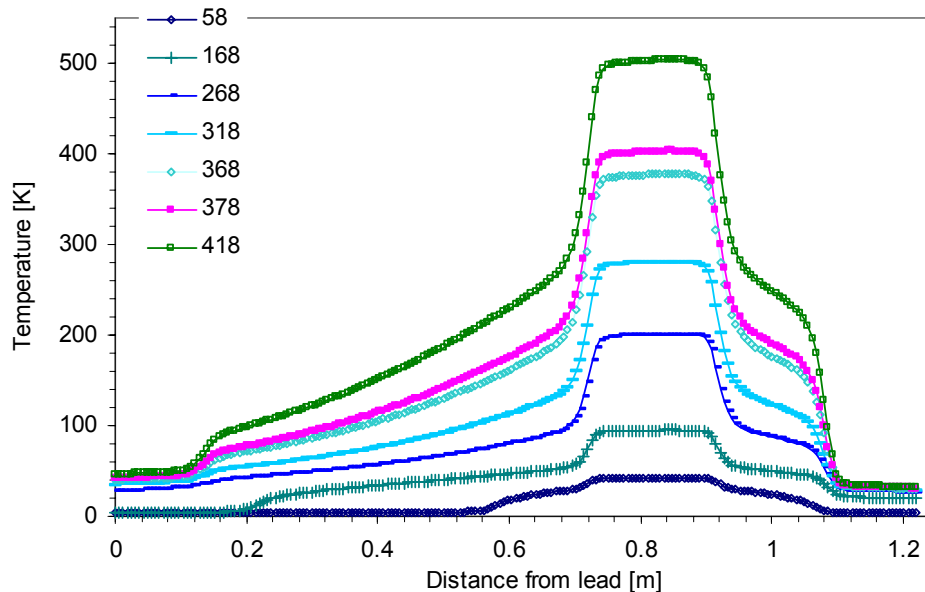


Fig. 4.28: Temperature profile up to 450 ms calculated with complete sample holder model. The temperature inside the splices rises slowly up to 31 K at 380 ms after the quench (which corresponds to a peak temperature of 400 K). The temperature at the ends of the cable resulting from this model is much lower than the temperature resulting from the single cable model.

The quench propagation in transverse direction is also fast. The bottom cable reaches 14.5 K after 34 ms from the beginning of the heat generation in the spot heater, just 3 ms after the quench of the top cable. During the experiment, this time difference was about 6 ms (Table 4.5). The small discrepancy might be due to the fact that during the experiment the current through the heater was raised slowly, by hand and therefore not in a reproducible way. After the quench start, the normal zone propagates with the same velocities as in the top cable.

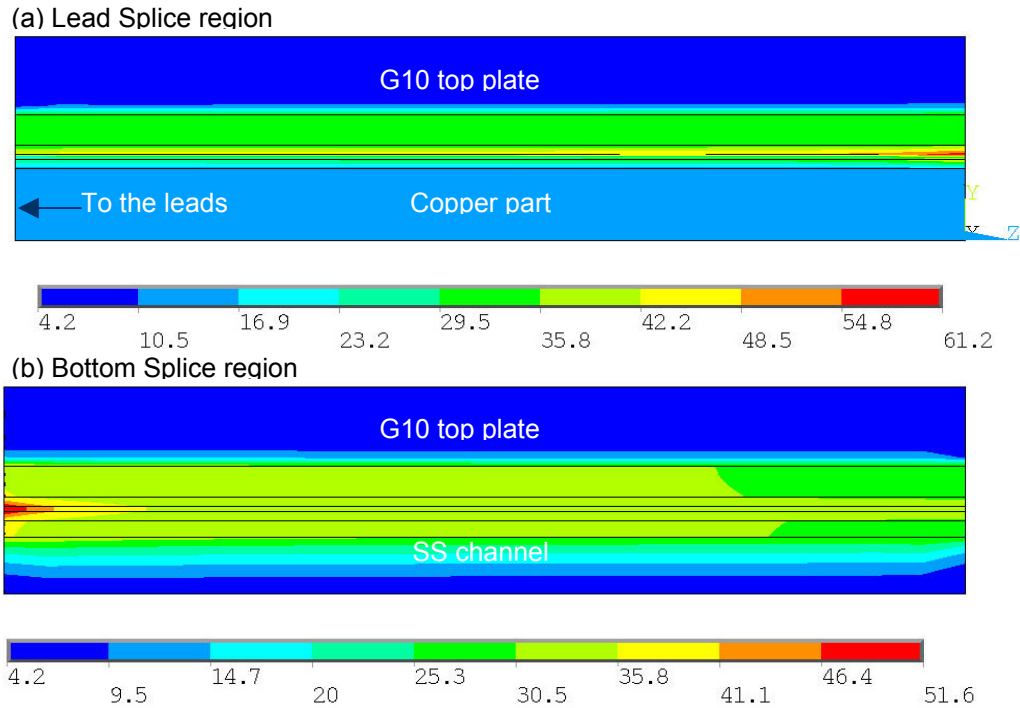


Fig. 4.29: Sample holder model resulting temperature distribution after 450 ms in the lead and bottom splice regions; cross section in the z-y plane.

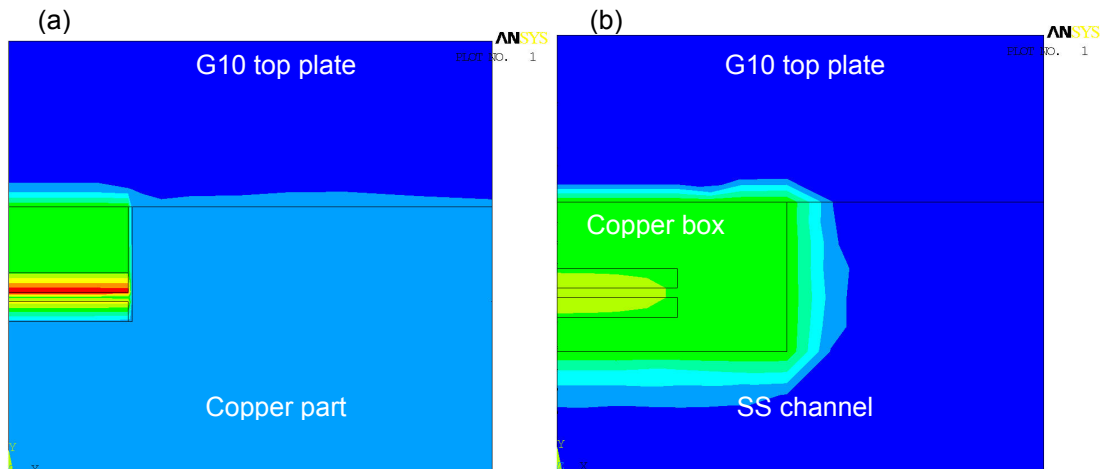


Fig. 4.30: Sample holder model resulting temperature distribution after 450 ms in the lead and bottom splice regions; cross section in the x-y plane.

The temperature distribution over the cross-section of the sample holder is shown in Fig. 4.31. We can see that the top cable is at a uniform peak temperature, and that the bottom cable is

at a quite uniform temperature also, slightly lower than the top cable. The two dummy cables are at a much lower temperature between 60 K and 35 K for the top one, and between 28 K and 22 K for the bottom one. The sample holder remains below 20 K, and the sidebars are above 40 K only in a small region close to the active cables, with a temperature profile decreasing fast to low temperatures.

The highest temperature gradient occurs through the insulation, as it was expected, since it has the lowest conductivity. Between the two active cables, the temperature varies from 400 K on one side, to 120 K in the center, to 350 K to the other side. The insulation between the top cable and the top dummy cable has a temperature gradient of 320 K over 0.2 mm. The insulation towards the sidebars has a similar temperature gradient. These temperature gradients are of concern since they might result in high shear stresses.

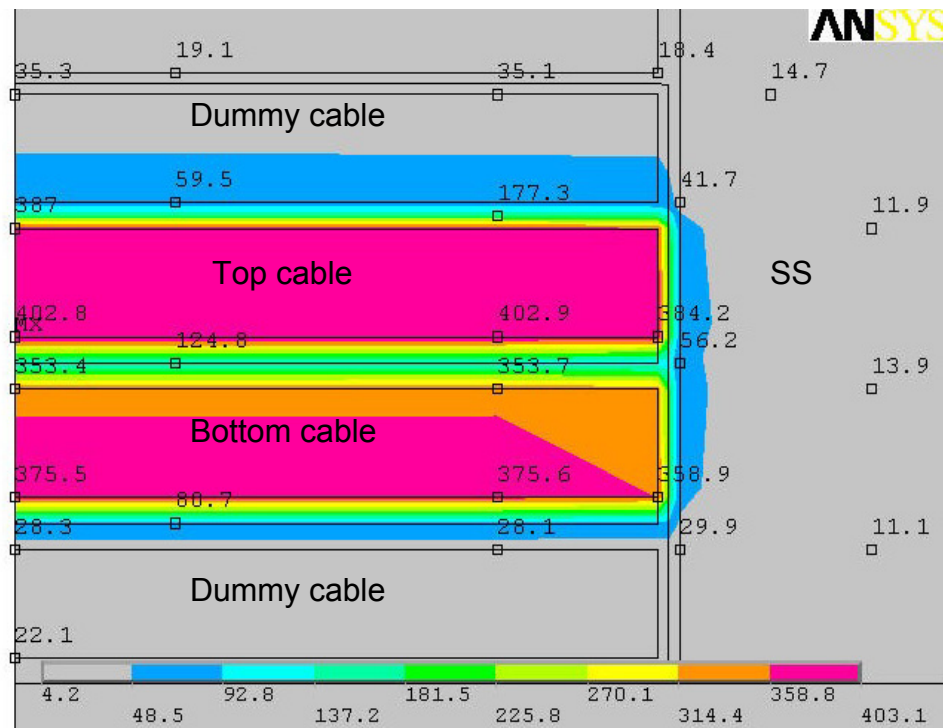


Fig. 4.31: Sample holder model: temperature distribution (in K) over the cross-section at 380 ms.

#### 4.4 Mechanical analysis

The total strain inside the  $\text{Nb}_3\text{Sn}$  filaments (intrinsic strain) is given, in general, by the sum of several contributions:

- 1) the pre-compression of the  $\text{Nb}_3\text{Sn}$  filaments, due to the differential thermal contraction between the  $\text{Nb}_3\text{Sn}$  filaments and the bronze/copper matrix, from the reaction temperature (600 C) to the peak temperature after the quench ( $T_{peak}$ );
- 2) any applied strain, such as:
  - the strain induced by the non-isotropic thermal expansion during the quench process, as discussed here;

- the strain caused by winding after reaction ( $\sim 0.18$  % in the bent sample), pre-stress and Lorentz forces;

Pre-stress and Lorentz forces, which can be neglected in this experiment, are relevant in the case of accelerator magnets. They have to be added to the stress contributions calculated here, when applying them to a magnet. During a quench, the current is initially stable, and starts decreasing significantly only after the quench protection system is effective, that is after the heater delay time in case of long magnets. The peak temperature could occur when the current is already moderate; therefore, summing the peak stress in the coil, due to pre-stress and Lorentz forces, with the quench-induced stress, yields a conservative estimate.

The measured intrinsic pre-compression for the strands used in the samples at 4.2 K is 0.28 %, and the irreversible intrinsic tensile strain is 0.64 % [4.8]. The irreversible intrinsic pre-compression strain was not measured, but it is known that these conductors are less sensitive to compressive than to tensile strain. At 400 K the intrinsic pre-compression is reduced with respect to the 4.2 K level, due to the smaller temperature difference to the reaction temperature. The intrinsic strain in the  $\text{Nb}_3\text{Sn}$  ( $\epsilon_{int}$ ) after cool-down from the reaction temperature  $T_{react}$  to the temperature  $T$  cannot easily be estimated because many other factors must be taken into account. These factors include the temperature dependence of the elasticity modulus of all the materials inside the strand, the yielding point of the copper/bronze matrix (depending on the previous thermal history), and the twist of the filaments inside the strand. A relative estimate of the intrinsic strain  $\epsilon_{int}(T_{peak})/\epsilon_{int}(4.2 \text{ K})$  can be made on the basis of the linear thermal contraction, the elastic modulus and the superconductor fraction in the strand. This procedure yields  $\sim 50$  % decrease of the intrinsic pre-compression at  $T_{peak} = 400 \text{ K}$  with respect to the measured intrinsic strain at 4.2 K.

The strain and stresses generated during the quench experiment are estimated using a simple analytical model, as well as using a FE model, described next.

#### 4.1.a Analytical estimate

##### - Uni-axial strain model:

A first estimate of the strain and stress level that develops inside the cable due to high temperature differences to the surrounding mechanical structure is given by a simple model of a cable restrained from expansion while being heated uniformly to peak temperature. This hypothesis corresponds to the approximation of infinitely rigid and completely cold sample holder. It is therefore a conservative estimate.

##### *Strain:*

The strain is calculated using a thermal contraction factor, measured on an impregnated  $\text{Nb}_3\text{Sn}$  cable stack, from room temperature to 77 K, as reported in Table 3.3, for the sample insulated with Kapton + E-glass [4.9]. The thermal contraction in the three directions (using the convention indicated in Fig. 4.32) are also reported in Table 4.13. The longitudinal thermal contraction was not measured for the specific sample, but previous measurements on similar samples showed that it is similar to the radial thermal contraction [4.10]. The integrated thermal

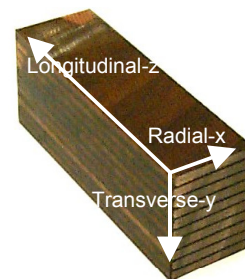


Fig. 4.32: Convention for axis labeling.

contraction increases by ~10% when cooling the samples further to 4.2 K [4.10], giving  $\alpha_z = \alpha_x = 0.34$  %, and  $\alpha_y = 0.45$  %.

The strain induced by a change from bath temperature ( $T_{bath}$ ) to a temperature  $T$ , is calculated with

$$\varepsilon_i(T) = c_i \cdot (T - T_{bath}); \quad c_i = \frac{\alpha_i}{(293 - 77) \text{ K}} \quad (4.6)$$

for each direction  $i = x, y, z$ . In case of a triangular temperature profile, with  $T_{peak}$  in the center and  $T_{bath}$  at the cold ends, the peak thermal strain ( $\varepsilon_2$ ) is reduced to half:

$$\varepsilon_{2i}(T) = \frac{c_i}{2} \cdot (T - T_{bath}) \quad (4.6')$$

The particular temperature profile calculated with the FE sample holder model yields a longitudinal strain of 2.22 mm/m, which is similar to that calculated with (4.6') for the triangular temperature profile.

	x	y	z	y-2 (triang.)	z-2 (triang.)
$\alpha$ 293-77 K (mm/m)	2.983	4.154	2.983	4.154	2.983
$\alpha$ 293-4.2 K (mm/m)	3.4	4.5	3.4	3.4	4.5
$E$ at 293 K (GPa)	31	24	31	24	31
$E$ at 4.2 K (GPa)	22	18	22	18	22
$\varepsilon$ (%)	-0.46	-0.62	-0.46	-0.31	-0.22
$\varepsilon_{tot}$ (%)	-0.57	-0.73	-0.57	-0.42	-0.33
$\sigma$ (MPa)	-86	-98	-86	-62	-57
$\sigma$ (MPa) Poisson	-163	-157	-139	-92	-77

Table 4.11: Mechanical properties for the estimation of strain and stress in the cable quench experiment, for a peak temperature of 400 K.

### Stress

The stress is calculated from the modulus  $E(T)$ , using a linear fit between measured data on cable stacks, at room temperature and at 4.2 K, in radial and transverse direction [4.11]. The modulus values are reported in Table 4.13. Equation (4.7) applies to the case of a uniform temperature distribution, and (4.9') for a longitudinal triangular temperature profile (neglecting the Poisson effect).

$$\sigma_i(T) = E_i(T) c_i (T - T_{bath}) \quad (4.7)$$

$$\sigma_{2i}(T) = \int_{T_{bath}}^T E_i(T) \cdot \frac{c_i}{2} dT \quad (4.7')$$

The calculation results are summarized in Fig. 4.33 and Fig. 4.34 and in Table 4.13.

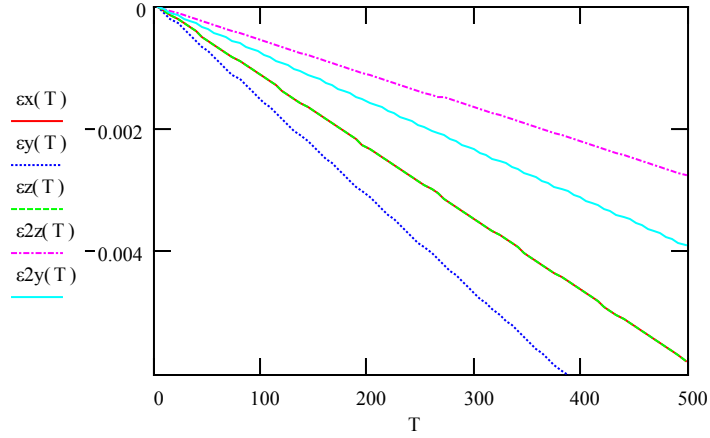


Fig. 4.33: Thermal expansion strain (m/m) at the hot spot, as a function of peak temperature (K), for all directions assuming a uniform temperature, and in case of triangular temperature profile in z and y-direction ( $\epsilon_2$ ).

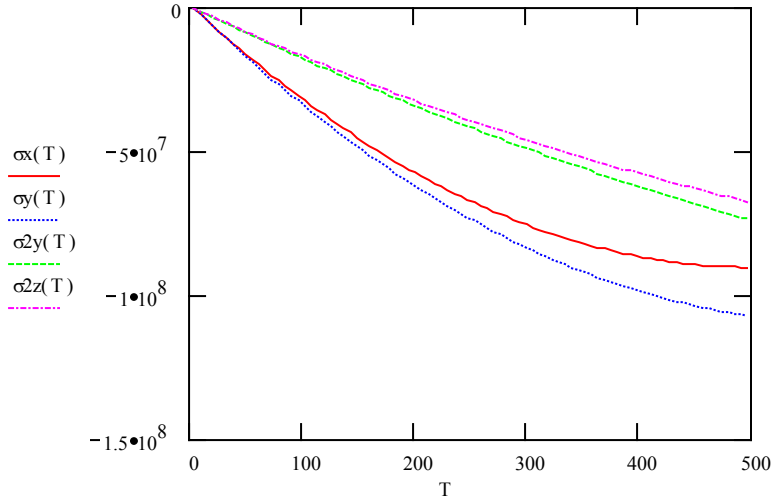


Fig. 4.34: Thermal expansion stress (Pa), at the hot spot, as a function of peak temperature (K), for all directions assuming a uniform temperature, and in case of triangular temperature profile in longitudinal direction ( $\sigma_2$ ).

### - 3-Dimensional model:

Considering also the Poisson effect leads to further enhancement of the stresses. The 3D stresses and strains can be calculated with the generalized form of Hooke's law (4.8),

$$\vec{\sigma}_3(T) = M_{es}^{-1}(T) \cdot \vec{\varepsilon}(T); \text{ with } M_{es}(T) = \begin{bmatrix} \frac{1}{E_x(T)} & \frac{-\nu_{xy}}{E_y(T)} & \frac{-\nu_{xz}}{E_z(T)} \\ \frac{-\nu_{yx}}{E_x(T)} & \frac{1}{E_y(T)} & \frac{-\nu_{yz}}{E_z(T)} \\ \frac{-\nu_{zx}}{E_x(T)} & \frac{-\nu_{zy}}{E_y(T)} & \frac{1}{E_z(T)} \end{bmatrix} \quad (4.8)$$

where  $M_{es}$  is the elasticity matrix of the generalized Hooke law.

The Poisson ratio was measured for similar samples, and the results are reported in [4.10]. Using the following values,

$$\nu_{xy} = \nu_{yx} = 0.3; \nu_{zy} = \nu_{yz} = 0.15; \nu_{xz} = \nu_{zx} = 0.15,$$

results in the stresses shown in 4.35, with a maximum at 400 K, of 160 MPa in radial and vertical direction, and 140 MPa in longitudinal direction.

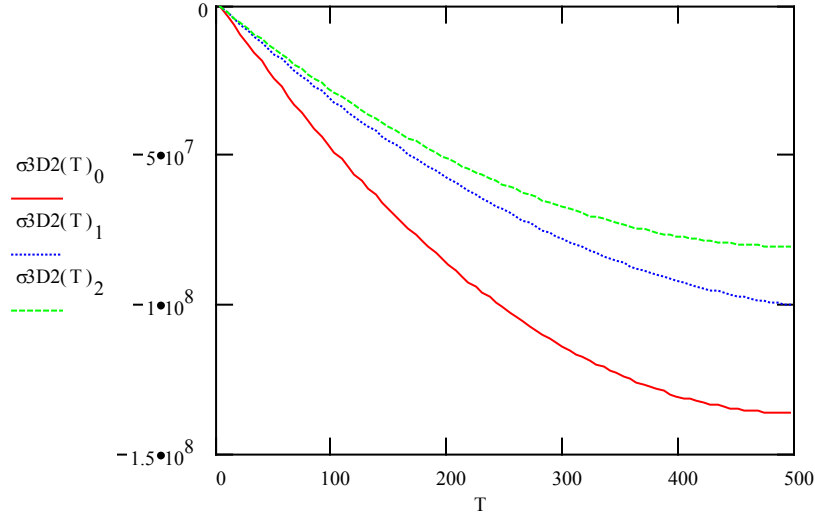


Fig. 4.35: Thermal expansion stress (Pa) at the hot spot, as a function of peak temperature (K). A uniform temperature in x-direction ( $\sigma_{3D2_0}$ ) and a triangular temperature profile in y and z-direction ( $\sigma_{3D2_1}$  and  $\sigma_{3D2_2}$ ) are assumed. The Poisson effect is included.

#### - Strain and stress summary and comments:

The results of this analytical model are summarized in Table 4.13. The total intrinsic strain ( $\epsilon_{tot}$ ) is calculated by summing the quench induced strain, calculated with (4.6) and the calculated, intrinsic pre-strain at 400 K of -0.14 %. This approach, which represents the sample as a bulk rather than with its complex geometry, was chosen for simplicity. Critical current measurements on cables under transverse pressure are good indicators for the stress limits in Rutherford cables. Some studies indicate a limit of about 150 MPa [4.12], other experiments showed no permanent degradation up to 180 MPa and little degradation at 210 MPa [4.13]. There is very little information available about the stress limits for stress applied to the thin edge of the cable, in the radial direction.

The total intrinsic compressive strain in longitudinal direction, estimated with the procedure outlined above, is -0.36 % with a triangular profile, and -0.45 % with a uniform temperature distribution. This level of strain is below the level of irreversible degradation known from elongation experiments on strands. In vertical direction, the total strain, calculated with the model above, is -0.45 % with a triangular profile, and -0.76 % with a uniform temperature distribution. This is a level of strain, which is expected not to induce permanent degradation, since Nb<sub>3</sub>Sn strands are less sensitive to compressive than to tensile strain. Measurements indicate that the irreversible intrinsic pre-compression strain is more (in modulus) than 0.7%



[5.12]. The stress calculated with the 3-D model, at a peak temperature of 400 K, for a uniform temperature profile in y-direction is about 100 MPa, and 62 MPa for the triangular profile. In the radial direction, the total strain at 400 K is about -0.7 %. The stress level is about 90 MPa. Therefore the results of this mechanical analysis support the experimental findings, which did not reveal any  $I_c$ -degradation for peak temperatures up to 400 K.

- Constant transverse pressure

It is important to remember at this point the assumption of the structure as infinitely rigid, and to discuss its validity. At the hot spot, in vertical direction, the sample is restrained by the pressure piston and the G10 plate. The pressure of the piston was set, before the quench, to 20 MPa. Even though the stress developed during the quench, might lead to a temporary increase in the pressure, since the response of the pressure system is not immediate, the sample cannot be considered completely constrained. In addition, the G10 top-plate, bolted to the stainless steel u-channel is not a very rigid structure. Keeping the pressure on the broad face of the cable constant (at 20 MPa) reduces the stresses also in x and z-direction (Table 4.14).

Main	x	y	z	Shear	$\sigma_y=20$ MPa	$\varepsilon_y=0$	
$\varepsilon$	-0.46	+ 0.134	-0.46	$\gamma$	0.60	0.16	%
$\varepsilon_2$	-0.46	+ 0.086	-0.22	$\gamma_2$	0.55	0.24	%
$\sigma$	-109	-20	-106	$\tau$	45	27	MPa
$\sigma_2$	-102	-20	-60	$\tau_2$	41	29	MPa

Table 4.12: Strain and stress for a peak temperature of 400 K keeping a constant pressure in y-direction. The subscript 2 refers to a triangular temperature profile in both y and z-direction.

Even if in this case the stresses in x, y, and z directions are below the irreversible limits, the highly non-isotropic expansion generated higher shear stress and strains than in the case of a completely constrained sample. The values listed in Table 4.14 were calculated using Mohr's circle in a 3-dimensional model (equations 4.9).

$$\tau_{max} = 1/2 |\sigma_{max} - \sigma_{min}| ; \gamma_{max} = |\varepsilon_{max} - \varepsilon_{min}| , \quad (4.9)$$

where  $\sigma_{max}$  and  $\sigma_{min}$ , and  $\varepsilon_{max}$  and  $\varepsilon_{min}$  were chosen as the maximum and minimum stress and strain respectively, between the components of the stress and strain vectors in the x, y, and z directions, which are also the principal directions (no shear stress and strain).

The shear stress values are high if compared with the shear strength of the epoxy resin, which is about 43 MPa (a value that varies between different epoxy mixtures). Composites, as impregnated fiberglass, have higher shear strength, depending on the strength of the fibers, on the epoxy content, and on the pattern of the texture. Imperfections in the impregnation, such as voids or large grains of epoxy without glass-fibers, may generate weak points, where the shear stress behavior is dominated by the epoxy. Considering the shear strength of the cable stack as that of epoxy provides therefore a conservative limit.

The burn marks of sample 1 after the quench test (Fig. 4.10) could be the result of insulation damage following excessive shear stress and overheating. The shear stress was higher at the sides of the hot spot, because of higher temperature gradients, and that's were most of the damage appeared. The fact that the insulation was not affected at the spot heater location might be explained by the pressure piston, which might have conducted the heat away from that region.

The ANSYS simulation with the sample holder model did not include the pressure piston, but included the pressure bar (made of stainless steel). The FE model results indicates that at the edges of the high field region there are indeed high temperature gradients, but the highest temperature occurred at the spot heater location.

## References

- 
- [4.1] L. Imbasciati, P. Bauer, G. Ambrosio, S. Mattafirri, J. Miller, G. Miller, "Quench-Tests On Nb<sub>3</sub>Sn Cables - Run 1," Fermilab, Technical Division note TD-01-075, Nov. 2001
  - [4.2] L. Imbasciati, et al., "Effect of Thermo-Mechanical Stress during Quench on Nb<sub>3</sub>Sn Cable Performance," in press, *IEEE Trans. Appl. Supercond.*, June 2003, proceedings of ASC02
  - [4.3] L. Summers, R. Walsh, J. Miller, "A Facility for the Characterization of the Critical Current of Superconductors as a Function of Strain and Magnetic Field," *IEEE Trans. Appl. Supercond.*, Vol. 5, No. 2, p. 1896, June 1995
  - [4.4] J. Miller, R. Walsh, M. Haslow, W. Kenney, G. Miller, "Characterization of High-Current Nb<sub>3</sub>Sn Cable-In-Conduit Conductors vs. Applied Sheath Strain," *proceedings of the 1997 CEC/ICMC Portland,OR*
  - [4.5] P. Bauer et al., "Critical Current Measurements of Superconducting Cables at the National High Magnetic Field Laboratory – Documentation / User Guide Version 1.0.," Fermilab Technical Division Note, TD-99-039, 1999
  - [4.6] J. Ekin, personal communication, Measurements at MIT of HP1-ITER IGC strand, October 2001
  - [4.7] M. N. Wilson, "Superconducting Magnets," Clarendon Press Oxford, 1983, chapter 5
  - [4.8] L. Imbasciati et al., "Thermo-Mechanical Characterization of Insulated and Epoxy-Impregnated Nb<sub>3</sub>Sn Composites," in press, *IEEE Trans. Appl. Supercond.*, ASC 2002
  - [4.9] D. R. Chichili et al., "Investigation of Cable Insulation and Thermo-Mechanical Properties of Nb<sub>3</sub>Sn Composite," *IEEE Trans. Appl. Supercond.*, Vol. 10 N. 1, pp 1317-1320, 2000
  - [4.10] R. Conway, G. Ambrosio, P. Bauer, D.R. Chichili, L. Elementi, J.-M. Rey, "Calibration of Fixture for Bi-axial Loading of Epoxy Impregnated Nb<sub>3</sub>Sn Cable Ten-Stack, using Epoxy, G10, and Aluminum Samples," TD-01-077, Dec. 01
  - [4.11] J.M. van Oort, "Critical current degradation in Nb<sub>3</sub>Sn superconductors in accelerator magnets," *Ph.D. Thesis*, Univ. of Twente
  - [4.12] D.R. Dietderich, R.M. Scanlan, R.P. Walsh, J.R. Miller, "Critical Current of Superconducting Rutherford Cable in High Magnetic Fields with Transverse Pressure," *IEEE Trans. Applied Supercond.*, Vol. 9, N. 2, June 1999
  - [4.13] S. Caspi, "Calculating Quench Propagation with ANSYS," in press, *IEEE Trans. Appl. Supercond.*, proceedings of ASC 2002

# 5. Quench Experiment on Subscale Nb<sub>3</sub>Sn Magnet

Chapter 5 Table of Contents:	Page
5. Quench Experiment on Subscale Nb <sub>3</sub> Sn Magnet	1
5.1 Concept of the experiment	2
5.2 Experiment setup	3
5.2.a General features of LBNL Subscale Magnet Program	3
5.2.b Set up for the quench test	5
5.2.c Description of the magnet for the quench test (SM05)	7
5.3 Description of the Test	13
5.3.a Training and ramp rate study	13
5.3.b Spot heater study	14
5.3.c Thermal shock study	15
5.4 Adiabatic quench process simulation	20
5.4.a Quench Integral	20
5.4.b Quench simulations	22
5.5 Mechanical analysis	23
References	27

## 5.1 Concept of the experiment

The studies presented in chapter 2 showed that, during quenches in long Nb<sub>3</sub>Sn magnets for particle accelerators, peak temperatures above 300 K can arise at the quench origin. Nb<sub>3</sub>Sn is a brittle material and it has yet to be determined to what extent it is affected by thermo-mechanical stresses during a magnet quench. Rapid thermal expansion of conductor and large temperature gradients during a magnet quench can affect the performance, for example causing detrainning, or even result in permanent damage of the magnet. For the design of a reliable Nb<sub>3</sub>Sn accelerator magnet, it is necessary to define the maximum temperature that is acceptable in the coils during a quench. Although critical current versus strain data are well established for Nb<sub>3</sub>Sn strands, little is known how these limitations apply in the case of the thermal shock experienced by the conductor during a magnet quench.

A “quench experiment” was performed on cables (Chapter 4) in order to measure the critical current degradation as a function of the peak temperature during a quench. This experiment indicated that, for impregnated coils, a limiting temperature could be the glass transition point of the insulation, which occurs at about 400 K for epoxy resins. At that temperature, the epoxy becomes soft and, even if the transition is reversible, the changes in its electrical and mechanical properties increase the probability of a short circuit.

In order to reproduce as realistically as possible the thermo-mechanical conditions in a cable during a magnet quench, we continued the experimental program on a small Nb<sub>3</sub>Sn magnet, within a collaboration between Fermilab and Lawrence Berkeley National Laboratory (LBNL). In this chapter, we describe the experiment conditions, the results, and analytical calculations of the stresses/strains induced in the conductor during the magnet quench.

The experiment was performed on a LBNL Subscale Magnet (SM). A coil was instrumented with a spot heater and two voltage taps across the spot heater section in the high field region of the magnet. The magnet was trained until a quench plateau was reached (at about 9 kA, 10.5 T). The quench experiment followed a procedure similar to the one used for the cable quench experiment. At a current below the quench current, a dump time delay was set, and a quench was started with the spot heater. The Joule heating of the cable during the quench, for the programmed delay time, allowed the temperature to rise at the spot heater location. The temperature was measured via the resistivity of the cable segment underneath the spot heater. Since the process was fast (lasting few seconds at most) high thermal gradients between the “hot spot” and the surroundings, induced thermo-mechanical stresses (“thermal-shock”).

The magnet quench current was measured after each high temperature excursion, in order to establish the effects of the thermal-shock test on the magnet performance as a function of the peak temperature.

The mechanical analysis was performed after the experiment using models temperature profiles (both in space and in time) based on the measured resistance data.

## 5.2 Experiment setup

### 5.2.a General features of LBNL Subscale Magnet Program

The Subscale Magnet Program [5.1], [5.2] was launched at LBNL with the aim of addressing R&D issues in a fast and cost effective way. Building a small magnet (about 1/3 scale with respect to a short model magnet) requires a significantly lower amount of resources than a short model accelerator magnet. In addition, the magnet structure is completely reusable. A sub-scale mechanical model was first used to test the pressurized bladder technology for applying pre-stress to the structure [5.3], a technology that was then successfully used for short model magnets (for example RD-3 magnet series). Each coil is made of ~20-meter long sub-sized cable (8 mm wide, 1.3 mm thick), and tests can be performed in a small cryostat, without the use of large background field magnets. Therefore, the Subsize Magnets are an effective way to test state-of-the-art conductor.

The LBNL Subscale Magnet parameters are:

- Field range: 8 – 12 tesla
- Maximum current: 8 – 10 kA
- Magnet inductance: 0.2 – 0.4 mH
- Stored energy: < 20 kJ
- Two “double-pancake” racetrack coils (i.e. each coil is wound in two layers without splice)
- Conductor per coil: ~ 5 kg

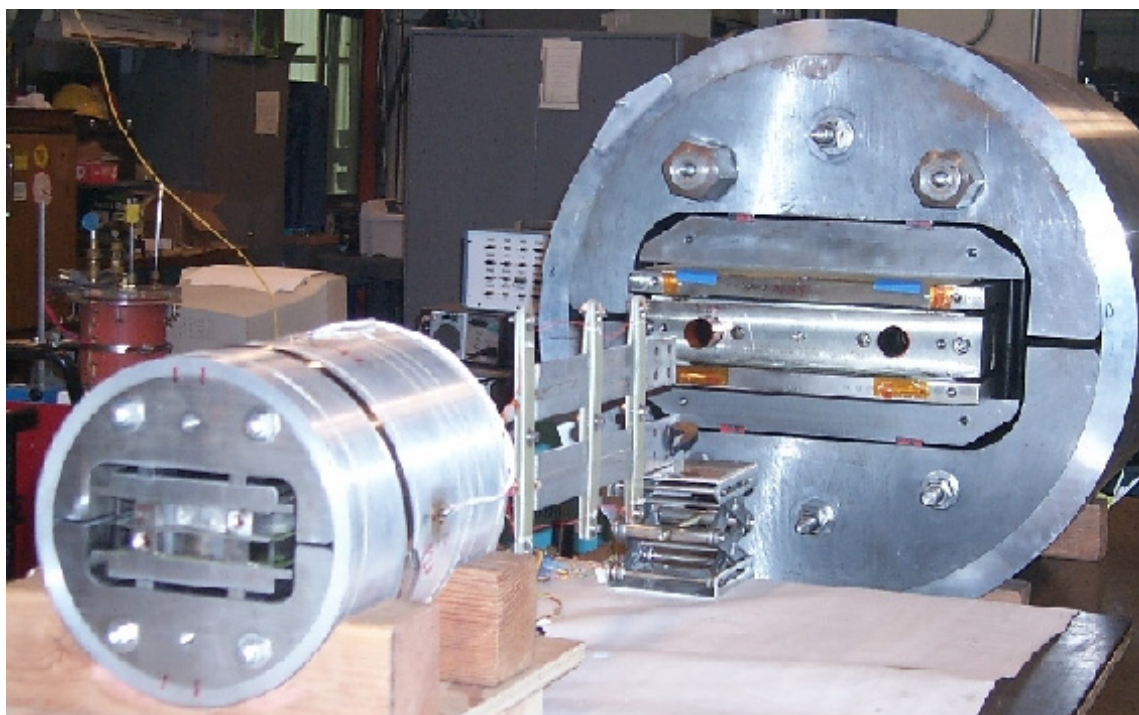


Fig. 5.1: Full-scale RD3 magnet (in the back), and Subscale Magnet (in the front) (LBNL Supercon Group).

### - Field distribution

The magnet design consists of two “double-pancake racetrack” coils, connected in a common coil configuration (i.e. the current in one coil flows in opposite directions with respect to the current in the other coil). As can be seen in Fig. 5.2, the magnet has no bore, and the coils are separated by a small gap. The field distribution, computed for the baseline configuration, is shown in Fig. 5.2 and in Fig. 5.3 [5.4]. The field pattern is typical of racetrack coils in a common coil configuration: the field is maximum along the inner edge of the first layer and close to zero towards the external side of the second layer.

The 3D analysis (Fig. 5.3) showed that the peak field occurs in the straight section thanks to the effect of the iron of the yoke, the island and the pads, in the shape as shown in Fig. 5.3. The peak field intensity in the ends is about 10 % less than the peak field in the straight section.

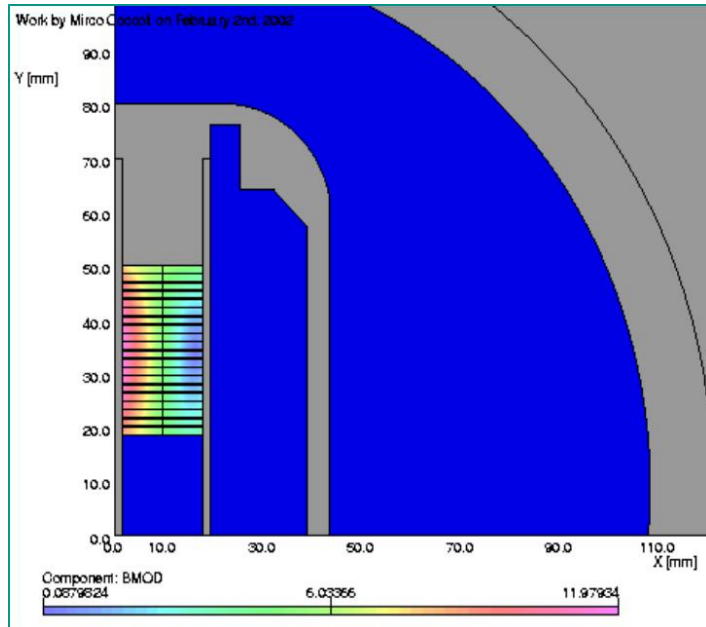


Fig. 5.2: Magnetic field intensity (tesla) in one quadrant of the cross section of the LBNL small magnet (calculated for SM01 at 9.9 kA).

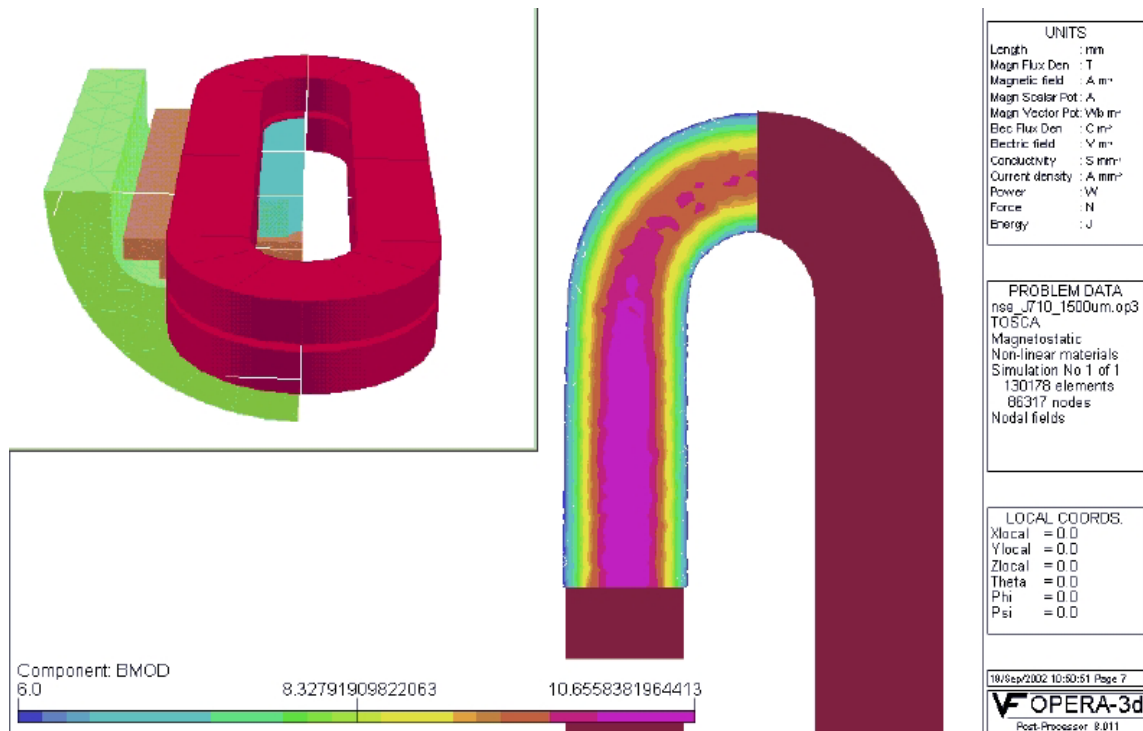


Fig. 5.3: Magnetic field intensity (tesla) in one quadrant of the LBNL small magnet (calculated for SM03 at 8864 A, with 3 mm gap between the coils, using the model shown in the left corner).

### - Instrumentation and Test

The Subscale Magnets are usually equipped with a very basic instrumentation, consisting of a couple of voltage taps across each splice, a temperature sensor for each module close to splices, and some resistive strain gauges on the shell mid-plane. There are no quench protection heaters, since the protection system relies on energy extraction through an external dump resistor of  $\sim 50 \text{ m}\Omega$ . Additional instrumentation is added when it is needed in order to study specific issues.

The Subscale Magnets are tested at the LBNL-Supercon test facility using a small cryostat, which does not require the use of a refrigerator. Liquid helium is transferred from dewars.

There are two different data acquisition systems. One data logger is used for recording the voltage signals during quench, with an acquisition rate of 0.2-1 ms, inversely proportional to the quench duration (having a fixed data file size). Another acquisition system is used to record fast events, such as magnetic flux changes due to conductor motion, which can be registered with an acquisition rate of the order of 10  $\mu\text{s}$ .

#### **5.2.b Set up for the quench test**

As described in the previous chapter, the quench tests on cables lacked some mechanical features characteristic of an accelerator magnet. In particular, the mechanical support in the cross-section of the cable sample holder was weak. The use of LBNL small coils allowed a continuation and an improvement of the quench tests program. In fact, the facility at LBNL allowed the use of state-of-the-art  $\text{Nb}_3\text{Sn}$  conductor, in a mechanical environment similar to that of an accelerator magnet. In order to have a clear indication of the effect of the peak temperature on the magnet performance, it is necessary to know first the magnet short sample limit. The LBNL Subscale Magnets, using standard cable and state-of-the-art  $\text{Nb}_3\text{Sn}$  strands, have routinely achieved the predicted short sample current in the past. In addition to reasons mentioned above, there were other factors, such as fabrication cost, helium consumption, and time required for measurement preparation, which made it more advantageous to perform the quench test on a Subscale Magnet than on an accelerator magnet model.

However, some details of the experiment set up had to be addressed in order to reach the conditions required to perform the test. In particular, previous testing of small magnets has shown a rapid current decay after a quench. Among the causes of the fast current decay are high quench propagation velocities, especially when the quench occurs very close to the short sample limit, a small inductance, and quench-back induced by the current decay. To understand the quench process in the Subscale Magnets, we looked at previous quench studies, on one of these magnets, SM01-a [5.5]. Fig. 5.4 shows two events that occurred during the test of SM01-a. One is a “spontaneous” quench, occurred during training of SM01-a, and the second is a spot heater induced quench, at a current just below the short sample limit. Fig. 5.4-left, shows the voltage imbalance between the two coils of the magnet. We can see that the “training” quench propagates very fast reaching a  $dV/dt$  of 1000 V/s in  $\sim 1 \text{ ms}$ . A few ms after the quench in the first coil, the voltage imbalance dropped, because the voltage in the second coil started to rise, due to the so-called quench-back. The voltage rise, during the quench induced by the spot heater, is much slower than during the training quench, and the quench-back does not occur, during the 20 ms before the dump connection.

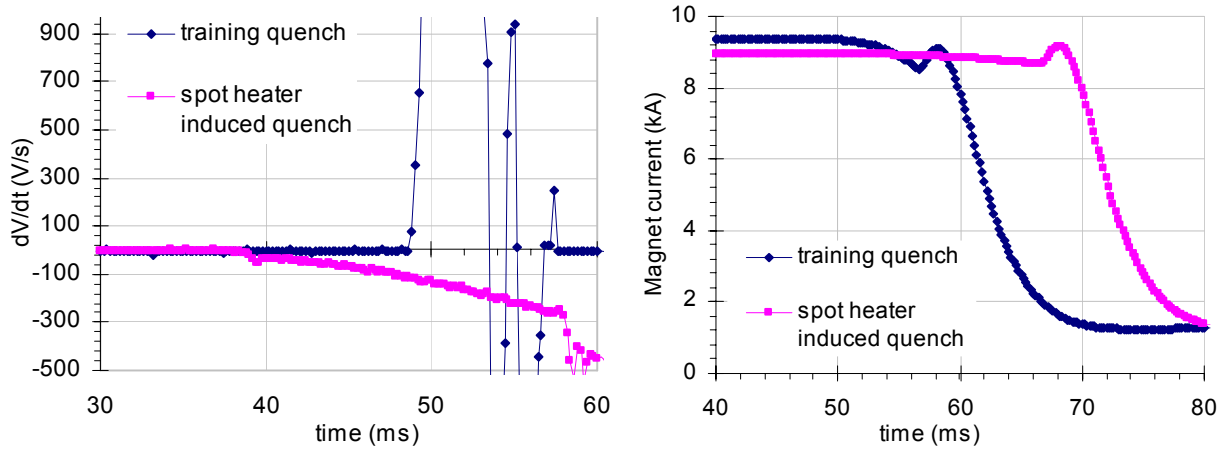


Fig. 5.4: Quench tests of magnet SM01-a: voltage difference between the two coils (left), and current decays (right), after a quench occurred during training and after a spot heater induced quench. The voltage rise after the quench that occurred during training is much steeper than the voltage rise after the spot heater induced quench.

The rate of the voltage rise affects the current decay, as shown in Fig. 5.4-right. The same figure shows that after the spot heater induced quench, the current decayed by about 300 A in 30 ms (total  $\Delta I/\Delta t = 10$  kA/s), while, after the spontaneous quench, the current decayed by  $\sim 800$  A in 8 ms (total  $\Delta I/\Delta t = 100$  kA/s). The instantaneous rates of current decay are even higher (Fig. 5.5-left). To understand the quench-back phenomenon, we should look at the results of ramp rate studies (Fig. 5.5-right), which indicate that ramp rates of 200 A/s, or higher, reduced the quench current to  $\sim 20\%$  of the maximum current. On the other hand, Fig 5.5 shows that the quench-back did not occur, during the quench induced by the spot heater, until the current drop was higher than the 50000 A/s. Therefore, we can say that the quench-back is not an immediate consequence of the current change, but there might be a time delay, possibly due to a thermal response to eddy current heating.

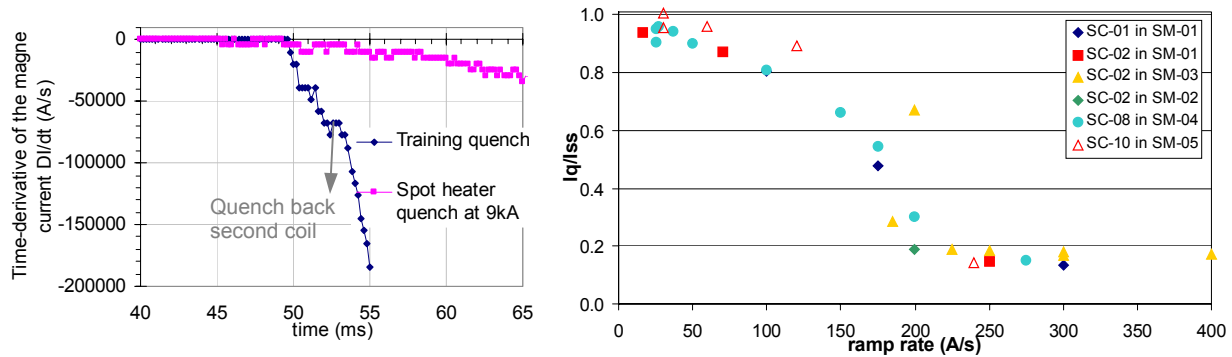


Fig. 5.5: Time-derivative of the magnet current for a training, and a spot heater induced quench of SM01-a (left), and ramp rate studies in several SM (right); SM01 consisted of SC01 and SC02.

In order to reach temperatures of 300 K or higher, some modifications were implemented in the experiment set up, in the attempt to maintain the current at a high level for a longer time than in previous magnet tests. As long as the current remains nearly constant, the quench back can be avoided, and the temperature increases faster.



During previous small magnet tests at LBNL, the power supply was set in the voltage mode, in order to have a stable current during ramps. In this mode, the current decreases after the quench according to the voltage rise, and the power supply works almost like a passive protection system. Quench simulations showed that, in voltage mode, the current decay time is very sensitive to quench propagation velocities, and that it may not be possible to reach temperatures of 300 K, if the quench velocities are 80 m/s or higher [5.6].

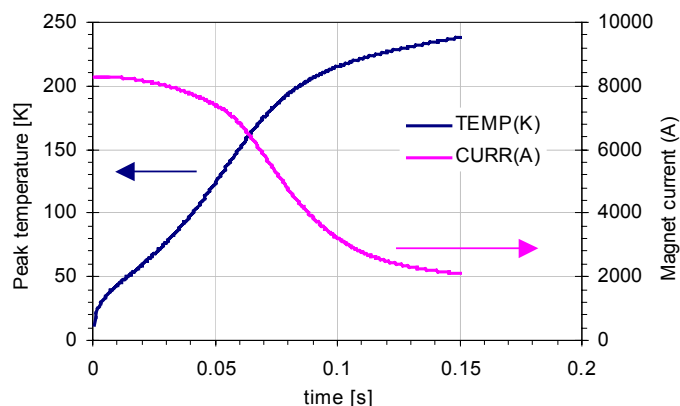


Fig. 5.6: Quench process simulation with initial longitudinal quench velocity of  $\sim 80$  m/s.

Therefore, the power supply was set in the current mode, in which the system supplies a constant current almost independently from the voltage of the magnet, up to 50-60 V. Nonetheless, in the first thermal cycle, even though the current generated by the power supply remained constant during quenches, part of the current flowed through another branch of the circuit. This additional circuit (consisting of a series of capacitors) was used to improve the stability of the current during the ramp. In the second thermal cycle, most of the capacitors were removed, in order to maintain high currents after the quench until the voltage limit was reached.

### 5.2.c Description of the magnet for the quench test (SM05)

The thermal shock quench test was performed on the fifth Subscale Magnet assembled at LBNL (named SM05), consisting of SC10 (the tenth coil of the SM program fabricated and instrumented for this test) and SC01 (the first coil of the SM program). Several modifications were introduced in the coil and magnet fabrication, in order to perform the thermal shock experiment.

#### - Conductor characteristics

The cable for the Subscale Magnets is fabricated at LBNL-Supercon-AFRD, by the superconducting magnet cable group. The strands used for fabricating was a Modified Jelly Roll (MJR) conductor, produced by Oxford Superconducting Technology (OST). The cable and conductor parameters for the coils of SM05 are listed in Table 5.1 (details in [5.7]). The heat treatment cycles are shown in Fig. 5.7. The cable insulation consisted of epoxy impregnated S2-glass sleeve.

The main difference between the strands used for SC01 and SC10 is the copper content. The conductor for SC10 had  $\sim 60\%$  copper content, while the one used in SC01 had only 44.9%, in order to have a lower critical current in SC10 than in SC01. In addition, the reaction cycle chosen for SC10 was shorter than the reaction cycle for SC01. Test results of this reaction cycle show a slightly lower critical current density in the non-copper area, and a RRR relatively high for this type of conductor. The lower critical current of SC10 than SC01 assured that the coil

under investigation determined the magnet current limit. In addition, a high RRR lowered the voltage rise during the quench, thus diminishing the current drop before activation of the dump switch.

Conductor parameters	Coil 1	Coil 10
N of strands	20	20
Manifactor	OST	OST
Cu:SC	0.81	1.5
Cable width (mm)	8	7.84
Cable thickness (mm)	1.3	1.27
Strand diameter (mm)	0.701	0.672
Pitch angle (°)	17	15.9
Packing factor	0.83	0.83
$J_c$ (A/mm <sup>2</sup> ) @12T/4.2K	2265	1763
$I_{SS}$ (A)*	9924	9101
$B_{peak}$ (T) in the coil at $I_{SS}$	11.985	10.57
Cu RRR	41	54
Insulation (mm)	0.15	0.15

Table 5.1: Conductor parameters of Subscale Magnet 5 coils.

\*Best performance of SM01 and SM05 respectively.

The critical current of two “witness” samples (two virgin strand samples reacted together with the coil) are reported in Table 5.2. The total field in the table is the sum of the background field and the self-field induced by the sample. The critical current of the cable is computed without taking into account possible degradation due to cable manufacture.

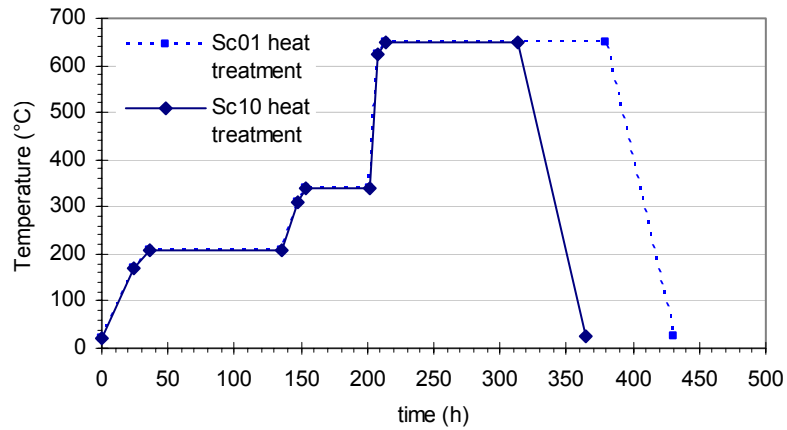


Fig. 5.7: Heat treatment cycle for Sc01 and SC10.

Total Field (T)	Strand Sample L 26 Current (A)	Cable Current (kA)	Strand Sample L 35 Current (A)	Cable Current (kA)	Average Current (kA)
10.16	448	8.96			8.96
11.13	368	7.36	365	7.3	7.33
12.1	296	5.92	293	5.86	5.89

Table 5.2:  $I_c$  measurements of virgin strand samples, at 4.2 K, of the same strand type as used in SC10.

The short sample current reported in Table 5.1 is the maximum current reached during the test of SM05 (Fig. 5.22). The peak field corresponding to this current was computed using the load line in Fig. 5.8. This load line was derived from a Finite Element model of SM05, which takes into account that the actual size of the gap between the two coils of SM05 was 7.8 mm (slightly larger than the gap of previous magnets). The point of intersection between the magnet load line and the strand critical current measurements is at 8.7 kA (10.34 T), slightly lower than the 9.1 kA maximum value reached during test.

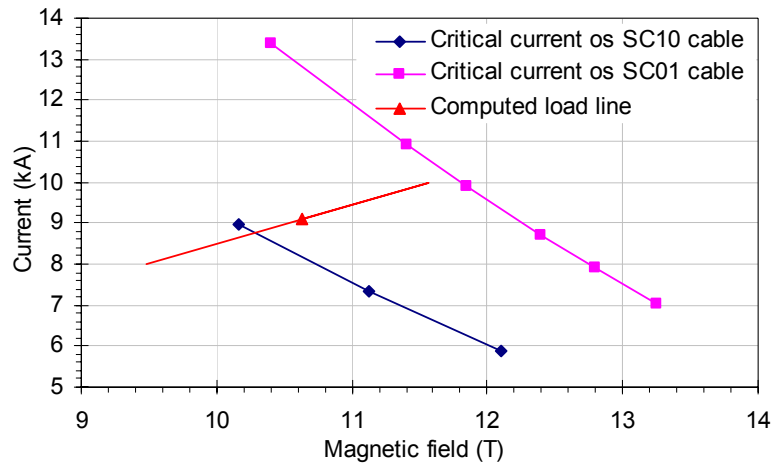


Fig. 5.8: SM05 load line and strand critical currents for SC10 and SC01. The measured maximum current reached during test is indicated by the triangle.

#### - SC10 instrumentation

SC10 was instrumented with a spot heater (SH) in the high field region, voltage taps (VT) across the spot heater, and a temperature sensor (TS), close to the spot heater. The spot heater and voltage taps positions over the inner layer of SC10 are indicated in Fig. 5.9. The spot heater was inserted in the highest field region (straight section of the inner layer), so that the effect of local degradation may result in a reduction of the magnet current.

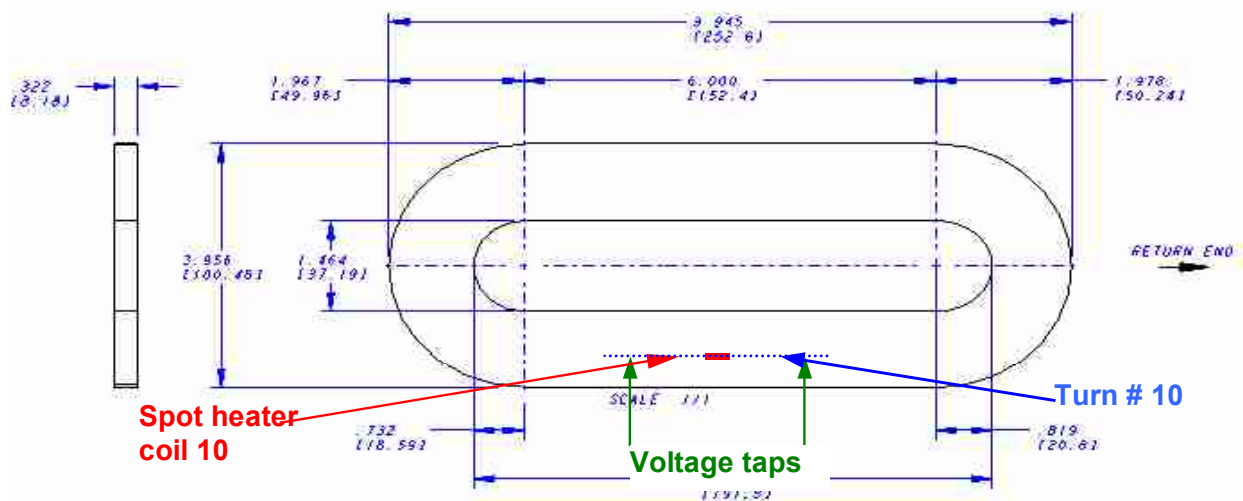


Fig. 5.9: Coil geometry and instrumentation scheme (all dimensions in inches [mm]).

### - Coil fabrication

After winding the first layer, with the standard tension of 40 lbs over the cable, the coil turned out to be thinner than expected, and an extra turn was added, for a total of 21 turns per layer. The total length of the cable used was 11.6 m for the first layer, and 11.2 m for the second.

The coil instrumentation was installed during winding of the second layer (top layer, which corresponds to the inner layer of the magnet assembly). A thin stainless steel spacer (0.127 mm) was inserted between turns # 10 and # 11. The stainless steel spacer was removed after reaction to install the spot heater. In addition, three thin copper strips were placed across the cable, on turn #10. Two of these strips were to be used as voltage taps, and one was used to attach the temperature sensor on it. The copper strips for the voltage taps were 88.9 mm apart (center to center), and the strip for the temperature sensor was 25.4 mm from the spot heater position.

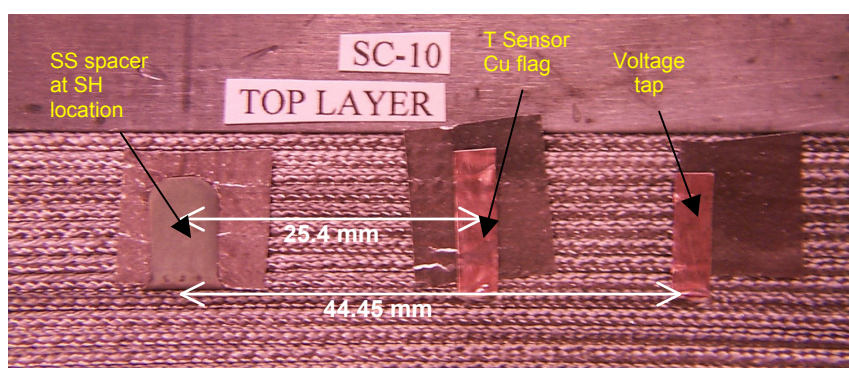


Fig. 5.10: Spacer at the spot heater location and copper flags for temperature sensor and voltage taps after reaction.

The two voltage taps leads, the spot heater, and the four stainless steel legs of the spot heater were fabricated by photo edging on a Kapton foil (“trace”). The four legs of the spot heater, allowed four-wire measurements of the spot heater resistance ( $\sim 2.5 \Omega$  at room temperature and  $1.6 \Omega$  at liquid helium temperature). The Kapton foil was trimmed to fit the coil dimensions. Cuts were made corresponding to the voltage tap locations, exposing the stainless steel trace, over which the copper flags were soldered. The spot heater was cut along three sides, bent, and inserted between turn # 10 and # 11. The spot heater insulation consisted of  $51 \mu\text{m}$ -thick Kapton, plus the cable insulation, between the spot heater and turn # 10, and of  $114 \mu\text{m}$ -thick Kapton, plus the cable insulation, between the spot heater and turn # 11.

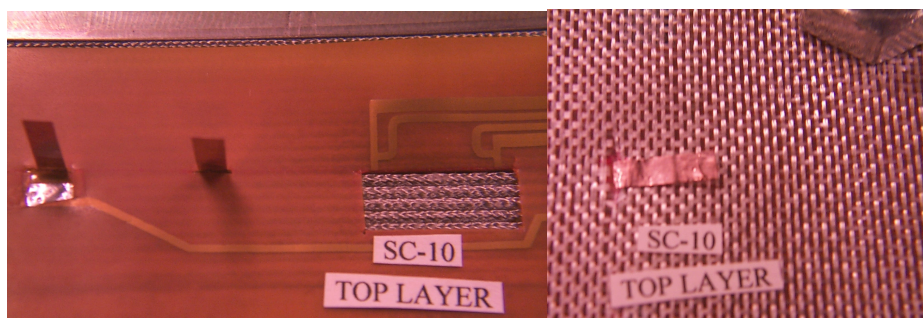


Fig. 5.11: The trace lies on the coil after reaction, before impregnation. The spot heater is inserted between two middle turns. The copper flags for temperature sensor and voltage taps emerge from the Kapton foil of the trace (left). Copper flag for the temperature sensor over the fiberglass mat on top of the coil (right).



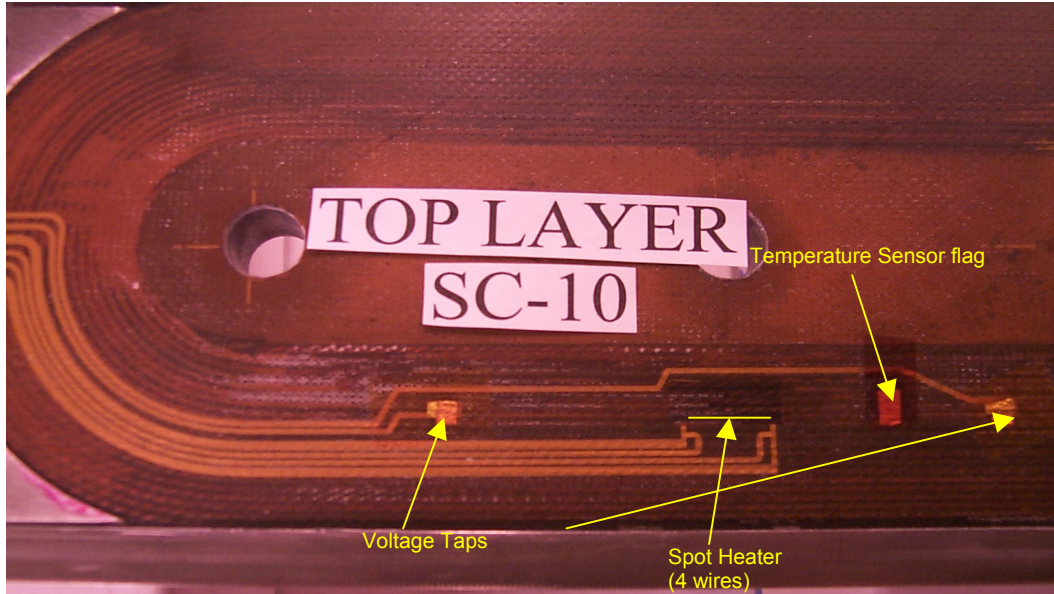


Fig. 5.12: After impregnation, top layer with instrumentation (inner layer in the magnet configuration).

After soldering the voltage taps to the trace, a 127  $\mu\text{m}$  fiberglass mat is laid on the coil, to help the epoxy impregnation of the entire coil. After impregnation, the coil was inspected, and it was seen that the impregnation was good on the top layer, and acceptable in the bottom layer (with some small voids at the lead side).

The temperature sensor (CERNOX<sup>TM\*</sup>, high temperature type) was installed after the coil impregnation, and before magnet assembly (see [5.7]). There is no bore between the two coils, but rather a spacer, made of two G10 (NEMA) plates near the coils, and several layers of insulation. It was decided to place a split spacer between the two coils, so that the two layers would follow the coils when they separate from each other under Lorentz forces. The NEMA plate adjacent to SC10 had a hole and a groove in order to accommodate the temperature sensor and its wires. Two twisted pairs of wires connected the temperature sensor allowed a four-wire measurement of its resistance. A small dab of Apiezon N was put on the contact area of the temperature sensor. The copper flag was trimmed to fit the sensor. A small amount of RTV was used to hold the sensor and to insulate the leads filling up the groove in the plate, near the sensor. A small plug of RTV-impregnated fiberglass was used to fill the hole in the NEMA plate and to hold the sensor in position. This material was chosen for the plug, in order to allow some pressure on the sensor, to improve the thermal contact, and to avoid the use of a hard material that could damage the sensor. After the first thermal cycle, we carefully investigated the accuracy of the peak temperature reading in the coil after a quench. It was then noticed that liquid helium would be able to penetrate around the plug and come in close contact with the sensor, on the side and on the top of the sensor case, and at the lead joints. The additional cooling, due to the contact with liquid helium, is believed to be the cause of the reduced temperature reading of the sensor, with respect with the temperature derived from the resistance measured during the experiment.



Fig. 5.13: Temperature sensor under the NEMA layer with the groove for the wires, and a hole for the temperature sensor; a cap of RTV-impregnated fiberglass protects the sensor.

\* Trade mark of Lakeshore Inc.

- SM05 assembly

In order to reduce the current decay after a quench, it was decided to increase the inductance as much as possible by opening the gap between the coils, thereby changing the position of the skins with respect to the standard SM configuration shown in Fig. 5.14. All the stainless steel skins were replaced by NEMA skins, and placed between the two coils. The gap increase between the two coils decreased the mutual inductance of the two coils, thus helping to avoid quench-back of SC01.

A low pre-stress was applied in order to allow separation, and therefore faster training (see training of SM01-a and SM01-b [5.5]). Therefore, minimum size keys of 6.35 mm were installed. From the dimension of the magnet components, the size of the central spacer was calculated to be 4.953 mm (see [5.7]).

The resulting pre-stress was calculated to be 6 MPa at 300 K and 97 MPa at 4.2 K.

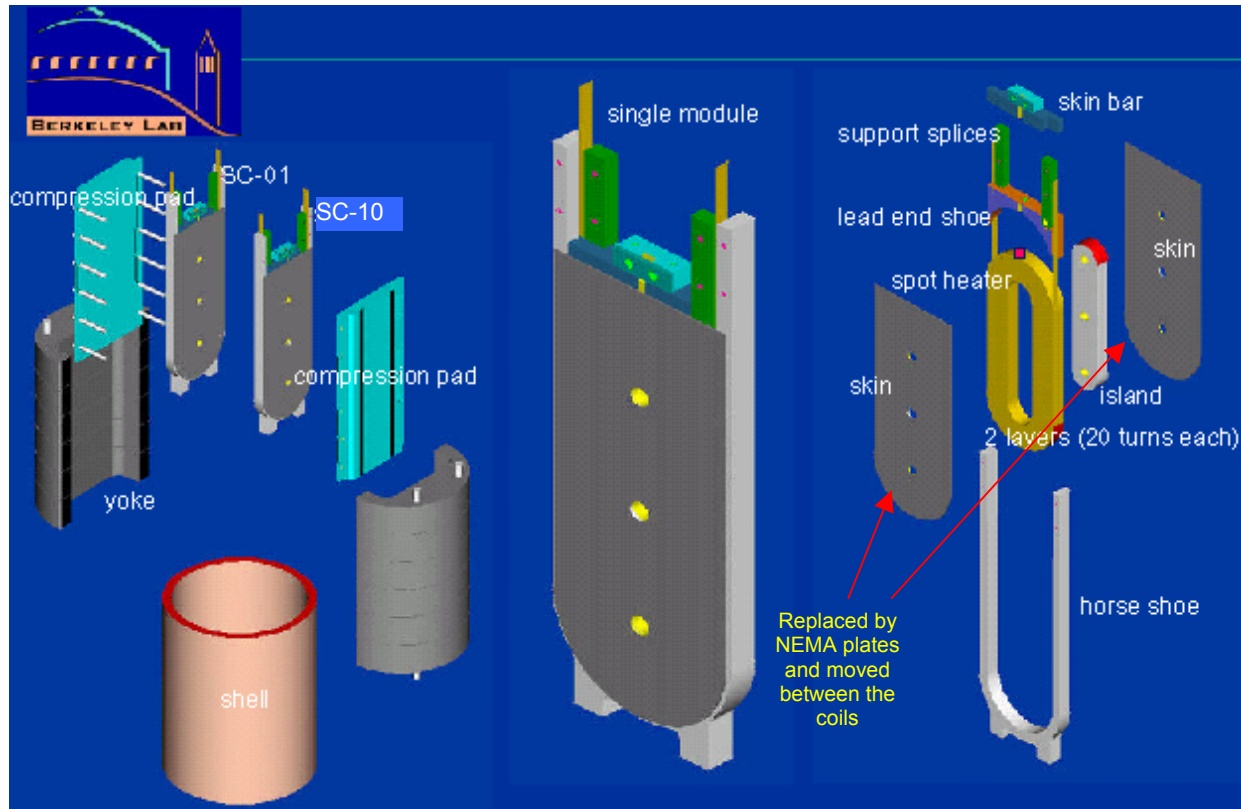


Fig. 5.14: Magnet assembly.

### 5.3 Description of the Test

Before the thermal shock experiment, several tests were performed on the magnet. Among those the residual resistivity ratio (RRR) of the coils was measured during cool down. It was 41 for SC-01, and 54 for SC-10.

#### 5.3.a Training and ramp rate study

The magnet training started by ramping the current up to the first quench, with a ramp rate of 15 A/s and holding every thousand amps for a while, following the standard test procedure at LBNL. The very first quench occurred at low current due to low liquid helium level. The second quench occurred at 97.7% of the computed short sample current (SS). The magnet trained very fast, reaching 101.3 % of SS at the fifth quench. The highest current reached was 8757 A (10.47 T), with a ramp rate of 15 A/s.

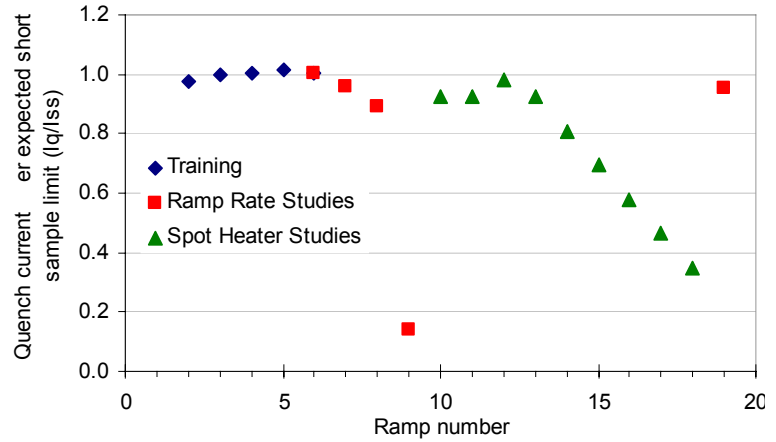


Fig. 5.15: Quench history of SM05-first thermal cycle.

During current ramps, the fast data logging system registered several events, similar to the one shown in Fig. 5.16-left. These events are interpreted as fast motion of conductor, or part of the coils. In fact we see that the signals of each coil have opposite signs, and therefore can be distinguished from power supply induced noise, and are also different from spikes due to flux motion in the superconductor, which have a lower frequency [5.8]. Some of the first training quenches were anticipated by similar fast motion signals. Successive quenches were not anticipated by fast motion (Fig. 5.16-right), showing improvement in the training process.

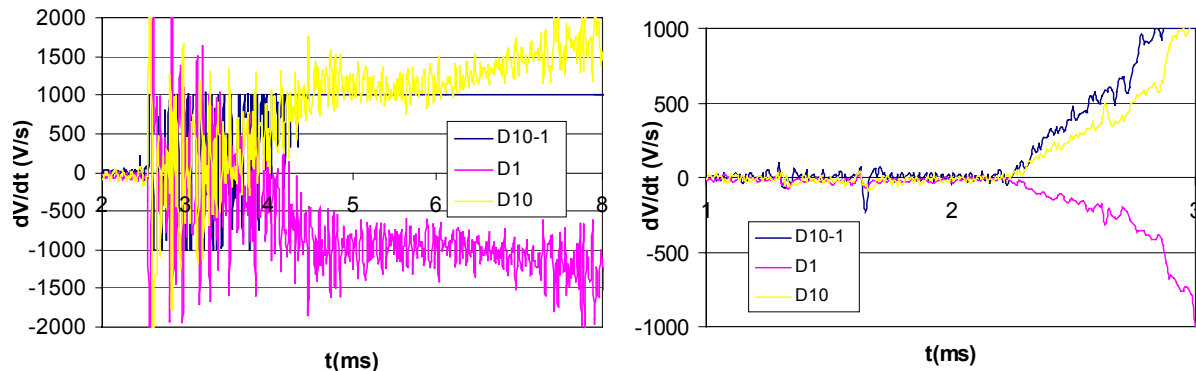


Fig. 5.16: Quench # 2 triggered by a fast motion event (left), and Quench # 6 (right). The signals correspond to the voltage derivative over coil 10, coil 1 and the difference between the two (D10, D1, and D10-1).

After the magnet training, the ramp rate dependence was measured. The results are shown in Fig. 5.17. The ramp rate dependence of SM05 was similar to that of other small magnets. It is characterized by a large drop of the quench current at ramp rates between 100 and 200 A/s [5.8].

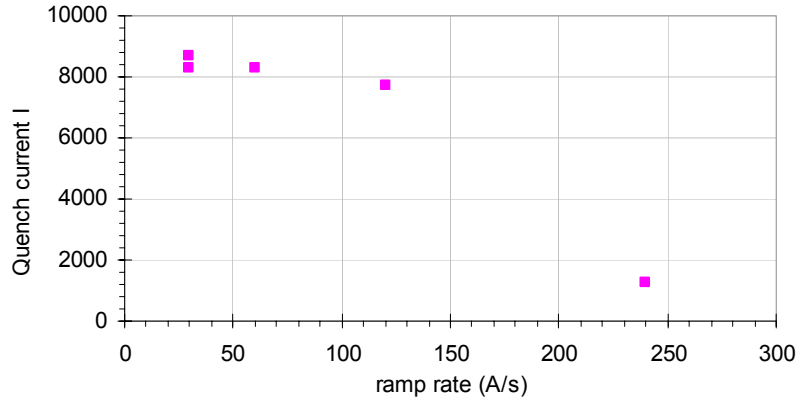


Fig. 5.17: Ramp rate sensitivity of SM05.

### 5.3.b Spot heater study

During the magnet test, spot heater studies were performed with the goal of finding the energy needed to initiate a quench. The spot heater was connected to an electronically controlled capacitor bank. At currents of six kA or below, the initial low voltage discharge would not induce a quench; when the voltage level was raised further, a quench was initiated. The procedure unfortunately prevented us from firing small amounts of energy at high currents in the magnet. On the other hand, it was possible to calculate more precisely the energy amount that induced the quench by integrating the power deposited in the coil from the start of the capacitor discharge until the moment the quench started (Fig. 5.18-right). The results of the quench energy test obtained by this method are summarized in Fig. 5.18-left.

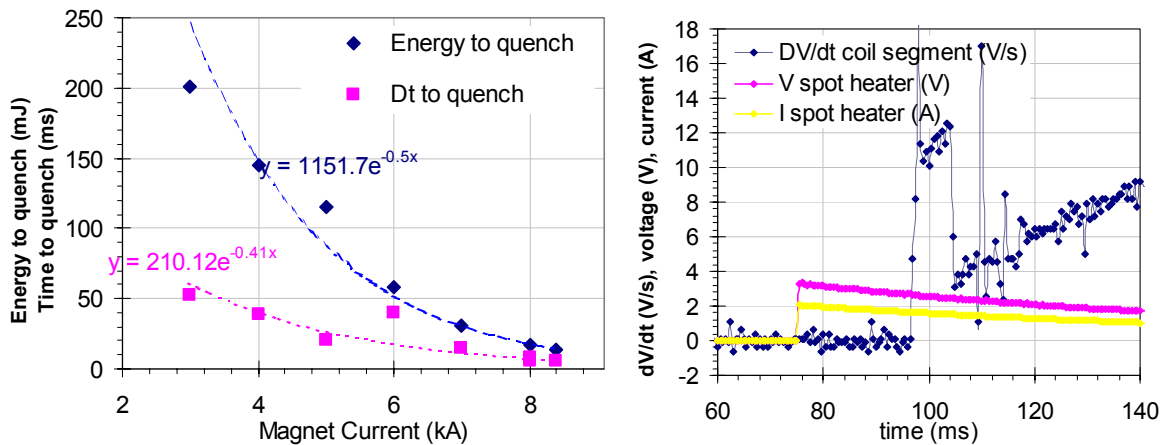


Fig. 5.18: Quench energy study: energy and time to quench after heater firing (left), and voltage rise (V/s) of the spot heater segment after capacitor discharge (voltage and current in the spot heater) for spot heater event H07 (right).

We have to notice that the energy amount reported here is not released solely in the strands, but it is distributed over the spot heater itself, the insulation of the spot heater (both sides), and the insulation of the cable. Therefore, the energy values reported here can be regarded as upper limits to the minimum quench energy.



From signals as shown in Fig. 5.18-right, it is possible also to evaluate the quench propagation velocity along the cable (so called longitudinal direction). In fact, we can see that the derivative of the voltage over the cable segment over the spot heater has a sharp rise and a sharp decrease, corresponding to the beginning of the quench, and to the end of the propagation up to the edges of the segment. The velocity calculated using this method, for the case represented in Fig. 5.18, is 5.3 m/s, at a magnet current of 5 kA, 20-30 m/s at 8-8.5 kA, and 2.4 at 3 kA.

### 5.3.c Thermal shock study

#### - First thermal cycle

The thermal shock test began in the following way: the magnet current was increase up to 8000 A ( $I/I_{ss} = 93\%$ ) at 30 A/s, a short dump delay time (10 ms) was set, and the quench was induced with the spot heater. The short delay time was chosen in order to check the procedure, before causing some damage to the magnet with an excessive “thermal shock”.

Due to the power supply settings mentioned before, the current did not remain constant after the quench, even though the voltage over the magnet was below the power supply voltage limit. The current fell to 7.4 kA before the dump switch was activated.

The test continued by repeating the spot heater induced quench at high current, with higher delays (40 and 60 ms). The voltage signals of these events (H03 and H04) show clearly that quench back occurs in SC01, 13-14 ms after the quench start in SC10. After the quench back, the voltage over the magnet rises faster, inducing a faster current decay. Before the dump activation, the current was ~4 kA in H03 (

Fig. 5.19).

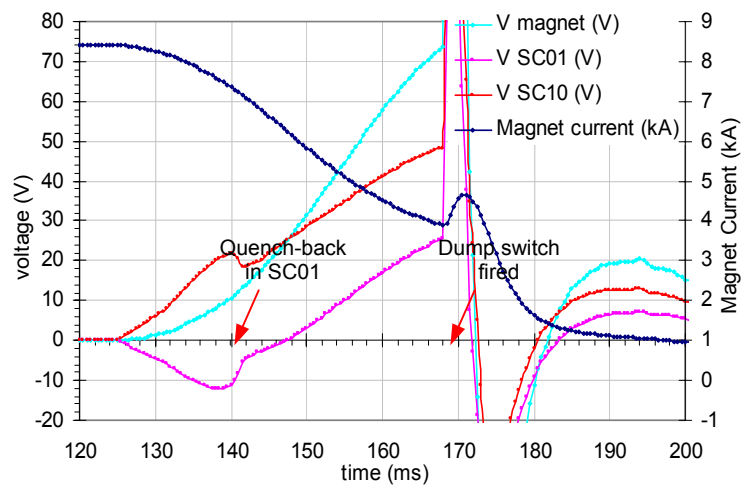


Fig. 5.19: Spot heater event # 3.

To reduce the quench propagation velocity and to avoid quench back, we continued the spot heater events series lowering the magnet current, and increasing the dump delay times. At 6 kA, the quench back was delayed to 70 ms, and at 5 kA and lower the quench back was not visible. The maximum temperature registered by the Cernox thermometer was ~195 K, during the last spot heater event (H09), at 3 kA. After H09, the magnet quench current could not be measured, and the test series was interrupted, because of lack of liquid helium. It was decided to warm up the magnet to room temperature, to perform a thermal cycle, while analyzing the data and planning for the following test series with higher peak temperatures.

### - Data analysis-first thermal cycle

The data analysis consisted in examining the voltage signal of the cable segment close to the spot heater, and the signals coming from the adjacent coil sections. One section included the half turns of the inner layer, from the spot heater to a splice ( $V10_{inner}$ ). The other section included the outer layer, and the other half turns of the inner layer, that is from the spot heater to the other joint ( $V10_{outer}$ ).

As an example, we present here in detail the last spot heater event of the first thermal cycle (H09). Fig. 5.20-left shows the voltage signals and the current decay during H09. The resistance (Fig. 5.20-right) was calculated dividing the voltage by the current (no inductive signal compensation, since the inductance was small).

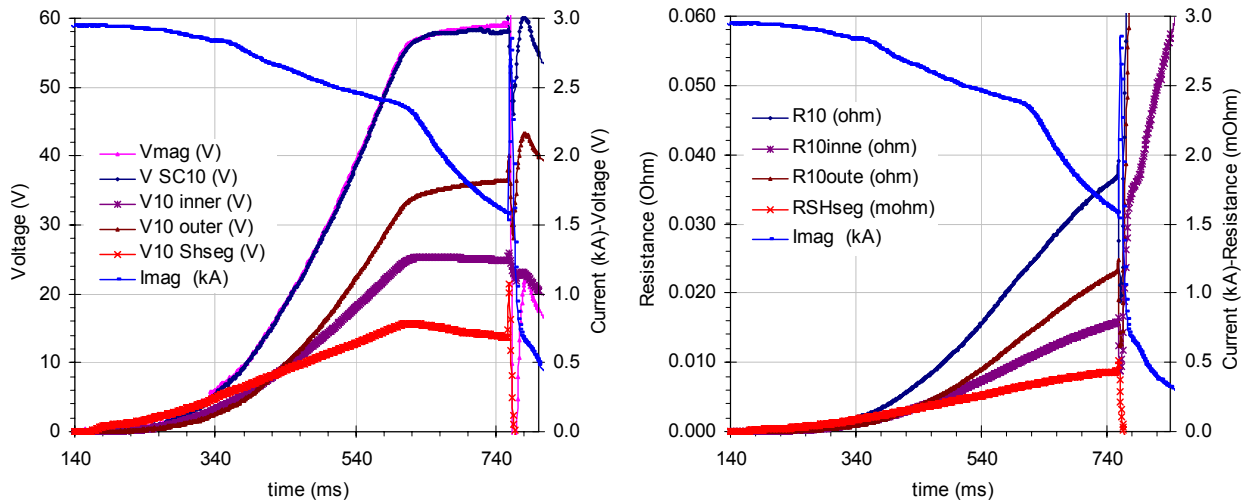


Fig. 5.20: Main voltage and current signals of the last spot heater event of the first thermal cycle (left); Resistance growth (right).

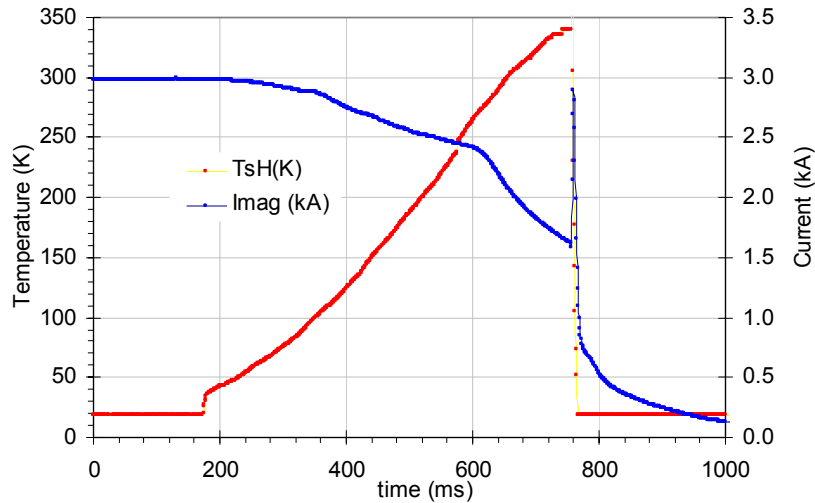


Fig. 5.21: Temperature and current of the last spot heater event of the first thermal cycle (H09).

The temperature (Fig. 5.21) was derived from the resistance of the coil segment close to the spot heater, by comparison with the resistance measured during the magnet warm up after the second thermal cycle (the temperature calibration is described in [5.7]). We can see that the peak temperature measured from the voltage signal (340 K) is much higher than the temperature measured by the sensor during the quench (195 K), probably due to cooling effects of the liquid helium close to the sensor (see Fig. 5.13).

The main results of all events of the first thermal cycle are summarized in Table 5.3

Ramp #	Current (kA)	Dump delay (ms)	Quench back time SC01 (ms)	MIIts ( $10^6 A^2 s$ )	T sensor (K)	R SHseg (mOhm)	T SHseg (K)
H01	8.0	10	14	1.29	80	0.074	84
H02	8.0	10	14.2	1.31	80	0.074	80
H03	8.4	40	13	2.11	102	0.161	128
H04	8.0	60	16.5	2.31	110	0.191	144
H05	7.0	80	33	2.79	120	0.240	175
H06	6.0	120	69.5	3.63	160	0.385	295
H07	5.0	140	117	3.63	152	0.386	285
H08	4.0	250	284.5	3.87	174	0.427	325
H09	3.0	500	470	4.12	195	0.440	340

Table 5.3: Spot heater events – first thermal cycle.

#### - Second thermal cycle

Before the second thermal cycle, the power supply was slightly modified, by removing capacitors from the circuit, which subtracted current from the magnet after the quench. This modification allowed a constant current for a longer time after the quench, until reaching the power supply limit. At that moment, the current started to decrease rapidly, and then quench back occurred in SC01. The power supply modification therefore helped increasing the temperature more rapidly during the quench.

Table 5.4 lists the main results of the spot heater events.

Ramp #	Current (kA)	Dump delay (ms)	MIIts ( $10^6 A^2 s$ )	RSHseg (mOhm)	TSHseg (K)	T sensor (K)
H10	5.0	200	3.7	0.393	292	194
H11	3.0	440	4.0	0.390	290	183
H12	3.0	440	4.0	0.388	290	185
H13	3.0	440	4.0	0.387	288	191
H14	3.0	450	3.7	0.334	250	165
H15	3.0	450	3.9	0.365	270	193
H17	3.0	514	4.1	0.401	300	198
H18	3.0	800	4.7	0.50	370	245
H19	3.0	1148	5.0	0.56	420	286
H20	3.0	1600	5.4	0.61	450	311
H21	3.0	2000	5.6	0.67	496	337
H22	3.0	2500	5.8	0.70	518	349
H23	3.0	3500	6.1	0.78	580	422

Table 5.4: Spot heater events – second thermal cycle.

The first training quench of the second thermal cycle occurred at 8810 A, a current not yet reached during the first thermal cycle. After this quench, we proceeded with the thermal shock test. During the first events (H10 to H17), the peak temperature reached about 300 K, even with increasing dump time delays, because the protection system had a limit to the voltage over the leads, which activated the dump switch before the set time delay. After the problem was resolved, the experiment continued repeating spot heater induced quenches at 3000 A, with increasing time delays.

The thermal shock test events of the second thermal cycle are summarized in Fig. 5.22. Each event is represented by a quench number (numbers continued from the first thermal cycle) and a quench current (left axis), or a peak temperature (right axis). The quench current points (diamonds and squares) represent the case of *ramp-to-quench* events, performed in order to check the short sample limit, and therefore to assess the magnet performance. The peak temperature points (triangles) represent the case of *thermal shock* events. The quench current points are represented by squares in the case the quench started within, or at, the voltage taps close to the spot heater; by diamonds, in the case the quench did not start in the spot heater segment. In this case, the quench usually propagated to the spot heater segment after a few ms.

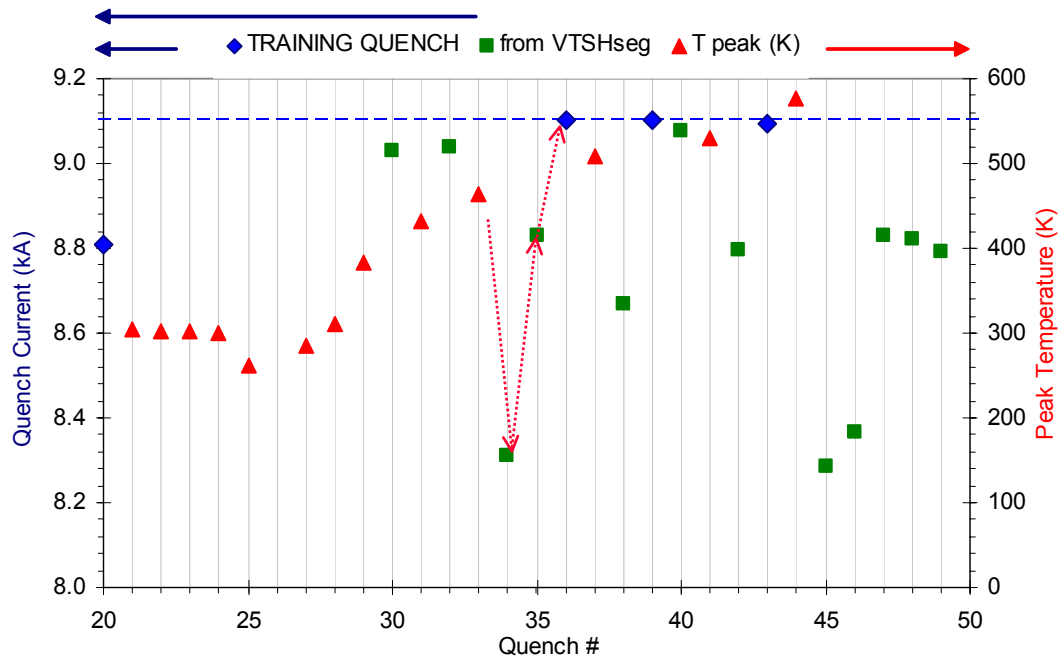


Fig. 5.22: Thermal shock tests during the second thermal cycle: quench current for performance check tests (referred to the left axis) and peak temperatures during quenches for thermal shock tests (referred to the right axis). Arrows highlight the first occurrence of de-training and re-training.

After reaching a peak temperature of 370 K in a thermal shock event (quench # 29), the magnet reached 9028 A in the following ramp-to-quench test, not showing any sign of degradation. The quench started close to the spot heater segment and the outer turns section, 0.4 ms before the quench in the inner turns section.

During the following thermal shock event, the magnet peak temperature reached 420 K. The following quench current was at the same level as the previous quench. The quench started close to the spot heater, with all three signals rising at the same time.

During the next thermal shock event (quench # 33), the magnet peak temperature reached 450 K, and the following quench current was 8311 A, 700 A below the previous quench current (8% current decrease). The voltage signals indicate that the quench started close to the spot heater, with all three signals rising at the same time. During the following current ramp, the magnet quenched at 8830 A, beginning from the spot heater region. The following quench occurred at 9100 A, the maximum current reached by the magnet. The quench did not start within the spot heater segment, where the voltage signal began rising 4 ms after the signals from the other two sections of the coil. Therefore, the 450 K peak temperature did not induce a permanent degradation, but the magnet suffered from temporary detraining.

The following thermal shock event, lasting two seconds, brought the temperature up to ~496 K. During the next current ramp, the magnet quenched at 8670 A, 4.3 % less than the previous quench current. The quench started simultaneously in all three sections of the coil, including the spot heater segment. The following quench occurred at the maximum current of 9101 A. The quench did not start within the spot heater segment, where the voltage began rising 4 ms after the voltage of the other two sections of the coil. During the next current ramp, the magnet quenched at 9077 A, just below the maximum current. The quench started close to the spot heater, very close to the outer section (reached in 0.4 ms), and then propagated to the inner section (in 1 ms).

The following thermal shock event, lasting two and half seconds, brought the temperature up to ~518 K. The following quench occurred at a current of 8796 A (3.4 % less than the maximum). The quench signals started simultaneously in all the three coil sections. The following magnet quench occurred at 9094 A, not within the spot heater segment, where the voltage started rising 4 ms after the voltage of the other two coil sections, as in the previous cases at this current level.

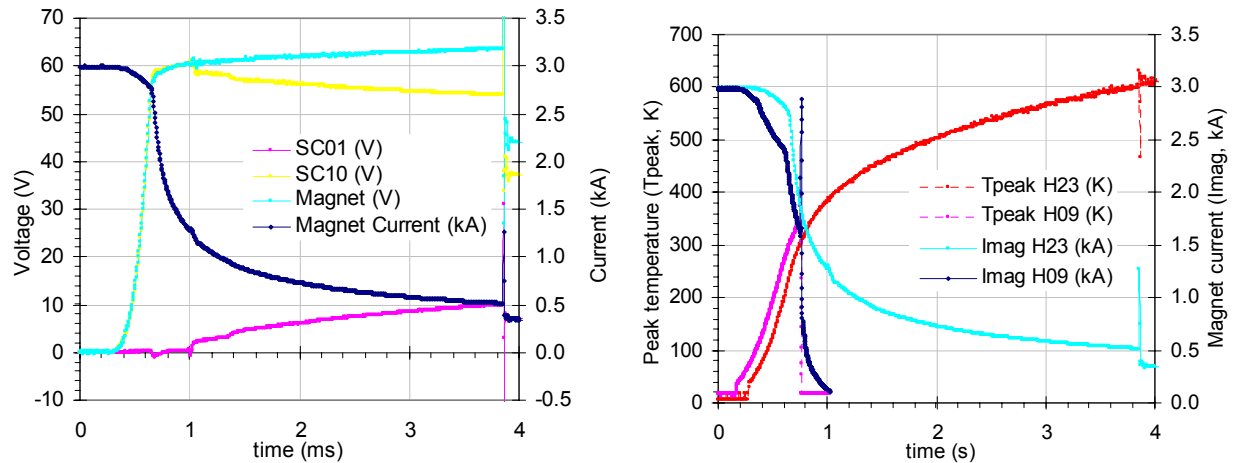


Fig. 5.23: Last spot heater event signals (left) and peak temperature (right); also shown the comparison with H09, last spot heater event of thermal cycle I.

During the final spot heater event (Fig. 5.23), after a delay of three and a half seconds, the temperature reached ~579 K. The following five quenches all occurred below the maximum current and started close to the spot heater together with the signals from the other coil sections. The quenches occurred at 8287 A (8.9 % less than the maximum), at 8364 A, at 8830 A (3 %), and finally, decreasing a small percentage, at 8791 A (3.4 % below the maximum current). This was the last quench of the second thermal cycle.

## 5.4 Adiabatic quench process simulation

### 5.4.a Quench Integral

The experimental results were compared with peak temperature calculations based on quench integrals (see 2.1.d). In the composite, in addition to copper, Nb<sub>3</sub>Sn, and bronze, the contributions to the specific heat of the epoxy and of the external cable insulation were considered as well. Fig. 5.24 shows the material properties used for calculating the quench integrals. Note that the specific heats of the insulating materials have been extrapolated from values around room temperature. Epoxy and epoxy composite are not usually employed above the glass transition temperature, which is between 410 and 430 K.

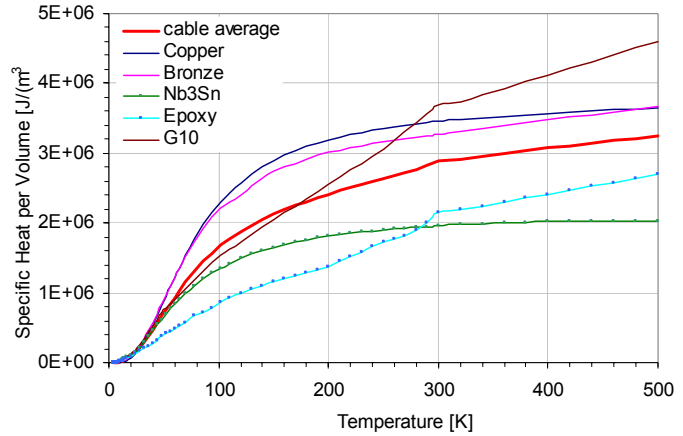


Fig. 5.24: Material properties used in calculations (see also chapter 3.4).

Table 5.5 reports the geometrical parameters used to calculate the quench integrals.

Component Material	Component Area (m <sup>2</sup> )	Density (Kg/m <sup>3</sup> )	Met.+Epoxy+Ins. Fraction	Metal+Epoxy Fraction	Metal only Fraction
Copper	4.87 10 <sup>-6</sup>	8.96 10 <sup>3</sup>	0.382	0.490	0.600
Bronze	1.93 10 <sup>-6</sup>	8.85 10 <sup>3</sup>	0.152	0.163	0.200
Nb <sub>3</sub> Sn	1.31 10 <sup>-6</sup>	8.04 10 <sup>3</sup>	0.103	0.163	0.200
Epoxy	1.82 10 <sup>-6</sup>	1.80 10 <sup>3</sup>	0.143	0.183	
G10	2.82 10 <sup>-6</sup>	1.15 10 <sup>3</sup>	0.221		
Tot. Ins. Fraction	4.64 10 <sup>-6</sup>		0.36	0.18	0.00
Total Area (m <sup>2</sup> )			1.28 10 <sup>-5</sup>	9.94 10 <sup>-6</sup>	8.12 10 <sup>-6</sup>

Table 5.5: Cable parameters used for the calculation of the quench integrals.

Fig. 5.25 shows the temperature versus quench integral, calculated with (2.7) for the conductor of SC10. The contribution of the insulation to the quench integral reduces significantly the peak temperature, for a given MII<sub>ts</sub> value. A quench integral of 4 MA<sup>2</sup>s corresponds to a temperature of 260 K, including all the insulation, versus 450 K, considering only the metal fraction. As shown in Fig. 5.25, the quench integral accumulated during last thermal shock event, which lasted 3.5 s, lies initially between the case “Metal only” and “Metal+Epoxy”. At 400 K and above, or over 1 s, the experimental curve lies between the case “Metal+Epoxy” and the case that includes also the external insulation.

Table 5.6 lists the peak temperatures derived from the resistance measurements, and compares these results with the temperatures from the sensor and from the computed quench integral.

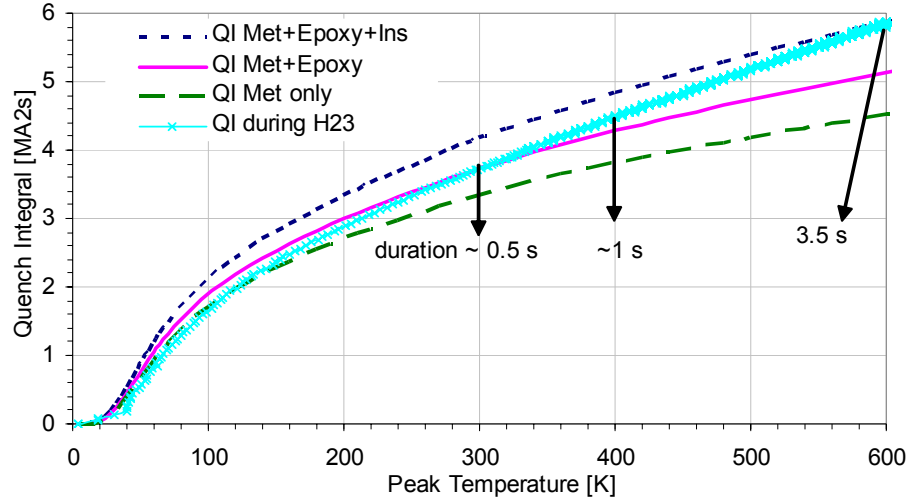


Fig. 5.25: Quench integral accumulated during the quench process as a function of peak temperature, in calculations and during last spot heater event (H23).

Ramp #	Current (kA)	MIIts ( $10^6 \text{A}^2\text{s}$ )	$T_{\text{SHseg}}$ (K)	T sensor (K)	T MIIts-Ins (K)	T MIIts-epo (K)	T MIIts-met (K)
H01	8.0	1.29	84	80	60	64	70
H02	8.0	1.31	80	80	60	64	70
H03	8.4	2.11	128	102	94	110	130
H04	8.0	2.31	144	110	110	120	150
H05	7.0	2.79	175	120	140	170	200
H06	6.0	3.63	295	160	230	280	360
H07	5.0	3.63	285	152	230	280	340
H08	4.0	3.87	325	174	260	320	400
H09	3.0	4.12	340	195	290	360	460
H10	5.0	3.7	313	194	240	300	380
H11	3.0	4.0	311	183	280	340	440
H12	3.0	4.0	309	185	280	340	440
H13	3.0	4.0	308	191	270	340	440
H14	3.0	3.7	270	165	240	290	360
H15	3.0	3.9	292	193	260	320	400
H17	3.0	4.1	319	198	290	360	460
H18	3.0	4.7	391	245	360	480	660
H19	3.0	5.0	439	286	420	560	
H20	3.0	5.4	470	311	480	660	
H21	3.0	5.6	515	337	540		
H22	3.0	5.8	536	349	570		
H23	3.0	6.1	597	422	640		

Table 5.6: Spot heater events – thermal cycle I and II.

### 5.4.b Quench simulations

Simulations of the quench process have been performed varying several parameters. First, quench simulations were performed varying the quench velocities. We noticed that the quench velocity is an important parameter since it determines how fast the power supply reaches the 50 V limit. The comparison between the quench velocity resulting from the classical formula used in QLASA and the measurements, showed that a correction factor of  $\sim 1.5$  must be applied (see chapter 3.6.a). The same correction factor seemed to fit the data from spot heater induced quenches in Small Magnets (Fig. 5.4). Fig. 5.26 shows the comparison of the quench simulation using QLASA program and the experimental data for H23, the last high temperature thermal shock event.

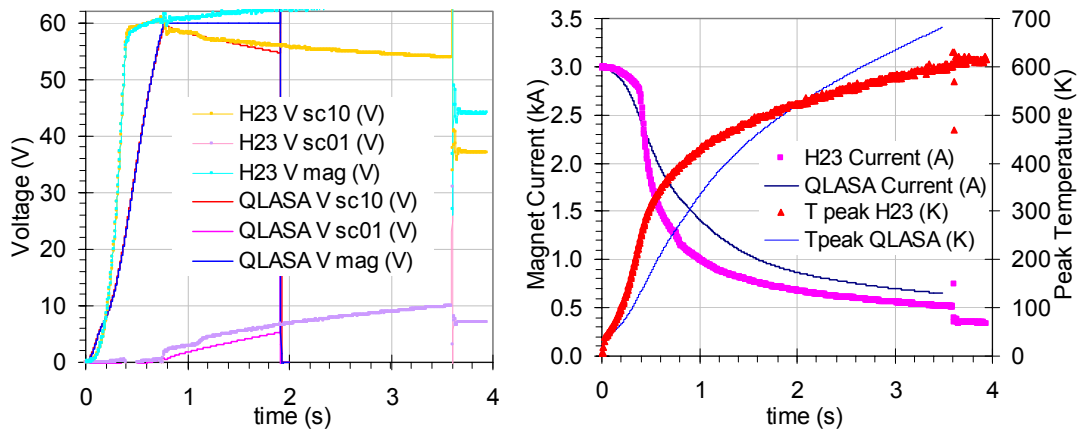


Fig. 5.26: Quench simulation (QLASA) and experimental data comparison for the last high temperature spot heater event (H23): voltage (left) and current and peak temperature (right).

With the use of this correction factor, the calculated and measured voltages agree initially, up to  $\sim 200$  ms. As the process continues, however, other factors begin to affect the quench process, which are difficult to simulate exactly. Fig. 5.26 shows that, after 200 ms, the voltage in the experiment rises much faster than during the simulation, resulting in a slower current decay than during the experiment, leading to a higher peak temperature in the simulation.

For example, the simulation has to take into account that the current in the magnet is reduced by the capacitors in the parallel branch of the circuit. To simulate this current reduction in the magnet, a parallel resistance was added to the QLASA model.

In addition, as shown in Fig. 5.25, the peak temperature is very sensitive to the amount of insulating material included in the  $QI$  calculations. A smaller insulation thickness was chosen, such that the calculated and experimental  $QI$ s agree within  $\sim 8\%$ .

Furthermore, there is the quench-back phenomenon. The quench back in SC01 was simulated by starting a new quench in the second coil. The results of the simulation show that the coil reached about 170 K at the end of the process. The resistance contribution of SC01 to the total magnet resistance affecting the current decay is negligible, if the quench-back is delayed enough after the quench in SC10. The voltage signals of H23 (Fig. 5.26) show that the quench-back in SC01 occurs only when the current starts to drop quickly, after the voltage limit of the power supply is reached. However, what is most difficult to simulate is the quench back in SC10. The scarcity of voltage taps, did not allow a better understanding of the quench propagation process.



The quench calculations used in this model cannot simulate the effect of eddy currents heating in SC10, or other mechanisms that might increase the quench propagation and lead to the so-called quench-back.

## 5.5 Mechanical analysis

An analytical mechanical model, similar to the one described in chapter 4, was adopted to study the mechanical response of the magnet during a quench generating high temperatures. The directions in this model are labeled following the same convention as in chapter 3 and 4, (see also Fig. 5.27).

The model estimates the strain and stress that develop inside the coil assuming an infinitely rigid mechanical structure. This hypothesis can be considered a good approximation in the radial direction, since the forces are contained by the aluminum shell of the magnet. In the other directions, the coil is restrained by the horseshoe, and the infinitely rigid boundary approximation is conservative.

The thermo-mechanical properties are reported in Table 5.7. The values in x and y directions were measured at LBNL [5.9]. Similar values of elasticity modulus were obtained at Fermilab on samples with S2-glass insulation, after massaging to 100 MPa [5.10]. The pre-stress on the coil after cool-down, was calculated to be about 97 MPa (see 5.2.b).

The longitudinal thermo-mechanical properties used in this model are taken from Fermilab measurements reported in [5.10]. The mechanical properties in longitudinal and radial directions should be determined mainly by the properties of the cable, such as strand diameter, transposition pitch angle, packing factor and pressure during impregnation. However, it is difficult to predict how the differences in the cable parameters and in the sample preparation, between the measured samples and the SC10 coil, resulted in different mechanical properties. The measured sample was made of reacted Nb<sub>3</sub>Sn trapezoidal cable with 28 strands (1 mm diameter). SC10, as described in 5.2.b, was made of a rectangular cable with 20 strands, (0.7 mm diameter). The insulation was in both cases a 150  $\mu$ m-thick S2-glass sleeve, impregnated with CTD-101 epoxy.

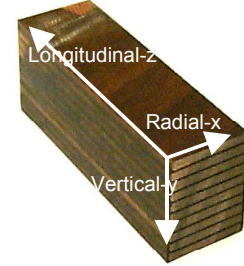


Fig. 5.27: Convention for axis labeling.

Mechanical properties	x	y	Z
$\alpha$ 293-4.2 K (mm/m)	3.08 *	3.36 *	3.08 **
$E$ at 293 K (GPa)	52 *	44 *	47 **
$E$ at 4.2 K (GPa)	52 *	44 *	56 **
Poisson ratio $\nu$ **	$\nu_{xy} = 0.3$	$\nu_{yz} = 0.15$	$\nu_{zx} = 0.15$

Table 5.7: Mechanical properties. Reference for \* is [5.9], and for \*\* is [5.10]

The temperature distribution inside the magnet is assumed to be uniform along the cable (longitudinal direction), and with a triangular profile in x and y direction. This distribution was estimated on the basis of the following considerations:

At 3 kA, the longitudinal quench propagation velocity is 2.4 m/s (see 5.3.b). Therefore, an entire turn is driven normal in  $\sim 0.1$  s, while the quench process took about 1 s to reach 400 K, at a magnet current of 3 kA. In addition, the quench-back might have increased the quench propagation speed.

The quench propagation in the vertical direction (turn-to-turn) was estimated to be about 0.05 m/s at 3 kA. Half a second is necessary to quench all the turns, at this speed. After 0.5 s, the current is already reduced to 1.5 kA, and it continued to decrease to 1 kA at 1 s, (400 K peak temperature). Therefore, the temperature increased slowly after 0.5 s, due to the reduced quench integral growth.

In radial (x) direction, we have to consider that the second coil (SC01) does not develop high temperatures (simulation results indicate a peak temperature of 170 K). Since one coil becomes “hot” and the other remains cold, we can roughly approximate the radial temperature profile as half at peak temperature, and half at bath temperature.

The pre-stress of 96 MPa given by the thermal contraction of the aluminum shell during cool-down, creates a strain at 4.2 K  $\varepsilon_{0x} = 0.185$  %.

#### *Uni-axial strain model*

In the uni-axial approximation, the strain induced by a change from bath temperature ( $T_{bath}$ ) to a maximum temperature  $T$ , is given by

$$\begin{aligned}\varepsilon_x(T) &= \varepsilon_{0x} + c_x(T - T_{bath})/2; & c_x &= \alpha_x/(293 - 4.2) \text{ K} \\ \varepsilon_y(T) &= c_y(T - T_{bath})/2; & c_y &= \alpha_y/(293 - 4.2) \text{ K} \\ \varepsilon_z(T) &= c_z(T - T_{bath}); & c_z &= \alpha_z/(293 - 4.2) \text{ K}\end{aligned}\tag{5.1}$$

The results are shown in Fig. 5.28. For a peak temperature of 400 K, the strain is -0.21 %, in x-direction, -0.27% in y- and -0.42% in z-direction (Table 5.8).

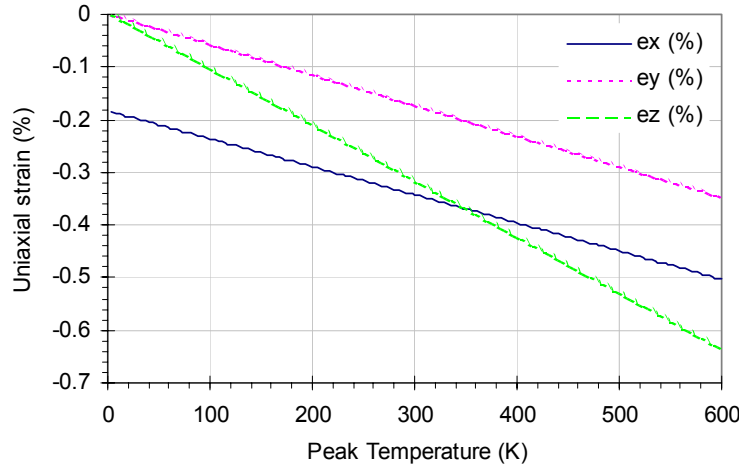


Fig. 5.28: Thermal expansion strain at the hot spot, as a function of peak temperature  $T$  (K), assuming a uniform temperature in z-direction, and a triangular temperature profile in x and y-direction.

The total strain inside the  $\text{Nb}_3\text{Sn}$  filaments (intrinsic strain) is given not only by (5.1), but also by the pre-compression of the  $\text{Nb}_3\text{Sn}$  filaments, due to the difference between the thermal

contraction of Nb<sub>3</sub>Sn and of the bronze/copper matrix, from the reaction temperature (650 K) to the peak temperature after the quench ( $T_{peak}$ ).

A typical intrinsic pre-compression for MJR Nb<sub>3</sub>Sn strands at 4.2 K is 0.3 % [5.11]. At 400 K, the intrinsic pre-compression is reduced with respect to the value at 4.2 K, due to the reduced differential thermal contraction of the materials between 400 K and the reaction temperature. The intrinsic strain in the Nb<sub>3</sub>Sn after cool-down, from the reaction temperature  $T_{react}$  to the temperature  $T$ , cannot easily be estimated, because many factors must be taken into account. These factors include the temperature dependence of the elasticity modulus of all the materials inside the strand, the yielding point of the copper/bronze matrix (depending on the previous thermal history), and the twist of the filaments inside the strand. A rough estimate of the intrinsic strain reduction  $\epsilon_{int}(T_{peak})/\epsilon_{int}(4.2 \text{ K})$  can be made on the basis of the thermal contraction coefficients, the elastic modulus and the Nb<sub>3</sub>Sn fraction in the strand. An estimate based on this procedure is that the intrinsic pre-compression at  $T_{peak} = 400 \text{ K}$  decreases by about 50% with respect to the intrinsic strain at 4.2 K.

The total intrinsic strain ( $\epsilon_{tot}$ ) is calculated by adding the quench-induced strain, calculated with (5.1), to the estimated thermal pre-strain at 400 K of -0.15 %. This approach was chosen to compare the results of the calculations to the limit of the conductor for the longitudinal strain. Measurements indicate that the irreversible intrinsic pre-compression strain is higher (in modulus) than 0.7% [5.12]. Therefore, the total intrinsic strain in longitudinal direction ( $\epsilon_{tot} = -0.57\%$ ) appears to be within the limits of irreversible degradation.

#### Calculation of the stress

The stress in longitudinal direction is calculated from the modulus  $E(T)$ , using a linear fit of data measured on cable stacks, at room temperature and at 4.2 K. In radial and transverse direction, the moduli are constant. The Poisson effect was neglected. The results are shown in Fig. 5.29.

$$\begin{aligned}\sigma_x(T) &= E_x [\epsilon_{0x} + c_x (T - T_{bath})/2] \\ \sigma_y(T) &= E_y c_y (T - T_{bath}) / 2 \\ \sigma_z(T) &= E_z (T) c_z (T - T_{bath})\end{aligned}\tag{5.2}$$

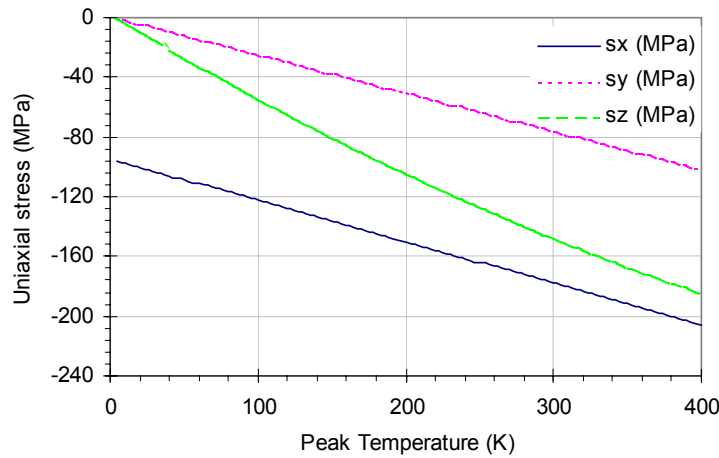


Fig. 5.29: Thermal expansion stress (MPa) at the hot spot as a function of peak temperature  $T$  (K), assuming a uniform temperature in z-direction, and a triangular temperature profile in x and y-direction

For a peak temperature of 400 K, the stress is about 200 MPa in x-direction, 110 MPa in y-direction, and 170 MPa in z-direction (Table 5.8).

The Poisson effect brings to a further enhancement of the stresses. Indicating the stress and strains as vectors, with the components relative to the main directions, we can calculate the stress using (5.3),  $M_{es}$  being the matrix of the generalized Hooke's law:

$$\vec{\sigma}_3(T) = M_{es}^{-1}(T) \cdot \vec{\varepsilon}(T); \quad M_{es}(T) = \begin{bmatrix} \frac{1}{E_x(T)} & \frac{-\nu_{xy}}{E_y(T)} & \frac{-\nu_{xz}}{E_z(T)} \\ \frac{-\nu_{yx}}{E_x(T)} & \frac{1}{E_y(T)} & \frac{-\nu_{yz}}{E_z(T)} \\ \frac{-\nu_{zx}}{E_x(T)} & \frac{-\nu_{zy}}{E_y(T)} & \frac{1}{E_z(T)} \end{bmatrix} \quad (5.3)$$

The resulting stresses are 336 MPa in radial, 236 MPa in vertical, and 262 MPa in longitudinal direction, for a peak temperature of 400 K. Because the coil support structure was not completely rigid in vertical and “longitudinal” direction (horseshoe and end-shoe), the stress in radial direction, calculated with this model, was most likely overestimated.

The contribution of Lorentz forces has to be added, in general, to the stress due to the thermal expansion during the quench process, the applied pre-stress, and pre-stress due to cool-down. In this experiment the Lorentz forces do not contribute significantly to the total stress, because of the low magnet current. In the general case of an accelerator magnet, the Lorentz forces can contribute significantly to the total stress, during the initial phase of quench, when the current is high. After the heater becomes effective, the current starts to decrease, and the peak temperature is reached when the current is already moderate. Therefore, this experiment, although it was performed at low current, can be regarded as useful for understanding the general case of an accelerator magnet.

The stresses in radial and vertical directions can be compared with experimental critical current measurements on cables as a function of applied stress. There are several studies about the dependence of the critical current of Rutherford cable on the transverse pressure in vertical direction. Some studies indicate a limit of about 150 MPa [5.13], other experiments showed no permanent degradation up to 180 MPa and little degradation at 210 MPa [5.14,15].

There aren't reliable measurements of the critical current sensitivity to pressure applied on the thin side of the cable. Mechanical measurements performed during the R&D of the common coil magnet at Fermilab, indicated that coil samples can withstand 150 MPa compressive stress, as long as the samples are supported in the transverse direction [5.16].

	x	y	z
$\varepsilon$ (%)	-0.21	-0.27	-0.42
$\varepsilon_{tot}$ (%)	-0.36		-0.57
$\sigma$ (MPa)	-206	-111	-169
$\tau$ (MPa)	$\tau_{x,y} = 47$	$\tau_{y,z} = 29$	$\tau_{x,z} = 18$
Irreversible limit	$\sigma = -150/-200$ MPa	$\sigma = -150/-200$ MPa	$\varepsilon_{tot} < -0.7\%$

Table 5.8: Uni-axial strain and stress model results, for a peak temperature of 400 K.

In conclusion, the results of this mechanical analysis show that the strain/stress levels, for a peak temperature of 400 K, in y- and z-direction are within the irreversible limits, while in x-direction, the stress resulting from this model is close to the critical value.

Even in the case of uni-axial stresses below the irreversible limits, the high anisotropic expansion generates high shear stress and strains. The values listed in Table 5.8 are calculated applying the Mohr's circle in a 3-dimensional model (5.4).

$$\tau_{max} = \frac{1}{2} |\sigma_{max} - \sigma_{min}|, \quad (5.4)$$

where  $\sigma_{max}$  and  $\sigma_{min}$ , are chosen as the maximum and minimum stress respectively, between the components of the stress vectors in the x-, y-, and z-directions, which are also the principal directions (no shear strain).

The shear stress value in the x,y plane (reported in Table 5.8) is above the shear strength of the epoxy resin, which is about 43 MPa (a value that varies between different epoxy mixtures). Composites, such as impregnated fiberglass, have higher shear strength, depending on the strength of the fibers, on the epoxy content, and on the pattern of the texture. Imperfections in the impregnation, such as voids or large grains of epoxy not filled with glass-fibers, may generate weak points, where the shear stress behavior is dominated by the epoxy. Considering the shear strength of a coil equal to the strength of epoxy provides therefore a conservative limit.

## References

- 
- [5.1] R.R. Hafalia et al., "An Approach For Faster High Field Magnet Technology Development," to be published, *IEEE Trans. Appl. Supercond.*, June 2003, proceedings of ASC02
  - [5.2] R.R. Hafalia, et al., "A new Support Structure for High Field Magnets", SC-MAG 738, Lawrence Berkeley National Laboratory, Sept., 2001 (MT-17).
  - [5.3] S. Caspi, et al, "The Use of Pressurized Bladders for Stress Control of Superconducting Magnets," *IEEE Trans. on Applied Supercond.*, vol. 11 No. 1, p. 2272, March 2001
  - [5.4] M. Coccoli, "Fabrication and Testing of Superconducting Cables and Subscale Magnets for a more effective approach to Future Accelerators R&D and Fabrication," *Laurea thesis*, University of Milan, Italy, April 2003
  - [5.5] M. Coccoli, L. Chiesa, "SM01a and SM01b Test Results," LBNL-50145 SC-MAG 775, Feb. '02
  - [5.6] L. Imbasciati, et al., "Proposal for quench-test on Nb<sub>3</sub>Sn small coil," Fermilab Technical Division note, TD-02-035, August 2002
  - [5.7] L. Imbasciati, et al., "Test Report of Thermal Shock Experiment on Subscale Nb<sub>3</sub>Sn Racetrack Magnet," TD-03-20, May '03
  - [5.8] L. Chiesa, et al., "Performance comparison of Nb<sub>3</sub>Sn Magnets at LBNL," to be published, *IEEE Trans. Applied Supercond.*, June 2003, proceedings of ASC02

- 
- [5.9] K. Chow et al., "Measurements of Modulus of Elasticity and Thermal contraction of Epoxy Impregnated Niobium-Tin and NbTi Composites," *IEEE Trans. Applied Supercond.*, ASC 1998
  - [5.10] D.R. Chichili, T.T. Arkan, J.P. Ozelis, I. Terechkine, "Investigation of cable insulation and thermo-mechanical properties of Nb<sub>3</sub>Sn composite," *IEEE Trans. Applied Supercond.*, Vol. 10 N. 1, p. 1317-1320, 2000
  - [5.11] J. Ekin and N. Cheggour private communication of measurement of MJR Nb<sub>3</sub>Sn strands performed at NIST
  - [5.12] N. Cheggour and D.P. Hampshire, "Unifying the Strain and Temperature Scaling Laws for the Pinning Force Density in Superconducting Niobium-Tin Multifilamentary wires," *Journal of Applied Physics*, Vol. 86, N. 1, July '99
  - [5.13] J.M. van Oort, "Critical current degradation in Nb<sub>3</sub>Sn superconductors in accelerator magnets," *Ph.D. Thesis*, Univ. of Twente
  - [5.14] P. Bauer et al., "Fabrication and Testing of Rutherford-type Cables for React and Wind Accelerator Magnets," *IEEE Trans. Applied Supercond.*, Vol. 11/1, March 2001
  - [5.15] D.R. Dietderich, R.M. Scanlan, R.P. Walsh, J.R. Miller, "Critical Current of Superconducting Rutherford Cable in High Magnetic Fields with Transverse Pressure," *IEEE Trans. Applied Supercond.*, Vol. 9, N. 2, June 1999
  - [5.16] I. Novitzky, private communication

## 6. Summary and Conclusions

### 6.1 Nb<sub>3</sub>Sn accelerator magnet development

The development of hadron colliders towards higher and higher particle energies has progressed together with the development of superconducting magnets that are needed to steer (dipole magnets) and focus (quadrupole magnets) the beams. The Large Hadron Collider (LHC) is designed to operate at 1.8 K to be able to reach 8.4 T operating field with the ductile NbTi superconductor. To further increase the magnetic field intensity for a next generation collider, a different superconducting material is necessary. Nb<sub>3</sub>Sn meets the essential requirements for the next generation of high field accelerator magnets, and promises even further improvements. Fermilab and several other laboratories in the world are developing 10-15 T Nb<sub>3</sub>Sn magnets using several design approaches. These programs were briefly reviewed in [chapter 1](#) of this thesis with particular emphasis on the Fermilab program, which aims at the development of magnets for the LHC luminosity upgrade and the Very Large Hadron Collider (VLHC). The LHC luminosity upgrade foresees the use of Nb<sub>3</sub>Sn quadrupoles at the interaction regions that can produce the high magnetic field gradients in a large magnet bore and withstand the increased heat-load due to radiation emanating from the interaction regions. The VLHC, according to the latest design, aims at reaching collision energies of 175 TeV in the center of mass, with 10-11 T dipole magnets, in its second stage. The current baseline dipole magnet design for the VLHC-2 is a single layer common coil design (Fig. 6.1-center). The large bending radius of the racetrack coils allows using the react-and-wind approach with the brittle Nb<sub>3</sub>Sn conductor. A simpler ‘racetrack’ coil magnet (Fig. 6.1-right) is also being developed to support the R&D towards the common coil magnet. Other dipole designs are being studied at Fermilab for a future hadron collider like VLHC-2, including shell type (cos $\theta$ ) designs (Fig. 6.1-left) which use the wind-and-react approach.

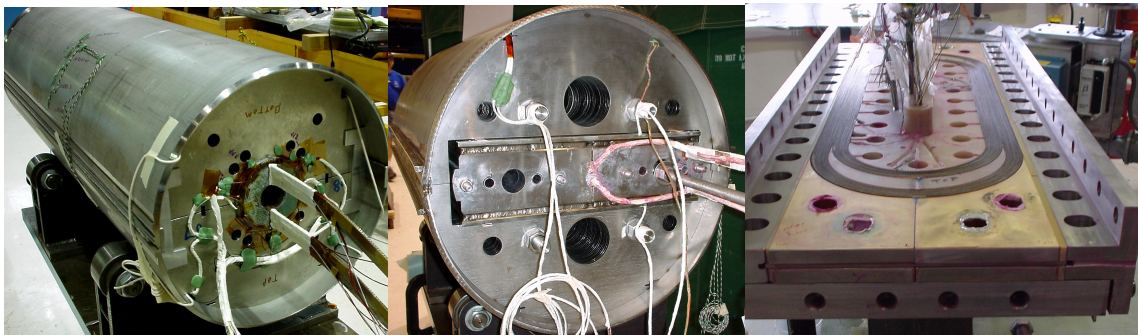


Fig. 6.1: Nb<sub>3</sub>Sn high field dipole magnets at Fermilab: cos $\theta$ , common coil, and racetrack designs.

## 6.2 Quench studies

Among the R&D issues related to  $\text{Nb}_3\text{Sn}$  superconducting magnets, there are quench protection issues. Protection of the superconducting magnet during a quench is important, in particular for long accelerator models, which cannot be protected simply by energy extraction. Long accelerator magnets with  $\text{Nb}_3\text{Sn}$  superconductor have not yet been built, but quench simulations (as described in [chapter 2](#)) indicate that peak temperatures above 300 K can arise during the quench, because of the high level of stored energy together with the high current densities carried in the  $\text{Nb}_3\text{Sn}$  superconductor. Numerical codes were developed to find the requirements for the protection of  $\text{Nb}_3\text{Sn}$  magnets. These codes were also used in studies, where magnet and conductor parameters were varied, in order to determine the optimal protection scenario. It was found that, in order to maintain the peak temperature below 400 K and the peak voltage below 1 kV, heaters covering 50% of the turns or more are necessary. The cos $\theta$  design magnet proposed for the VLHC, for example, requires a heater coverage of  $\sim 50\%$  of the turns, and the common coil magnet  $\sim 100\%$  (assuming a total heater delay time of 40 ms). Peak temperatures of 400 K exceed the standard 300 K limit for NbTi magnets. Furthermore, heater coverage larger than 50 % conflicts with the required heater redundancy.

The results of the quench protection study of the VLHC magnets raised questions about the general trends of quench protection parameters in  $\text{Nb}_3\text{Sn}$  high field magnets. For this purpose, an analytical approach to calculate the peak temperature was developed. Using this analytical approach, we were able to identify general trends of the peak temperature as a function of magnet parameters. These studies showed that in order to reduce the peak temperature during a quench in high field  $\text{Nb}_3\text{Sn}$  accelerator magnets without compromising conductor efficiency and cost by increasing copper fraction and magnet size, it is necessary to increase quench heater coverage and efficiency and/or reduce the heater delays (Fig. 6.2). This trend will be even more pronounced in view of future improvements of the critical current density in  $\text{Nb}_3\text{Sn}$  superconductor.

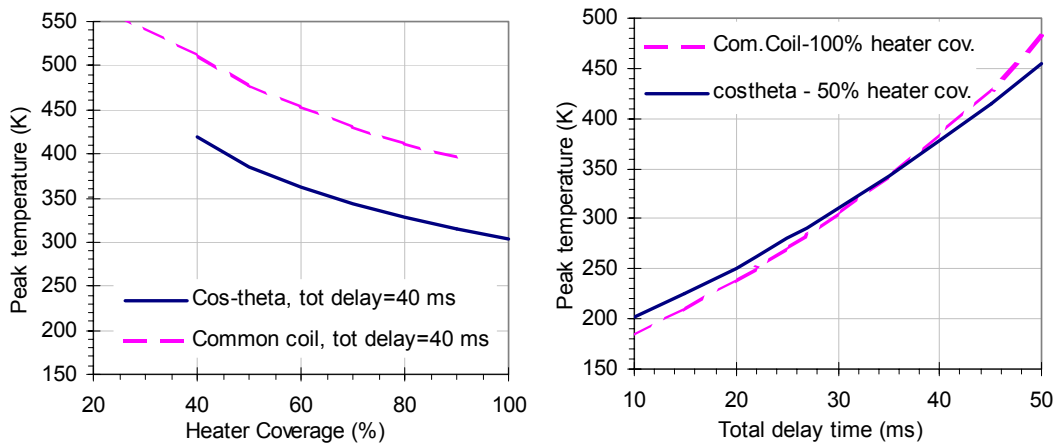


Fig. 6.2: Peak temperature vs. heater coverage, and peak temperature vs. total delay time

$\text{Nb}_3\text{Sn}$  is a brittle material and it has yet to be determined to what extent it is affected by thermo-mechanical stress during a magnet quench. Rapid thermal expansion of conductor and large temperature gradients during a magnet quench can affect the performance, for example in causing detaining, or even result in permanent damage of the magnet. It is necessary to define



the maximum temperatures that are allowed in the coils during a quench. Although critical current versus strain data are well established for Nb<sub>3</sub>Sn strands, little is known how these limitations apply in the case of the thermal shock experienced by the conductor during a magnet quench. This thesis is the first experimental and computational study addressing this issue in Nb<sub>3</sub>Sn accelerator magnets.

### 6.3 Material properties for quench studies

Material properties are key parameters affecting the quench process and their proper knowledge is essential for a safe design of a superconducting magnet. A collection of the main material properties affecting the quench process in Nb<sub>3</sub>Sn magnets is given in [chapter 3](#). Some of these properties, such as the specific heat and the electrical resistivity have been collected from literature. Others, however, have been found from especially dedicated experimental studies. Those are, for example, the thermal conductivity and thermo-mechanical properties.

The transverse (cable-to-cable) thermal conductivity of impregnated Nb<sub>3</sub>Sn cable stacks was measured, at cryogenic temperatures, for several samples with different insulations as well as without insulation (but epoxy impregnated). A model was developed to predict the thermal conductivity of a generic cable stack, taking into account its complex composite structure (strand contact thermal resistance, cable transposition pitch, etc.). The calculation results were compared with the measured data (see Fig. 6.3) and the model successfully applied in the magnet quench simulations.

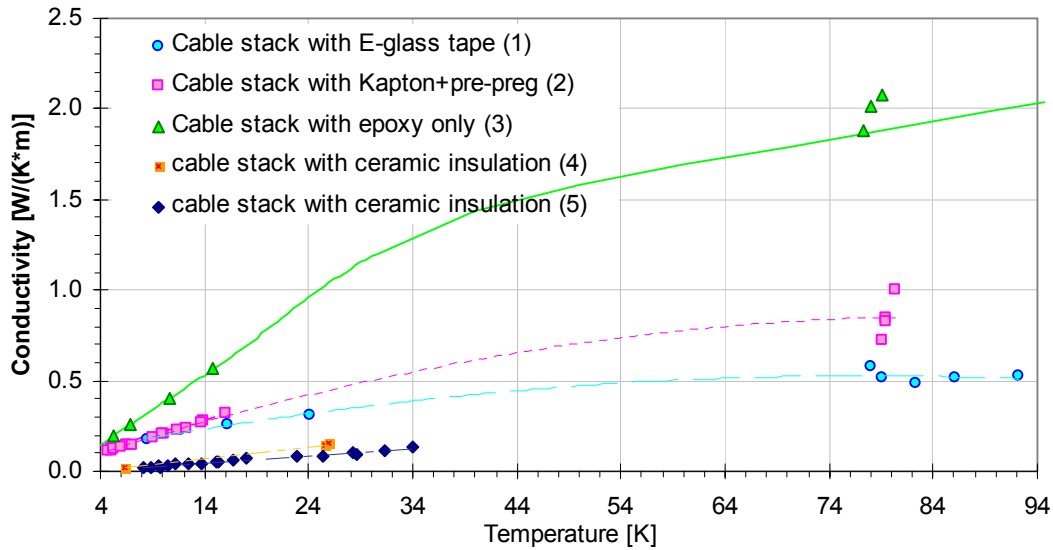


Fig. 6.3: Thermal conductivity of Nb<sub>3</sub>Sn cable stacks.

Thermal contraction coefficients and elasticity moduli of similar samples were also measured. These material properties are also difficult to predict, given the composite nature and the complex geometry of the cable stacks, but are essential parameters for performing thermo-mechanical analysis, and therefore to understand the stress/strain conditions during quenches in a superconducting magnet.

The Nb<sub>3</sub>Sn prototype magnets at Fermilab were used to measure important quench process parameters such as quench propagation velocities and quench heater time delays. The main quench heaters test results are:

- The measured minimum delay time was ~40 ms for the racetrack magnet at  $I/I_{SS} = 60\%$ , (with 33 W/cm<sup>2</sup> heater power) and ~30 ms for the cos $\theta$  magnet at  $I/I_{SS} = 45\%$  (with 13 W/cm<sup>2</sup>). Therefore, the goal of total heater delays below 40 ms (including quench detection time, as it is specified for the LHC NbTi magnets) seems to be realistic also for Nb<sub>3</sub>Sn magnets.
- The heater delay time depends strongly on the power per area, only below ~10 W/cm<sup>2</sup>, and it becomes less sensitive for larger power (as predicted by FE model results).
- Measured quench propagation velocities, at  $I_{SS} < 60\%$ , agree with calculated values, applying a multiplicative factor of ~1.5 to the “classical” formulas.

## 6.4 “Thermal-shock” quench experiments

The quench studies presented in chapter 2 showed that peak temperatures above 300 K can arise at the quench origin during the quench. It is necessary therefore to define the maximum acceptable temperature after a quench. An upper temperature limit is given by the melting point of solder (~500 K), since the quench might start near the conductor joints. For impregnated coils, a second limit could be the glass transition point of the insulation, which occurs at ~430 K for epoxy resins. At that temperature, the epoxy becomes soft and, even if the transition is reversible, the changes in its electrical properties increase the probability of a short circuit. In the case of magnets using Nb<sub>3</sub>Sn superconductor, an additional limit is introduced via the brittleness of Nb<sub>3</sub>Sn, which can be permanently degraded under the effect of stress. Although critical current versus strain data are well known for Nb<sub>3</sub>Sn, little is known about how to apply these limitations to the case of a cable thermally expanding in a magnet during a quench. To address the issue of the effects of the quench and the ensuing thermo-mechanical stress on the Nb<sub>3</sub>Sn magnet performance, an experimental and computational program was launched.

The experiment consisted in inducing a quench with a spot heater, located between two voltage taps, in a high field region. The current disconnection, after the quench, was delayed by a pre-defined amount, in order to allow Joule heating of the cable. The temperature rise during the quench was measured via the resistivity of the cable segment between the voltage taps. Since the process was very fast, high thermal gradients between the “hot spot”, where the quench started, and the surroundings induced the sought thermo-mechanical stresses. The critical current (or quench current) was measured after every excursion to high temperature, in order to assess the cable (or magnet) performance as a function of the peak temperature during a quench.

### 6.4.a Cable quench experiment

To measure the critical current degradation as a function of peak temperature during a quench, quench experiments were first performed on cables, in collaboration with the National High Magnetic Field Laboratory ([Chapter 4](#)). In a setting similar to that of critical current measurements of cables, two samples were tested. Each sample-holder contained two test-cables impregnated together with other two ‘dummy’ cables to better simulate the magnet environment. The samples tested were made of 0.7 mm-diameter ITER type Nb<sub>3</sub>Sn strands. One set of samples was reacted straight, while another set was reacted on a spool and straightened after reaction

during the sample-holder assembly, to measure the effect of bending strain. The magnetic field and the current were set to 8 T/8 kA, in order to operate near the critical surface of the samples. A pressure piston acting through the bore of the magnet gave the sample mechanical support and allowed application of a transverse pressure on the sample, set to  $\sim 20$  MPa in this test.

Peak temperatures up to 420 K were explored, without seeing critical current degradation in the straight sample. During the successive quench test, the peak temperature reached almost 500 K, but after that, during the last critical current measurement of straight sample, an early quench occurred in the cable and in the magnet shortly after, interrupting the quench test series. The data didn't show a transition curve, therefore it is not possible to assess a critical current degradation. The sample was then extracted from the magnet, and analyzed. The epoxy close to the voltage taps was burnt and the cables separated. The peak temperature in the bent sample reached 330 K without resulting in any critical current degradation.

#### 6.4.b Quench simulation with ANSYS

The quench process was simulated with numerical codes as well as with finite element (FE) models, using the ANSYS program. Coupling of the electrical and thermal variables is provided by a 3D solid element, with the two degrees of freedom, voltage and temperature. The quench propagation is determined by a resistivity function, varying from a very low value to the normal state value, with a fast rise at the generation temperature. The FE model allowed a completely integrated solution where the heat conduction from the cable to the environment (the other cables and the sample holder in this case) is already included in the calculation.

The calculation results show high temperature gradients between the coil and the surroundings, with temperature differences up to 320 K over 0.2 mm, across the insulation. These temperature gradients can produce high shear stresses, and epoxy cracking. A three-dimensional analytical mechanical model estimated the stress level to be below the irreversible limits in all dimensions, but possible shear stresses above the epoxy limit.

The fact that the insulation did not appear to be damaged at the spot heater location in the cable sample might indicate that the damage was caused by shear stresses as well as high temperatures, leading to an electrical failure of the insulation.

Most important, however, is that the FE model (as well as simpler analytical models) produced good agreement with experimental data, indicating a good understanding of the physics model, and adequate material properties.

Therefore, the quench simulation models for magnets, which were built upon the above, can be trusted.

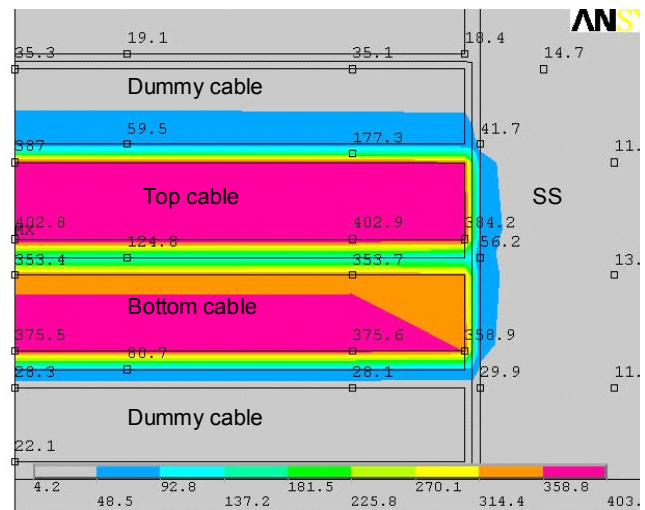


Fig. 6.4: Temperature distribution (K) over the cross-section of the cable sample holder.

### 6.4.c Small magnet quench experiment

The experimental program continued, in collaboration with the Lawrence Berkeley National Laboratory, by performing the quench experiment on a small Nb<sub>3</sub>Sn magnet ([Chapter 5](#)). The use of the LBNL Small Magnet program allowed performing the quench test with a state-of-the-art conductor, in a mechanical environment similar to that of an accelerator magnet. The LBL Subscale Magnet Program has been very successful in addressing R&D issues in a fast and cost effective way, with  $\sim 1/3$  scale with respect of a model magnet, and a magnet structure that is completely reusable, with the use of the pressurized bladders for applying pre-stress to the structure. The magnet consisted of two double-layer racetrack pancakes, assembled in a common coil configuration with a small gap in between. One of the two coils (named SC10) was prepared for this experiment. The cable of SC10 was a modified jelly roll conductor produced by OST with a 60 % copper fraction.

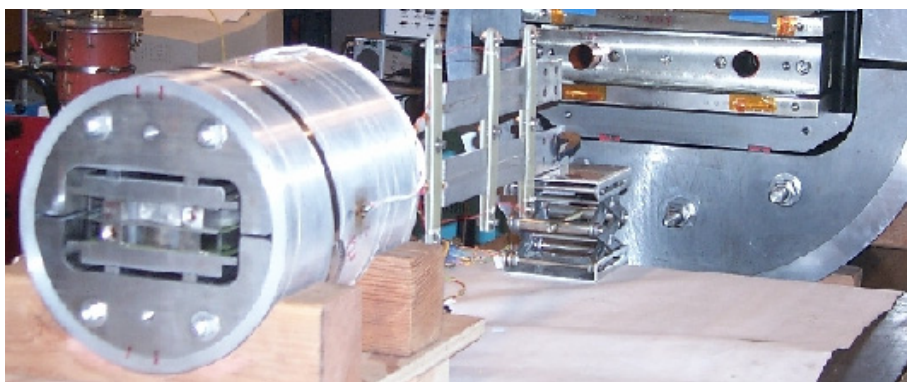


Fig. 6.5: LBNL Sub-sized magnet (in the front), and 1m prototype RD3 magnet in the back.

During the test, the magnet reached the maximum field of  $\sim 10.5$  T at the short sample current of 9.1 kA. The quench experiment followed a procedure similar to that of the cable tests. Temperature excursions up to 350 K were performed during the first thermal cycle. No degradation was detected. During the second thermal cycle, to reduce the quench propagation velocity and to avoid quench back, we continued the spot heater events series at a low magnet current (3 kA), using long dump delay times (1-3 s). Temperature excursions up to 430 K did not diminish the magnet quench performance. Only after temperature excursions over 450 K, did the magnet show detraining effects, which occasionally reduced the quench current by about 8%. Signs of irreversible degradation (reduction of the quench current by about 3%) appeared after temperature excursions over 580 K. An analytical model showed that the stresses and strains, up to  $\sim 400$  K, were below the known limits of Nb<sub>3</sub>Sn. Above 430 K, the mechanical state of the coil changed, due to the glass transition of the epoxy resin.

### 6.4.d Contribution of insulation to thermal balance during quench

The quench experiments performed on cables, and on the small magnet, provided also a useful check of the quench integral calculations using the adiabatic heat balance equation (2.7), and the material properties reported in chapter 3 (Fig. 3.16-18).

It is well known that in NbTi magnets the liquid helium present in or in the vicinity of the coils absorbs heat from the coils during the quench process. Nb<sub>3</sub>Sn magnets are usually impregnated, and liquid helium is therefore not present on the surface of the conductor. The impregnation (or impregnated insulation), however, is capable of playing a similar role, i.e. to absorb heat generated in the conductor and to therefore reduce the peak temperature. On the basis of a simple diffusivity argument, such as discussed in chapter 2, it can be shown that the heat will be conducted tens to hundreds of  $\mu\text{m}$  into the insulation during the quench process.

The quench tests conducted in the context of this thesis have allowed an evaluation of this effect. Shown in Fig. 6.6 are the experimental quench integrals as a function of temperature in the hot-spot found in the cable and small magnet quench tests, compared to the results of adiabatic quench integral calculations assuming varying amounts of insulation in the conductor. More precisely the different options are: the bare metal cable, the bare metal with voids filled with epoxy and the fully insulated cable.

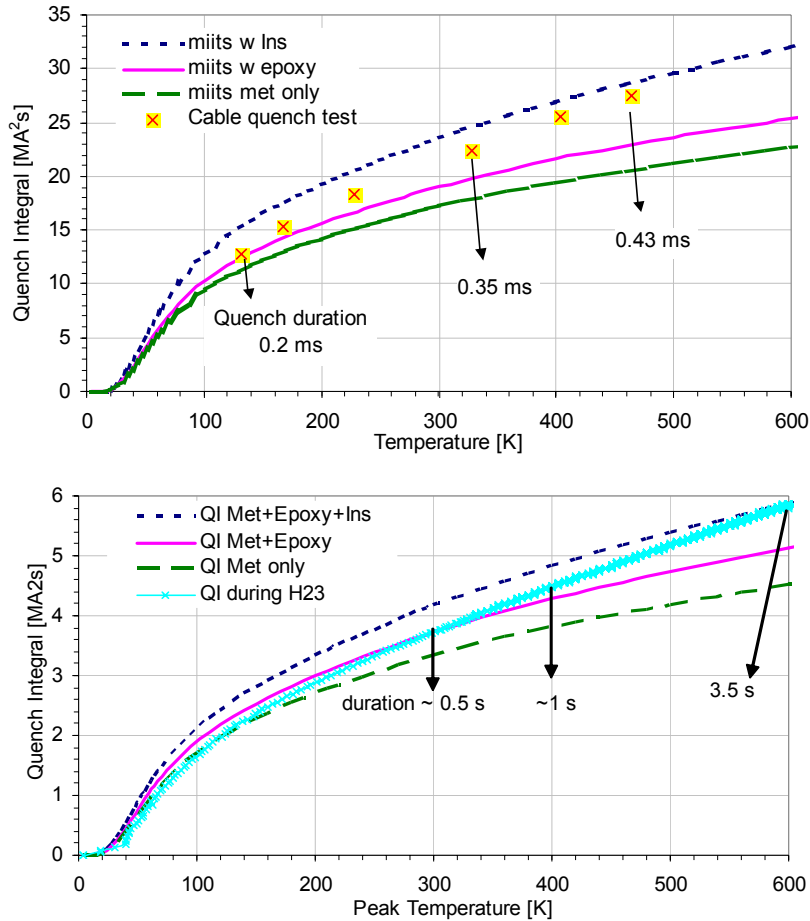


Fig. 6.6: Quench integral accumulated during the quench experiments performed on cables (above), and during the small magnet experiment (below), compared to curves calculated using the heat balance equation including metal components only, with epoxy resin and with 0.15 mm insulation.

As shown in the plots the experimental data tend to agree with the fully insulated cases at larger temperature, whereas they agree with the pure metal case at lower temperatures. This behavior is consistent with the diffusivity argument, given that the temperature scale is in fact

also a time scale: the shorter the time, the more “adiabatic”, i.e. the less insulation material participates in the process. Therefore, these measurements indicate that, in simulations of the quench process to high peak temperatures for epoxy impregnated Nb<sub>3</sub>Sn magnets, part of the insulation needs to be included in the thermal balance (up to 0.1 mm at 600 K).

## 6.5 Conclusions

Quench experiments were performed on cables and on a small Nb<sub>3</sub>Sn magnet to investigate the effects of peak temperatures during quenches on Nb<sub>3</sub>Sn magnets performance. The experiments indicate that peak temperatures up to 400 K do not compromise the magnet performance, if the stresses and strains in the conductor remain below its limits.

At about 430 K, the epoxy resin undergoes a reversible glass transition, which can temporarily weaken the insulation. Temperature excursions over 430 K, caused a premature quench during the cable test which could have been related to an electrical failure, and detraining effects in the magnet. Analytical mechanical models indicate that the stresses and strains during quenches at 400 K, were below the known limits of Nb<sub>3</sub>Sn conductor, and that shear stresses reached about 40 MPa, in the region of the epoxy shear strength. The cable sample that reached ~500 K was damaged, while the magnet showed signs of irreversible degradation (reducing the maximum current of ~ 3%) only after temperature excursions over 580 K.

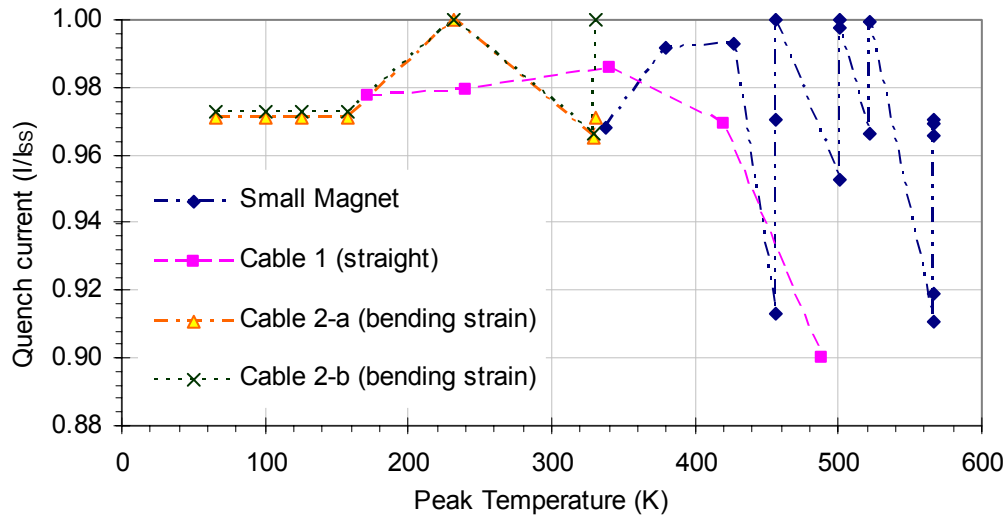


Fig. 6.8: Summary of quench experiments: reduced current (quench current divided by maximum current) vs. peak temperatures reached during the preceding quench test. The lines represent the temporary sequence of the peak temperature events.

## 6.6 Outlook

The investigation of the effects of the peak temperature during quench on Nb<sub>3</sub>Sn magnet performance should continue with quench experiments on Nb<sub>3</sub>Sn magnets with different designs, and with more in-depth analyses of the thermo-mechanical response of a magnet during quench.

## Acknowledgments

First I want to thank Pierre Bauer, who not only supervised this work, but also shared with me the joys and the efforts to accomplish it.

Thanks to all the people of Fermilab, at the Technical Division, who made this work possible. I could not imagine anything like this before coming here. Giorgio Ambrosio and Peter Limon gave me the first opportunity to work here (through the connection of my first advisor Lucio Rossi, whom I want to thank for introducing me to the world of superconducting magnets). Thanks to Alexander Zlobin, John Tompkins, Mike Lamm, and Bob Kephart for supporting the continuation of the work here, as a Ph.D. student.

I would like to thank my advisor Hans Kirchmayr who gave me the opportunity to continue my studies at the Technical University of Vienna, and Klaus Hense for helping in printing this thesis.

Thanks to the LBL Superconducting Group, in particular Steve Gourlay, Alan Lietzke, Shlomo Caspi and Luisa Chiesa.

Thanks also to the NHMFL magnet group, for the support they provided, in particular John Miller, George Miller, Bruce Brandt and Scott Hannah.

I want to thank especially Giorgio Ambrosio, not only for the continued supervision of my work (without being “official” supervisor), but also for being a great friend. The tea break was a refreshing moment during the day. Thanks also to our “tea-break patron” John Tompkins, and our coffee club technician and supporter Dave Burk.

Thanks to Mark Baumeister for sustaining me during the last rush, and to my family and friends close and far, but still close in affection.